ISSN 2712-8172

MAGAZINE OF CIVIL ENGINEERING

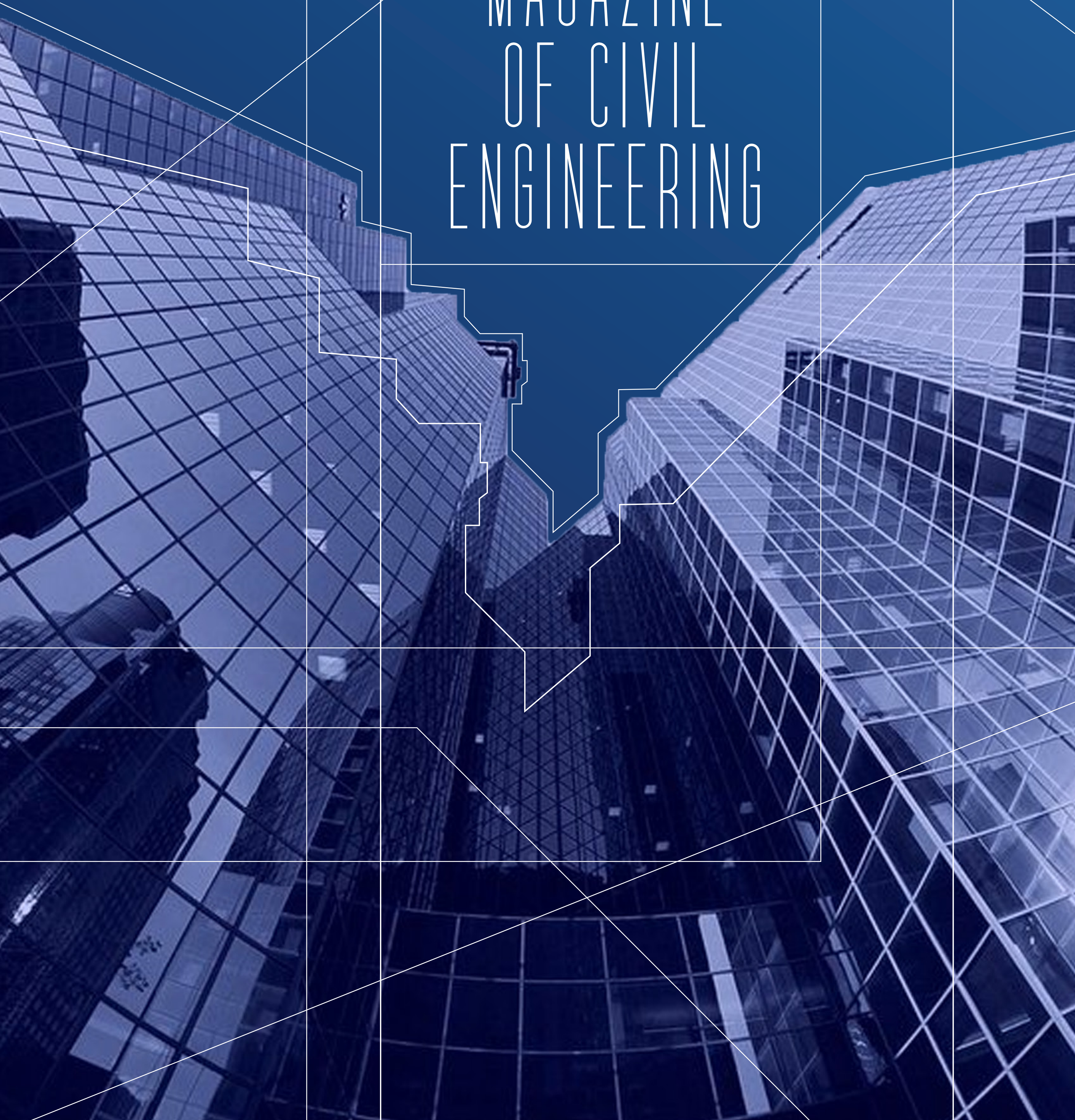

Magazine of Civil Engineering

ISSN 2712-8172

Online peer-reviewed open-access scientific journal in the field of Civil and Construction Engineering

Founder and Publisher: Peter the Great St. Petersburg Polytechnic University

This journal is registered by the Federal Service for Supervision of Communications, Information Technology, and Mass Media (ROSKOMNADZOR) in 2020. Certificate El No. FS77-77906 issued February 19, 2020.

Periodicity: 8 issues per year

Publication in the journal is open and free for all authors and readers.

Indexing: Scopus, Web of Sceince (ESCI, RSCI), DOAJ, Compendex, Google Academia, Index Copernicus, ProQuest, Ulrich's Serials Analysis System, CNKI

Corresponding address: 29 Polytechnicheskaya st., Saint Petersburg, 195251, Russia

Chief science editor:
D.Sc., Galina L. Kozinetc

Deputy chief science editors:
D.Sc., Sergey V. Korniyenko

Executive editor: Ekaterina A. Linnik

Translator, editor: Irina Ye. Lebedeva

Proofreader: Philipp Chrysanthes S. Bastian

DT publishing specialist:
Anastasiya A. Kononova

Contacts:
E-mail: mce@spbstu.ru
Web: http://www.engstroy.spbstu.ru

Date of issue: 19.05.2025

© Peter the Great St. Petersburg Polytechnic University. All rights reserved.
© Coverpicture – Polina A. Ivanova

Editorial board:

T. Awwad, PhD, professor, Damascus University, Syrian Arab Republic
A.I. Belostotsky, D.Sc., professor, StaDyO Research & Engineering Centre, Russia
A.I. Borovkov, PhD, professor, Peter the Great St. Petersburg Polytechnic University, Russia
M. Veljkovic, PhD, professor, Delft University of Technology, The Netherlands
R.D. Garg, PhD, professor, Indian Institute of Technology Roorkee (IIT Roorkee), India
M. Garifullin, PhD, postdoctoral researcher, Tampere University, Finland
T. Gries, Dr.-Ing., professor, RWTH Aachen University, Germany
T.A. Datsyuk, D.Sc., professor, Saint-Petersburg State University of Architecture and Civil Engineering, Russia
V.V. Elistratov, D.Sc., professor, Peter the Great St. Petersburg Polytechnic University, Russia
O.N. Zaitsev, D.Sc., professor, Southwest State University, Russia
T. Kärki, Dr.-Ing., professor, Lappeenranta University of Technology, Russia
G.L. Kozinetc, D.Sc., professor, Peter the Great St. Petersburg Polytechnic University, Russia
D.V. Kozlov, D.Sc., professor, National Research Moscow State Civil Engineering University, Russia
S.V. Korniyenko, D.Sc., professor, Volgograd State Technical University, Russia
Yu.G. Lazarev, D.Sc., professor, Peter the Great St. Petersburg Polytechnic University, Russia
M.M. Muhammadiev, D.Sc., professor, Tashkent State Technical University, Republic of Uzbekistan
H. Pasternak, Dr.-Ing.habil., professor, Brandenburgische Technische Universität, Germany
F. Rögener, Dr.-Ing., professor, Technology Arts Science TH Köln, Germany
V.V. Sergeev, D.Sc., professor, Peter the Great St. Petersburg Polytechnic University, Russia
T.Z. Sultanov, D.Sc., professor, Tashkent Institute of Irrigation and Agricultural Mechanization Engineers, Republic of Uzbekistan
A.M. Sychova, D.Sc., professor, Military Space Academy named after A.F. Mozhaysky, Russia
M.G. Tyagunov, D.Sc., professor, National Research University "Moscow Power Engineering Institute", Russia
M.P. Fedorov, D.Sc., professor, Peter the Great St. Petersburg Polytechnic University, Russia
D. Heck, Dr.-Ing., professor, Graz University of Technology, Austria
P. Cao, D.Sc., professor, Jilin University, China
A.G. Shashkin, D.Sc., PI Georekonstruktsiya, LLC, Russia
B.M. Yazyev, D.Sc., professor, Don State Technical University, Russia

Contents

Magazine of Civil Engineering. 2025. 18(3). Article No. 13501

Magazine of Civil Engineering

ISSN
2712-8172

journal homepage: http://engstroy.spbstu.ru/

Research article
UDC 624
DOI: 10.34910/MCE.135.1

Optimal distribution of piles under a concrete bridge abutment subject to vertical and torsion loads

A.Q. Hasan

Southern Technical University, Basrah, Iraq

✉ *a.almubarak@stu.edu.iq*

Keywords: pile group, bridge abutment, torsion load, pile distribution, ABAQUS

Abstract. The transmission of torsional load from the bridge abutment to the pile foundation has a great influence on the behavior of piles The situation is worsened by the combined loading on the outriggers, such as torsion, vertical, and lateral loads. This study focuses on the importance of distributing the piles under bridge abutment subjected to torsion loads in addition to vertical loads, where a suitable distribution is found to provide better behavior of the piles. Four groups of piles were taken under the bridge abutment, each containing six piles with different distributions. Torsional and vertical loads were applied to the bridge abutment to ensure the transfer of loads with a realistic effect. ABAQUS software was used for the simulation after the experimental work. The results of different pile distributions were very from the design point of view, as it was found that the distribution of the piles under the bridge abutment must be in a multi-line shape (rectangular distribution of the piles), because it forms a rigid mass with the surrounding soil, which is able to withstand torsional loads. In addition, it is preferable to avoid using single-distributed piles, since their response is very high and the failure occurs faster than in other groups.

Citation: Hasan, A.Q. Optimal distribution of piles under a concrete bridge abutment subject to vertical and torsion loads. Magazine of Civil Engineering. 2025. 18(3). Article no. 13501. DOI: 10.34910/MCE.135.1

1. Introduction

Numerous studies have investigated group piles under lateral, vertical, torsion, and combined loading conditions in recent years [1–6].

In [7], a model consisting of pile groups was used represented by a flexible beam-column elements with soil represented by an elastic linear spring to study the torsion behavior that occurred in the pile heads as a result of applying simultaneously horizontal and torsion loads on the group of piles. The study proved that uneven shear force distribution is important in pile design.

In [8], an analytical method to study the behavior of the pile group was developed, by coupling torsional resistances with lateral force. The approach involved analyzing piles under multidirectional lateral loads to compute induced torsion, followed by evaluation of horizontal load effects, ultimately combining these interactions for both single piles and pile groups consisting of 2×2 and 3×3 piles. This research provided key insights into torsion angles under random horizontal loading and the influence of pile spacing on torsional stiffness.

In [9], a finite element model was used to study the nonlinear behavior of groups of piles subjected to torsion loads. Groups of 1×2, 2×2, and 3×3 piles embedded in sandy soil were subjected to buckling and bending. The study assumed linear pile behavior and non-linear soil response. The results showed that the torsional strength increased with the increase in the pile size, spacing, length, and the soil stiffness, while the pile cap contributed 7 % of the total head resistance.

The present study analyzes the behavior of concrete bridge abutment subjected to vertical and torsion loads transmitted to the concrete piles. The change in the distribution of the piles under the bridge abutment will be studied to identify optimal configuration for the best structural behavior.

2. Methods

2.1. Problem

Bridge abutments are important structural elements that bear the loads from the bridge deck. They are subjected to vertical, lateral, and torsion loads that are transmitted directly to the piles through the pile cap. A bridge abutment (Fig. 1) located on the Khawr az-Zubayr Waterway in Basra governorate was analyzed, and the static and dynamic loads from the bridge deck were calculated and transferred directly to the abutment. A hypothetical dynamic torsion load was applied to the bridge abutment to simulate torsional loads on the abutment.

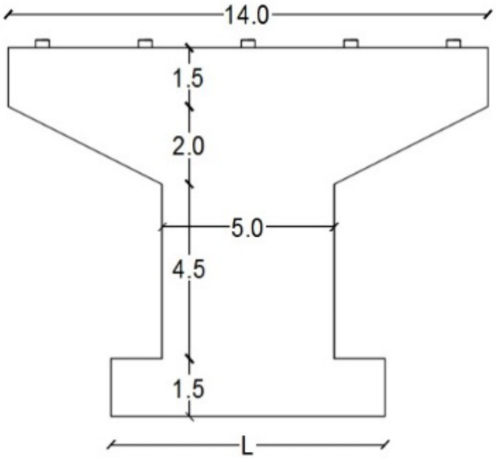

Figure 1. Bridge abutment dimensions.

For the pile distribution (Fig. 2), four groups were considered, each containing six piles with the same diameter of 80 cm and length of 20 m, but with different configurations:

- the first group was arranged with one line;
- the second was arranged with two lines;
- the third had a random distribution;
- the fourth had a circular distribution.

All the piles were connected with a pile cap, whose dimensions depended on the distribution of piles.

Soil is another critical factor influencing the behavior of the piles. The site soil was characterized as sandy clay soil, and the piles were submerged in it.

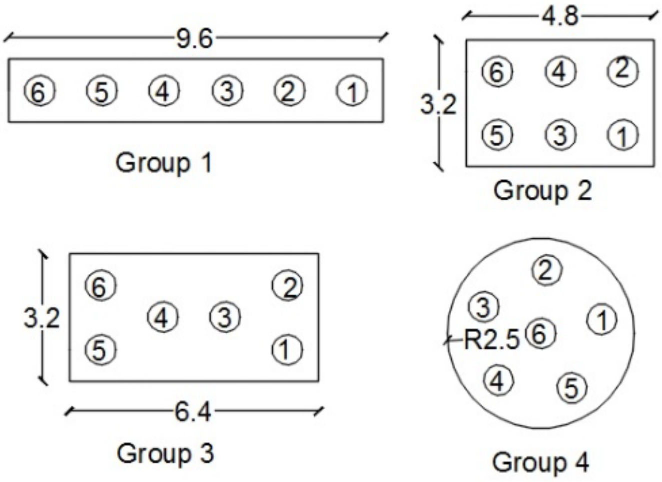

Figure 2. Pile distribution in groups under bridge abutment.

2.2. Modeling of the Problem

ABAQUS software was used for the simulation after the experimental work.

Element selection

Reinforced concrete abutments and piles were represented by a 20-node quadratic brick element C3D20, which is a three-dimensional non-linear element consisting of 20 nodes. While the soil was represented by a 20-node quadratic brick porous element C3D20P to accurately model soil plasticity and consolidation under loading. Reinforced bars were represented by a three-dimensional elastic beam element B32 consisting of three nodes, assumed to be embedded in the concrete. Fig. 3 shows the modeling in the ABACUS software of the problem for four case studies, including bridge abutments and soil [10–13].

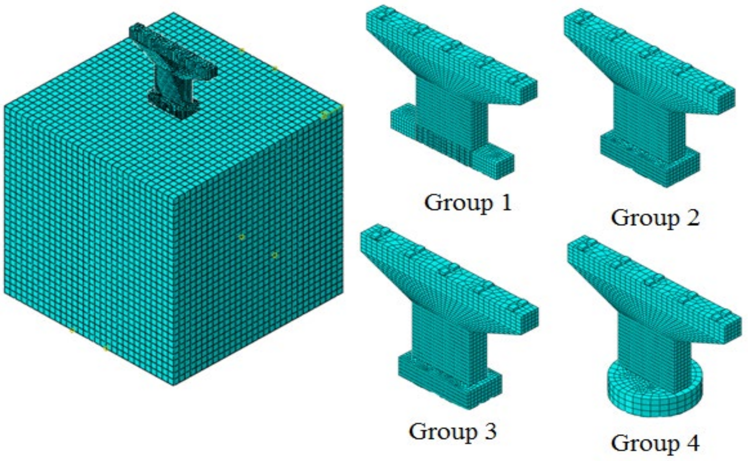

Figure 3. Finite element modeling of abutments and soil for all the four case studies.

Material properties

The material behavior reflects the actual distortions that occur in the material. For example, the Concrete Damage Plasticity (CDP) model was used to represent the concrete behavior (bridge abutment and piles), while the Mohr–Coulomb model was used to represent soil plasticity and deformations (Table 1). The plastic material was used for the steel with a yield strength of 420 MPa, zero plastic strain, an elastic modulus of 210 GPa and Poisson’s ratio of 0.3 [14–16].

Table 1. Material Properties [15].

		Concrete		
Dilation angle	**Eccentricity**	**fb0/fc0 ratio**	**Stress invariant ratio *k***	**Viscosity parameter μ**
35	0.1	1.16	0.667	0
Elastic modulus, GPa		23.5	Poisson’s ratio	0.2
Density, kg/m^3		2400		
		Soil		
Elastic modulus, GPa		14	Poisson’s ratio	0.4
Density, kg/m^3		1600		
Cohesion		30	Friction angle, degrees	40

Boundary conditions

A surface-to-surface interaction was defined between piles and soil, a penalty friction coefficient was adopted equal to 0.36, and all reinforced steel was represented by an embedded element in the concrete. As for the soil boundaries, it was fully fixed at the bottom, and pinned at the sides according to the movement direction. The distance from the pile cap to the soil edge was approximately 8 times the pile width [17, 20].

Loading and analysis

Vertical loads were calculated from the dead loads (bridge self-weight and additional permanent loads) and live loads (vehicle traffic). Torsion load was simulated using two equal and opposite forces. A dynamic analysis was performed to obtain realistic structural responses [21-24].

Verification in the ABAQUS software

The validation, based on [25], involved a 2×2 pile group embedded in loose sandy soil (Fig. 4). The piles consisted of aluminum tubes (diameter = 15.74 mm, thickness = 0.9 mm, length = 300 mm), with a 30 mm-thick aluminum alloy pile cap. ABAQUS simulation results for horizontal displacement vs. shear force (Fig. 5) and torque vs. twist angle (Fig. 6) at the pile head showed good agreement with experimental data [25]

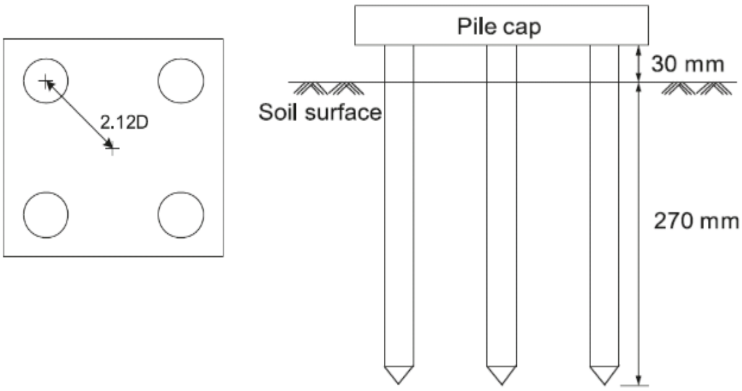

Figure 4. Pile group details for experimental work [20].

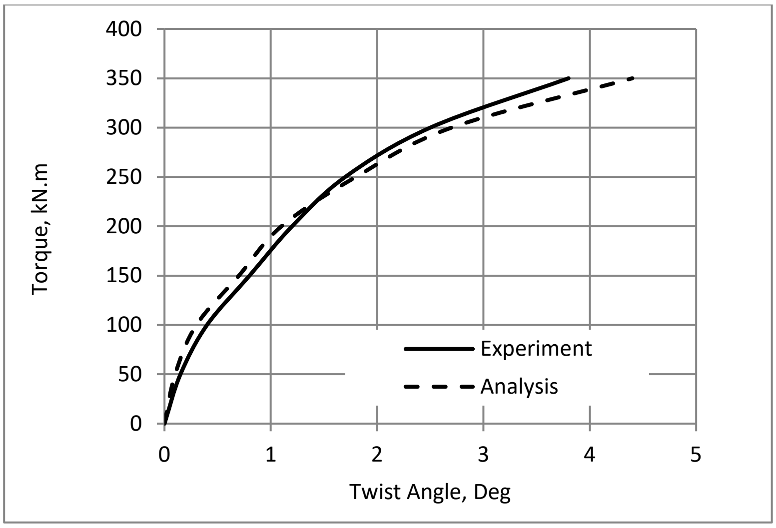

Figure 5. Shear force vs. displacement for experiment and analysis verification.

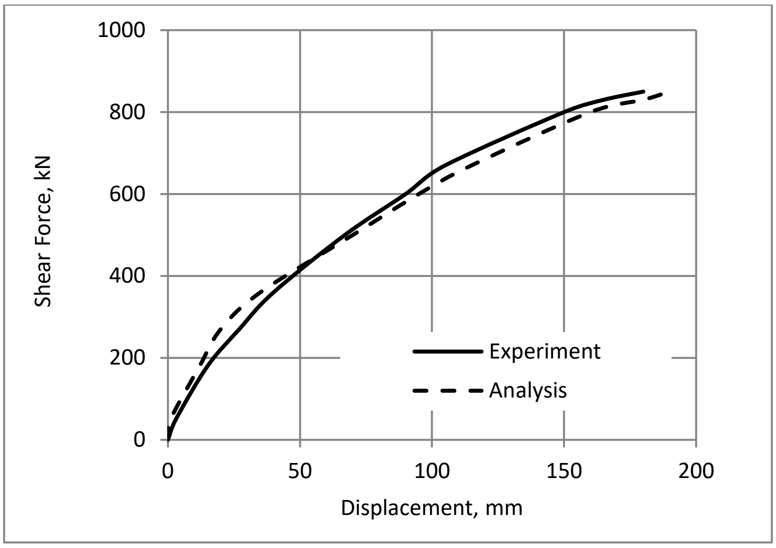

Figure 6. Torque vs. twist angle for experiment and analysis verification.

3. Results and Discussion

3.1. Load – vertical displacement

Fig. 7 shows the relationship between the load and the vertical displacement in the pile cap for the four groups. It can be observed that Group 1 exhibited the highest response, while Group 2 showed the lowest response. This is due to the distribution pattern of the piles. Despite having equal surface areas, Group 1 showed higher stiffness along the long side of the cap compared to the other groups, which makes the greater response. Groups 3 and 4 were characterized by a large surface area but demonstrated lower stiffness compared to Group 1. When changing the distribution of the piles from Group 1 to the other groups, the load capacity was reduced by 60, 27, and 22 %, respectively.

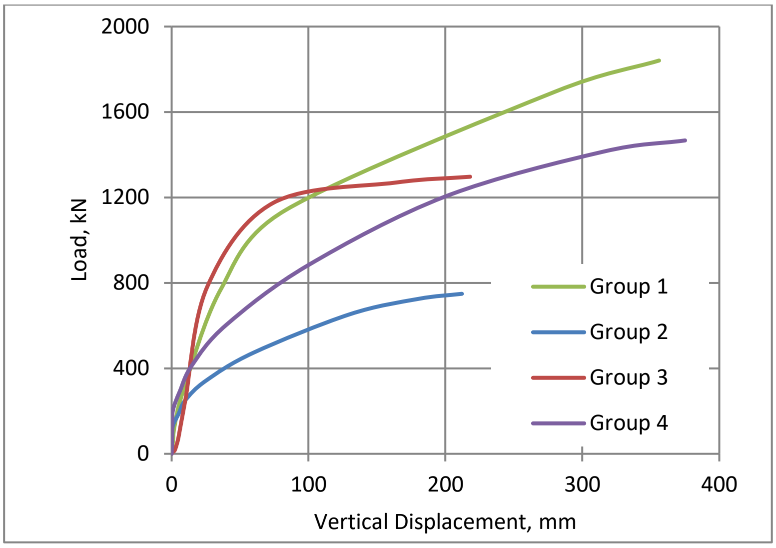

Figure 7. Load–vertical displacement for all the four pile groups.

3.2. Torsion vs. twist angle

Although Group 1 exhibits strong stiffness in the longitudinal direction, which gave the highest endurance of the forces, it showed the lowest results for torsion vs. twist angle due to the weakness in the transverse direction. The other groups, especially Group 3, demonstrated excellent endurance because of the high stiffness in the longitudinal and transverse directions, with the amount of torsion increased by 66 %. And Group 4 demonstrated a 15 % increase in torsional capacity. Group 2 exhibited excellent torsional behavior with high stiffness but with an increase in the moments, the twist angle became minimal, due to the near equal stiffness in both directions. Fig. 8 show the torsion and Twist angle relation for the groups.

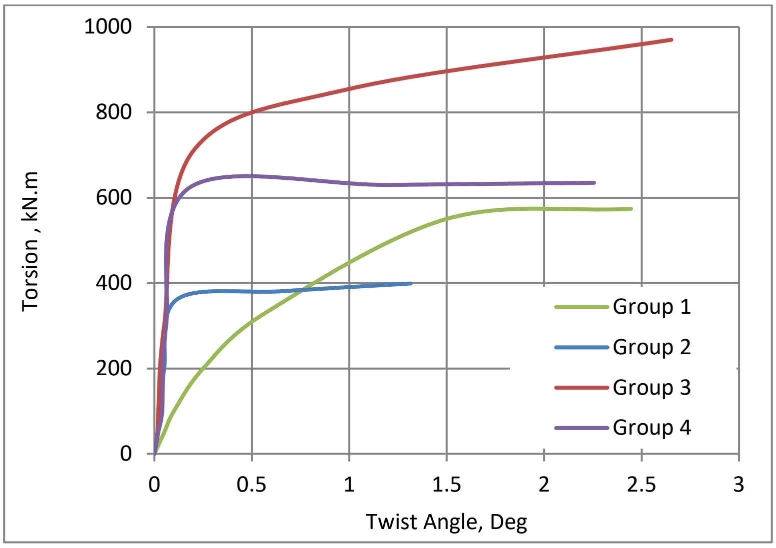

Figure 8. Torsion vs. twist angle for all the four pile groups.

3.3. Displacement along pile length

Fig. 9 shows the lateral displacement along the piles. The displacement distribution depends on the location of the pile and the amount of lateral load applied to it. In Group 1, displacements at the pile head ranged from 25 mm in the outriggers far from the load (P1) to 150 mm in the piles close to the load (P2), representing the highest lateral displacements. Group 2 had the lowest lateral displacement of 30 mm for almost all the piles due to the proximity of the piles to each other, making it work as a single block. The load was applied almost equally on all the piles. In Group 3, the displacement distribution varied in the pile head: some of the nearby piles (in the middle, P3) had high displacement of 75 mm, while the other (P4) – 70 mm, and the side piles ranged between 45 and 60 mm due to the position of the load. In Group 4, the results of the displacements in the pile head varied from 40 to 50 mm due to the distribution of the piles symmetrically and closely under the load. The ratio of the pile fixed depth varied from 15 to 17 m due to the torsion occurring in the groups.

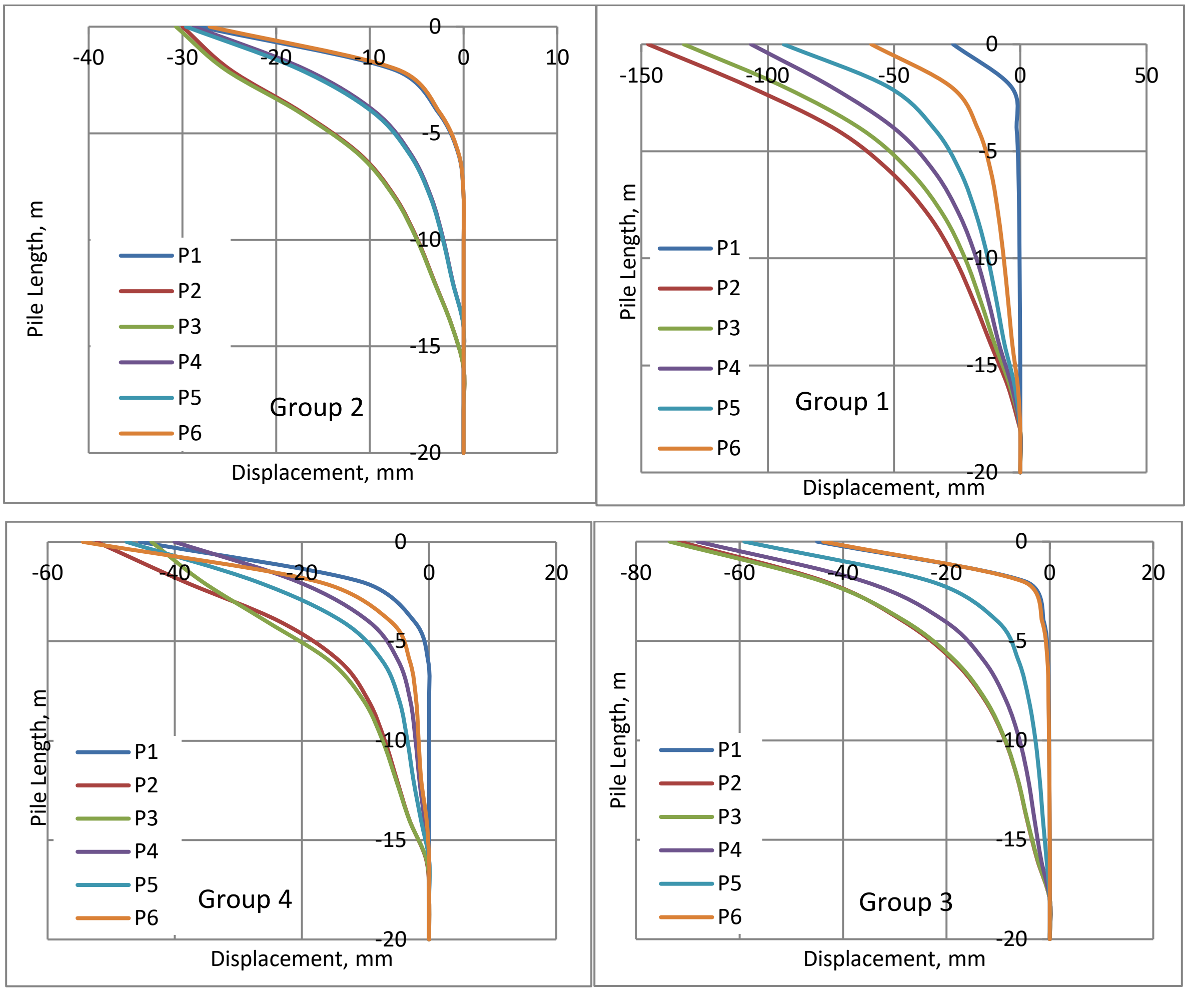

Figure 9. Lateral displacement along pile length for all the four pile groups.

3.4. Twist angle along pile length

Group 2 also had the lowest response in case of the deflection angle (Fig. 10) due to the proximity location of the piles to each other, where the maximum twist angle was 1.3°, significantly smaller than the other groups. Group 4 had similarly small twist angle of 2.1° due to the distribution of the piles close to each other. Groups 1 and 3 had almost the same maximum twist angle of 2.5°, because the bridge abutment is directly supported by these piles. All the twist angles disappear (become zero) at a depth of 14 m, and this is a good indicator that corresponds to the fixed pile depth.

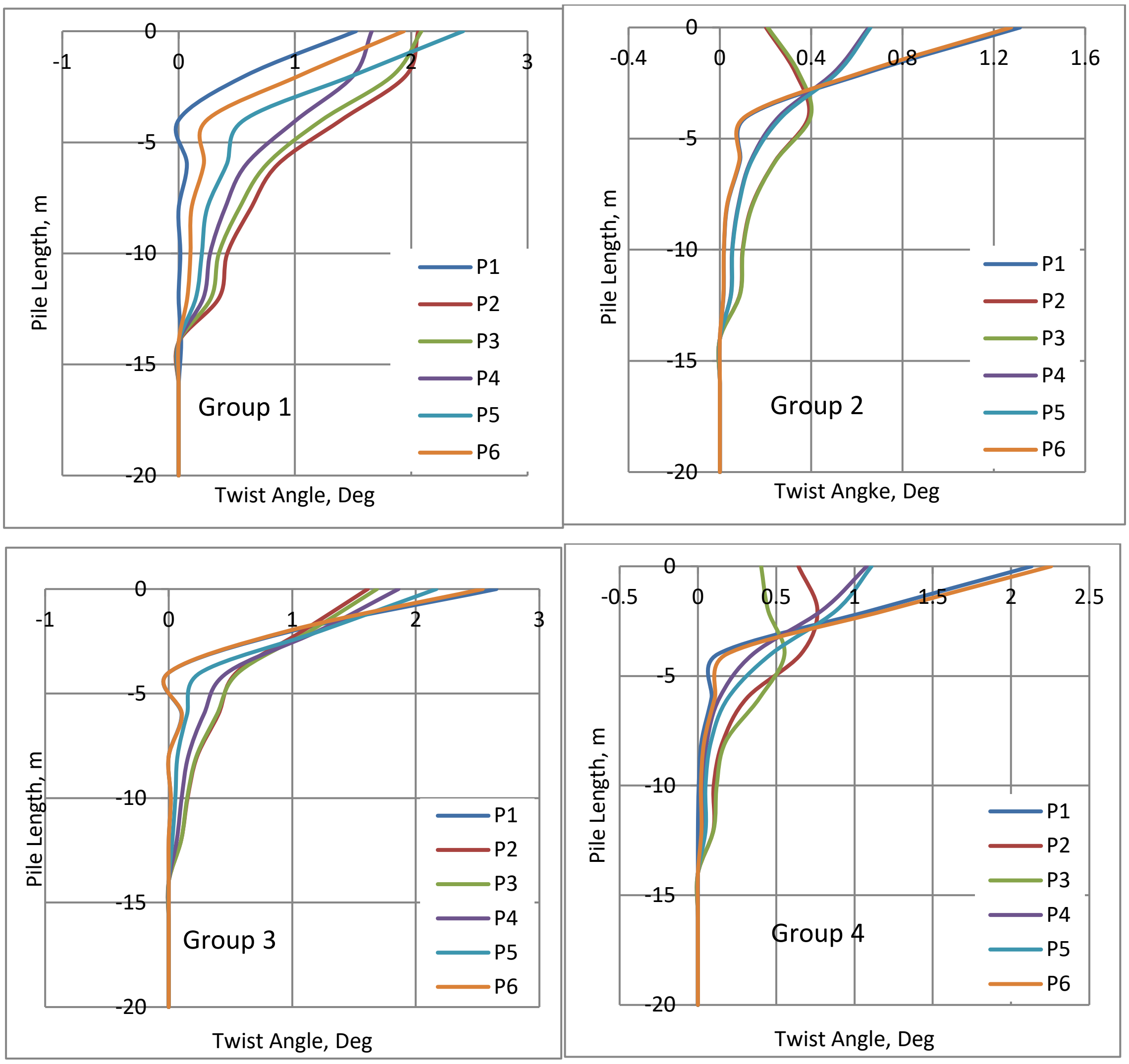

Figure 10. Twist angle along pile length for all the four pile groups.

3.5. Shear force along pile length

Shear forces distributed on the pile head are very important, with lower shear forces indicating greater stability. Fig. 11 shows the distribution of piles for the four pile groups. Group 2 had the lowest shear forces (600 kN) on the pile head among the other groups, while Group 1 had the highest shear forces (1900 kN). Groups 1 and 3 differed in the distribution of shear forces on the pile head, but Groups 2 and 4 had almost equal shear forces at the pile head, because the distribution of the piles was close to each other and the distribution of loads was equal. The inflection point of the shear forces (Fig. 11) at a depth of 1 m was the result of the strong resistance of the soil to the applied loads. The forces reduced to zero at a depth of 7.5 m, indicating that all force was transferred from piles to the soil.

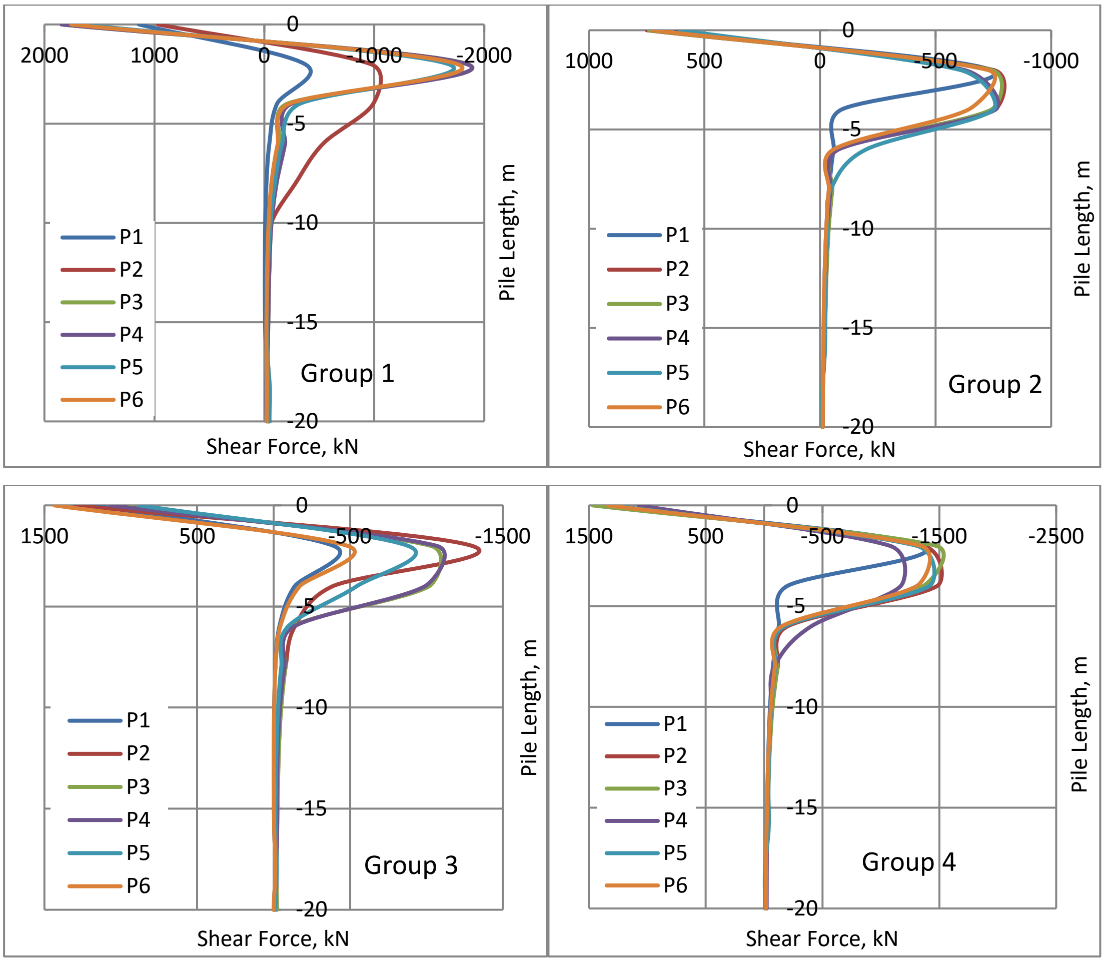

Figure 11. Shear force along pile length for all the four pile groups.

3.6. Bending moment along pile length

Fig. 12 shows the distribution of bending moment along the pile length for the four pile groups. Group 2 was less responsive than the other groups. Groups 2 and 4 had the same distribution of bending moment along the pile length with minor differences in value, while in Group 3, the corner piles (P1, P6) had the highest bending moment values due to its distance from the center of the applied torsion. In Group 1, the distribution of bending moment was successive between the piles, with piles P1, P3, and P5 showing smaller values compared to the piles P2, P4, and P6. The fixed moment depth occurred at 12 m from the soil level, the zero value indicating the transfer of all moments from the pile to the soil.

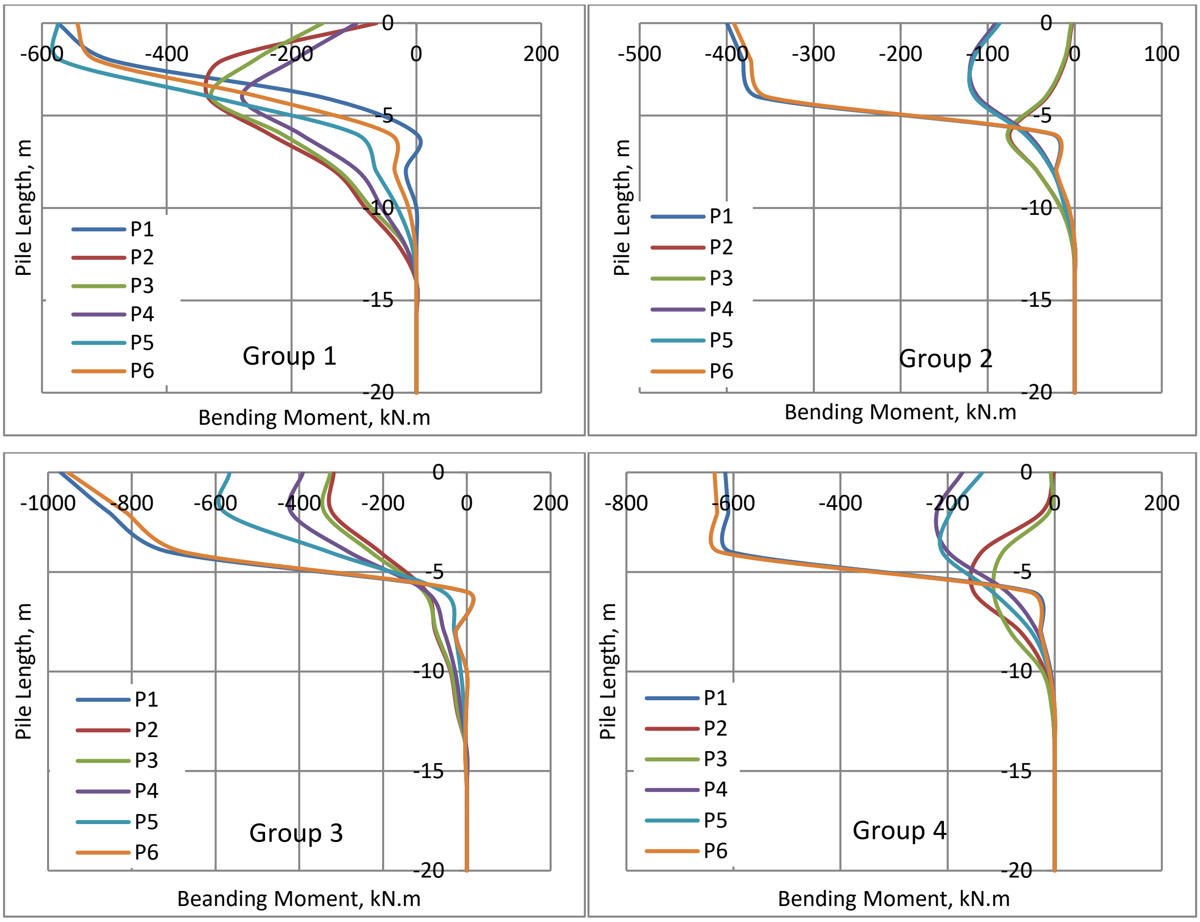

Figure 12. Bending moment along pile length for all the four pile groups.

4. Conclusion

From the results and discussion above, some important factors that are useful when designing deep foundations (piles) can be deduced, which are as follows:

1. The distribution of piles under bridge abutments is very important and needs to be considered in foundation design.
2. Distributing piles in multiple closely spaced lines (rectangular or square arrangement) is much more effective than a random pile distribution.
3. The ABAQUS analysis produced results very close to experimental data, confirming its reliability for solving torsion-related problems.
4. Group 1 (single-line piles) exhibited high displacement due to weak stiffness in the short direction, where the load concentrated on only two middle piles.
5. The higher load in Group 1 resulted from its 9.6 m pile cap length, followed by Group 3 (6.4 m), Group 4 (5 m), while Group 2 showed minimal load and displacement.
6. Group 1 had the poorest torsion-twist angle response due to low stiffness, whereas Group 2 showed marginally better performance.
7. Displacement along the pile length was lowest in Group 2, followed by Group 4, Group 3, and finally Group 1 with the highest response.
8. Group 2's minimal twist angle resulted from closely spaced piles acting as a rigid mass; Group 4 performed similarly, while other groups suffered from suboptimal pile arrangements.
9. The fixed pile depth occurred at 14–17 m for both lateral displacement and twist angle, with variations attributable to pile distribution and soil conditions.
10. Shear forces peaked in Group 1 due to load concentration on central piles, while Group 2's uniform force distribution yielded the lowest values. Group 4's results were comparable to Group 2.

11. Bending moments were highest in distant piles and lowest in proximate ones. Group 2 showed minimal moment response, contrasting with Group 3's higher values for the aforementioned reason.
12. Complete shear force transfer occurred at 7.5 m depth, and bending moments fully transferred at 12 m for all groups, owing to surrounding soil stiffness.
13. The shear force inflection point at 1 m depth for all piles reflected the soil's high load resistance.
14. Fixity moment depth and fixed pile length remained constant regardless of pile group distribution.
15. For this study, Group 2 (rectangular distribution) is recommended due to its low response, as closely spaced piles and soil formed a rigid mass resisting torsional loads. Group 4 (circular distribution) is a viable alternative given its similar performance.

References

1. Hasan, A.Q., Qasim, R.M. A Study of The Effect of Loaded Pile Groups on Neighboring Fuel Storage Tanks. IOP Conference Series: Materials Science and Engineering. 2020. 671. Art. no. 012077. DOI: 10.1088/1757-899X/671/1/012077
2. Zhang, L., Tsang, C.Y.M. Three-dimensional analysis of torsionally loaded large-diameter bored pile groups. Tall Buildings. 2005. Pp. 311–317. DOI: 10.1142/9789812701480_0048
3. Zidan, A.F., Ramadan, O.M. A hybrid MC-HS model for 3D analysis of tunnelling under piled structures. Geomechanics and Engineering. 2018. 14(5). Pp. 479–489. DOI: 10.12989/gae.2018.14.5.479
4. Stuedlein, A.W., Barbosa, A.R., Li, Q. Evaluation of torsional load transfer for drilled shaft foundations. Final report. SPR 304-701. Oregon Department of Transportation. Salem, OR. Federal Highway Administration. Washington, DC, 2016. 159 p. URL: https://rosap.ntl.bts.gov/view/dot/30955/dot_30955_DS1.pdf (date of application: 25.07.2025).
5. Hasan, A.Q. Analytical and Experimental Response of Single Pile to Pure Torsion. International Journal of Civil Engineering and Technology. 2019. 10(3). Pp. 841–851.
6. Kong, L.G, Chen, R.P., Wang, S.H., Chen, Y.M. Response of 3×3 Pile Groups in Silt Subjected to Eccentric Lateral Loading. Journal of Geotechnical and Geoenvironmental Engineering. 2015. 141(7). Art. no. 04015029. DOI: 10.1061/(ASCE)GT.1943-5606.0001313
7. Hasan, A.Q., Qasim, R.M. Study The Behavior of Pile Group Under Torsional and Horizontal Load. Journal of Physics: Conference Series. 2021. 1773. Art. no. 012032. DOI: 10.1088/1742-6596/1773/1/012032
8. Chen, S.L., Kong, L.G., Zhang, L.M. Analysis of pile groups subjected to torsional loading. Computers and Geotechnics. 2016. 71. Pp. 115–123. DOI: 10.1016/j.compgeo.2015.09.004
9. Zidan, A.F., Ramadan, O.M.O. Three-dimensional analysis of pile groups subject to torsion. Geotechnical Research. 2019. 7(2). Pp. 103–116. DOI: 10.1680/jgere.19.00037
10. Qasim, R.M., Hasan, A.Q. Investigating the Behavior of Offshore Platform to Ship Impact. Civil Engineering Journal. 2020. 6(3). Pp. 495–511. DOI: 10.28991/cej-2020-03091486
11. Naylor, D.J., Pande, G.N., Simpson, B., Tabb, R. Finite elements in geotechnical engineering. Pineridge Press. Swansea, UK, 1981. 245 p. DOI: 10.1002/nag.1610060409
12. ABAQUS/CAE User's Manual. Hibbitt, Karlsson & Sorensen, Inc. 2000. URL: https://www.researchgate.net/profile/Slimani-Faouzi/post/Can_anybody_provide_me_the_tutorial_for_warm_deep_drawing_in_Abaqus/attachment/59d63615c49f478072ea3d1c/AS%3A273635439251467%401442251180785/download/ABAQUS%5B1%5D.CAE+Users+Manual.pdf (date of application: 25.07.2025).
13. Reese, L.C., Van Impe, W. Single Piles and Pile Groups Under Lateral Loading. 2nd edn. CRC Press. Boca Raton, 2011. 53 p.
14. Wood, D.M. Soil Behaviour and Critical State Soil Mechanics. Cambridge University Press. NY, 1990. 462 p.
15. Poulos, H.G. Torsional Response of Piles. Journal of the Geotechnical Engineering Division. 1975. 101(10). Pp. 1019–1035. DOI: 10.1061/AJGEB6.0000203
16. Fioravante, V. On the Shaft Friction Modelling of Non-Displacement Piles in Sand. Soils and Foundations. 2002. 42(2). Pp. 23–33. DOI: 10.3208/sandf.42.2_23
17. Hasan, A.Q. Dynamic analysis of steel offshore structures considering the effect of soil-structure interaction. PhD thesis. Basrah, 2016.
18. Anoyatis, G., François, S., Orakci, O., Tsikas, A. Soil–pile interaction in vertical vibration in inhomogeneous soils. Earthquake Engineering & Structural Dynamics. 2023. 52(14). 4582–4601. DOI: 10.1002/eqe.3968
19. Boyko, I., Krivenko, O., Gavryliuk, O. Numerical simulation of interaction bored pile and soil mass with taking into account the dilatancy of the soil. Bases and Foundations. 2023. DOI: 10.32347/0475-1132.46.2023.9-16
20. Alver, O., Eseller-Bayat, E. Effect of Soil Damping on the Soil–Pile–Structure Interaction Analyses in Cohesionless Soils. Applied Sciences. 2022. 12(18). 9002. DOI: 10.3390/app12189002
21. Qiao, S., Dong, Ch., Li, G., Wang, G. Modified Interaction Method for Response of Group Piles Considering Pile–Soil Slip. Mathematics. 2022. 10(15). 2616. DOI: 10.3390/math10152616
22. Yu, Y., Bao, X., Liu, Z., Chen, X. Dynamic Response of a Four-Pile Group Foundation in Liquefiable Soil Considering Nonlinear Soil-Pile Interaction. Journal of Marine Science and Engineering (JMSE). 2022. 10(8).:1026. DOI: 10.3390/jmse10081026
23. Tretiakova, O. Model of pile-frozen soil interaction in a closed form. Magazine of Civil Engineering. 2022. 115(7). Article No.1501. DOI: 10.34910/MCE.115.1
24. Ali, A.M., Essa, M.J.K., Hassan, A.Q. Dynamic analysis of offshore piles embedded in elastoplastic soft clay. Proceedings of International Engineering and Construction. 2016. DOI: 10.14455/ISEC.res.2016.112
25. Kong, L.G., Zhang, L.M. Experimental study of interaction and coupling effects in pile groups subjected to torsion. Canadian Geotechnical Journal. 2008. 45(7). Pp. 1006–1017. DOI: 10.1139/T08-038

Information about the author:

***Abdulameer Qasim Hasan Al-Mubarak**, PhD*
ORCID: https://orcid.org/0000-0002-4502-5346
E-mail: a.almubarak@stu.edu.iq

Received: 13.11.2022. Approved: 22.12.2024. Accepted: 22.04.2025.

Magazine of Civil Engineering

ISSN
2712-8172

journal homepage: http://engstroy.spbstu.ru/

Research article

UDC 624.04

DOI: 10.34910/MCE.135.2

Rectangular flat finite element for modeling the process of crack formation

Yu.Ya. Tyukalov

Vyatka State University, Kirov, Russian Federation

yutvgu@mail.ru

Keywords: finite element method, crack width, tensile strength, stiffness matrix, possible displacements, crack tip

Abstract. A rectangular flat finite element is proposed that allows modeling the process of crack formation without changing the initial elements' grid. The proposed finite element can be used to calculate structures made of reinforced concrete, masonry, fiber concrete, and other materials with low tensile strength. To calculate structures with existing cracks, their position can be specified as initial data. The finite element was formed based on the stress fields approximations and the principle of possible displacements to obtain the equilibrium equations of nodes. To calculate the stiffness matrix of the finite element, the principle of minimum additional energy was used, to which algebraic equilibrium equations were added using the Lagrange multiplier method. After a crack formation in the centre of finite element, additional degrees of freedom were introduced into its nodes, determining the possible mutual displacement of the element's parts separated by the crack. The calculations were performed for a rectangular elastic bending beam with a low tensile strength. The reinforcement was located in the tensile zone of the beam. For comparison, the beam was also calculated using standard finite elements. The comparison of the results, including the crack width, for the two solutions showed that they coincided with high accuracy. The maximum displacements differ by 1.5 %, the maximum stresses in compressed concrete and reinforcement differ by less than 1 %. The crack width for the two solutions differs by no more than 5–7 %.

Citation: Tyukalov, Yu.Ya. Rectangular flat finite element for modeling the process of crack formation. Magazine of Civil Engineering. 2025. 18(3). Article no. 13502. DOI: 10.34910/MCE.135.2

1. *Introduction*

In the construction of industrial and civil buildings, materials such as reinforced concrete and masonry are widely used. Such materials have low tensile strength, so cracks occur in them. The formation and growth of cracks causes a redistribution of forces and stresses in the structural elements. A number of scientific articles are devoted to the problem of calculating structures with cracks [1–3]. In [2, 4, 5], Extended Finite Element Method (XFEM) and substructure methods were used for crack modeling. In [2], the structures are divided into several substructures, and XFEM is employed to model the presence of cracks within each substructure. To evaluate the proposed method, four examples have been considered. In [6], a finite element formulation is developed that modeled a local crack as imposed strain to simulate fracture in quasi-brittle materials. For simplicity, only tensile crack has been considered. The structure is modeled as an averaged continuum, using constant strain triangles. Cracks can develop along the element edges by controlling the forces normal to the potential crack direction at the nodes. In [7], a novel local mesh refinement numerical manifold method with variable-midside-node elements for fracture analysis in solids is presented. In the framework of conventional numerical manifold method, a local mesh refinement algorithm was proposed to achieve automatic multilevel refinement to the original coarse mesh in a focused region. In [8], a constitutive model coupling the rotating smeared crack model and the plasticity model in incremental sequentially linear analysis is proposed.

In [9], the sequentially linear approach based on the exponential softening is proposed to solve the divergence problem of computational process due to negative stiffness encountered in fracture analysis of concrete or masonry structure, and nonlinear response is obtained through several linear analyses. In [10–13], the formation of cracks in various beam systems is investigated. The article [10] presents a novel strain-based beam finite element family for the analysis of softening and localization of longitudinal deformations in planar frames made of brittle materials. In the analysis, the softening region was limited only to a discrete crack, which was treated as an “exclude” element point, i.e., the deformation quantities in the crack were considered separately from the deformations in the immediate vicinity of the crack. Localized deformations are connected to the element only through kinematic quantities, which used to describe the crack opening. The problem of analyzing the stress-strain state of shells, plates and nodal connections taking into account cracks is investigated in [14–17]. In [17], an innovative fiber beam-column model updating method based on static deflection and crack width is proposed. The fiber beam-column finite element program COMPONA-MARC, developed in this laboratory, is modified to efficiently simulate the nonlinear cracking behavior of reinforced concrete flexural members.

A large number of scientific papers are devoted to the study of crack propagation based on fracture mechanics [18–20]. In [18], a numerical model for wing crack initiation and propagation due to shear slip is presented. The governing mathematical model is based on linear elastic fracture mechanics and contact mechanics, along with failure and propagation criteria for multiple mixed-mode fracture propagation. The numerical solution approach is based on a combination of the finite element method combined with quarter point elements to handle the singularity at the fracture tips. In [21], a method to achieve smooth nodal stresses in the XFEM application is presented. The salient feature of the method is to introduce an “average” gradient into the construction of the approximation, resulting in improved solution accuracy, both in the vicinity of the crack tip and in the far field. Due to the higher-order polynomial basis provided by the interpolants, the new approximation enhances the smoothness of the solution without requiring an increased number of degrees of freedom. An alternative formulation of the finite element method, which is based on stress approximations, is presented in [22–25]. The solution is based on the additional energy functional, to which, using the Lagrange multiplier method, the algebraic equilibrium equations of the finite element mesh nodes are added. The equilibrium equations are constructed with the principle of possible displacements.

In [26], a new finite element formulation for the analysis of reinforced concrete slabs is proposed, accounting for concrete cracking and reinforcement yielding. The proposed formulation, developed within the framework of Lumped Damage Mechanics, considers that all inelastic effects **are** localized in lines and relates all numerical parameters to the mechanical properties of the slab. The problem of formation and propagation of cracks in bending plates is studied in [27–29]. In [27], the crack is modelled as a rotational spring with additional rotational freedoms being added to the finite element nodes. The method is validated against published results for through-the-depth cracks. Cracks with varying direction, location, depth, and length are used to study the effects of changing the crack parameters. A novel refined numerical method for simulating cross-scale crack propagation in 3D massive concrete structure is proposed in [30]. The applicability of the proposed method is verified by a three-point bending test of the beam with regular and irregular cracks. Finally, the simulation analysis of the roller-compacted concrete dam with cross-scale irregular cracks is performed based on the monitoring cracks. The modifications of the traditional finite element method that allow modeling the formation and propagation of cracks are presented in [31, 32]. In [33], an innovation is proposed to use precise shell-solid finite element models to study the redistribution factor of composite frame structures under horizontal loads considering concrete cracking. Using shell-solid finite element models, the cracking behavior due to the slab spatial composite effect can be considered. In [34], the strain compliance crack model is proposed to capture, as reported by tests, the specifics of various cases of crack spacing and width analysis involving primary and secondary cracks in reinforced concrete beams. The model dwells on calculating crack spacing based on the reinforcement strain profile. The works [35–37] also present methods for solving stability and statics problems based on stress approximation, as well as mixed approximations.

The problem of developing methods for calculating building structures taking into account the process of crack formation remains relevant. The largest number of scientific articles are devoted to studies of the crack propagation under constant load based on fracture mechanics. The purpose of this work is to develop a flat finite element that will allow modeling the process of crack formation under loading without changing the finite element mesh.

2. Methods

Stiffness matrix of an equilibrium rectangular finite element without a crack.

To construct the stiffness matrix, we use the following stresses approximations over a finite element domain:

$$\sigma_x = a_1 + a_4 y, \ \sigma_y = a_2 + a_5 x, \ \tau_{xy} = a_3. \tag{1}$$

Similar approximations were used in [35] to construct a flat finite element of arbitrary shape. Thus, the shear stresses are constant in the finite element region, and the normal stresses along the X and Y axes vary linearly. The stress approximations (1) satisfy the homogeneous differential equations of equilibrium of the plane problem of elasticity theory.

Let us write expressions (1) in matrix form:

$$\sigma = \mathbf{Ha}, \ \sigma = \begin{Bmatrix} \sigma_x \\ \sigma_y \\ \tau_{xy} \end{Bmatrix}, \ \mathbf{H} = \begin{bmatrix} 1 & 0 & 0 & y & 0 \\ 0 & 1 & 0 & 0 & x \\ 0 & 0 & 1 & 0 & 0 \end{bmatrix}, \ \mathbf{a} = \begin{Bmatrix} a_1 \\ a_2 \\ a_3 \\ a_4 \\ a_5 \end{Bmatrix}. \tag{2}$$

Consider the stiffness matrix construction of a rectangular finite element (Fig. 1), which will be used later to model the process of crack formation in the structure tension zones.

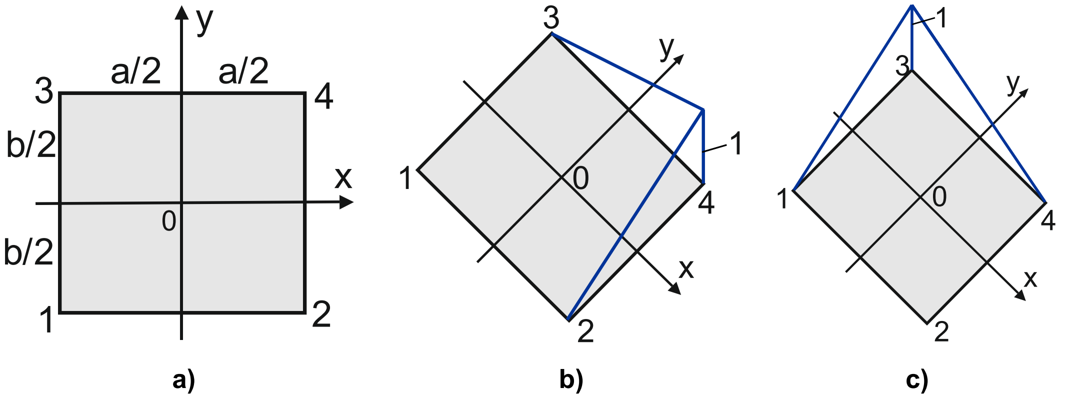

a) b) c)

Figure 1. Rectangular finite element: a) coordinate system; b) possible displacement of node 4; c) possible displacement of node 3.

The nodal unknowns vector includes the displacements of a node along the X and Y axes, respectively:

$$\mathbf{u}_i^{\mathrm{T}} = \left(u_{x,i} \ \ u_{y,i} \right). \tag{3}$$

The stiffness matrix is obtained using the principles of minimum additional energy and possible displacements. The principle of possible displacements is written as follows:

$$\delta \mathrm{U}_i + \delta \mathrm{V}_i = 0, \tag{4}$$

where $\delta \mathrm{U}_i$ is the deformations energy with possible displacement of the node; $\delta \mathrm{V}_i$ is the potential of nodal reactions, equal to the work of the reaction taken with a minus sign.

By considering the possible displacements of nodes, we can obtain algebraic equilibrium equations for them. To approximate the possible displacements vector over the finite element domain, we use the following functions:

$$\delta u_x = \delta u_y = N_i(x, y) = \frac{1}{4}\left(1 + \frac{4 x x_i}{a^2}\right)\left(1 + \frac{4 y y_i}{b^2}\right), \ i = 1, 2, 3, 4. \tag{5}$$

where x_i, y_i are the nodal point coordinates in the local coordinate system (Fig. 1). Using (5), we obtain expressions for the deformations corresponding to the possible displacement of the node along the X axis:

$$\delta \varepsilon_x = \frac{\partial N_i(x, y)}{\partial x} = \frac{x_i}{a^2}\left(1 + \frac{4 y y_i}{b^2}\right), \ \delta \tau_{xy} = \frac{\partial N_i(x, y)}{\partial y} = \frac{y_i}{b^2}\left(1 + \frac{4 x x_i}{a^2}\right). \tag{6}$$

And with the possible displacement of the node along the Y axis, we obtain, respectively:

$$\delta\varepsilon_y = \frac{\partial N_i(x,y)}{\partial y} = \frac{y_i}{b^2}\left(1+\frac{4xx_i}{a^2}\right),\ \delta\tau_{xy} = \frac{\partial N_i(x,y)}{\partial x} = \frac{x_i}{a^2}\left(1+\frac{4yy_i}{b^2}\right). \tag{7}$$

The deformation energy for possible displacement of node i along the X axis:

$$\delta \mathrm{U}_{i,x} = t\int_{-b/2}^{b/2}\int_{-a/2}^{a/2}\left(\sigma_x\delta\varepsilon_x + \tau_{xy}\delta\gamma_{xy}\right)\mathrm{d}x\mathrm{d}y = a_1\frac{tbx_i}{a} + a_4\frac{tbx_iy_i}{3a} + a_3\frac{tay_i}{b}, \tag{8}$$

where t is the finite element thickness.

Similarly, we obtain the deformation energy expression for the possible displacement along the Y axis:

$$\delta \mathrm{U}_{i,y} = t\int_{-b/2}^{b/2}\int_{-a/2}^{a/2}\left(\sigma_y\delta\varepsilon_y + \tau_{xy}\delta\gamma_{xy}\right)\mathrm{d}x\mathrm{d}y = a_2\frac{tay_i}{b} + a_5\frac{tax_iy_i}{3b} + a_3\frac{tbx_i}{a}. \tag{9}$$

We write the equilibrium equations (3) for node i in a matrix form:

$$\mathbf{L}_i\mathbf{a} - \mathbf{R}_i = 0; \tag{10}$$

$$\mathbf{L}_i = \begin{bmatrix} \frac{tbx_i}{a} & 0 & \frac{tay_i}{b} & \frac{tbx_iy_i}{3a} & 0 \\ 0 & \frac{tay_i}{b} & \frac{tbx_i}{a} & 0 & \frac{tax_iy_i}{3b} \end{bmatrix},\ \mathbf{R}_i = \begin{Bmatrix} R_{i,x} \\ R_{i,y} \end{Bmatrix}. \tag{11}$$

The system of equilibrium equations for all nodes of the element has the following form:

$$\mathbf{La} - \mathbf{R} = 0,\ \mathbf{L} = \begin{bmatrix} \mathbf{L}_1 \\ \mathbf{L}_2 \\ \mathbf{L}_3 \\ \mathbf{L}_4 \end{bmatrix},\ \mathbf{R} = \begin{Bmatrix} \mathbf{R}_1 \\ \mathbf{R}_2 \\ \mathbf{R}_3 \\ \mathbf{R}_4 \end{Bmatrix}. \tag{12}$$

Let us introduce the notation for the material stiffness matrix:

$$\mathbf{E}^{-1} = \frac{t}{E}\begin{bmatrix} 1 & -\mu & 0 \\ -\mu & 1 & 0 \\ 0 & 0 & 2(1+\mu) \end{bmatrix}, \tag{13}$$

where $\mathrm{E},\ \mu$ are the elasticity modulus and Poisson’s ratio of the material. We represent the deformations additional energy of the finite element in the following form:

$$\mathrm{E} = \frac{1}{2}\mathbf{a}^{\mathrm{T}}\mathbf{Da} \to \min,\ \mathbf{D} = \int_{-b/2}^{b/2}\int_{-a/2}^{a/2}\mathbf{H}^{\mathrm{T}}\mathbf{E}^{-1}\mathbf{H}\mathrm{d}x\mathrm{d}y; \tag{14}$$

$$\mathbf{D} = \frac{abt}{\mathrm{E}}\begin{bmatrix} 1 & -\mu & 0 & 0 & 0 \\ -\mu & 1 & 0 & 0 & 0 \\ 0 & 0 & 2(1+\mu) & 0 & 0 \\ 0 & 0 & 0 & \frac{b^2}{12} & 0 \\ 0 & 0 & 0 & 0 & \frac{a^2}{12} \end{bmatrix}. \tag{15}$$

Using the Lagrange multiplier method, we add the equilibrium equations (12) to the functional (14):

$$\mathrm{E} = \frac{1}{2}\mathbf{a}^{\mathrm{T}}\mathbf{D}\mathbf{a} + \mathbf{u}^{\mathrm{T}}\left(\mathbf{L}\mathbf{a} - \mathbf{R}\right) \to \min. \tag{16}$$

By equating the derivatives of expression (16) with respect to vectors $\mathbf{a}$ and $\mathbf{u}$, we obtain the following equations:

$$\mathbf{D}\mathbf{a} + \mathbf{L}^{\mathrm{T}}\mathbf{u} = 0,\ \ \mathbf{L}\mathbf{a} - \mathbf{R} = 0. \tag{17}$$

Expressing the vector from the first equation $\mathbf{a}$ and substituting it into the second equation, we obtain:

$$\mathbf{a} = -\mathbf{D}^{-1}\mathbf{L}^{\mathrm{T}}\mathbf{u}; \tag{18}$$

$$\mathbf{K}\mathbf{u} = \mathbf{R}; \tag{19}$$

$$\mathbf{K} = \mathbf{L}\mathbf{D}^{-1}\mathbf{L}^{\mathrm{T}}. \tag{20}$$

Thus, the expression for the stiffness matrix of the finite element $\mathbf{K}$ is obtained. Note that the matrix consists of 8 rows and columns.

Stiffness matrix of an equilibrium rectangular finite element with a crack.

We obtain an expression for the finite element stiffness matrix after a crack has formed in it. We agree that a crack is formed if the maximum principal stress at the finite element center reaches the material tensile strength $\mathrm{R_t}$. At the center of the finite element, the coordinates (x, y) are zero, so the stresses are determined by only three parameters:

$$\sigma_x = a_1,\ \ \sigma_y = a_2,\ \ \tau_{xy} = a_3. \tag{21}$$

The maximum principal stress at the finite element center and the crack inclination angle will be determined by the following well-known expressions:

$$\sigma_1 = \frac{\sigma_x + \sigma_y}{2} + \sqrt{\frac{\left(\sigma_x - \sigma_y\right)^2}{4} + \tau_{xy}^2} \geq \mathrm{R_t}; \tag{22}$$

$$\alpha_{cr} = \frac{1}{2}\mathrm{acrtg}\frac{2\tau_{xy}}{\left(\sigma_x - \sigma_y\right)}. \tag{23}$$

Depending on the inclination angle, there are two possible options for the crack location in the element. In the first option, the nodes 1 and 3 are located on one crack side, and the nodes 2 and 4 are located on the other. In the second variant, the nodes 1 and 2 are located on one side, and the nodes 3 and 4 are located on the other side (Fig. 2).

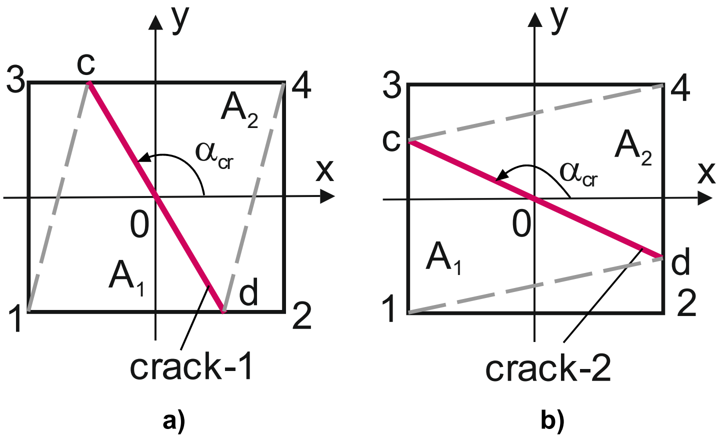

Figure 2. Variants of crack cd location.

Consider the first variant of the crack location. After the crack has formed, we introduce additional degrees of freedom into the nodes of the finite element. These degrees of freedom are associated with the possibility of shifting two parts of the element A_1 and A_2, separated by a crack, relative to each other. Thus, after the crack formation, the number of degrees of freedom in the nodes of the finite element increases. Let us denote the vector of additional degrees of freedom in node i:

$$\mathbf{u}_i^{cr} = \begin{Bmatrix} u_{i,x}^{cr} \\ u_{i,y}^{cr} \end{Bmatrix}. \tag{24}$$

To approximate the possible displacements of the main and additional degrees of freedom of the nodes, we also use functions (5). Fig. 3 shows the displacement functions from the main and additional possible displacements of nodes 3 and 4.

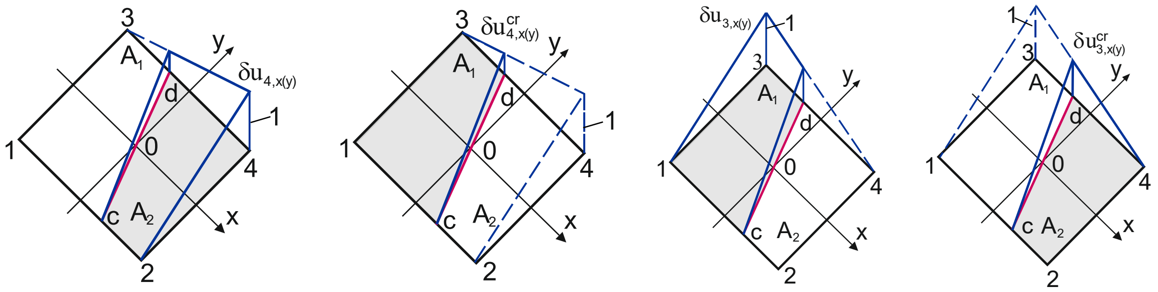

a) b) c) d)

Figure 3. Main and additional possible displacements of nodes after the crack cd formation:

a) $\delta u_{4,x(y)}$; **b)** $\delta u_{3,x(y)}$; **c)** $\delta u_{4,x(y)}^{cr}$; **d)** $\delta u_{3,x(y)}^{cr}$.

After the crack has formed, the main possible displacements of the node cause displacements only in the region of the finite element adjacent to this node. This region is limited by the crack line. The additional possible displacements cause displacements and deformations only in the opposite region of the finite element, located behind the crack line (Fig. 3b). In both cases, the same functions (5) are used to approximate the possible displacements. The possible displacements of nodes 1 and 2 are accepted similarly.

Due to the discontinuity of displacements and deformations, the number of parameters required to approximate the stresses increases. The stresses approximate parameters are different in the two regions of the finite element (25):

$$\mathbf{a}^{\mathrm{T}} = \left(a_1^1 \;\, a_2^1 \;\, a_3^1 \;\, a_4^1 \;\, a_5^1 \;\, a_1^2 \;\, a_2^2 \;\, a_3^2 \;\, a_4^2 \;\, a_5^2 \right). \tag{25}$$

The first five parameters are used to approximate the stresses in the region A_1, the remaining five are used to approximate the stresses in the region A_2. Expressions (1) are used to approximate the stresses in each region of the finite element.

When calculating the deformation energy, integration is performed only over a part of the finite element. For example, for the main possible displacement of node i along the X axis, the deformation energy is calculated using the following formula:

$$\delta \mathrm{U}_{i,x} = t \int\limits_{\mathrm{A}_i} \left(\sigma_x \delta\varepsilon_x + \tau_{xy} \delta\gamma_{xy} \right) \mathrm{dA}, \;\; \mathrm{A}_i = \begin{cases} \mathrm{A}_1, \; i = 1,3 \\ \mathrm{A}_2, \; i = 2,4 \end{cases}. \tag{26}$$

For additional possible displacement along the X axis, integration is performed over the opposite region of the finite element relative to the crack:

$$\delta \mathrm{U}_{i,x}^{cr} = t \int\limits_{\mathrm{A}_i} \left(\sigma_x \delta\varepsilon_x + \tau_{xy} \delta\gamma_{xy} \right) \mathrm{dA}, \;\; \mathrm{A}_i = \begin{cases} \mathrm{A}_1, \; i = 2,4 \\ \mathrm{A}_2, \; i = 1,3 \end{cases}. \tag{27}$$

For integration, the quadrangular region is divided into two triangles, indicated in Fig. 2 by a dotted line. For each triangular region, the integrals were calculated analytically using triangular coordinates. Let us introduce for the domain A_1 the designations of the necessary integrals, calculated analytically:

$$\begin{gathered}\mathrm{I}_x^1=\int\limits_{13c} x\mathrm{dA}+\int\limits_{1cd} x\mathrm{dA},\ \mathrm{I}_y^1=\int\limits_{13c} y\mathrm{dA}+\int\limits_{1cd} y\mathrm{dA},\ \mathrm{I}_{xy}^1=\int\limits_{13c} xy\mathrm{dA}+\int\limits_{1cd} xy\mathrm{dA},\\ \mathrm{I}_{xx}^1=\int\limits_{13c} x^2\mathrm{dA}+\int\limits_{1cd} x^2\mathrm{dA},\ \mathrm{I}_{yy}^1=\int\limits_{13c} y^2\mathrm{dA}+\int\limits_{1cd} y^2\mathrm{dA}.\end{gathered} \tag{28}$$

The similar designations are adopted for the region A_2 : $\mathrm{I}_x^2,\ \mathrm{I}_y^2,\ \mathrm{I}_{xx}^2,\ \mathrm{I}_{yy}^2,\ \mathrm{I}_{xy}^2$. Using (26), we obtain the matrix $\mathbf{L}_i$ elements for the main possible displacement of node i:

$$\mathbf{L}_i=$$

$$=\begin{bmatrix}\frac{x_i}{a^2}\left(\mathrm{A}_k+\frac{4y_i}{b^2}\mathrm{I}_y^k\right) & 0 & \frac{y_i}{b^2}\left(\mathrm{A}_k+\frac{4x_i}{a^2}\mathrm{I}_x^k\right) & \frac{x_i}{a^2}\left(\mathrm{I}_y^k+\frac{4y_i}{b^2}\mathrm{I}_{yy}^k\right) & 0\\ 0 & \frac{y_i}{b^2}\left(\mathrm{A}_k+\frac{4x_i}{a^2}\mathrm{I}_x^k\right) & \frac{x_i}{a^2}\left(\mathrm{A}_k+\frac{4y_i}{b^2}\mathrm{I}_y^k\right) & 0 & \frac{y_i}{b^2}\left(\mathrm{I}_x^k+\frac{4x_i}{a^2}\mathrm{I}_{xx}^k\right)\end{bmatrix}, \tag{29}$$

$$k=\begin{cases}1,\ i=1,3\\ 2,\ i=2,4\end{cases}.$$

The matrix $\mathbf{L}_i^{cr}$ elements for additional possible displacement are calculated by changing the index k values to the opposite values:

$$\mathbf{L}_i^{cr}=$$

$$=\begin{bmatrix}\frac{x_i}{a^2}\left(\mathrm{A}_k+\frac{4y_i}{b^2}\mathrm{I}_y^k\right) & 0 & \frac{y_i}{b^2}\left(\mathrm{A}_k+\frac{4x_i}{a^2}\mathrm{I}_x^k\right) & \frac{x_i}{a^2}\left(\mathrm{I}_y^k+\frac{4y_i}{b^2}\mathrm{I}_{yy}^k\right) & 0\\ 0 & \frac{y_i}{b^2}\left(\mathrm{A}_k+\frac{4x_i}{a^2}\mathrm{I}_x^k\right) & \frac{x_i}{a^2}\left(\mathrm{A}_k+\frac{4y_i}{b^2}\mathrm{I}_y^k\right) & 0 & \frac{y_i}{b^2}\left(\mathrm{I}_x^k+\frac{4x_i}{a^2}\mathrm{I}_{xx}^k\right)\end{bmatrix}, \tag{30}$$

$$k=\begin{cases}1,\ i=2,4\\ 2,\ i=1,3\end{cases}.$$

The matrix of equilibrium equations, which are similar (12), for a finite element is composed of the matrices (29) and (30):

$$\mathbf{L}=\begin{bmatrix}\mathbf{L}_1 & \mathbf{O}\\ \mathbf{O} & \mathbf{L}_2\\ \mathbf{L}_3 & \mathbf{O}\\ \mathbf{O} & \mathbf{L}_4\\ \mathbf{O} & \mathbf{L}_1^{cr}\\ \mathbf{L}_2^{cr} & \mathbf{O}\\ \mathbf{O} & \mathbf{L}_3^{cr}\\ \mathbf{L}_4^{cr} & \mathbf{O}\end{bmatrix}. \tag{31}$$

The matrix consists of 10 columns, corresponding to different stress approximation parameters, and 16 rows, corresponding to the node's possible displacements.

For the second crack variant (Fig. 2), in expressions (29) and (30), it is necessary for the parameter k to replace the pair of indices 1.3 with the pair 1.2 and the indices 2.4 with the pair 3.4. In addition, in (31), the position of the matrices $\mathbf{L}_i$, $\mathbf{L}_i^{cr}$ must be changed to the following:

$$\mathbf{L}=\begin{bmatrix}\mathbf{L}_1 & \mathbf{O}\\ \mathbf{L}_2 & \mathbf{O}\\ \mathbf{O} & \mathbf{L}_3\\ \mathbf{O} & \mathbf{L}_4\\ \mathbf{O} & \mathbf{L}_1^{cr}\\ \mathbf{O} & \mathbf{L}_2^{cr}\\ \mathbf{L}_3^{cr} & \mathbf{O}\\ \mathbf{L}_4^{cr} & \mathbf{O}\end{bmatrix}. \qquad (32)$$

The matrix $\mathbf{D}$, similar to (13), has the following form:

$$\mathbf{D}=\begin{bmatrix}\mathbf{D}_1 & \mathbf{O}\\ \mathbf{O} & \mathbf{D}_2\end{bmatrix}. \qquad (33)$$

$$\mathbf{D}_i=\frac{t}{\mathrm{E}}\begin{bmatrix}\mathrm{A}_i & -\mu\mathrm{A}_i & 0 & \mathrm{I}_y^i & -\mu\mathrm{I}_x^i\\ & \mathrm{A}_i & 0 & -\mu\mathrm{I}_y^i & \mathrm{I}_x^i\\ & & 2(1+\mu) & 0 & 0\\ & \text{symmetric} & & \mathrm{I}_{yy}^i & -\mu\mathrm{I}_{xy}^i\\ & & & & \mathrm{I}_{xx}^i\end{bmatrix}. \qquad (34)$$

The finite element stiffness matrix is also calculated by formula (20) and contains 16 rows and columns. The A global stiffness matrix for all structure is formed from the matrix stiffness of the finite elements.

Depending on the presence of cracks in the finite elements, there may be 2, 4 or 6 unknowns in a node. If there are no cracks in all elements surrounding the node, then there are only two unknowns in the node. If there are cracks in elements only to the right (bottom) or left (top) of the node, then there are four unknowns in the node. If there are cracks in the elements located to the right and left (bottom and top) of the node, then there are six unknowns in the node (Fig. 4).

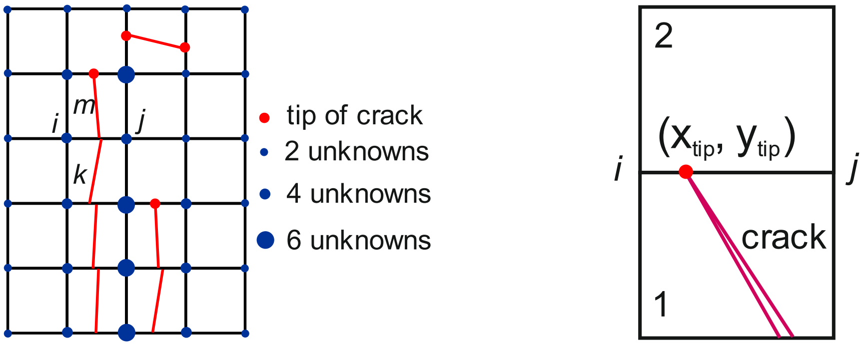

a) b)

Figure 4. Cracks: a) the unknowns' number in a node, depending on the cracks location; b) the tip of a crack.

The determination of crack opening width.

For a finite element, the crack opening width is determined at points c and d in the direction to the crack normal (Fig. 2). The width of the crack opening in the direction of the local axes X and Y is determined by the difference in the displacements of its sides, according to the following formulas:

$$w_{c,x}^{cr}=u_{4,x}N_4\left(x_c,y_c\right)+u_{3,x}^{cr}N_3\left(x_c,y_c\right)-u_{3,x}N_3\left(x_c,y_c\right)-u_{4,x}^{cr}N_4\left(x_c,y_c\right); \qquad (35)$$

$$w_{c,y}^{cr} = u_{4,y} N_4 \left(x_c, y_c\right) + u_{3,y}^{cr} N_3 \left(x_c, y_c\right) - u_{3,y} N_3 \left(x_c, y_c\right) - u_{4,y}^{cr} N_4 \left(x_c, y_c\right). \tag{36}$$

Then, the crack width in the direction of the normal to it is equal to:

$$w_{c,n}^{cr} = w_{c,x}^{cr} \cos\left(\alpha_{cr} - \pi/2\right) + w_{c,y}^{cr} \sin\left(\alpha_{cr} - \pi/2\right). \tag{37}$$

For point d, the crack width is determined similarly:

$$w_{d,x}^{cr} = u_{2,x} N_2 \left(x_d, y_d\right) + u_{1,x}^{cr} N_1 \left(x_d, y_d\right) - u_{1,x} N_1 \left(x_d, y_d\right) - u_{1,x}^{cr} N_2 \left(x_d, y_d\right); \tag{38}$$

$$w_{d,y}^{cr} = u_{2,y} N_2 \left(x_d, y_d\right) + u_{1,y}^{cr} N_1 \left(x_d, y_d\right) - u_{1,y} N_1 \left(x_d, y_d\right) - u_{1,y}^{cr} N_2 \left(x_d, y_d\right); \tag{39}$$

$$w_{d,n}^{cr} = w_{d,x}^{cr} \cos\left(\alpha_{cr} - \pi/2\right) + w_{d,y}^{cr} \sin\left(\alpha_{cr} - \pi/2\right). \tag{40}$$

The closing of crack edges at its tip.

The crack tip is located at the boundary of two finite elements, one of which has no crack (Fig. 4). At the top of the crack, its banks come together (Fig. 4b). The vertical and horizontal displacements of the crack tip in element 1 must be equal to the corresponding displacements of this point in finite element 2, in which there is no crack. In the element 2, the displacements of the crack tip are determined only by the main displacements of nodes i and j:

$$u_{x,tip} = u_{i,x} N_i \left(x_{tip}, y_{tip}\right) + u_{j,x} N_j \left(x_{tip}, y_{tip}\right); \tag{41}$$

$$u_{y,tip} = u_{i,y} N_i \left(x_{tip}, y_{tip}\right) + u_{j,y} N_j \left(x_{tip}, y_{tip}\right). \tag{42}$$

In finite element 1, the displacements of the crack sides are determined by the main and additional displacements of one of the nodes i or j. The displacements of the crack tip on the left side are expressed through the displacements of node i:

$$u_{x,tip}^{left} = u_{i,x} N_i \left(x_{tip}, y_{tip}\right) + u_{j,x}^{cr} N_j \left(x_{tip}, y_{tip}\right); \tag{43}$$

$$u_{y,tip}^{left} = u_{i,y} N_i \left(x_{tip}, y_{tip}\right) + u_{j,y}^{cr} N_j \left(x_{tip}, y_{tip}\right). \tag{44}$$

Equating expressions (41) and (42) to expressions (43) and (44), respectively, we obtain:

$$u_{j,x}^{cr} = u_{j,x}, \;\; u_{j,y}^{cr} = u_{j,y}. \tag{45}$$

Considering the displacements of the crack tip on the right side, we obtain:

$$u_{i,x}^{cr} = u_{i,x}, \;\; u_{i,y}^{cr} = u_{i,y}. \tag{46}$$

Equalities (45) and (46) mean that the corresponding additional and main unknowns at the nodes belonging to the side on which the crack tip is located must be equal to each other. Simply assigning the same numbers to the corresponding main and additional unknowns ensures equalities (45) and (46).

The iterative algorithm for the problem solving.

In this article, we consider an algorithm for solving the problem for the case of a linear $\sigma\left(\varepsilon\right)$ diagram shown in Fig. 5.

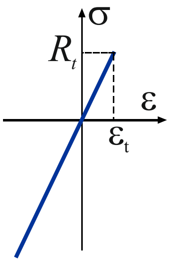

Figure 5. Material deformation diagram.

A material corresponding to such a diagram is elastic, but if the tensile stresses reach the tensile strength, brittle failure occurs and a crack appears. The nonlinear behavior of a structure made of such material is determined by the successive occurrence of cracks in the tension zones. The main stages of the iterative solution are shown in Fig. 6.

```
1. Compute the number of unknowns $n_d$ and the tape width of the equation system $l_d$.
2. Accept $\mathbf{u} = \mathbf{0}$.
3. Compute the load vector $\mathbf{R}$.
4. Compute the elements of stiffness matrix $\mathbf{K}(\mathbf{u})$.
5. Solve the linear equation system $\mathbf{Ku} = \mathbf{R}$.
6. Compute the vector of first principal stresses of the finite element centers $\mathbf{S}_1$.
7. Find the element of vector $\mathbf{S}_1$ with the maximum value $s_i$.
8. If $s_i \ge \mathrm{R}_t$, then:
    8.1. Add the additional unknowns $u^{cr}$ into the nodes of the finite element i.
    8.2. Recompute the number of unknowns $n_d$ and tape width $l_d$ of the equation system.
    8.3. Recompute the load vector $\mathbf{R}$.
    8.4. Go to line 4.
9. Compute the stresses of finite elements $\boldsymbol{\sigma}$ and width of cracks $\mathbf{w}_{\mathrm{cr}}$.
10. Exit.
```

Figure 6. Iterative solution algorithm.

The iterative algorithm allows determining the sequence of crack formation. When a new crack is formed, additional unknowns are added to the nodes of the finite element if the corresponding unknowns were not added to these nodes in previous iterations. For example, if a crack has formed in element m (Fig. 4a), and in element k a crack has formed in previous iterations, then there is no need to introduce additional unknowns into nodes i and j. During the iterations, the numbers of finite elements, in which cracks have formed, are noted. If new cracks do not form, then the solution is obtained and the iterations are finished. The number of necessary iterations is determined by the number of cracks that can occur under the given loads.

3. Results and Discussion

As a test, calculation of a bending, hinged beam was performed for the action of a uniformly distributed load. The beam length is 6 m. Half of the beam was calculated. To increase the beam rigidity, reinforcement is added to the stretched zone. The reinforcement is located at a distance of 30 mm from the lower edge. The reinforcement is modeled by rod finite elements working in tension and compression. The characteristics of the beam are given in Table 1.

Table 1. Beam parameters.

Beam						Reinforcement		
0.5L, m	h, m	t, m	E, kPa	R_t, kPa	μ	h_0, m	E_a, kPa	A_a, m^2
3	0.6	0.4	30000000	1140	0.25	0.57	200000000	0.003

The beam was divided by height into 20 and by length into 40 finite elements (Fig. 7). Along line AB, vertical displacements at the nodes were excluded, and along line CD, horizontal displacements were excluded. A uniformly distributed load was applied of the beam upper edge in the form of concentrated forces to the nodes.

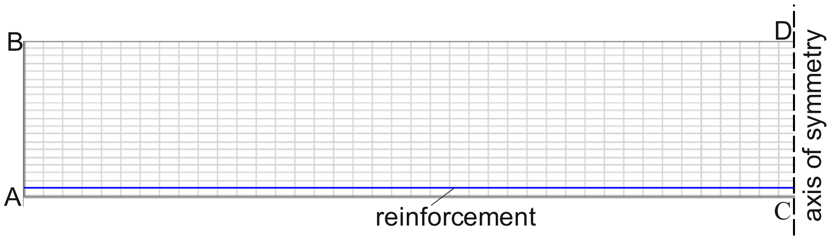

Figure 7. Finite elements mesh and reinforcement of proposed (Cr-FE).

Fig. 8 shows the position and size of crack opening, as well as the stresses in the reinforcement at different values of uniformly distributed load q. From Fig. 8, one can trace the sequence of crack formation.

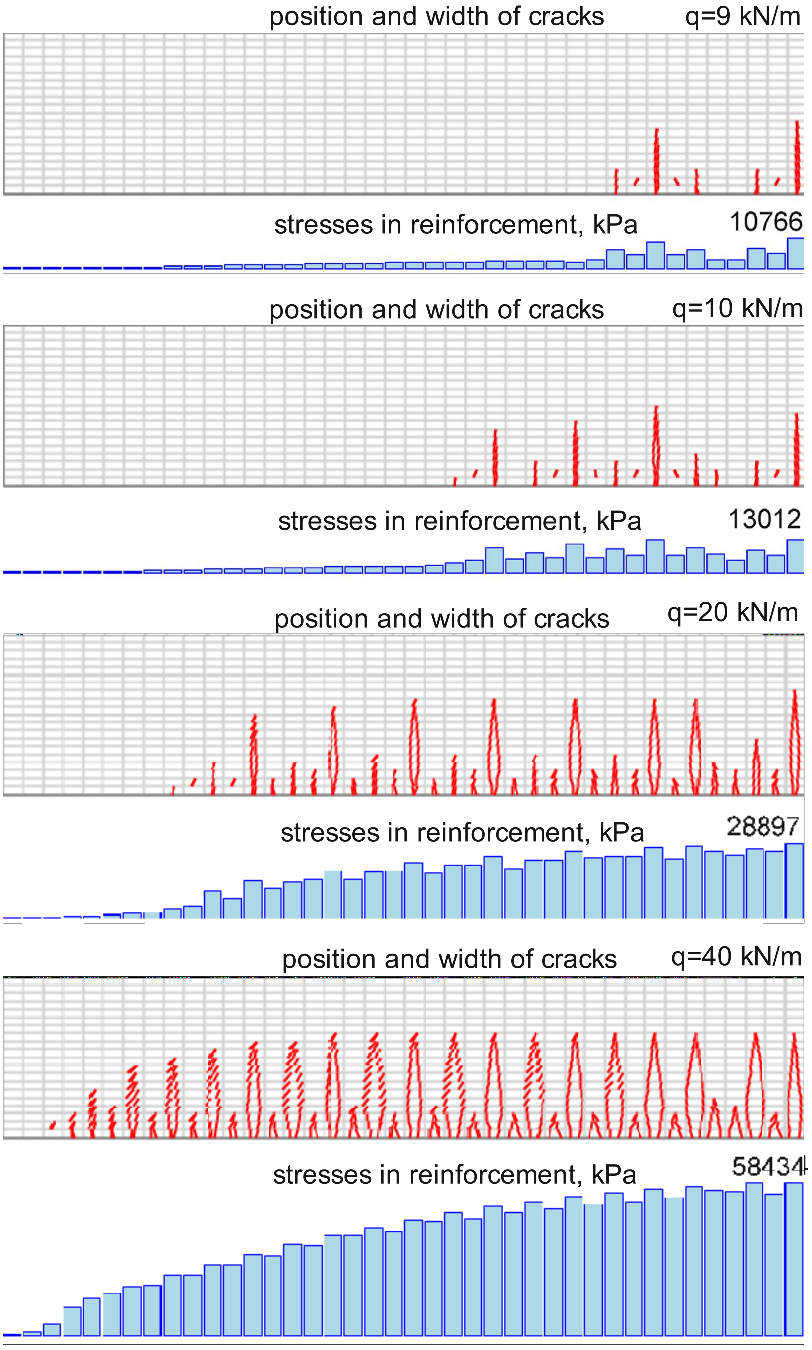

Figure 8. Position and width of cracks, and stresses in reinforcement with increasing load from *q* = 9 kN/m to *q* = 40 kN/m. The width of cracks is shown 500 times greater than the actual one.

To compare the results, beam calculations were performed using standard flat rectangular finite elements (Fig. 9). The beam was calculated for the load q = 20 kN/m after all cracks had formed. All beam parameters, including reinforcement, were taken to be the same. Along the lines, where cracks had formed, the nodes of adjacent finite elements were separated. In Fig. 9, such lines are marked in red. To simplify the calculation scheme, the slope of all cracks is taken to be 90 degrees. The reinforcement was divided by length into 40 rod finite elements (Fig. 7).

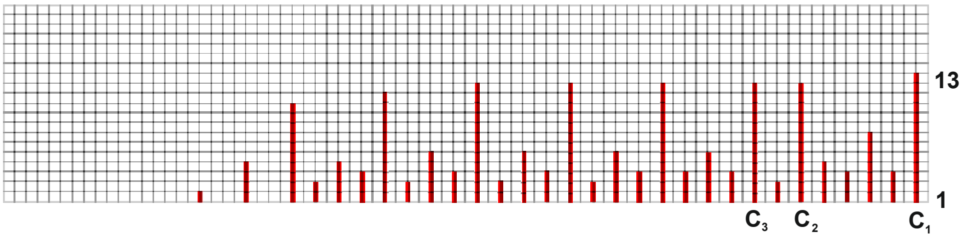

Figure 9. Standard finite element mesh. The beam is divided into 20 elements along the height and into 80 elements along the length. The red lines show the nodes separation of adjacent elements by cracks. The load is q = 20 kN/m.

Tables 2–4 provide the values of the opening width for cracks C_1, C_2, C_3 (Fig. 9). For standard finite elements, the data are given in the rows designated FE, and for the proposed finite elements in the rows designated Cr-FE. For standard finite elements [38], the crack width was defined as the difference in the node's displacements along the X axis of two finite elements, separated by a crack. Comparison of the results given in Tables 2–4 for the two solutions shows that they agree with high accuracy. Note that for other cracks, the same good agreement of crack opening values is observed. This indicates that the proposed finite element allows to get enough accurate determination of the crack width in the calculated structure.

Table 2. Width of crack C_1 opening from bottom to top, mm. The load value is q = 20 kN/m.

Type of FE		1	2	3	4	5	6	7	8	9	10	11	12	13
Cr-FE	down	0.016	0.022	0.027	0.032	0.034	0.033	0.031	0.029	0.026	0.022	0.018	0.013	0.007
	up	0.023	0.027	0.032	0.034	0.033	0.031	0.029	0.026	0.022	0.018	0.013	0.007	0
FE [36]	down	0.018	0.022	0.027	0.030	0.032	0.032	0.030	0.028	0.025	0.021	0.0165	0.012	0.007
	up	0.022	0.027	0.030	0.032	0.032	0.030	0.028	0.025	0.021	0.0165	0.012	0.007	0

Table 3. Width of crack C_2 opening from bottom to top, mm. The load value is q = 20 kN/m.

Type of FE		1	2	3	4	5	6	7	8	9	10	11	12
Cr-FE	down	0.012	0.022	0.030	0.037	0.041	0.040	0.036	0.032	0.027	0.022	0.016	0.010
	up	0.022	0.033	0.038	0.041	0.040	0.036	0.032	0.027	0.022	0.016	0.009	0
FE [35]	down	0.014	0.022	0.030	0.036	0.039	0.038	0.035	0.031	0.026	0.021	0.016	0.010
	up	0.022	0.030	0.036	0.039	0.038	0.035	0.031	0.026	0.021	0.016	0.010	0

Table 4. Width of crack C_3 opening from bottom to top, mm. The load value is q = 20 kN/m.

Type of FE		1	2	3	4	5	6	7	8	9	10	11	12
Cr-FE	down	0.012	0.022	0.030	0.037	0.039	0.037	0.034	0.029	0.025	0.020	0.014	0.008
	up	0.022	0.030	0.037	0.039	0.037	0.034	0.029	0.025	0.020	0.014	0.008	0
FE [36]	down	0.014	0.022	0.030	0.035	0.037	0.035	0.032	0.028	0.024	0.019	0.013	0.008
	up	0.022	0.030	0.035	0.037	0.035	0.032	0.028	0.024	0.019	0.013	0.008	0

Table 5. The comparison of calculations results.

Type of element	Vertical displacement Zmax, mm	Compressive stress $\sigma_{x,\max}$, kPa	Stress in reinforcement $S_{\max}$, kPa
Cr-FE	2.77	4538	28936
FE [36]	2.73	4575	28857

Table 5 presents the main calculation results for comparison. The comparison of the results demonstrates good agreement between the values of the maximum vertical displacement, maximum stresses in the beam compressed zone, and maximum tensile stresses in the reinforcement. The maximum displacements differ by 1.5 %, the maximum stresses in compressed concrete and reinforcement differ by less than 1 %. The crack width for the two solutions differs by no more than 5–7 %.

In this paper, the case of active loading is considered, when the cracks do not close. For the proposed finite element, taking into account the possible closing of cracks and friction forces between the crack's sides is not difficult and easily implemented. To calculate taking into account physical nonlinearity, it is necessary to change the iteration algorithm. When using the elastic solution method, we should simply use the secant modulus instead of the initial modulus of elasticity. All formulas remain the same.

4. Conclusions

1. A rectangular flat finite element is proposed that allows modeling the process of crack formation without changing the initial elements' grid. The finite element is based on the stress fields approximations and the principle of possible displacements, with the help of which the equilibrium equations of nodes are obtained. The simple linear functions are used for possible displacements. To approximate stresses, linear functions were used, ensuring the fulfillment of the equilibrium equations in the finite element region in the absence of a distributed load. To calculate the stiffness matrix of a finite element, the principle of minimum additional energy was used, to which algebraic equilibrium equations were added using the Lagrange multiplier method. After a crack formation in the center of finite element, additional degrees of freedom were introduced into its nodes, determining the possible mutual displacement of the element's parts.
2. The calculations were performed for a rectangular bending beam with a low tensile strength. The reinforcement was located in the tensile zone of the beam. The beam was divided by height into 20, and by length into 40 proposed finite elements. For comparison, the beam was also calculated using standard finite elements. In this case, the beam was divided into 80 finite elements along its length, and the nodes along the crack lines of adjacent finite elements were different. The comparison of the results, including the crack width, for the two solutions showed that they coincided with high accuracy. The test beam was calculated in an elastic setting. To calculate taking into account physical nonlinearity, it is necessary to change only the iteration algorithm. When using the elastic solution method, we should simply use the secant modulus instead of the initial modulus of elasticity. All formulas remain the same.
3. The proposed finite element can be used to calculate structures made of reinforced concrete, masonry, fiber concrete, and other materials with low tensile strength. To calculate structures with existing cracks, their position can be specified as initial data. The proposed flat finite element allows modeling the process of crack formation under load without changing the finite element mesh.

References

1. Bai, X., Wang, X. Simulation of cracking processes of the rectangular cavern surrounding rock based on a continuum–discontinuum method. Engineering Fracture Mechanics. 2024. 307. Article no. 110304. DOI: 10.1016/j.engfracmech.2024.110304
2. Ghadimi, S., Zamani-Ahari, G., Kourehli, S.S. A novel approach to crack modeling using extended finite element and substructures methods. Structures. 2024. 68. Article no. 107219. DOI: 10.1016/j.istruc.2024.107219
3. Koutromanos, I. A C^0 scalar field approach for describing sprain variables in finite element analysis of fracture. Computers & Structures. 2024. 294. Article no. 107259. DOI: 10.1016/j.compstruc.2023.107259
4. Zhou, X.-P., Chen, J.-W., Berto, F. XFEM based node scheme for the frictional contact crack problem. Computers & Structures. 2020. 231. Article no. 106221. DOI: 10.1016/j.compstruc.2020.106221
5. Deng, H., Yan, B., Koyanagi, J. Improved XFEM for 3D interfacial crack modeling. Mechanics of Materials. 2023. 186. Article no. 104811. DOI: 10.1016/j.mechmat.2023.104811
6. Scamardo, M., Franchi, A., Crespi, P. A non-standard numerical method for finite element modelling of tensile cracks in quasi-brittle material. Computers & Structures. 2022. 258. Article no. 106664. DOI: 10.1016/j.compstruc.2021.106664
7. Wang, K., Tang, C., Li, G., Zhang, H., Lu, Z. Modeling fracture problems by the local mesh refinement NMM with variable-midside-node elements. Computers & Structures. 2023. 279. Article no. 106984. DOI: 10.1016/j.compstruc.2023.106984
8. Yu, C. A coupled smeared crack-plasticity model in incremental sequentially linear analysis for mixed failure modes. Computers & Structures. 2022. 269. Article no. 106824. DOI: 10.1016/j.compstruc.2022.106824
9. Kim, U.-J., Kim, I.-G., Yun, K., Jon, M.-G., Kim, U.-B. A novel sequentially linear approach based on exponential saw-tooth softening in fracture analysis of quasi-brittle material. Computers & Structures. 2024. 297. Article no. 107317. DOI: 10.1016/j.compstruc.2024.107317
10. Češarek Kolšek, J., Planinc, I., Bratina, S. A novel family of strain-based finite elements for the analysis of the material softening of planar frames. Computers & Structures. 2024. 301. Article no. 107442. DOI: 10.1016/j.compstruc.2024.107442
11. Do, T.M.D., Lam, T.Q.K. Design parameters of steel fiber concrete beams. Magazine of Civil Engineering. 2021. 102(2). Article no. 10207. DOI: 10.34910/MCE.102.7

12. Li, Z., Zhu, H., Du, C., Gao, D., Yuan, J., Wen, C. Experimental study on cracking behavior of steel fiber-reinforced concrete beams with BFRP bars under repeated loading. Composite Structures. 2021. 267. Article no. 113878. DOI: 10.1016/j.compstruct.2021.113878
13. Nuguzhinov, Zh., Vatin, N., Bakirov, Zh., Khabidolda, O., Zholmagambetov, S., Kurokhtina, I. Stress-strain state of bending reinforced beams with cracks. Magazine of Civil Engineering. 2020. 97(5). Article no. 9701. DOI: 10.18720/MCE.97.1
14. Klochkov, Yu.V., Pshenichkina, V.A., Nikolaev, A.P., Vakhnina, O.V., Klochkov, M.Yu. Stress-strain state of elastic shell based on mixed finite element. Magazine of Civil Engineering. 2023. 120(4). Article no. 12003. DOI: 10.34910/MCE.120.3
15. Liu, H., Zhong, H. Transverse free vibration analysis of thin sectorial plates by the weak form quadrature element method. Journal of Vibration and Control. 2024. 289. Pp. 5560–5577. DOI: 10.1177/10775463231225276
16. Lukashevich, A.A. Finite element models based on the approximation of discontinuous stress fields. Magazine of Civil Engineering. 2022. 110(2). Article no. 11004. DOI: 10.34910/MCE.110.4
17. Xiao, J.-L., Nie, X., Liu, Y.-F., Fan, J.-S. Structural performance assessment of RC flexural members through crack-based fibre beam-column model updating. Computers & Structures. 2023. 281. Article no. 107029. DOI: 10.1016/j.compstruc.2023.107029
18. Dang-Trung, H., Keilegavlen, E., Berre, I. Numerical modeling of wing crack propagation accounting for fracture contact mechanics. International Journal of Solids and Structures. 2020. 204–205. Pp. 233–247. DOI: 10.1016/j.ijsolstr.2020.08.017
19. Zhao, J.W., Feng, S.Z., Tao, Y.R., Li, Z.X. Stable node-based smoothed extended finite element method for fracture analysis of structures. Computers & Structures. 2020. 240. Article no. 106357. DOI: 10.1016/j.compstruc.2020.106357
20. Khoei, A.R., Nikbakht, M. An enriched finite element algorithm for numerical computation of contact friction problems. International Journal of Mechanical Sciences. 2007. 49(2). Pp. 183–199. DOI: 10.1016/j.ijmecsci.2006.08.014
21. Peng, X., Kulasegaram, S., Bordas, S.P.A., Wu, S.C. An extended finite element method with smooth nodal stress. arXiv:1306.0536. 2013. DOI: 10.48550/arXiv.1306.0536
22. Tyukalov, Yu.Ya. Calculation of bending plates by finite element method in stresses. IOP Conference Series: Materials Science and Engineering. 2018. 451(1). Article no. 012046. DOI: 10.1088/1757-899X/451/1/012046
23. Tyukalov, Yu.Ya. Calculation of circular plates with assuming shear deformations. IOP Conference Series: Materials Science and Engineering. 2019. 687(3). Article no. 033004. DOI: 10.1088/1757-899X/687/3/033004
24. Tyukalov, Yu.Ya. Triangular prism finite element based on piecewise constant stress approximations. Magazine of Civil Engineering. 2023. 121(5). Article no. 12105. DOI: 10.34910/MCE.121.5
25. Tyukalov, Yu.Ya. Arbitrary quadrangular finite element for plates with shear deformations. Magazine of Civil Engineering. 2021. 107(7). Article no. 10707. DOI: 10.34910/MCE.107.7
26. Cunha, R.N., Amorim, D.L.N.F., Proença, S.P.B., Flórez-López, J. Modeling the initiation and propagation of complex networks of cracks in reinforced concrete plates. Engineering Structures. 2024. 308. Article no. 117993. DOI: 10.1016/j.engstruct.2024.117993
27. Luo, Y., Featherston, C.A., Kennedy, D. A hybrid model for modelling arbitrary cracks in isotropic plate structures. Thin-Walled Structures. 2023. 183. Article no. 110345. DOI: 10.1016/j.tws.2022.110345
28. Liu, J., Zhao, X.-L., Xin, H., Zhang, Y. Prediction of fatigue crack propagation in center cracked steel plate strengthened with partially covered CFRP strip. Thin-Walled Structures. 2023. 189. Article no. 110917. DOI: 10.1016/j.tws.2023.110917
29. Song, Z., Lai, S.-K., Dai, J.-G. Refined models for free vibration analysis of elastic plates with part-through surface cracks. Thin-Walled Structures. 2023. 182(B). Article no. 110312. DOI: 10.1016/j.tws.2022.110312
30. Min, Q., Li, M., Zhang, M., Lian, H., Jacquemin, T., Bordas, S.P.A. Node projection strategy for FEM simulating cross-scale crack propagation in massive concrete structures. Engineering Structures. 2023. 293. Article no. 116665. DOI: 10.1016/j.engstruct.2023.116665
31. Wang, C., Ping, X., Wang, X. An adaptive finite element method for crack propagation based on a multifunctional super singular element. International Journal of Mechanical Sciences. 2023. 247. Article no. 108191. DOI: 10.1016/j.ijmecsci.2023.108191
32. Zhou, L., Wang, J., Wang, Y., Li, X., Chai, Y. The enriched finite element method-virtual crack closure technique for cracked structures. Thin-Walled Structures. 2023. 187. Article no. 110756. DOI: 10.1016/j.tws.2023.110756
33. Tao, M.-X., Wang, Y.-L., Zhao, J.-Z. Internal force redistribution caused by cracking of concrete in composite frame structures under lateral load. Engineering Structures. 2023. 283. Article no. 115876. DOI: 10.1016/j.engstruct.2023.115876
34. Kaklauskas, G., Sokolov, A., Sakalauskas, K. Strain compliance crack model for RC beams: primary versus secondary cracks. Engineering Structures. 2023. 281. Article no. 115770. DOI: 10.1016/j.engstruct.2023.115770
35. Tyukalov, Yu.Ya. Equilibrium finite elements for plane problems of the elasticity theory. Magazine of Civil Engineering. 2019. 91(7). Pp. 80–97. DOI: 10.18720/MCE.91.8
36. Lalin, V.V., Rybakov, V.A., Diakov, S.F., Kudinov, V.V., Orlova, E.S. The semi-shear theory of V.I. Slivker for the stability problems of thin-walled bars. Magazine of Civil Engineering. 2019. 87(3). Pp. 66–79. DOI: 10.18720/MCE.87.6
37. Lalin, V.V., Rybakov, V.A., Ivanov, S.S., Azarov, A.A. Mixed finite-element method in V.I. Slivker's semi-shear thin-walled bar theory. Magazine of Civil Engineering. 2019. 89(5). Pp. 79–93. DOI: 10.18720/MCE.89.7
38. Karpilovskiy, V.S., Kriksunov, E.Z., Malyarenko, A.A., Mikitarenko, M.A., Perelmuter, A.V., Perelmuter, M.A. Vychislitelnyy kompleks SCAD [Computer complex SCAD]. Moscow: SKAD SOFT, 2009. 647 p.

Information about the author:

***Yury Tyukalov**, Doctor of Technical Sciences*
ORCID: https://orcid.org/0000-0001-6184-2365
E-mail: yutvgu@mail.ru

Received: 20.09.2024; Approved: 05.04.2025; Accepted: 15.04.2025.

Magazine of Civil Engineering

journal homepage: http://engstroy.spbstu.ru/

ISSN
2712-8172

Research article

UDC 624.21/.8

DOI: 10.34910/MCE.135.3

Aeroelastic vibrations of arch bridge suspensions

Yu.A. Gosteev , ***I.S. Konovalov, A.D. Obuhovskiy, S.D. Salenko***
Novosibirsk State Technical University (NSTU), Novosibirsk, Russian Federation

gosteev@corp.nstu.ru

Keywords: aeroelastic vibrations, vortex-induced vibrations, galloping, aerodynamics of bridges, section model, cantilever model, wind loads

Abstract. The article identifies the causes of aeroelastic vibrations of suspensions on the arch bridge with the main span of more than 200 m. The study aims to determine the range of dangerous wind speeds and maximum amplitudes of these vibrations. This research is necessary due to intense vibrations of suspensions on the operated structure at wind speeds of 10÷15 m/s. The authors have studied models of bridge span structure and suspensions. Experimental tests as well as flow calculations using application packages have been carried out in the wind tunnel at NSTU. The study has provided verification of the vibration calculation method in the recently approved Russian regulations and comparison of the calculation with the current European method. It has been found that the cause of vibrations of the bridge suspensions is vortex-induced vibrations (VIV), while the central span of the bridge is not subject to aeroelastic vibrations. The experimental results coincide with the calculations and observations of the behavior of the suspensions of the bridge under moderate crosswind. The obtained results will be used in the future to develop methods of suspension vibration damping.

Acknowledgements: The authors would like to thank D.A. Krasnorutskiy for his cooperation in carrying out modal calculations on span structure and its elements.

Citation: Gosteev, Yu.A., Konovalov, I.S., Obuhovskiy, A.D., Salenko, S.D. Aeroelastic vibrations of arch bridge suspensions. Magazine of Civil Engineering. 2025. 18(3). Article no. 13503. DOI: 10.34910/MCE.135.3

1. *Introduction*

The investigation of bridges as complete systems and their individual structural components – particularly suspensions – became essential with the advent of long-span bridge construction. Due to the length of the span structures, it is not possible to make them sufficiently rigid, therefore, such structures as cable-stayed and arched are used. One of the promising directions of building is using polymer materials for the base of bridges, which have some advantages over reinforced concrete structures [1]. In addition, there is also a risk of occurring aeroelastic vibrations during bridge constructing while launching spans [2]. Poorly streamlined bodies such as elastic long-rod suspensions can occur in bridge structures. The cross-sections of these elements can be cylindrical, rectangular, square, etc. The dynamic interaction of such cross-sections with the air flow has been studied by many authors both in Russia [3, 4] and abroad [5–14]. [15] described a similar case of aeroelastic vibrations for cylindrical suspensions of an arch bridge and ways to reduce vibrations. The relevance of research in this area is supported by using modern computational fluid dynamics (CFD) tools with artificial neural networks [16] for designing bridge and high-rise building.

In addition to studies of the interaction of poorly streamlined bodies with the air flow, there are also studies, which aim to find effective ways to dampen vibrations or, at least, reduce their intensity. For example, [17, 18] presented the passive ways to reduce vortex-induced vibrations (VIV) on a circular cylinder by means of a perforated surface. For a square prism, the paper [19] investigated a method to reduce wind load by rounding edges. [20] described corner fins installment that is another way (both passive and active) to reduce VIV. The paper [21] proposed an interesting way of active wind load control, which can be used for high-rise buildings. The present work deals with the problem of occurring suspension vibrations in bridges caused by the interaction of the suspensions with the wind flow.

Based on the external geometric shapes of the span structures section (Fig. 1) it can be suggested that the structure may be subject to aeroelastic vibrations such as VIV and stall flutter. The cross-section shape of the suspensions (Fig. 2) allows to suggest that they may be subject to aeroelastic vibrations such as VIV and galloping.

Possible causes of suspension vibrations are aerostatic vibrations of:

1) the suspensions in the wind flow;
2) the span structures in the wind flow;
3) the span structures due to road traffic.

The purposes of this research are:

- to study the mechanism of occurrence and development of aeroelastic vibrations of bridge elements;
- to determine the range of wind velocities, at which dangerous aeroelastic vibrations of elements may occur;
- to estimate maximum vibration amplitudes to find ways to reduce aeroelastic vibrations.

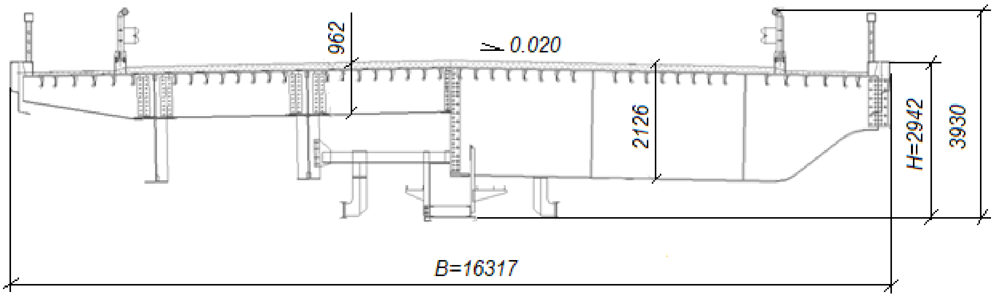

Figure 1. Cross-section of the span structures around the studied suspensions.

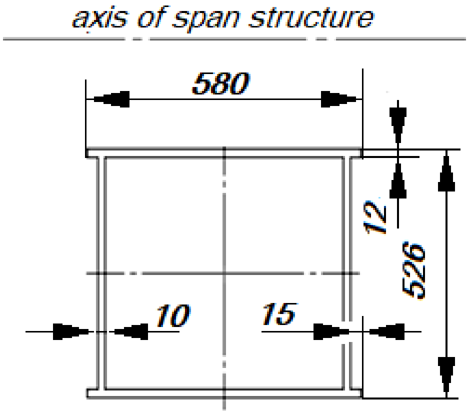

Figure 2. Cross-section of suspensions.

2. Methods

2.1. Preliminary Calculations

For preliminary assessment of the vibration characteristics, the frequencies and shapes of natural vibrations of the bridge were calculated, the shapes of suspension vibrations were identified for further analysis of aeroelastic vibrations.

As a result of calculations, two tones were identified, which were confirmed by full-scale measurements. The 30th tone of natural vibrations corresponds to the frequency of suspension vibrations along the span structure bridge; the frequency equals $f_y =$ 2.88 Hz. The frequency and shape of vibrations have been confirmed by full-scale measurements at a wind speed of 10–12 m/s and with the direction close to perpendicular to the span structures. The calculations have also showed vibrations of suspensions across the span structures. They correspond to the 60th tone and the frequency $f_x = 3.82$ Hz.

Numerical calculations of the cross-flow of a fixed suspension model with the wind direction across the span structure ($\alpha = 0°$) showed the presence of a track of vortices descending from the surface of the model (Fig. 3). Spectral analysis of fluctuations of the lifting force acting on the model revealed the main frequency, corresponding to the frequency of the vortices shedding with the Strouhal number $Sh_a = 0.13$. At the natural vibration frequency of the suspension $f_y = 2.88$ Hz, the critical wind speed on the middle of the suspension is $V_{cr,y} = f_y H / Sh_a = 12.8$ m/s.

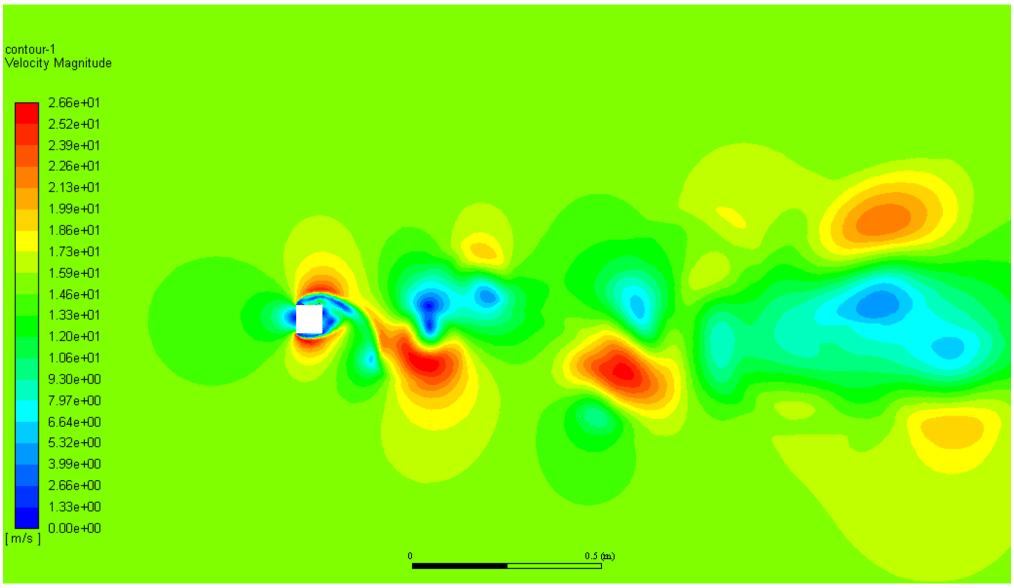

Figure 3. Velocity isolines at *t* = 1 s.

A preliminary assessment of the maximum vibration amplitudes was carried out according to the GOST[1] and Eurocode[2].

Initially, height and width of the cross-section suspension are $H =$ 0.580 m and $B =$ 0.526 m, linear mass is $m =$ 188 kg/m, logarithmic decrement of damping is $\delta =$ 0.02, Strouhal number is $Sh = Sh_a = 0.13$, air density is $\rho =$ 1.225 kg/m^3.

According to the methodology described in GOST[3], equation used to estimate the maximum relative amplitude is:

$$\overline{A}_{\max} = 0.7 \frac{B}{H} \frac{1}{\mathrm{Sc}} \frac{1}{\mathrm{Sh}^2} Kc_{\mathrm{a,max}},$$

where $\mathrm{Sc} = 2 m_e \delta / (\rho H^2)$ is the Scruton number, m_e is the equivalent linear mass of the span structure or its element (if a uniform mass distribution is $m_e = m$), δ is the logarithmic decrement of damping of the

---

[1]. Federal Agency on Technical Regulating and Metrology (Rosstandart). Automobile roads of the general use. Bridge constructions. The rules of the aeroelastic stability. Calculation and verification. GOST R 59625–2022. 2022. 42 p.

[2] European Committee for Standardization (CEN). Eurocode 1: Actions on structures – Part 1–4: General actions – Wind actions. EN 1991-1-4:2005. 2005. 146 p.

[3] Federal Agency on Technical Regulating and Metrology (Rosstandart). Automobile roads of the general use. Bridge constructions. The rules of the aeroelastic stability. Calculation and verification. GOST R 59625–2022. 2022. 42 p.

span structure or its element, $\mathrm{Sh} = fH / V$ is the Strouhal number, depending on the cross-section shape and relative width B / H of the span structure section or its element; K is the modal shape factor, K = 0.1 ([21], Appendix B, Table B.1); $c_{a,max}$ is the maximum value of the exciting aerodynamic coefficient, without experimental data it is allowed to take $c_{a,max} = 0.1$.

As a result, the following values of maximum amplitudes have been obtained: according to the GOST[4], $\overline{A}_{\max} = 0.021$, $A_{\max} = 0.012$ m, according to the Eurocode[5], $\overline{A}_{\max} = 0.092$, $A_{\max} = 0.053$ m.

2.2. Model Description

To study the dependencies of relative vibrations amplitudes on the reduced velocity (amplitude-velocity characteristics, AVC), two identical suspension models with different methods of fixing in a wind tunnel have been used: spring-fixed suspension model and cantilever-fixed model. The cross-section of both models is made to a scale of 1:7.5, the length of the models is 600 mm, the aspect ratio is λ = 7.8. To maintain two-dimensional flow conditions, end plates with a diameter of 300 mm have been positioned at the ends of the models. [22] described the effect of the end plates in more detail. The model on a spring elastic suspension (Fig. 4) is fixed in the working section of the wind tunnel with end plates and has 8 spring-loaded attachment points. Four springs are located on one side of the model and connected to elastic elements with strain gauges. The installation allows to record the movements of the model in the longitudinal and transverse direction of the flow and torsional movements in the pitch angle. The beam of the model is fixed between the end plates on both sides by clamping elements, which allows to change the orientation of the model in the flow according to the attack angle.

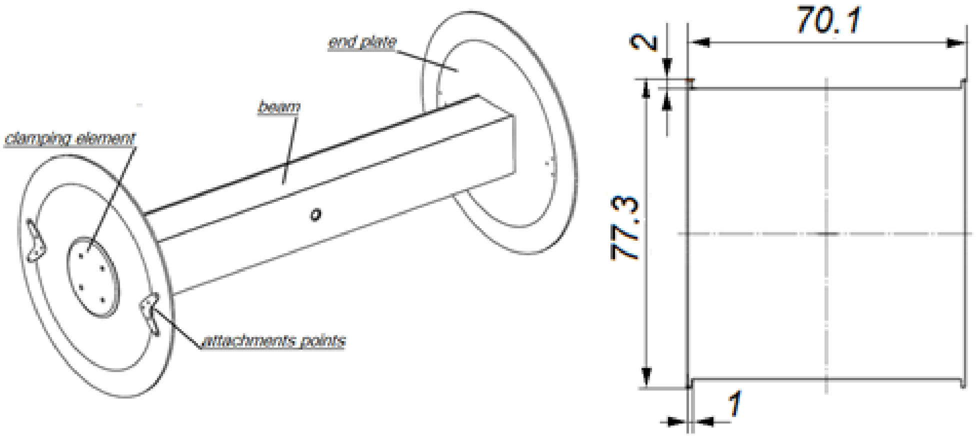

Figure 4. Model general view and cross-section dimensions.

This type of attachment for the model in the wind tunnel test is quite simple and convenient. However, the natural frequency of the elastic suspension is constant, when the attack angle of the model changes, which actually occurs as the wind direction changes. In fact, the full-scale suspension of the bridge has different mechanical rigidity in perpendicular directions and different frequencies of natural vibrations in the first tone, equal to $f_{xn} = 3.82$ Hz and $f_{yn} = 2.88$ Hz, the ratio is $f_{yn} / f_{xn} = 0.75$. It is difficult to ensure the constancy of f_{yn} / f_{xn} on an elastic suspension over the entire range of attack angles. For simulating the frequency ratio, a cantilever-fixed model has been made (Fig. 5). The model is installed on a rigid fixed base outside the wind tunnel with an elastic element. The role of elastic element is performed by a girder milled from aluminum D16T with an I-beam profile, so the natural frequency ratios of the model are $f_{xm} = 18.2$ Hz and $f_{ym} = 13.3$ Hz, $f_{ym} / f_{xm} = 0.73$; and deviations from the natural frequency ratio of the full-scale suspension are 3 %.

---

[4] Ibid.

[5] European Committee for Standardization (CEN). Eurocode 1: Actions on structures – Part 1–4: General actions – Wind actions. EN 1991-1-4:2005. 2005. 146 p.

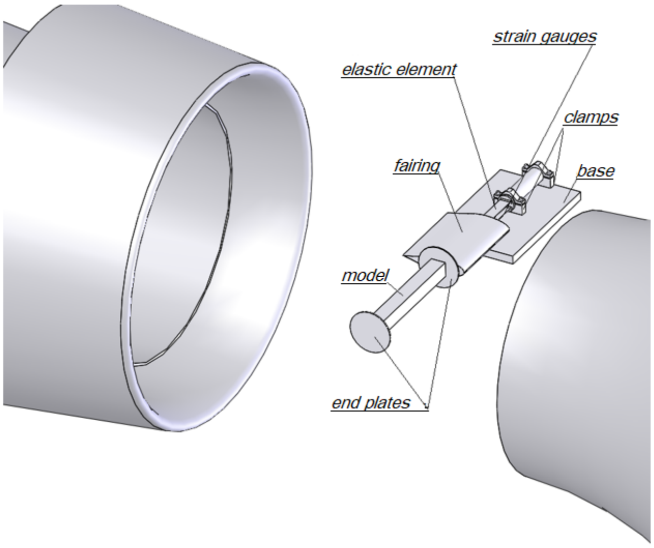

Figure 5. General view of a cantilever-fixed model.

Furthermore, a model of the span structure bridge was made to evaluate AVC, since the suspension vibrations can be caused by vibrations of the span structure in the wind flow. The method of fixing the model in the wind tunnel test and the experimental conditions are the same as for the suspension model of the bridge installed on an elastic suspension.

The Reynolds numbers for models and full-scale structures are in the region of self-similarity of the flow, which is in the range of Reynolds numbers ($10^4 < \mathrm{Re} < 10^7$), so their aerodynamic characteristics have not undergone significant changes.

3. *Results and Discussion*

3.1. AVC of Span Structure Model on an Elastic Spring Suspension

The investigation began with aerodynamic testing of the span structure model to identify potential causes of bridge suspension vibrations. The obtained AVC are shown on dimensionless graphs. The relative amplitude of the investigated model $\overline{A} = A / H$ is plotted along the vertical axis; where *A* is the amplitude of the model, *H* is the overall height of the model, and the relative velocity equals to $\overline{V} = 1/\mathrm{Sh}$ or $\overline{V} = V / (fH)$ plotted along the horizontal axis. The results of the aerodynamic experiments, presented in Fig. 6, showed the absence of intense vibrations of the span structure model at all tested velocities, corresponding to the natural wind speed at $V_{\max} = 1.5V_{\mathrm{calc}}$ at span level. The amplitudes of vertical vibrations of the span structure at the $V_{\max}$ speed did not exceed 18 mm in terms of a full-scale structure. This suggests that the span structure vibrations cannot be the cause of intense suspension vibrations.

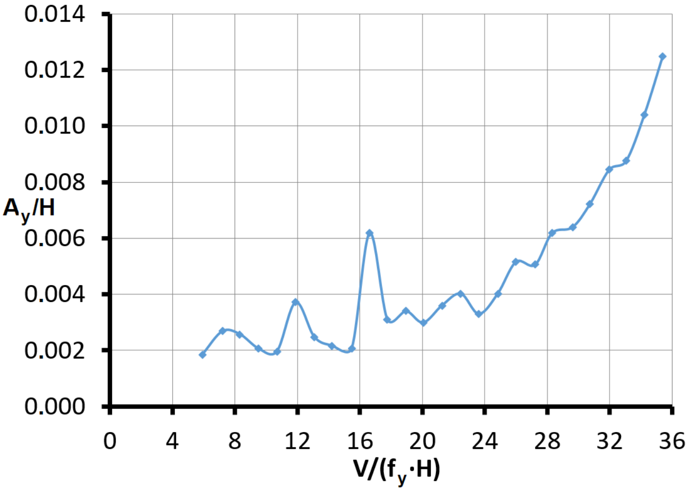

Figure 6. AVC of the span structure model on elastic suspension.

3.2. AVC of Suspension Models of the Bridge on Elastic Suspension

The aerodynamic experiment was conducted in the T-503 open wind tunnel under the following conditions: turbulence intensity $\varepsilon \approx 0.3\%$ in steady flow; flow velocity varied from 5 to 20 m/s; Reynolds numbers equal to $2.5\cdot(10^4\div10^5)$, in the range of self-similarity; flow velocity stability was ±0.5 %. AVC measurements are recorded for 0°, 45°, 90° angles of attack (Fig. 7); for the vibration amplitudes in the direction across the flow, the logarithmic decrement of damping is $\delta \approx 0.007$. For the convenience of recalculating velocities and amplitudes to full-scale dimensions, the AVC graphs are given in dimensionless form (Fig. 8). The vibrations were unstable, the oscillogram signal was averaged to the standard deviation and multiplied by the coefficient $\sqrt{2}$. [23] described a similar method of processing the received amplitude signals in detail.

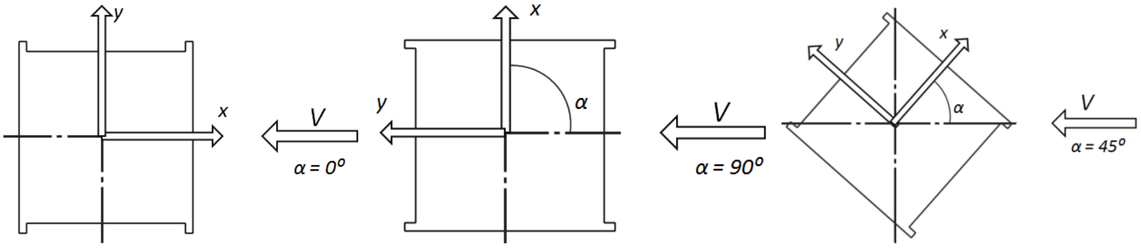

Figure 7. Attack angles of the model.

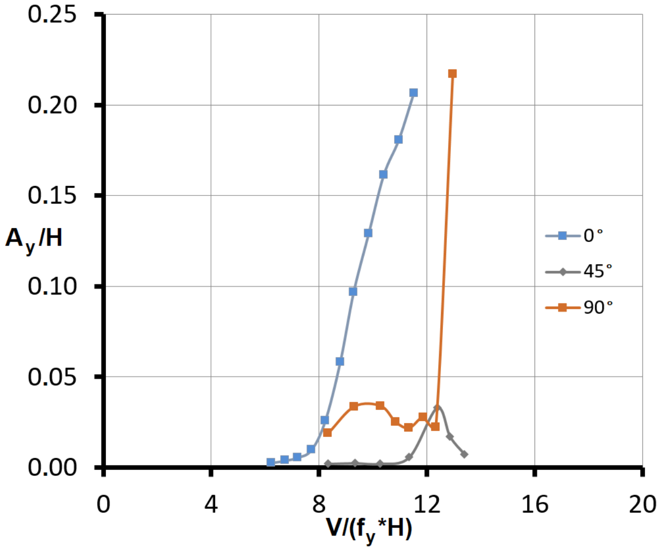

Figure 8. AVC of the sectional suspension model ($\alpha = 0°…90°$).

From the graphs, it can be seen that at a relative velocity $\overline{V} = 8$, corresponding to the Strouhal number $\mathrm{Sh} = 0.125$, and at an angle of attack $\alpha = 0°$, appearing vibrations gradually increase to a relative amplitude $\overline{A} = 0.2$ at a relative velocity $\overline{V} = 11.5$. The experiment could not be conducted at higher speeds due to the risk of damaging the elastic suspension elements. When the model is positioned at α =90°, the relative amplitude does not exceed the value of $\overline{A} = 0.03$ up to the relative velocity $\overline{V} = 12.5$. The amplitude increases with speed. The same Strouhal number values were observed when the model was positioned at $\alpha = 45°$. In this position, an insignificant amplitude maximum was observed.

The aerodynamic experiments on elastic suspension with various damping degrees were carried out at the angle of attack $\alpha = 0°$ (Fig. 9). For this purpose, stepped dampers of various diameters, similar in shape to spherical ones, were fixed to the middle of the lower surface of the model on a vertical spoke. The increase in the weight of the model due to the damper installation was less than 1%. The damping was carried out in a viscous fluid, which made it possible to conduct aerodynamic experiments at higher speeds without damage to the suspension elements of the model.

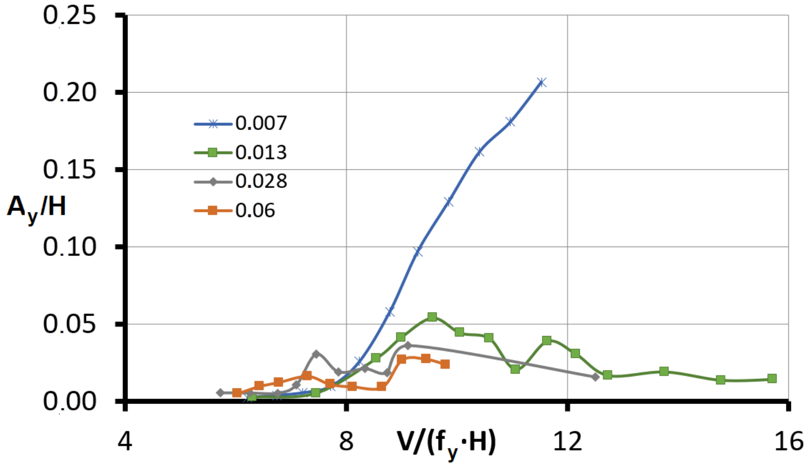

Figure 9. AVC models on an elastic suspension with different vibration decrements of damping ($\delta = 0.007…0.06$).

From the graphs, it can be seen that the maximum of the amplitude is observed at a relative velocity $\overline{V} = 10.5$, at the value of the vibration decrement of damping $\delta = 0.013$. The vibration amplitude decreases at higher speeds.

3.3. *AVC of the Cantilever-fixed Bridge Suspension Model*

The experimental conditions for the cantilever-fixed model are the same as for the elastic suspension model. However, this configuration has the following parameters: the rigidity ratio, the natural vibration frequencies along both axes of the model cross-section, and the strength of the elastic beam in the experimental setup. This allowed us to measure the amplitude of the vibrations in the model over the entire range of operating speeds. Aerodynamic wind tunnel tests were carried out at attack angles $\alpha = (0 \div 90)°$ with a step of (5÷10)°, without additional damping. AVC results for two extreme and one average values of $\alpha = 0°$, 45°, 90° are shown in Fig. 10. The logarithmic decrements of damping for $\alpha = 0°$ are $\delta_y = 0.006$ and for $\alpha = 90°$ are $\delta_x = 0.0065$.

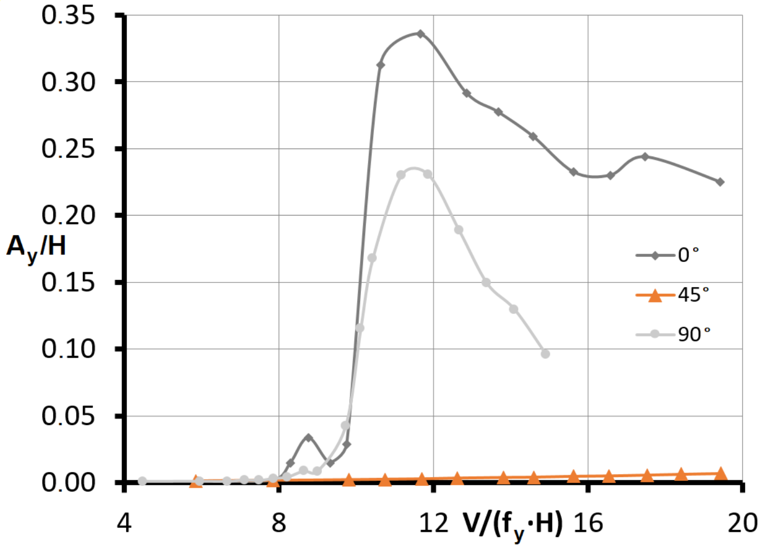

Figure 10. AVC of the cantilever-fixed model perpendicular to the flow ($\alpha = 0°…90°$).

The maximum relative amplitude for vibrations along the OY axis of the model is $\overline{A} = 0.34$, as the amplitude along the OX axis is $\overline{A} = 0.24$. Unstable vibrations with small amplitudes occur at relative velocity $\overline{V} = 8$ and higher. When the relative velocity $\overline{V} = 9 \div 10$ is reached, the amplitude increases significantly and reaches its maximum values. In the relative velocities $\overline{V} = 8 \div 10$, hysteresis is also observed. [24] noted a similar phenomenon for galloping a rectangular prism with aspect ratio up to $\lambda = 10$. The critical Strouhal number for the model at angles of attack $\alpha = 0°$ and $\alpha = 90°$ was $\mathrm{Sh} = 0.086$. After reaching the maximum rate without additional damping of the model, the amplitude decreases but remains significant, which is probably due to the transition to galloping. At the attack angle $\alpha = 45°$, no noticeable vibrations were detected in any directions.

The measured logarithmic damping decrement of full-scale suspension vibrations of the bridge, when the wind direction is perpendicular to the bridge, equals to $\delta = 0$. However, according to GOST[6], the value $\delta = 0.02$ was taken for calculation. The experiments were conducted with different damping degrees of the model for determining the dependence of the exciting aerodynamic force coefficient on the relative amplitude (Figs. 11 and 12). Further experiments were conducted due to the significant difference among the decrements of the cantilever-fixed model from the value.

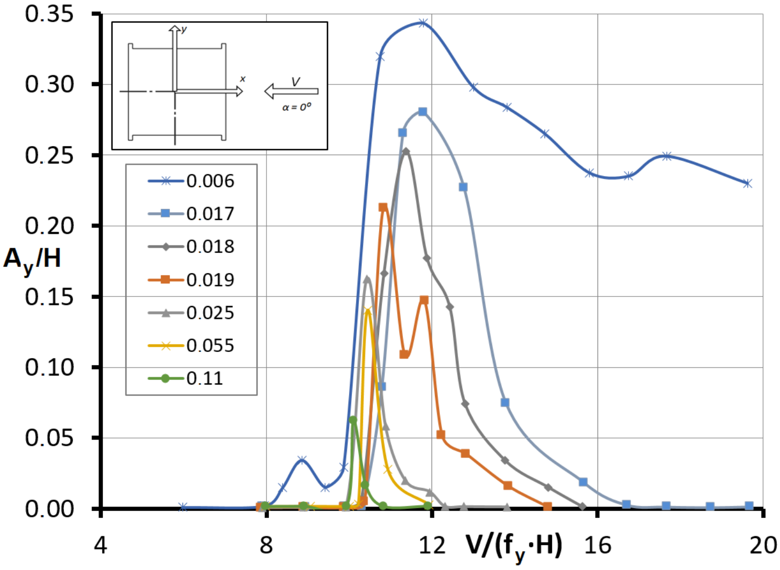

Figure 11. Damping effect on the AVC of the cantilever-fixed model when the wind direction is perpendicular to the span of the bridge ($\delta = 0.006…0.11$).

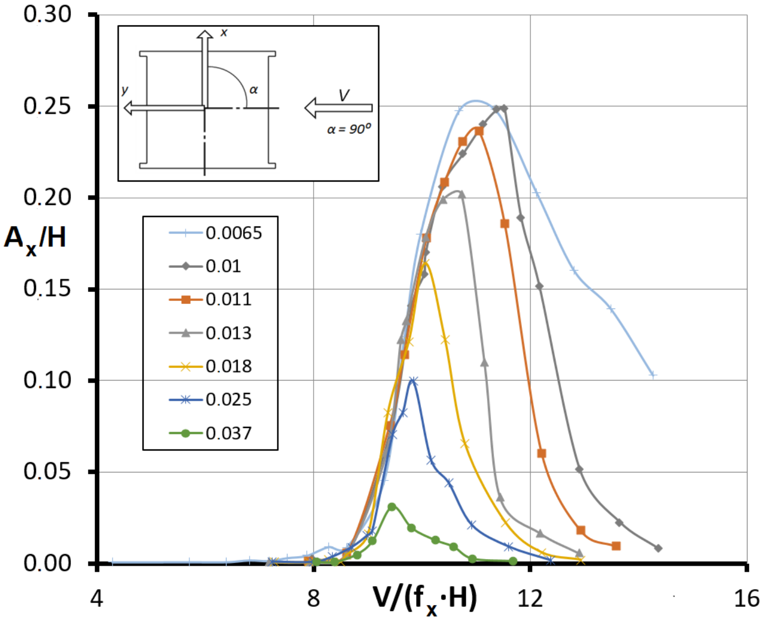

Figure 12. Damping effect on the AVC of the cantilever-fixed model when the wind direction is parallel to the bridge span ($\delta = 0.0065…0.037$).

---

[6] Federal Agency on Technical Regulating and Metrology (Rosstandart). Automobile roads of the general use. Bridge constructions. The rules of the aeroelastic stability. Calculation and verification. GOST R 59625–2022. 2022. 42 p.

Table 1. Logarithmic decrement of damping models with different damping degrees.

No. of the damper	Without a damper	D3	D4	D5	D5,5	D6	D7
$\delta_x(A_{max})$	0.0065	0.010	0.011	0.013	0.018	0.025	0.037
$\delta_y(A_{max})$	0.006	0.017	0.018	0.019	0.025	0.055	0.11

When $\delta = 0.02$, as taken from GOST[7], and using the method of amplitude measurement for the cantilever-fixed model applied in this study, the relative amplitude is $\overline{A}_{\max} = 0.22$. This value differs from the calculated one, specified in the same GOST, ($\overline{A}_{\max} = 0.21$) by only 4 %.

When measured on a full-scale suspension $\delta = 0.015$ and average amplitude of about 70 mm with a wind speed of ≈12 m/s, the measured relative amplitude is $\overline{A}_{\max} = 0.12$. This is two times lower than the experimental and calculated amplitude. This can be related to the unstable direction (±10° from perpendicular direction to the span structure) and wind speed observed in full-scale conditions.

Based on the cantilever-fixed model experiment results, the dependences of the aerodynamic exciting coefficients c_a on the relative amplitude (Fig. 13) $c_{a,y}\left(\overline{A}_y\right)$ and $c_{a,x}\left(\overline{A}_x\right)$ were determined according to the method described in GOST[8]. The coefficient c_a is used to calculate the maximum relative amplitude of the vibrations.

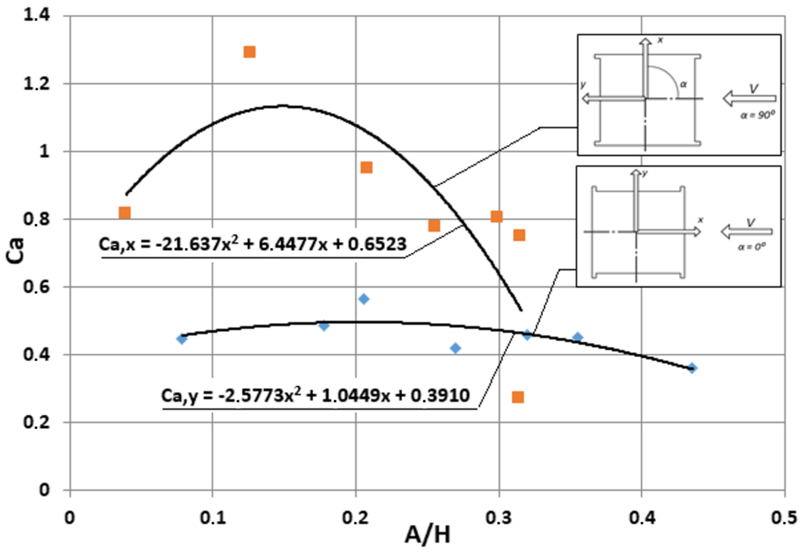

Figure 13. Dependence of the aerodynamic exciting coefficients $c_{a,y}$ and $c_{a,x}$ on the relative amplitude of the vibrations.

4. Conclusions

1. When investigating the causes of aeroelastic vibrations of the bridge, calculations and experiments have revealed that the wind resonance of the suspensions of a bridge is the main cause of these vibrations.
2. The span of the bridge is not subject to dangerous aeroelastic vibrations. At the same time, the range of VIV velocity at the level of suspensions has found to be 12÷18 m/s. It indicates the frequent occurrence of aeroelastic vibrations, which requires finding ways to reduce vibrations on the building in operation.

---

[7] Ibid.

[8] Ibid.

3. New data on the aerodynamic characteristics of an H-shaped section, geometrically similar to a square section, have been obtained. The results show that a slight difference from a well-studied square section leads to significant changes in the aerodynamic exciting coefficient. And the aerodynamic exiting coefficient differs by more than two times for angles of attack of 0° and 90° for the H-shaped section.

4. The aerodynamic studies of structures with a slight difference from the cross-section shapes, given in the standard and reference works, should be conducted.

References

1. Gosteev, Y., Konovalov, I., Lebedev, A., Obukhovskiy, A., Salenko, S., Yashinov, A. Numerical and Experimental Studies of the Use of Fiber-Reinforced Polymers in Long-Span Suspension Bridges. Energies. 2022. 15(5). Article no. 1864. DOI: 10.3390/en15051864
2. Gosteev, Yu.A., Obuhovskiy, A.D., Salenko, S.D. Influence of the shape on aerodynamic characteristics of girder bridges. Magazine of Civil Engineering. 2014. 5. Pp. 63–72. DOI: 10.5862/MCE.49.7
3. Kazakevich, M.I. Aerodinamicheskaia ustoichivost' nadzemnykh i visiachikh truboprovodov [Aerodynamic stability of above-ground and suspended pipelines]. Moscow: Nedra, 1977. 200 p.
4. Devnin, S.I. Aerogidromekhanika plokhoobtekaemykh konstruktsii [Aerohydromechanics of poorly streamlined structures]. Leningrad: Sudostroenie, 1983. 331 p.
5. Novak, M. Galloping Oscillations of Prismatic Structures. Journal of Engineering Mechanics Division. 1972. 98(1). Pp. 27–46. DOI: 10.1061/JMCEA3.0001575
6. Mannini, C., Marra, A.M., Bartoli, G. VIV–galloping instability of rectangular cylinders: Review and new experiments. Journal of Wind Engineering and Industrial Aerodynamics. 2014. 132. Pp. 109–124. DOI: 10.1016/j.jweia.2014.06.021
7. Larsen, A., Larose, G.L. Dynamic wind effects on suspension and cable-stayed bridges. Journal of Sound and Vibration. 2015. 334. Pp. 2–28. DOI: 10.1016/j.jsv.2014.06.009
8. Chen, W.-L., Zhang, Q.-Q., Li, H., Hu, H. An experimental investigation on vortex induced vibration of a flexible inclined cable under a shear flow. Journal of Fluids and Structures. 2015. 54. Pp. 297–311. DOI: 10.1016/j.jfluidstructs.2014.11.007
9. Li, M., Li, S., Liao, H., Zeng, J., Wang, Q. Spanwise correlation of aerodynamic forces on oscillating rectangular cylinder. Journal of Wind Engineering and Industrial Aerodynamics. 2016. 154. Pp. 47–57. DOI: 10.1016/j.jweia.2016.04.003
10. Daniotti, N., Jakobsen, J.B., Snæbjörnsson, J., Cheynet, E., Wang, J. Observations of bridge stay cable vibrations in dry and wet conditions: A case study. Journal of Sound and Vibration. 2021. 503. Article no. 116106. DOI: 10.1016/j.jsv.2021.116106
11. Yangchen, D., Shouying, L., Zhengqing, C. Experimental investigation on wake-induced vibrations of the hangers of suspension bridges based on three-dimensional elastic test model. Engineering Structures. 2021. 234. Article no. 111985. DOI: 10.1016/j.engstruct.2021.111985
12. Wang, B., Zhang, M., Xu, F. Experimental investigation on the vortex-induced vibration of a rectangular 4:1 cylinder under skew winds. Journal of Wind Engineering and Industrial Aerodynamics. 2022. 229. Article no. 105114. DOI: 10.1016/j.jweia.2022.105114
13. Ge, Y., Zhao, L., Cao, J. Case study of vortex-induced vibration and mitigation mechanism for a long-span suspension bridge. Journal of Wind Engineering and Industrial Aerodynamics. 2022. 220. Article no. 104866. DOI: 10.1016/j.jweia.2021.104866
14. Haque, M.N., Katsuchi, H., Yamada, H., Nishio, M. Investigation of Flow Fields Around Rectangular Cylinder Under Turbulent Flow by LES. Engineering Application of Computational Fluid Mechanics. 2014. 8(3). Pp. 396–406. DOI: 10.1080/19942060.2014.11015524
15. Fujino, Y., Kimura, K., Tanaka, H. Wind Resistant Design of Bridges in Japan: Developments and Practices. Springer. Tokyo, 2012. 256 p. DOI: 10.1007/978-4-431-54046-5
16. Elshaer, A., Bitsuamlak, G., Damatty, A. Aerodinamic optimization to reduce wind loads on tall building. Resilient Infrastructure. 2016. June. Article no. NDM-530.
17. Gao, D.-L., Chen, W.-L., Li, H., Hu, H. Flow around a slotted circular cylinder at various angles of attack. Experiments in Fluids. 2017. 58. Article no. 132. DOI: 10.1007/s00348-017-2417-8
18. Chen, W.-L., Gao, D.-L., Yuan, W.-Y., Li, H., Hu, H. Passive jet control of flow around a circular cylinder. Experiments in Fluids. 2015. 56. Article no. 201. DOI: 10.1007/s00348-015-2077-5
19. Carassale, L., Freda, A., Marrè-Brunenghi, M. Experimental investigation on the aerodynamic behaviour of square cylinders with rounded corners. Journal of Fluids and Structures. 2014. 44. Pp. 195–204. DOI: 10.1016/j.jfluidstructs.2013.10.010
20. Wang, Q., Jiang, Q., Hu, G., Chen, X., Li, C., Xiao, Y. Aerodynamic characteristics of a square cylinder with corner fins. Advanced in Bridge Engineering. 2021. 2. Article no. 20. DOI: 10.1186/s43251-021-00042-x
21. Ding, F., Kareem, A. Tall Buildings with Dynamic Facade Under Winds. Engineering. 2022. 6(12). Pp. 1443–1453. DOI: 10.1016/j.eng.2020.07.020
22. Shmigirilov, R., Ryabinin, A. Vliyaniye kontsevykh shayb na poperechnoye obtekaniye pryamougolnoy plastiny malogo udlineniya [Influence of end plates on the transversal flow past rectangular plate of small aspect ratio]. Estestvennye i matematicheskie nauki v sovremennom mire [Natural and mathematical sciences in the modern world]. 2015. 5(29). Pp. 158–162.
23. Zhou, S., Zou, Y., Hua, X., Liu, Z. Comparison of Two-Dimensional and Three- Dimensional Responses for Vortex-Induced Vibrations of a Rectangular Prism. Applied Sciences. 2020. 10(22). Article no. 7996. DOI: 10.3390/app10227996
24. Lyusin, V.D., Ryabinin, A.N. Issledovanie vliianiia udlineniia prizmy na ee aerodinamicheskie kharakteristiki i amplitudu kolebanii pri galopirovanii [Investigation of the influence of an elongated prism on its aerodynamic characteristics and vibration amplitude during galloping]. Vestnik of Saint Petersburg University. Mathematics. Mechanics. Astronomy. 2011. 2. Pp. 139–145.

Information about the authors:

Yuri Gosteev, *PhD in Physics and Mathematics*
E-mail: gosteev@corp.nstu.ru

Ilya Konovalov,
E-mail: iluhster@mail.ru

Alexander Obuhovskiy, *PhD in Technical Sciences*
E-mail: agd@craft.nstu.ru

Sergey Salenko, *Doctor of Technical Sciences*
E-mail: salenkosd@yandex.ru

Received: 25.09.2023. Approved: 05.05.2025. Accepted: 06.05.2025.

Magazine of Civil Engineering

ISSN
2712-8172

journal homepage: http://engstroy.spbstu.ru/

Research article

UDC 697.1 : 628.8

DOI: 10.34910/MCE.135.4

Temperature mode of a room at proportional-integrated regulation of climate systems

O.D. Samarin ✉

Moscow State University of Civil Engineering (National Research University), Moscow, Russian Federation

✉ *samarin-oleg@mail.ru*

Keywords: microclimate, temperature, heat balance, heat gain, regulation, proportional-integral algorithm, transmission coefficient, civil engineering, building, construction industry

Abstract. The complex including a room serviced by automated microclimate control systems, heat and mass exchange equipment of such systems and their technical means of automation is very complicated for mathematical description of transient processes under conditions of thermal disturbances when solving problems of ensuring comfort of internal meteorological parameters and synthesis of automatic control systems. The nonlinearity of the process of temperature wave propagation in the arrays of enclosing structures leads to a significant error in the case of representation of the room as a linear inertial link. Therefore, the correct mathematical description of transient processes in this case leads to nonlinear differential equations of the Emden–Fowler type, the solution of which in the considered conditions is not expressed in elementary functions and requires numerical methods. One of the most complicated variants in this case is the use of combined proportional-integral law of air conditioning system control in the absence of local heating-cooling systems. Then the solution can be obtained in a parametric form containing a generalized dimensionless parameter of the automated climate control system, including the proportional and integral components transfer factors and the air throughput of the system. The paper shows that in this case, with the growth of the integral component, the dynamic error, i.e., the largest deviation of the room temperature from the setpoint, and the control time are reduced; at the same time, for small moments of time, all the calculated curves describing the temperature behavior asymptotically coincide with the initial heating curve. After reducing the solution to a dimensionless form, the universal dependencies for the indoor temperature behavior depending on the characteristics of the room and regulator parameters, suitable for use in the engineering practice, are obtained. The calculations performed for a typical representative room, in comparison with the relevant experimental data, confirm the reliability of the obtained results and their applicability for mass design.

Citation: Samarin, O.D. Temperature mode of a room at proportional-integrated regulation of climate systems. Magazine of Civil Engineering. 2025. 18(3). Article no. 13504. DOI: 10.34910/MCE.135.4

1. Introduction

As an object of the research, the proposed work considers the behavior of the indoor air temperature in a room, in which a comfortable set of internal meteorological parameters is maintained by central air systems of microclimate provision equipped with automation devices using a combined proportional-integral (PI-) control algorithm.

It should be noted that the development of scientific research in the field of calculations of the transient thermal regime of rooms, analysis of the operation of the equipment of microclimate systems servicing them and their automation systems, as well as methods of their selection, was traditionally carried out in several parallel directions. One of them concerned the processes in the indoor air and in the enclosing structures under different nature of variable thermal disturbances, both periodic and one-time. In this direction, the developed engineering and analytical theories included, in particular, the theory of thermal stability, the method of “response factor”, and other solutions, including those considering cooling of the buildings during their emergency cutoff from heat supply systems or, on the contrary, initial heating up of premises as a result of a heat supply jump, e.g., [1–3]. This could involve climate systems but mainly in terms of their role in the overall heat balance of the facility as a source of relevant additional heat inputs or their removal. In addition, in some cases, the issues of optimization of thermal protection properties of enclosures and operation modes of heating and heat supply systems could be resolved using economic methods, but the results obtained in this case are not usually generalized to other objects [4]. With the development of computer engineering, numerical methods are certainly added to engineering-analytical methods, although it should be noted that works with their application are still more common abroad. Here, we can note, in particular, publications [5–7]: their advantage can be considered to be the inclusion of experimental data in addition to numerical calculations, which allows identifying the theoretical model.

The processes directly in the heat and mass exchange equipment for inflow treatment or in heat supply systems were usually considered separately, using specific methods including heat balance and heat transfer equations, in particular, and, in [1, 2], including in a dimensionless form, although it is quite obvious that such equipment constitutes a single system with the room and technical means of automation. Finally, the issues of regulation of climatic systems were usually considered from the standpoint of the theory of automatic control, which operates with the concepts of system links represented as a “black box”, actually disregarding the physical essence of the processes occurring in them. To simplify the equations and to obtain solutions in an engineering form, these links are usually considered as linear [1, 2, 6, 7], which, as will be seen from the following description, gives a significant error for transient processes in the rooms. This kind of separate consideration leads to a considerable number of publications devoted to the study of processes in specific individual objects, for example, in ventilated facades with account of the operation of the natural ventilation system only [8], or even the paper of the author of the proposed work [9], in which a very simple dependence for the penetration velocity of a heat wave in a thick-walled cylindrical structure was found. The same features are characteristic for the works, the authors of which are engaged in solving inverse problems of searching for initial data and characteristics, for example, thermophysical properties of building materials, according to the results of temperature behavior measured in one way or another, in particular [10, 11].

In some cases, the use of numerical methods makes it possible to build a comprehensive model taking into account all the above-mentioned systems and factors, but due to their specificity such approaches cannot provide universal engineering methods suitable for tentative estimates and for introduction into normative and reference documents, since they require individual calculations on the computer for each particular object. In addition, this may require knowledge of a large number of parameters of the room and engineering systems, which should be used as input data for the relevant program, e.g., [12]. Still less suitable for the engineering practice, due to the lack of specific sufficiently simple analytical or graphical dependencies, are the methods that have been recently gaining ground, based on the so-called fuzzy logic [13, 14] and other cross-system concepts [15, 16], as well as works devoted to the general principles of energy saving in buildings through various solutions to reduce energy consumption, including automation of climate systems [17–19]. Thus, to date, there are practically no models and solutions that allow joint consideration of nonstationary processes in the rooms serviced by automated microclimate systems, with account of their physical essence, interconnection and mutual influence and available for application in mass design.

In previous works, the author made attempts of such a comprehensive consideration for the simplest variants of laws of control: proportional (P-) [20] and integral (I-) [21, 22]. However, in practice, especially for air conditioning systems, more complex algorithms are used for more accurate maintenance of internal meteorological parameters and ensuring the required comfort in the serviced zone of the room. One of the most common of them is a combination of the said laws, namely PI-control combining some of their advantages, in particular, the relative speed of P-controllers and the zero static error of integrators. Therefore, it seems relevant to continue the research of transient modes in indoor and climatic systems for this case as well.

Thus, the object of the research is to build a mathematical model of nonstationary thermal processes in a complex including a room and heat and mass exchange equipment of automated central air conditioning systems servicing it, controlled by a PI-algorithm, and to develop a methodology for evaluating such a regime, suitable for use in engineering practice and taking into account all the main parameters of the system.

Thus, the tasks of the work are as follows:

– to formulate a system of differential equations describing transient processes in a room under a jump-like thermal disturbance and its assimilation by central air climatic systems equipped with a PI-controller;

- to obtain the solution of this system describing the behavior of indoor air temperature in the specified conditions, recording it in a dimensionless form and its analysis under different initial data, including the change of the ratio between P- and I-components of the law of control;
- to search for possible asymptotics of the detected solution at limiting values of the room and regulator parameters;
- to compare the results with the available experimental data, including those obtained by other authors, and to construct correlations linking the system parameters and indoor temperature which would be suitable for application in mass design.

2. Methods

As in the works [20–22], using the concept of excess temperature $\theta_{in} = t_{in} - t_{in.0}$, where $t_{in.0}$ is a controlled level of inside air temperature t_{in}, or the so-called input reference, for a sudden change in thermal disturbance and its compensation due to the operation of a central air conditioning system that simultaneously performs ventilation functions, the equation of the convective heat balance for the room as a whole can be written as follows:

$$Q_{in} + G_s c_a \left(\theta_s - \theta_{in}\right)/3.6 - B\sqrt{\tau}\frac{\mathrm{d}\theta_{in}}{\mathrm{d}\tau} = 0, \tag{1}$$

where Q_{in} is the inflow of explicit convective heat into the room air from sources, W; τ is the time interval, s, from the moment of occurrence of a thermal disturbance; G_s is the mass flow rate of the intake air, kg/h, which is equal to the flow rate of the exhaust G_{ex}, since the air balance of the room, unlike from thermal, almost happens instantly-stationary; c_a is the specific mass heat capacity of air equal to 1.005 kJ/(kg·K); $\theta_s = t_s - t_{in.0}$ is the excessive inflow rate, K.

Similarly [20–22], parameter B, W·s$^{1/2}$/K, in equation (1) is determined by the formula:

$$B = \sum \left\lfloor A_m \sqrt{\lambda c \rho} \right\rfloor_i, \tag{2}$$

where λ, c and ρ are, respectively, the thermal conductivity, W/(m·K), the specific heat capacity, J/(kg·K), and the density of the material layer of the i-th massive enclosing structure (external and internal walls, ceilings, partitions) facing inside the room; A_m is the area of each of the listed fences, m^2.

If the value of θ_{in} is automatically maintained by a regulator implementing a continuous PI-law, the complementary constraint equation is easiest to write in this form:

$$\frac{\mathrm{d}\left(\theta_s - \theta_{in}\right)}{\mathrm{d}\tau} = -K_i\theta_{in} - K_p\frac{\mathrm{d}\theta_{in}}{\mathrm{d}\tau}, \tag{3}$$

where K_i is equivalent coefficient of transfer of integral component of the automated system s^{-1}, by the channel "$\theta_{in} \rightarrow$ derivative of the difference between $\theta_s - \theta_{in}$", K_p is the same for proportional component by the channel "$\theta_{in} \rightarrow$ difference between $\theta_s - \theta_{in}$" (dimensionless). Differentiating term-by-term (1) by τ in order to be able to substitute expression (3) there, we bring (1) to the canonical form:

$$\frac{\mathrm{d}^2\theta_{in}}{\mathrm{d}\tau^2} + \left(\frac{1}{2\tau} + \frac{C}{\sqrt{\tau}}\right)\frac{\mathrm{d}\theta_{in}}{\mathrm{d}\tau} + \frac{D}{\sqrt{\tau}}\theta_{in} = 0. \tag{4}$$

The parameters C, $s^{-1/2}$, and D, $s^{-3/2}$ can be determined by the formulas:

$$C = \frac{G_s c_a K_p}{3.6B}; \quad D = \frac{G_s c_a K_i}{3.6B}. \tag{5}$$

Thus, formally (4) coincides with the equation obtained previously by the author in [21], but the coefficients C and D have a different physical meaning and are expressed differently in terms of the original data. After substitution, the relation $z=\sqrt{\tau}$ (4) can be reduced to a somewhat simpler form, in which the first of the terms including the first derivative disappears:

$$\frac{\mathrm{d}^2\theta_{in}}{\mathrm{d}z^2}+2C\frac{\mathrm{d}\theta_{in}}{\mathrm{d}z}+4zD\theta_{in}=0. \tag{6}$$

It is easy to see that for $C=0,$ i.e., with the exclusion of the proportional component of the regulator, (6) will be an Emden–Fowler equation [23, 24]. However, in the general case under consideration, at $C\neq 0,$ the methods used in these works are no longer suitable, although some general properties of the equation and, as a consequence, its solutions associated with nonlinearity due to the presence of a multiplier z at the third term are still preserved. Therefore, we transform the resulting equation further in order to highlight the singularity at $z=0,$ namely, we present the solution as a product of $\theta_{in}=zf\left(z\right)$ and then we make another replacement of the independent variable, that is, we assume $x=4Dz^3$ – a dimensionless time argument, from which, respectively, $z=\left(\frac{x}{4D}\right)^{1/3}$. Then from (6), we get:

$$9x\frac{\mathrm{d}^2f}{\mathrm{d}x^2}+\left[12+6C\left(\frac{x}{4D}\right)^{1/3}\right]\frac{\mathrm{d}f}{\mathrm{d}x}+\left[1+\frac{2C}{\left(4Dx\right)^{1/3}}\right]f=0. \tag{7}$$

If we now assume that $K=\frac{2C}{\left(4D\right)^{1/3}}=K_p\sqrt[3]{\frac{2}{K_i}\left(\frac{G_sc_a}{3.6B}\right)^2}$ is a generalized dimensionless parameter of the automated climate system, we can finally obtain:

$$9x\frac{\mathrm{d}^2f}{\mathrm{d}x^2}+\left[12+3Kx^{1/3}\right]\frac{\mathrm{d}f}{\mathrm{d}x}+\left[1+\frac{K}{x^{1/3}}\right]f=0. \tag{8}$$

Obviously, $f\left(0\right)=1,\ \mathrm{d}f\left(0\right)/\mathrm{d}x=1/12$ should be taken as the initial conditions for (8).

It is clear that the solution of equation (8) gives a universal dependence that is applicable for any objects and conditions. Therefore, in a dimensional form, the ratio for the current ambient air temperature will look like this:

$$\theta_{in}=\frac{2Q_{in}\sqrt{\tau}}{B}f\left(x\right). \tag{9}$$

At the same time, if we consider (8) for little periods of time, we can notice that the first term can already be neglected, and we get a 1st-order equation with separable variables. In this case, its solution will be represented by $f\left(x\right)=\exp\left(-f_1\left(x\right)\right),$ where the auxiliary function f_1 is defined as an integral:

$$f_1\left(x\right)=\frac{1}{12}\int_0^x\frac{1+Kx^{-1/3}}{1+Kx^{1/3}/4}\,\mathrm{d}x, \tag{10}$$

or asymptotically for small K and x:

$$f_1\left(x\right)=\frac{1}{12}\left[\left(1-\frac{K^2}{4}\right)x+\frac{3}{2}Kx^{2/3}\right]. \tag{11}$$

3. Results and Discussion

Fig. 1 shows the type of functions $f\left(x\right)$ for various values of parameter K from 0 to 4, obtained by numerical solution (9) using a computer program by the Runge–Kutta method of the 4th order. According to (5) and (6), we have here $x = \frac{4G_{in}c_a K_i}{3.6B}\tau^{3/2}$.

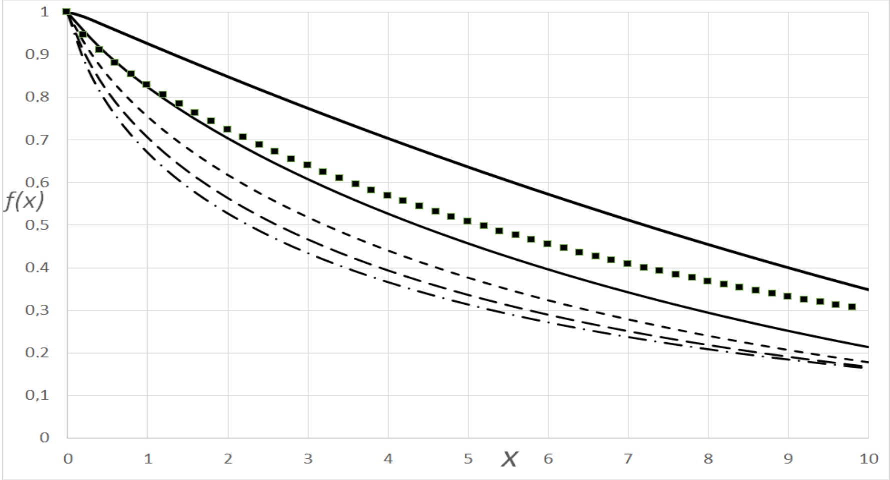

Figure 1. Dimensionless dependence $f(x)$ for K = 0, 1, 2, 3, and 4 (lines from top to bottom), for K = 1 with the use of (11) (square markers).

By virtue of the above, the constructed graphs can serve as a universal nomogram, which can be used in engineering calculations in combination with formula (9). For comparison, square markers show a curve using expression (11) at K = 1.

The nature of the change of θ_{in} for one of the rooms in a public building, previously considered by the author in [20, 21], is shown for clarity in Fig. 2. At the same time, it was assumed that Q_{in} = 500 W, B = 12,000 W·s$^{1/2}$/K in accordance with the structural solutions of the room and the thermal properties of its enclosing structures, the inflow flow rate G_s = 430 kg/h and K_p = 0.84, from where C = 0.0084 s$^{-1/2}$, and the coefficients K_i were considered equal to 0 (that is, for the limiting case of purely proportional regulation), $8.4 \cdot 10^{-6}$, $8.4 \cdot 10^{-5}$, and $8.4 \cdot 10^{-4}$, whence, respectively, D = 0, $8.4 \cdot 10^{-8}$, $8.4 \cdot 10^{-7}$, and $8.4 \cdot 10^{-6}$ s$^{-3/2}$. Then, the parameter K by its definition will acquire the values ∞, 2.4, 1.11, and 0.52. With the exception of the first one, they lie within the limits for which the graphs in Fig. 1 are calculated. As for K_i = 0, it requires separate consideration, since there is an analytical solution obtained by the author in [20], although the original equation (6) can be solved numerically and directly at D = 0, and from (5), the corresponding result is obtained by the limiting transition $K \to \infty$.

From Fig. 2, it is easy to see that, as in the case of control objects represented as a linear inertial link, the appearance of an integral component of the regulator immediately leads to the fact that the residual temperature deviation, or static control error, becomes zero, and the maximum value of θ_{in} gradually decreases with increasing K_i, as does the control time. At the same time, at small τ, all curves coincide asymptotically, which confirms the conclusions about the proportionality of θ_{in} and $\sqrt{\tau}$ in the mode of initial heating or cooling of the room.

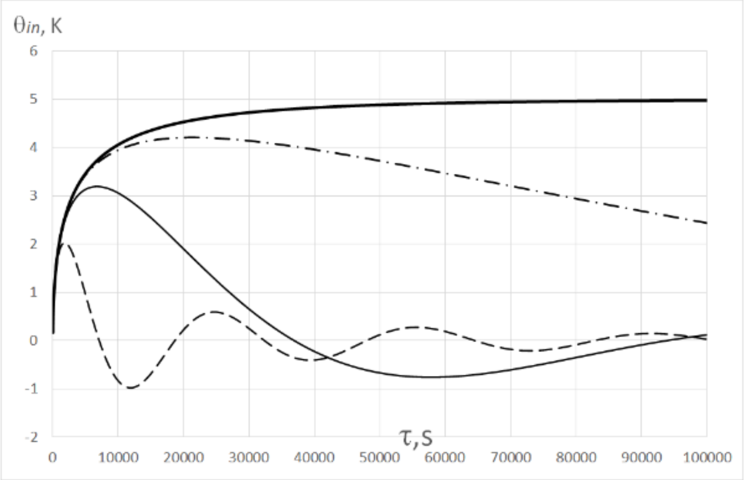

Figure 2. Dependence of θ_{in} on time for a specific room at K_i = 0, 8.4·10^{-6}, 8.4·10^{-5}, and 8.4·10^{-4} (from top to bottom).

In Fig. 3, the dotted line shows the results of experimental measurements in the representative room shown above at Q_{in} = 500 W. The measurements were carried out similarly to those presented in [21] using Testo 0560 1110 Mini penetration thermometer with a division of 0.1°, which was installed in the center of the room at a height of 1 m from the floor. In fact, the regulation of the air conditioning system was carried out positionally ("on/off"), but due to the high frequency of switching, it was approaching continuous. The solid line represents the data of direct numerical integration of the original equation (6) using a computer program by the 4th-order Runge–Kutta method. The best match within the accuracy of the measuring device is observed at K_p = 0.0167 and K_i = 0.0125 s^{-1}, which corresponds to the values of the parameters C = 8.33·10^{-5} s$^{-1/2}$ and D = 6.25·10^{-5} s$^{-3/2}$ with the value of B = 24000 W·s$^{1/2}$/K, that is, in 2 times higher than was accepted for calculations in Fig. 2, since a separate room was viewed here and, thus, the temperature wave propagated only in one direction.

It should only be kept in mind that for small τ, the coincidence of theoretical and experimental dependence turns out to be somewhat worse, which can be explained by the influence of the thermal inertia of the indoor air volume, which was not directly taken into account when writing the initial equation (1), as a result of which the measured temperatures are obtained up to a certain point lower than according to (6). The same applies to the rightmost area of the graph, after the temperature has passed the maximum. This issue has already been analyzed to some extent by the author in [20, 21], where it was noted that, apparently, another limitation used in conclusion (1) is already beginning to affect here, namely the assumption that the temperature wave does not have time to penetrate to the outside the surface of the fence or up to its axis of symmetry. Nevertheless, since from the point of view of using the results in engineering practice, we are primarily interested in the value and moment of the greatest temperature deviation, the coincidence can be considered satisfactory.

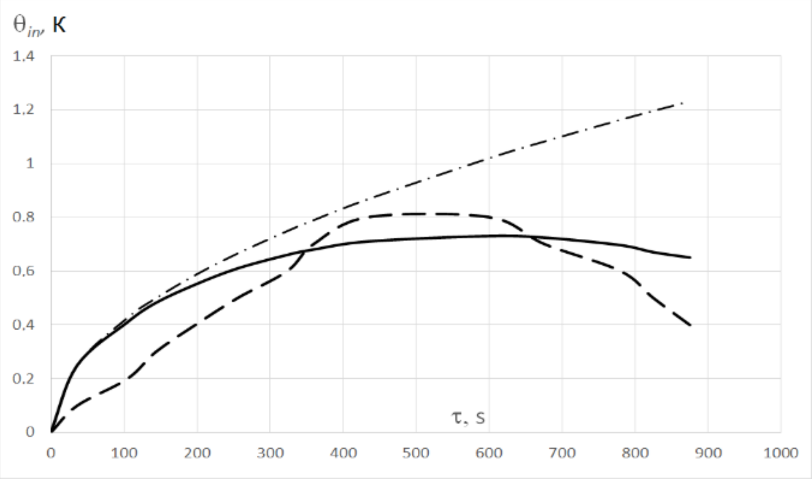

Figure 3. Dependence of θ_{in} on time for a specific room in a full-scale experiment (solid line – calculation by (6), dotted line – experiment, dashed dot – initial heating curve).

Thus, comparison with experimental data can be used to identify a mathematical model, that is, to identify the actual parameters of the control system, which would be difficult to determine directly. For comparison, the dashed dot line depicts the process of initial heating of a given room in the case of Q_{in} = 500 W and the absence of compensation for heat gain by expression (9) at $f\left(x\right)$ = 1 [20, 21]. It is not difficult to notice that both the theoretical solution (6) and the experimental results, although to a somewhat lesser extent, asymptotically coincide with the initial heating curve at small τ, which further confirms their correctness.

In addition, Fig. 4 shows a comparison of the calculation results for (6) for the same room but with slightly different initial parameters, namely K_p = 0.071 and K_i = 0.025 s^{-1}, which corresponds to the values of parameters C = 3.55·10^{-4} s$^{-1/2}$ and D = 1.25·10^{-4} s$^{-3/2}$ also at a value of B = 24000 W·s$^{1/2}$/K, with the data of full-scale measurements of the non-stationary thermal regime of the room, which is equipped with the automated air heating system under similar control conditions given in [25] (dotted line), after normalization by the magnitude of the maximum temperature deviation.

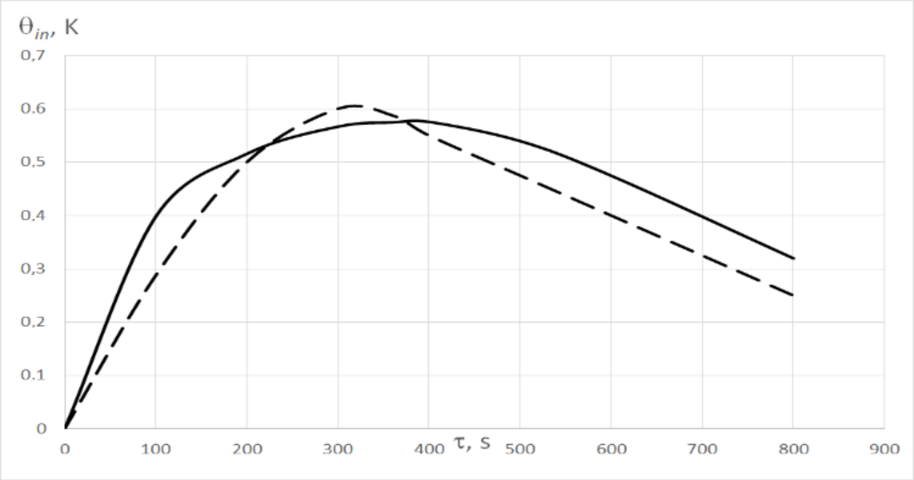

Figure 4. Dependence of θ_{in} on time for the room under study (solid line – according to equation (6), dotted line – measurement data [25]).

It can be seen that in almost the entire time interval under consideration since the appearance of the thermal disturbance, experimental measurements give a similar nature of dependence, which further confirms the theoretical provisions of the proposed work, and the discrepancies have the same appearance as in Fig. 3 and can be explained in a similar way.

4. Conclusion

- It has been shown that the mathematical description of transient processes at a jump-like thermal disturbance in the room serviced by central air conditioning systems, formulated in the previous works of the author in the form of the differential equation of the Emden–Fowler type, is a limiting case arising at exclusion of the P-component of the regulator.
- It is noted that the solution of the obtained system of equations for the PI-law of control still retains some properties characteristic of the Emden–Fowler type equations, namely, it has a specific feature at $\tau = 0$ and admits a representation in the form of a product of $zf\left(z\right)$, where $z = \sqrt{\tau}$.
- It has been proved that the presence of the P-component of the regulator can be taken into account by introducing a generalized dimensionless parameter of the automated climatic system K, including the P- and I-components transfer factors and the air throughput of the system.
- It has been shown that the reduction of the solution to a dimensionless form allows constructing universal correlations for the behavior of the indoor temperature depending on the characteristics of the room and regulator parameters, suitable for use in engineering calculations, its argument including the product of the transfer factor of the I-component and $\tau^{3/2}$ value.
- It has been demonstrated that the dynamic error, i.e., the largest deviation of the room temperature from the setpoint, and the control time decrease with the growth of the I-component;

at the same time, for small moments of time, all the calculated curves describing the temperature behavior asymptotically coincide with the initial heating curve.

- It is noted that the change in the behavior of the solution at the appearance and strengthening of the integral component of the regulator qualitatively coincides with the known regularities in the representation of the room as a linear inertial link.
- It has been confirmed experimentally using field measurements in a typical representative room that the discrepancy between the actual and theoretical values of θ_{in} is within the measurement accuracy and the usual error of engineering calculation, at least in the zone of maximum temperature deviation from the setpoint, which is of the greatest interest for engineering applications.

References

1. Rafalskaya, T. Safety of engineering systems of buildings with limited heat supply. IOP Conference Series: Materials Science and Engineering. 2021. 1030. Article no. 012049. DOI: 10.1088/1757-899X/1030/1/012049
2. Rafalskaya, T.A. Simulation of thermal characteristics of heat supply systems in variable operating modes. Journal of Physics: Conference Series. 2019. 1382. Article no. 012140. DOI: 10.1088/1742-6596/1382/1/012140
3. Mansurov, R., Rafalskaya, T., Efimov, D. Mathematical modeling of thermal technical characteristics of external protections with air layers. E3S Web of Conferences. 2019. 97. XXII International Scientific Conference “Construction the Formation of Living Environment” (FORM-2019). Article no. 06007. DOI: 10.1051/e3sconf/20199706007
4. Avsyukevich, D.A., Shishkin, E.V., Litvinova, N.B., Mirgorodskiy, A.N. Thermoeconomic model of a building's thermal protection envelope and heating system. Magazine of Civil Engineering. 2022. 113(5). Article no. 11302. DOI: 10.34910/MCE.113.2
5. Rulik, S., Wróblewski, W., Majkut, M., Strozik, M., Rusin, K. Experimental and numerical analysis of heat transfer within cavity working under highly non-stationary flow conditions. Energy. 2020. 190. Article no. 116303. DOI: 10.1016/j.energy.2019.116303
6. Bilous, I., Deshko, V., Sukhodub, I. Parametric analysis of external and internal factors influence on building energy performance using non-linear multivariate regression models. Journal of Building Engineering. 2018. 20. Pp. 327–336. DOI: 10.1016/j.jobe.2018.07.021
7. Millers, R., Korjakins, A., Lešinskis, A., Borodinecs, A. Cooling Panel with Integrated PCM Layer: A Verified Simulation Study. Energies. 2020. 13(21). Article no. 5715. DOI: 10.3390/en13215715
8. Petrichenko, M.R., Nemova, D.V., Kotov, E.V., Tarasova, D.S., Sergeev, V.V. Ventilated façade integrated with the HVAC system for cold climate. Magazine of Civil Engineering. 2018.1(77). Pp. 47–58. DOI: 10.18720/MCE.77.5
9. Samarin, O.D. The periodic temperature oscillations in a cylindrical profile with a large thickness. Magazine of Civil Engineering. 2019. 1(85). Pp. 51–58. DOI: 10.18720/MCE.85.5
10. Li, N., Chen, Q. Experimental study on heat transfer characteristics of interior walls under partial-space heating mode in hot summer and cold winter zone in China. Applied Thermal Engineering. 2019. 162. Article no. 114264. DOI: 10.1016/j.applthermaleng.2019.114264
11. Marino, B.M., Muñoz, N., Thomas, L.P. Estimation of the surface thermal resistances and heat loss by conduction using thermography. Applied Thermal Engineering. 2017. 114. Pp. 1213–1221. DOI: 10.1016/j.applthermaleng.2016.12.033
12. Bilous, I.Yu., Deshko, V.I., Sukhodub, I.O. Building energy modeling using hourly infiltration rate. Magazine of Civil Engineering. 2020. 4(96). Pp. 27–41. DOI: 10.18720/MCE.96.3
13. Faouzi, D., Bibi-Triki, N., Draoui, B., Abène, A. Modeling a Fuzzy Logic Controller to Simulate and Optimize the Greenhouse Microclimate Management using MATLAB SIMULINK. International Journal of Mathematical Sciences and Computing (IJMSC). 2017. 3(3). Pp. 12–27. DOI: 10.5815/ijmsc.2017.03.02
14. Latif, M., Nasir, A. Decentralized stochastic control for building energy and comfort management. Journal of Building Engineering. 2019. 24. Article no. 100739. DOI: 10.1016/j.jobe.2019.100739
15. Ryzhov, A., Ouerdane, H., Gryazina, E., Bischi, A., Turitsyn, K. Model predictive control of indoor microclimate: Existing building stock comfort improvement. Energy Conversion and Management. 2019. 179. Pp. 219–228. DOI: 10.1016/j.enconman.2018.10.046
16. Serale, G., Capozzoli, A., Fiorentini, M., Bernardini, D., Bemporad, A. Model Predictive Control (MPC) for Enhancing Building and HVAC System Energy Efficiency: Problem Formulation, Applications and Opportunities. Energies. 2018. 11(3). Article no. 631. DOI: 10.3390/en11030631
17. Belussi, L., Barozzi, B., Bellazzi, A., Danza, L., Devitofrancesco, A., Fanciulli, C., Ghellere, M., Guazzi, G., Meroni, I., Salamone, F., Scamoni, F., Scrosati, C. A review of performance of zero energy buildings and energy efficiency solutions. Journal of Building Engineering. 2019. 25. Article no. 100772. DOI: 10.1016/j.jobe.2019.100772
18. Sha, H., Xu, P., Yang, Z., Chen, Y., Tang, J. Overview of computational intelligence for building energy system design. Renewable and Sustainable Energy Reviews. 2019. 108. Pp. 76–90. DOI: 10.1016/j.rser.2019.03.018
19. Kharchenko, V., Ponochovnyi, Y., Boyarchuk, A., Brezhnev, E., Andrashov, A. Monte-Carlo Simulation and Availability Assessment of the Smart Building Automation Systems Considering Component Failures and Attacks on Vulnerabilities. Advances in Intelligent Systems and Computing. 2019. 761. Contemporary Complex Systems and Their Dependability (DepCoS-RELCOMEX 2018). Pp. 270–280. DOI: 10.1007/978-3-319-91446-6_26
20. Samarin, O.D. The calculation of the thermal mode of a room with automatic regulation of climate systems. Vestnik MGSU [Monthly Journal on Construction and Architecture]. 2020. 15(4). Pp. 585–591. DOI: 10.22227/1997-0935.2020.4.585-591
21. Samarin, O.D. Thermal mode of a room with integrated regulation of cooling systems. Magazine of Civil Engineering. 2021. 3(103). Article no. 10312. DOI: 10.34910/MCE.103.12
22. Samarin, O.D. Thermal mode of a room with integrated regulation of microclimate systems. Magazine of Civil Engineering. 2022. 8(116). Article no. 11610. DOI: 10.34910/MCE.116.10

23. Carillo, S., Zullo, F. Ermakov–Pinney and Emden–Fowler Equations: New Solutions from Novel Bäcklund Transformations. Theoretical and Mathematical Physics. 2018. 196(3). Pp. 1268–1281. DOI: 10.1134/S0040577918090027
24. Pikulin, S.V. Parametrization of Solutions to the Emden–Fowler Equation and the Thomas–Fermi Model of Compressed Atoms. Computational Mathematics and Mathematical Physics. 2020. 60(8). Pp. 1315–1328. DOI: 10.1134/S0965542520080138
25. Lysak, O. Analysis of the temperature distribution in a space heated by a dynamic (fan) storage heater. Eastern-European Journal of Enterprise Technologies. 2017. 3(8). Pp. 17–25. DOI: 10.15587/1729-4061.2017.103778

Information about the author:

Oleg Samarin*, PhD in Technical Sciences*
ORCID: https://orcid.org/0000-0003-2533-9732
E-mail: samarin-oleg@mail.ru

Received: 16.04.2024. Approved: 29.04.2025. Accepted: 29.04.2025.

Magazine of Civil Engineering. 2025. 18(3). Article No. 13505

Magazine of Civil Engineering

journal homepage: http://engstroy.spbstu.ru/

ISSN
2712-8172

Research article

UDC 69

DOI: 10.34910/MCE.135.5

Experimental evaluation of negative skin friction on floating pile in gypseous soil

A.H. Mohsen✉, B.S. Albusoda
Scientific Research Commission, Baghdad, Iraq
✉ *abeer.h.mohsin@src.edu.iq*
abeer.mohsin2001D@coeng.uobaghdad.edu.iq

Keywords: negative skin friction, NSF, steel pile, drag load, gypseous soil

Abstract. Gypseous soils are characterized by an open structure with developed porosity and high gypsum content, which determines their metastable state. When saturated with water, a decrease in volume occurs as a result of a decrease in matrix suction and degradation of cementation bonds, leading to rapid settlement. When a pile is installed in this type of soil, this can cause negative skin friction (NSF) along its surface, which increases the load pressure and reduces the safety factor. In this study, a laboratory model was used to evaluate NSF developed along the external surface of a steel pile embedded in gypseous soil. The effect of the degree of saturation, dry unit weight, length/diameter (L/D) ratio, and relative settlement between the soil and the pile on the magnitude of NSF, which can be described as a downward drag load along the pile shaft, has been studied. The results show that NSF increases with increasing L/D ratio by 66 % at the maximum collapse potential and decreases with increasing dry unit weight and degree of saturation by 26–60 % for L/D = 15 and by 78–137 % for L/D = 10. The maximum drag load occurs with zero water content and L/D = 15.

Citation: Mohsen, A.H., Albusoda, B.S. Experimental evaluation of negative skin friction on floating pile in gypseous soil. Magazine of Civil Engineering. 2025. 18(3). Article no. 13505. DOI: 10.34910/MCE.135.5

1. Introduction

Negative skin friction (NSF) generated along the pile shaft can significantly impact engineering construction when the soil foundation is collapsible during inundation. This phenomenon may lead to a reduction in the bearing capacity of the pile foundation, an increase in the pile load, and a consequent decrease in the safety factor calculated during the design processes [1–4].

There are two types of studies that have been carried out on this subject:

a) Field studies

Despite the high costs associated with these tests and changing environmental conditions (such as variation in water table level and temperature over extended testing periods) required to generate and develop NSF, these tests provide clear insights into the behavior of piles subjected to the NSF in collapsible soils [5–9].

b) Laboratory model studies

In laboratory settings, piles with specific properties are subjected to the drag load, which is developed during inundation of the collapsible soil with water under different conditions (such as time of inundation, application of ultimate or allowable load on the pile head, and surcharge on the soil surface). In addition, some studies have explored methods to reduce NSF by coating the pile shaft with bituminous materials [10–13].

Recent research has advanced the understanding of pile-negative friction in loess soil, which is one of the most important types of collapsible soil [14, 15]. Other studies have focused on artificial collapsible soils, such as sand-kaolin mixtures with varying clay and water content.

The centrifuge model tests for both single and group pipe piles, installed in sandy saturated soil with dry density ranging from 1.249 to 1.682 gm/cm^3, showed that the settlement soil layer, pile stress, and pile-top displacement varied with the variation of surcharge load on the soil surface. According to the results, the neutral plane of a single pile shifted from 0.8 to 0.95 L (where L is the length of the pile in sand) as the surcharge load increased from 20 to 120 kPa. Applying a load to the pile head reduced NSF compared to surcharge only conditions, but the elevation of the neutral plane increased [16].

Artificial collapsible soil was prepared by mixing sand and kaolin with different water contents to achieve different collapse potentials (18, 9, 4.2, and 12.5 %). It was used to investigate the variation of NSF under different inundation pressures, degrees of saturation, and directions of inundation. The results showed that the collapse potential as well as the degree of saturation significantly affected NSF along the end-bearing pile shaft. Bottom-up inundation resulted in a higher neutral plane elevation than top-down inundation. To verify the results obtained during the experimental work, a numerical model was created in the PLAXIS 2D program [17].

Recently, China has been building high-rise buildings on collapsible soils (loess soils), which account for about 6.6% of the country’s total area. That is why the collapsibility of the loess soil layer should not be ignored. Therefore, the use of a pile foundation is more suitable for transferring loads to deeper, stable layers. But the loess soil softens upon water immersion, producing additional downward pressure and settlement on the pile. This prompted the researchers to study the effect of cumulative relative collapse amount, the influence of pile type, and the effect of collapsibility change on the NSF with water immersion. The small relative displacement between the pile and the surrounding soil is enough to generate large NSF. Driven precast piles exhibited higher maximum NSF than that of the bored concrete pile due to compaction and surcharge surface loading. Bored concrete piles showed rapid NSF development and the variation in collapsibility of loess soil due to the changing of both natural water content and dry density. Finally, surcharge loading and pre-wetting could reduce NSF [18].

In [19], NSF along the shaft of two types of piles was calculated using a laboratory model: floating pile and end-bearing pile in gypseous soil (with 42% gypsum content) from the Bahr Al-Najaf region, Iraq. The researchers found that the final settlement for the end-bearing pile is less than that for the floating pile with the same degree of saturation. But the maximum value of NSF for the end-bearing pile is smaller than that for the floating pile due to differences in soil-pile relative displacement. A scale model was used to investigate the variation and the distribution of NSF on piles in loess soil. The results showed that the loess soil exhibited layered settlement under immersion conditions, as well as negative and positive friction on the pile surface and two neutral sites. Negative friction pulls the pile downward, increasing the axial force of the pile. Higher soil elastic modulus at the pile tip increased maximum NSF and lowered the neutral point position. By representing the laboratory model through a numerical model, it was found that the results were close to the experimental ones [20].

The collapsible gypseous soil covers 20–30% of Iraq's landmass and is distributed in the northwest, west, and southwest regions of Iraq, with gypsum content exceeding 60 % in some regions [21, 22].

The aim of this study is to evaluate NSF along the shaft of a pile embedded in gypseous soil by using a laboratory model and to study the effect of different parameters on the development of drag load along the shaft of piles, such as collapse potential, soil density, and degree of saturation.

2. Methods

2.1. Laboratory Model

The model used in this study consisted of an iron tank box with dimensions of 80×80×80 cm, manufactured from a 6-mm-thick iron plate and an iron frame. A mechanical jack was employed to conduct a pile load test, determining the allowable load after assuming the factor of safety according to the scientific standards. Moreover, the applied load was measured using an S-shaped load cell with a capacity of 2 tons. The bottom of the box featured three openings to allow water to enter the soil, connected to a water tank positioned 30 cm above the surface of the final soil layer, as shown in Fig. 1.

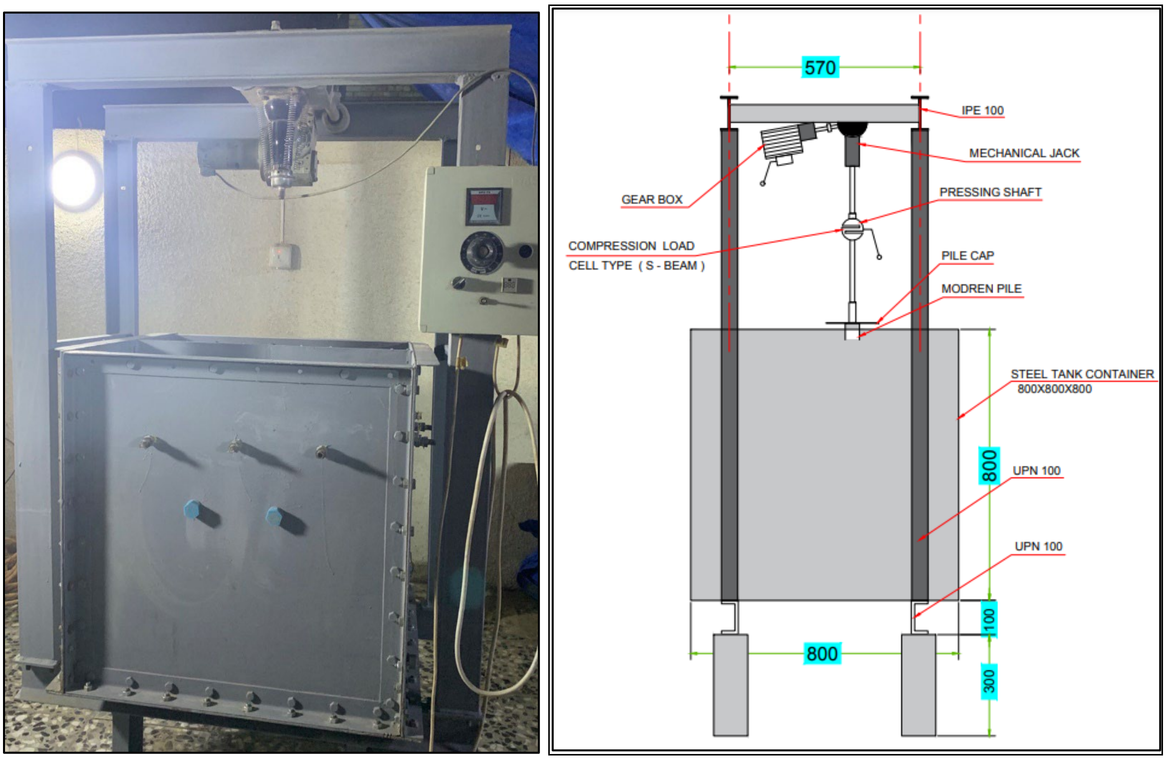

a) b)

Figure 1. Laboratory model: a) steel box container, b) sketch for laboratory model.

2.2. Soil Used

Gypseous soil that was used in this study was brought from Tikrit city, Iraq. This soil had the following chemical composition:

- gypsum content – 60 %;
- SO_3 – 28 %
- CL – 0.032 %;
- organic content – 0.51 %;
- T.S. S – 77 %;
- pH – 8.25 %.

It was sieved through No. 10 before use. The soil characteristics are listed in Table 1, and the grain size distribution is shown in Fig. 2.

Table 1. Properties of gypseous soil.

Properties	Value	Specification
Soil classification	SM	USCS
Gypsum content	60 %	[23]
Liquid limit	26 %	ASTM 423-66
Plastic limit	Non-plastic	ASTM D424-59
Max dry density	17 kN/m^3	ASTM 698-00a
Optimum water content	12.5%	ASTM 698-00a
Cohesion	18 kPa	ASTM D3080-89
Angle of internal friction at field density 12.7 kN/m^3	40°	ASTM D3080-89
Specific gravity with water	2.39	ASTM D854-02
Specific gravity with kerosene	2.37	Manual of soil laboratory testing[1]

---

[1] Head, K.H. Manual of Soil Laboratory Testing. 1. Pentech Press. London, 1980. 422 p.

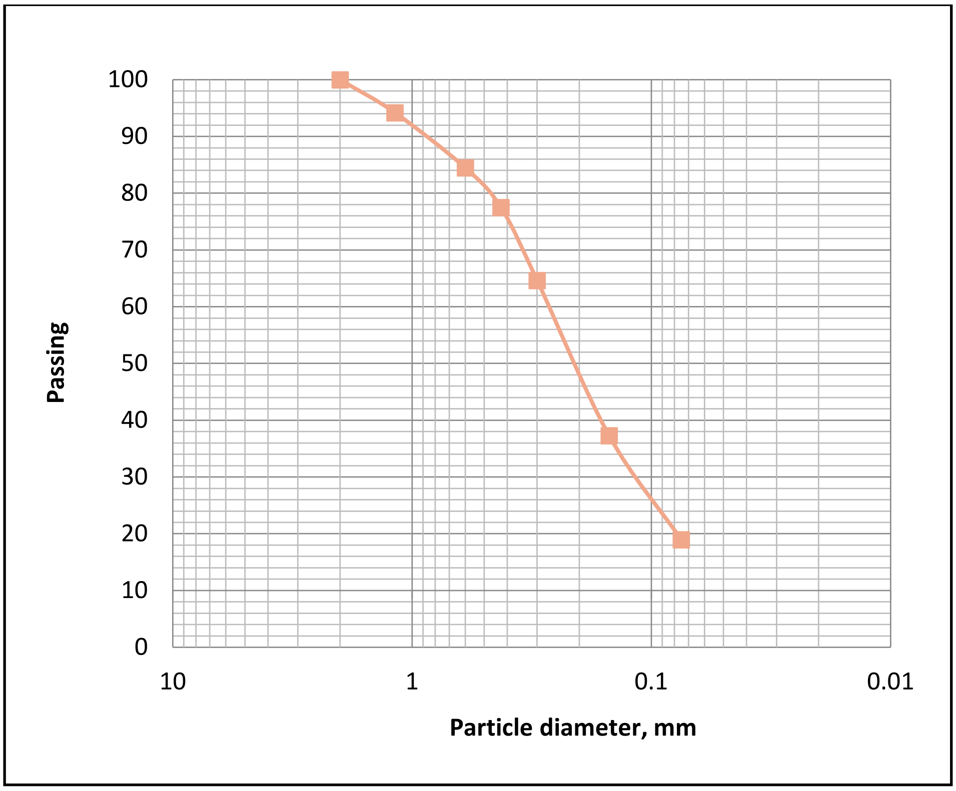

Figure 2. Grain size distribution curve of gypseous soil.

2.3. Properties of the Pile, Strain Gauge, and Load Cell

Two types of steel piles with different lengths, 30 and 20 cm, with an outer diameter of 2.1 cm and an inner diameter of 1.95 cm, were used. The surface of these piles was roughened by a knurling machine to ensure full friction between the pile and soil. The 30-cm-long pile was provided with eight electrical strain gauges of the Rosette type and fixed at positions 5, 10.5, 19.5, and 29.5 cm from the top of the pile. Similarly, the 20-cm-long pile was equipped with six strain gauges positioned at 5, 10.5, and 19.5 cm from the top of the pile as shown in Fig. 3.

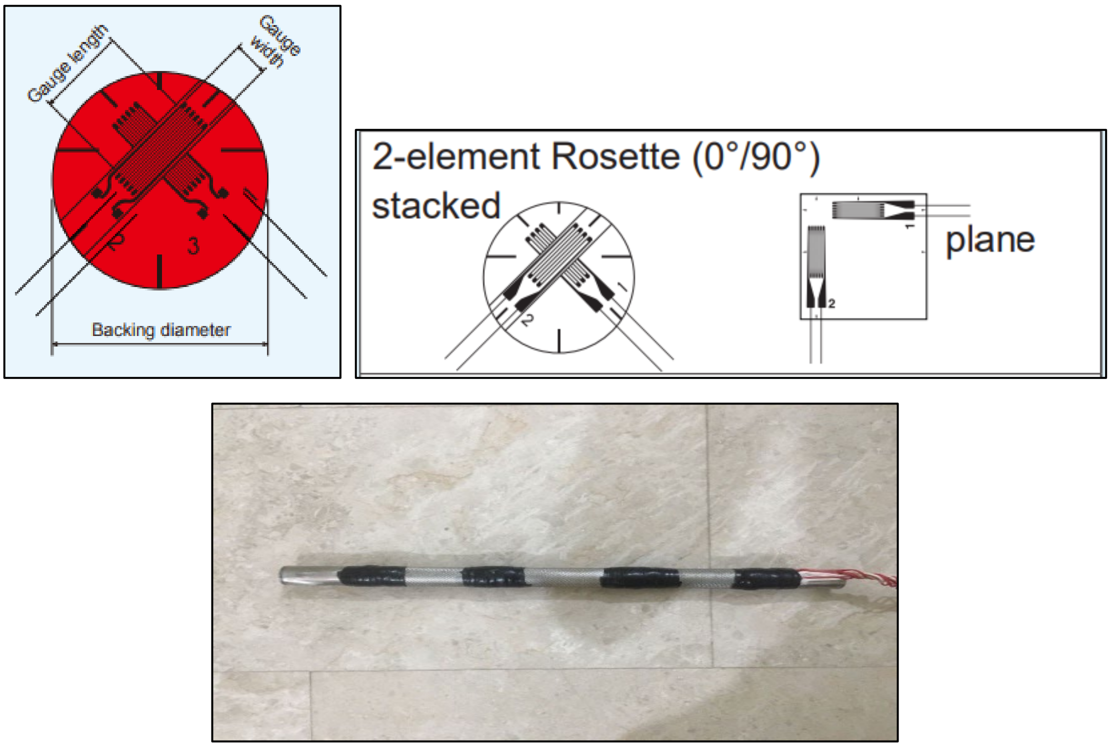

Figure 3. Strain gauge Rosette and its distribution along the pile.

The properties of the strain gauges are shown in Table 2.

Table 2. Properties of strain gauges[2].

Gauge length	Gauge resistance	Gauge factor
3 mm	118.5±0.5Ω	2.08±1

Each Rosette has two strain gauges arranged perpendicularly and bonded with a specialized adhesive. After installation, the strain gauges were coated with a special coating material (W-1), and wrapped with SB-type tape to ensure waterproofing. At the end of each pile, a load cell with 50 kg capacity was used to calculate the end-bearing resistance. This load cell was placed within an iron chamber and was attached to the pile using rubber tape of an appropriate type as shown in Fig. 4.

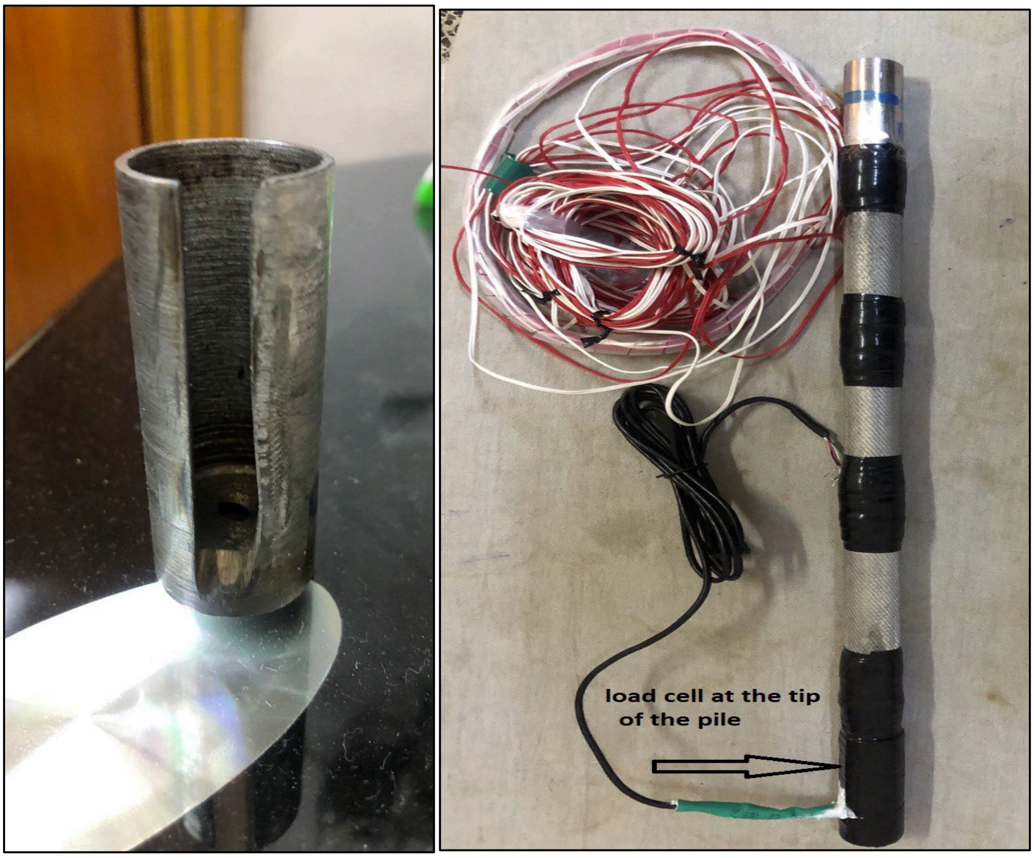

a) **b)**

Figure 4. 50 kg-capacity load cell measuring end-bearing resistance: a) iron chamber for the load cell, b) load cell at the tip of the pile inside the chamber.

2.4. Methodology

Due to the fact that the fine materials percentage in the soil used in this study (gypseous soil) is high, the compaction curve in Fig. 5 was used to estimate the dry unit weight for the collapse tests, enabling a more accurate study of pile behavior in gypseous soil during inundation. The collapse potential values for each dry unit weight, obtained from a single collapse test [24], are shown in Table 3. Based on the results obtained, four dry unit weights have been adopted as shown in Table 3. It is important to note that the severity of the gypseous soil's collapsibility was characterized according to [24].

---

[2] Tokyo Measuring Instruments Laboratory Co., Ltd. [Online]. URL: https://www.tml.jp/eng/documents/Catalog/straingauge2023-2024_E1007H_web.pdf (date of application: 17.07.2025)

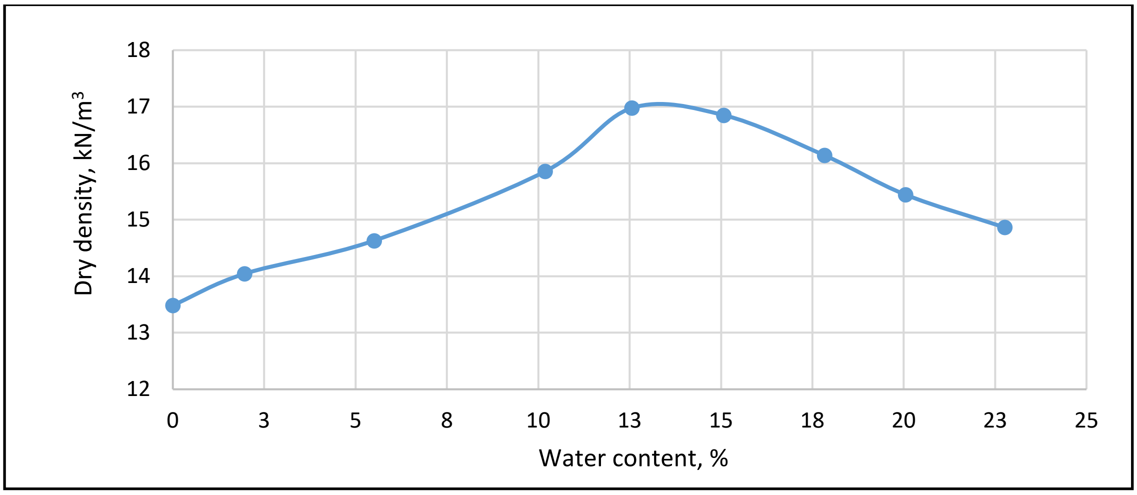

Figure 5. Compaction curve of the used soil.

Table 3. Results of the single collapse test.

Degree of saturation, %	Water content, %	Dry unit weight, kN/m^3	Collapse potential, %
0	**0**	**13.5**	**11.4**
5	**1.5**	**14**	**9.9**
10	3	14.2	9.5
15	**4.2**	**14.4**	**8.6**
20	5.1	14.6	6.5
25	**6.2**	**14.9**	**5.3**
30	7.2	15	3.8
35	8	15.2	2.9
45	9.6	15.5	2.9
60	11	16.1	0.28
80	12.6	17	0.28
90	15	17	0.28

*The highlighted values have been considered in the tests of NSF on piles as initial test conditions

After determining the required densities for layering the gypseous soil in the laboratory model, a 10-cm-thick layer of gravel was placed at the bottom of the model. Then, the soil was layered to a 50 cm height using a hand hammer, during which each board pile was installed according to its embedded length in the gypseous soil. A surcharge load of 4 kPa was applied to the soil surface and around the piles to represent the top soil layer in field conditions.

Prior to testing, LVDTs were placed on each pile and on the soil surface to record the settlement. All strain gauges, the load cell at the tip of the pile, and LVDTs were connected to a data logger and computer system to monitor and record data during the test.

Typically, the test began by immersing the lower gravel layer through the holes in the bottom of the model. Once the water has submerged the gravel layer, the bottom water supply was closed, and inundation commenced from the top until full soil saturation was achieved. This inundation procedure simulated various field conditions including rainfall, surface runoff, irrigation, poor drainage, and flooding. Test data were recorded throughout the process, as illustrated in Fig. 6. The time required for the test was 2 days.

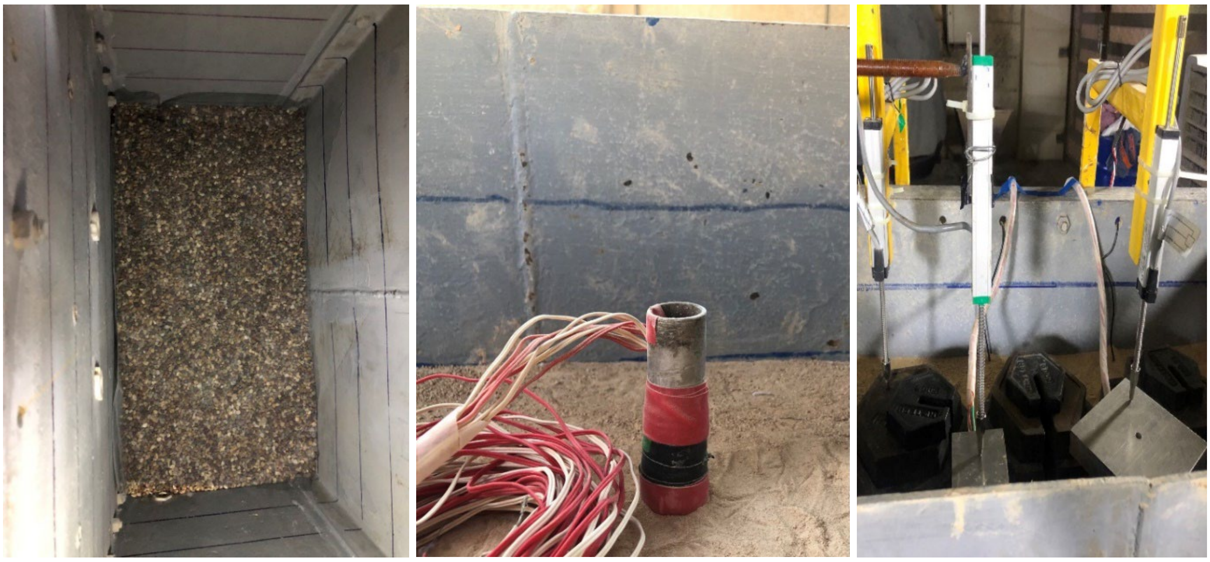

a) gravel layer **b) pile embedded in soil** **c) LVDT and surcharge on the soil surface and the pile**

d) inundations from the top **e) data logger and computer to save test data**

Figure 6. Preparation of the NSF model test.

3. Results and Discussion

The presence of NSF in pile foundation in collapsible soil is a significant source of concern during construction and design due to:

1. Drag load (additional force) generated by NSF and its impact on the pile strength.
2. Additional settlement (drag settlement) caused by NSF and its effect on the design limitation of settlement.

For end-bearing piles, NSF influences the structural pile capacity because the soil beneath the pile is stable (e.g., rock or dense sand). In the floating pile, the effect of NSF must be taken into account in the design processes for both structural and geotechnical pile capacity. It should be noted that considering the drag force as a result of negative friction (an external force) is incorrect, leading to overly conservative calculations in the design. Therefore, it must be treated as an internal force developing within a static equilibrium soil pile system under some conditions [26].

3.1. Relationship between NSF and Collapse Potential

The collapse potential of gypseous soil decreases with an increase in the water content [15]. As presented in Table 3, four values of collapse potential (11.4, 9.6, 8.6, and 5.3 %) were selected corresponding to the dry unit weights (13.5, 14, 14.4, and 14.9 kN/m^3, respectively). As shown in Figs. 7–9, NSF resistance increases with increased collapse potential, while no NSF occurs at a collapse potential of 5.6 % and dry unit weight of 14.9k N/m^3 as shown in Fig. 10 for both pile lengths. The collapse potential had a sufficient influence on the drag load development on the pile shaft due to the soil collapse during inundation [17]. During inundation, the bonds break and the soil strength is lost due to the reduction of cementing action of gypsum under wetting. NSF magnitude correlates directly with pile embedment length. The depth, at which the shear stress along the pile shift transitions from NSF to positive shaft resistance, when the relative displacement between the pile and surrounding soil is zero, is called the neutral plane [26]. It typically occurs in the lower third of the pile [6, 28]. In addition, 30-cm-length pile at the collapse potential of 9.6 and 8.6 % showed two neutral planes, which agrees with [4].

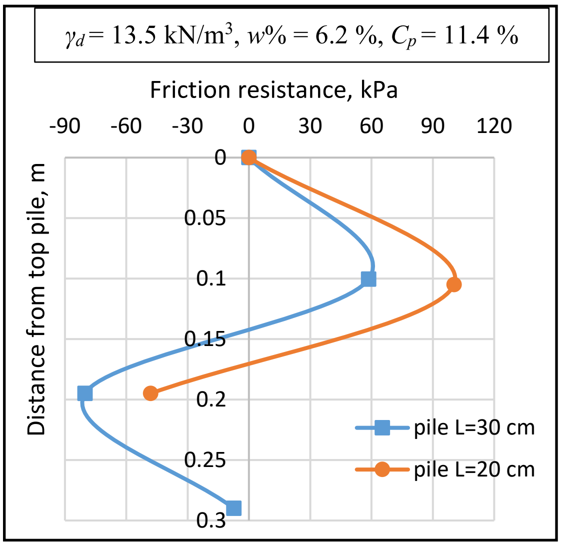

Figure 7. NSF along the shaft of the pile.

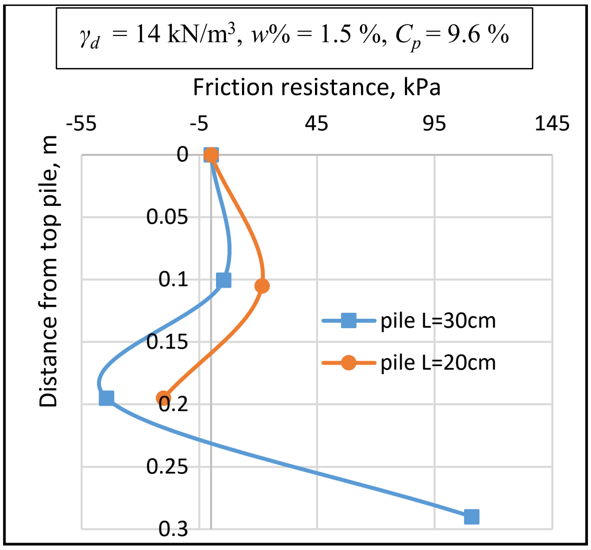

Figure 8. NSF along the shaft of the pile.

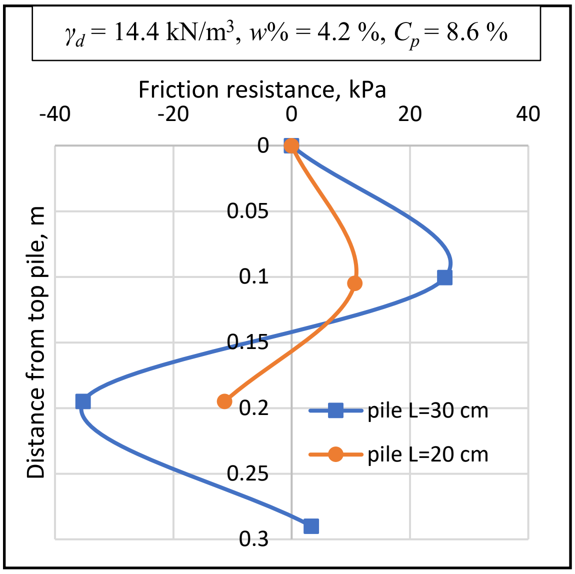

Figure 9. NSF along the shaft of the pile.

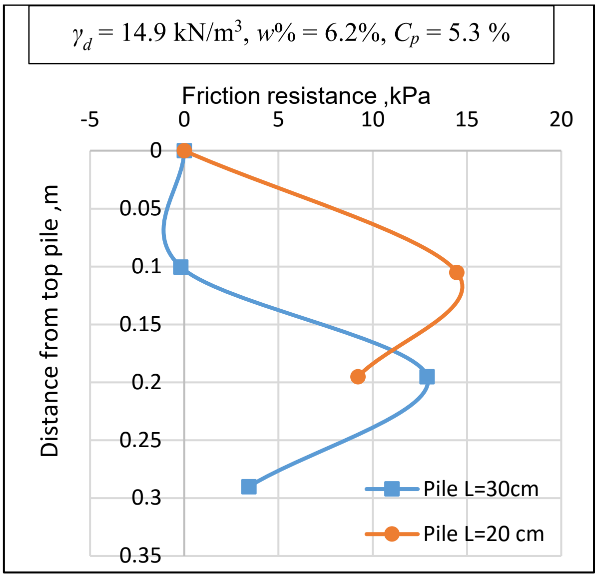

Figure 10. NSF along the shaft of the pile.

3.2. Relationship between Drag Load, Dry Density and Degree of Saturation

Gypseous soil has significant collapse potential due to its metastable structure, which has a low dry density and moisture content. In other words, large volume changes and sudden collapses occur when the soil is soaking [27–29]. As shown in Fig. 11, maximum drag load (peak NSF) increases with a decrease in the degree of saturation and decreases with an increase in the dry density of soil due to a high decrease in the void ratio of soil, which can occur with compaction. The maximum drag load occurs at zero saturation.

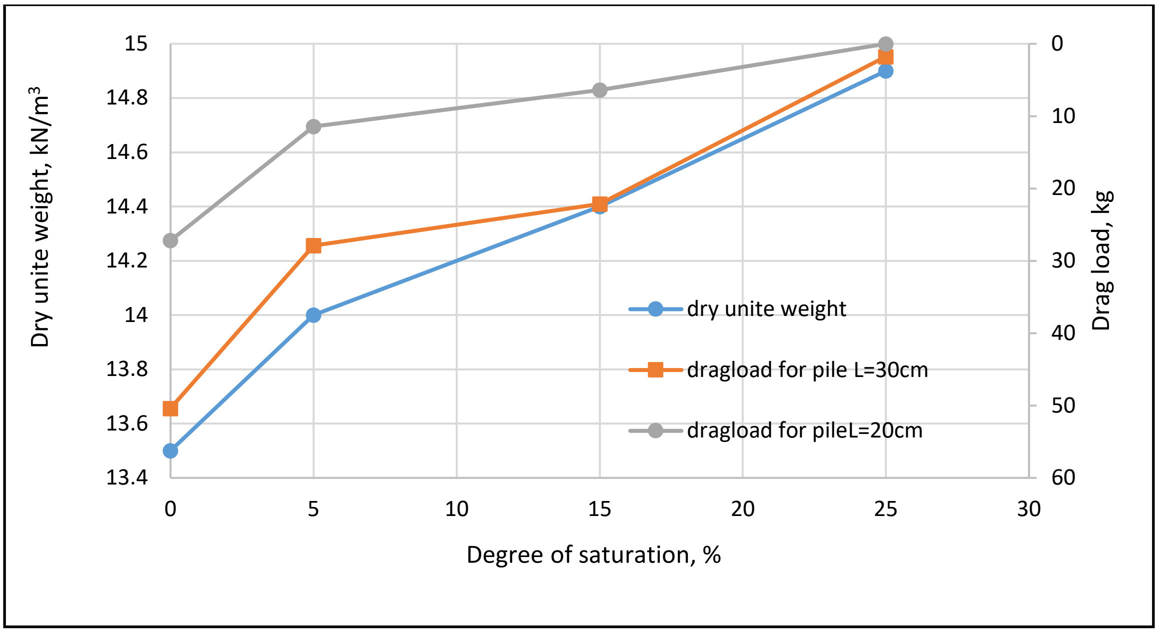

Figure 11. Variation of drag load with dry unit weight and degree of saturation.

3.3. Relationship between Drag Load, Soil Settlement and Pile Settlement

NSF generation primarily results from soil-pile relative settlement. Extremely small movement (≥ 1 mm) can cause NSF force and reverse the shear-force direction along the shaft of the pile [6]. Moreover, large deformations and rapid settlement can occur because of the cemented gypsum bond dissolution during inundation. The relative settlement between soil and pile is high at zero degree of saturation, while 25% saturation produces insufficient relative movement to generate NSF as shown in Figs. 12–15. The soil displacement near the bottom of the pile is smaller than or equal to the pile displacement, which produces positive skin friction along the shaft. Therefore, soil-pile relative settlement of about 1–3 mm (for a long pile) and about 1–2.5 mm (for a short pile) is enough to generate a drag load on the pile in the gypseous soil.

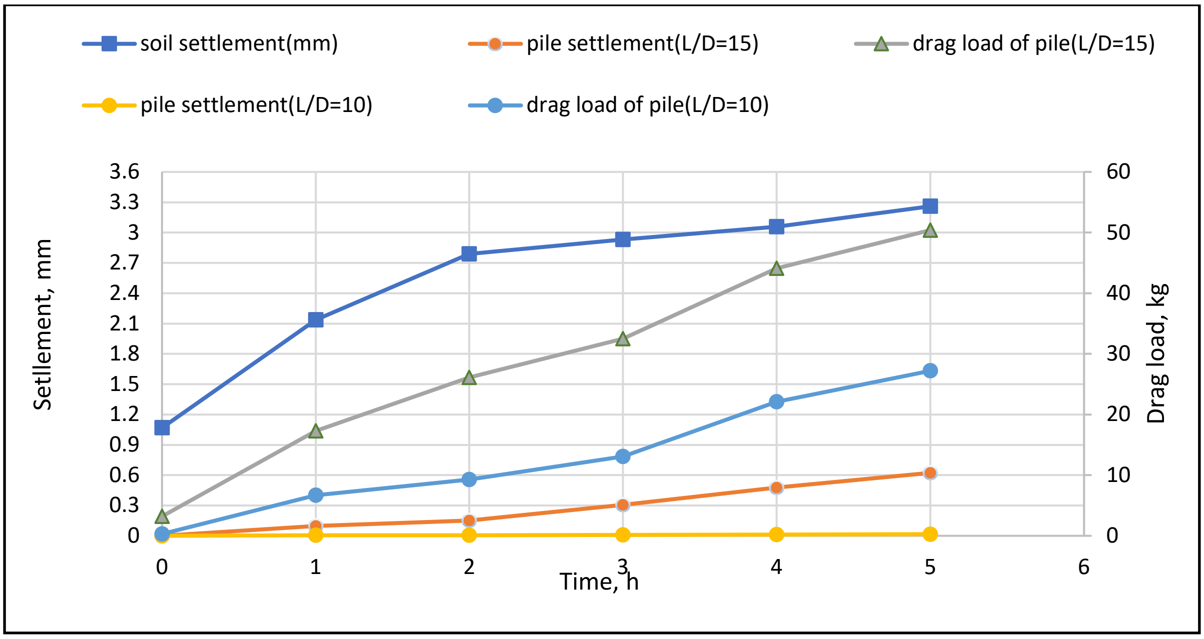

Figure 12. Variation of the settlement of pile and soil with drag load force for C_p = 11.4 %.

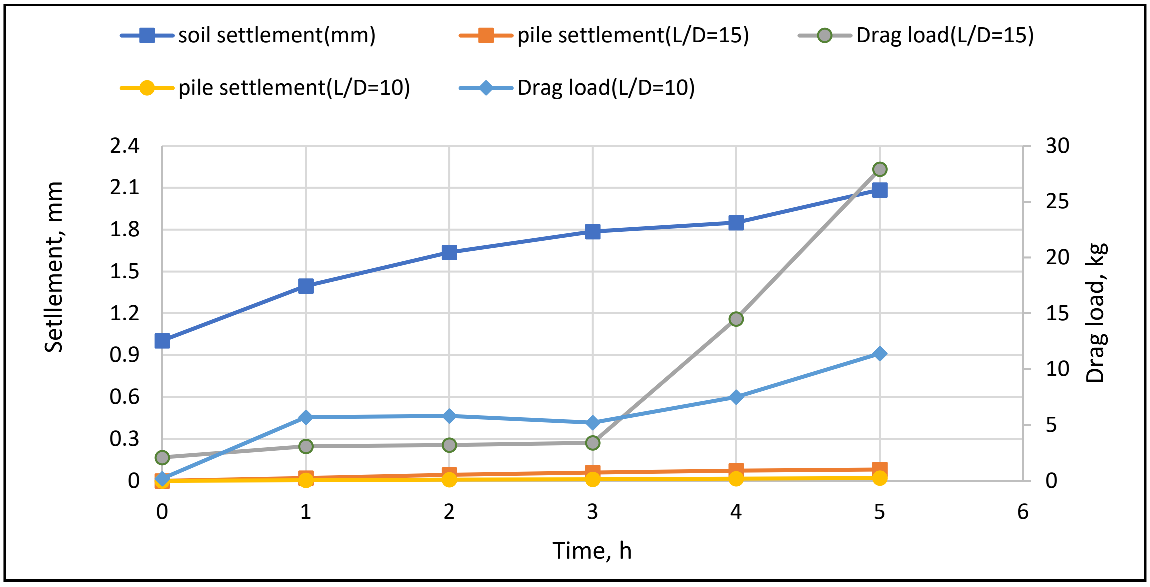

Figure 13. Variation of the settlement of pile and soil with drag load force for C_p = 9.6 %.

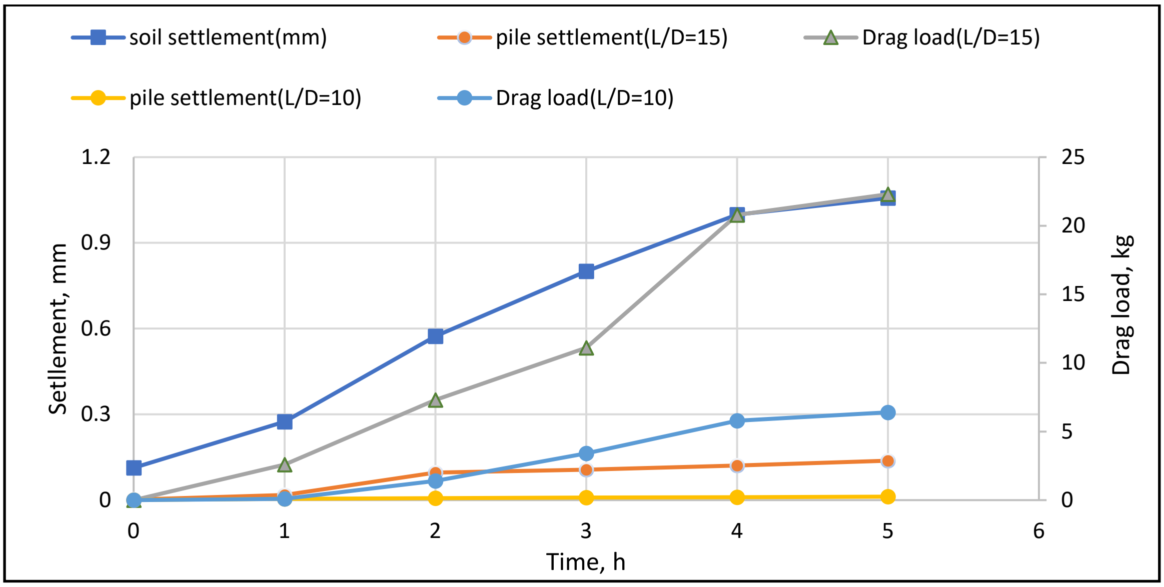

Figure 14. Variation of the settlement of pile and soil with drag load force for C_p = 8.6 %.

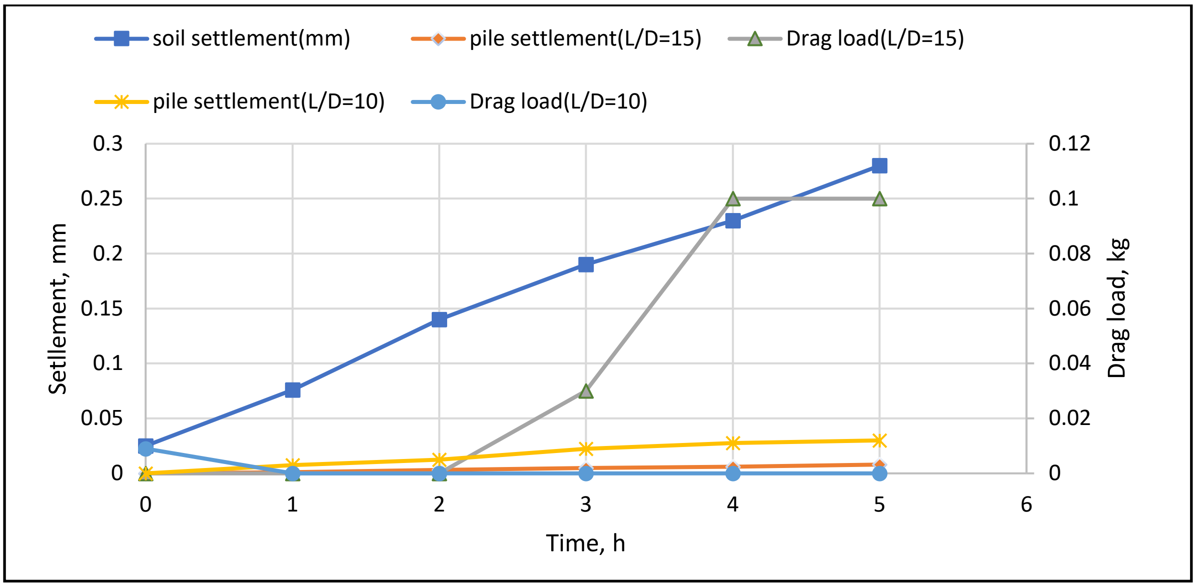

Figure 15. Variation of the settlement of pile and soil with drag load force for C_p = 5.3 %.

4. Conclusion

The article examined the development of NSF along the shaft of the pile during the gypseous soil inundation using a physical model, gypseous soil, and piles with two distinct length/diameter (L/D) ratios. The following conclusions can be obtained based on the results:

1. Submergence of gypseous soil samples with varying densities and water contents alters collapse potential values. In other words, not all collapse potential values are sufficient to produce NSF, therefore, the recommended safety factor during the design process will change as the drag load is developed along the pile shaft.

2. Piles with a slenderness ratio L/D = 15 exhibit substantially higher NSF resistance than those with L/D = 10, attributed to increased soil-pile interaction area. NSF resistance increases by 66, 119, and 211% for collapse potentials of 11.4, 9.9, and 8.6%, respectively.

3. In its natural state, gypseous soil has a high void ratio and a low dry density. The cementation bonds will break up during inundation, increasing the compressibility of gypseous soil. Accordingly, when soil is compacted at a high dry density, the void ratio in the soil decreases, which lowers the soil's ability to collapse, and water cannot easily dissolve the cementing bonds between the soil particles.

4. For pile length = 30 cm, NSF resistance increases by 26% when the degree of saturation decreases from 20 to 5% and by 60% when the degree of saturation decreases from 5 to 0%, respectively. For pile length = 20 cm, NSF resistance increases by 78% when the degree of saturation decreases from 20 to 5% and by 137% when the degree of saturation decreases from 5 to 0%, respectively.

References

1. Abd-Alhameed, H.J., Albusoda, B.S. Impact of eccentricity and depth-to-breadth ratio on the behavior of skirt foundation rested on dry gypseous soil. Journal of the Mechanical Behavior of Materials. 2022. 31(1). Pp. 546–553. DOI: 10.1515/jmbm-2022-0057
2. Noor, S.T., Hanna, A., Mashhour, I. Numerical Modeling of Piles in Collapsible Soil Subjected to Inundation. International Journal of Geomechanics. 2013. 13(5). Pp. 514–526. DOI: 10.1061/(ASCE)GM.1943-5622.0000235
3. Huang, T., Gong, W.M., Dai, G.L., Zheng, J.H., Xu, G. P. Experimental study of time effect of negative skin friction on pile. Rock and Soil Mechanics. 2013. 34(10). Pp. 2841–2846.
4. Ye, S., Zhao, Z., Zhu, Y. Study on negative friction of pile foundation in single homogeneous soil layer in collapsible loess area of Northwest China. Arabian Journal of Geosciences. 2021. 14. Article no. 1137. DOI: 10.1007/s12517-021-07508-2
5. Bjerrum, L., Johannessen, I.J., Eide, O. Reduction of negative skin friction on steel piles to rock. Proceedings of the 7th International Conference on Soil Mechanics and Foundation Engineering. Mexico City, 1969. 2. Pp. 27–34.
6. Fellenius, B.H., Broms, B.B. Negative skin friction for long piles driven in clay. Proceedings of the 7th International Conference on Soil Mechanics and Foundation Engineering. Mexico City, 1969. 2. Pp. 93–98.
7. Fellenius, B.H. Down-drag on Piles in Clay due to Negative Skin Friction. Canadian Geotechnical Journal. 1972. 9(4). Pp. 323–337. DOI: 10.1139/t72-037
8. Fellenius, B.H. Unified design of piles and pile groups. Transportation Research Record. 1989. Article no. 1169. Pp. 75–82.
9. Grigoryan, A.A. Construction on loess soils. Soil Mechanics and Foundation Engineering. 1991. 28. Pp. 44–49. DOI: 10.1007/BF02304644
10. Thomas, J., Fahey, M., Jewell, R. Pile down-drag due to surface loading. Centrifuge 98. 1998. 1. Pp. 507–512.
11. Lee, C.J., Chen, C.R. Negative Skin Friction on Piles Due to Lowering of Groundwater Table. Journal of the Southeast Asian Geotechnical Society. 2003. 34(1). Pp. 13–25.
12. Leung, C.F., Liao, B.K., Chow, Y.K., Shen, R.F., Kog, Y.C. Behavior of Pile Subject to Negative Skin Friction and Axial Load. Soils and Foundations. 2004. 44(6). Pp. 17–26. DOI: 10.3208/sandf.44.6_17
13. Feng, Z., Hu, H., Zhao, R., He, J., Dong, Y., Feng, K., Zhao, Y., Chen, H. Experiments on Reducing Negative Skin Friction of Piles. Advances in Civil Engineering. 2019. 2019. Article no. 4201842. DOI: 10.1155/2019/4201842
14. Houston, S.L., Houston, W.N., Zapata, C.E., Lawrence, C. Geotechnical engineering practice for collapsible soils. Geotechnical and Geological Engineering. 2001. 19. Pp. 333–355. DOI: 10.1023/A:1013178226615
15. Al-Mufty, A.A. Effect of gypsum dissolution on the mechanical behavior of gypseous soils. PhD thesis. Baghdad, 1997.
16. Huang, T., Zheng, J., Gong, W. The Group Effect on Negative Skin Friction on Piles. Procedia Engineering. 2015. 116. Pp. 802–808. DOI: 10.1016/j.proeng.2015.08.367
17. Mashhour, I. Experimental study on negative skin friction on piles in collapsible soils due to inundation. PhD thesis. Montreal, 2016.
18. Xing, H., Liu, L. Field Tests on Influencing Factors of Negative Skin Friction for Pile Foundations in Collapsible Loess Regions. International Journal of Civil Engineering. 2018. 16(10). Pp. 1413–1422. DOI: 10.1007/s40999-018-0294-z
19. Al-Damluji, O.A., Albusoda, B.S., Ali, A.H. Performance evaluation of a model pile in gypseous soil. Proceedings of the 16th Asian Regional Conference on Soil Mechanics and Geotechnical Engineering (16ARC 2019). Taipei, 2019. Pp. 14–18.
20. Zhao, Z., Ye, S., Zhu, Y., Tao, H., Chen, C. Scale model test study on negative skin friction of piles considering the collapsibility of loess. Acta Geotechnica. 2022. 17. Pp. 601–611. DOI: 10.1007/s11440-021-01254-1
21. Albusoda, B.S., Salman, R. Bearing Capacity of Shallow Footing on Compacted Filling Dune Sand Over Reinforced Gypseous Soil. Journal of Engineering. 2013. 19(5). Pp. 532–542. DOI: 10.31026/j.eng.2013.05.01

22. Mohsen, A.H., Albusoda, B.S. The Collapsible Soil, Types, Mechanism, and identification: A Review Study. Journal of Engineering. 2022. 28(5). Pp. 41–60. DOI: 10.31026/j.eng.2022.05.04
23. Al-Mufty, A.A.-E., Nashat, I.H. Gypsum content determination in gypseous soils and rocks. Proceedings of the 3rd Jordanian International Mining Conference. Amman, 2000. 2. Pp. 485–492.
24. American Society for Testing and Materials (ASTM). Standard Test Method for Measurement of Collapse Potential of Soils. ASTM D5333-92. ASTM. West Conshohocken, 1996. 3 p. DOI: 10.1520/D5333-92R96
25. Pells, P., Robertson, A., Jennings, J.E., Knight, K. A guide to construction on or with materials exhibiting additional settlement due to “collapse” of grain structure. International Journal of Rock Mechanics and Mining Sciences & Geomechanics Abstracts. 1975. 12(9). P. 131. DOI: 10.1016/0148-9062(75)91203-61975
26. Aram, A. Analysis of Piles for Negative Skin Friction. Fourth Year Project. 2010. URL: https://www.scribd.com/document/149135616/analysis-of-piles-for-negative-skin-friction (date of application: 22.07.2025).
27. Nashat, A.A., Ludeman, L.C. Detection and estimation of chirp signals using state space representation. 1992 IEEE International Symposium on Circuits and Systems (ISCAS). San Diego, 1992. 3. Pp. 1609–1612. DOI: 10.1109/ISCAS.1992.23018
28. Sasam, S.I., Alsaidi, A.A., Mukhlef, O.J. Behavior of Reinforced Gypseous Soil Embankment Model under Cyclic Loading. Journal of Engineering. 2013. 19(7). Pp. 830–844. DOI: 10.31026/j.eng.2013.07.05
29. Albusoda, B.S., Alahmar, M.M. The Behavior of Gypseous Soil under Vertical Vibration Loading. Journal of Engineering. 2014. 20(1). Pp. 21–30. DOI: 10.31026/j.eng.2014.01.02

Information about the authors:

Abeer Mohsen*,*

ORCID: https://orcid.org/0009-0009-7697-2926

E-mail: Abeer.mohsin2001D@coeng.uobaghdad.edu.iq

abeer.h.mohsen@src.edu.iq

Bushra Suhale Albusoda*,*

ORCID: https://orcid.org/0000-0001-6375-4430

E-mail: dr.bushra_albusoda@coeng.uobaghdad.edu.iq

Received: 17.12.2022. Approved: 15.09.2024. Accepted: 15.03.2025.

Magazine of Civil Engineering

ISSN
2712-8172

journal homepage: http://engstroy.spbstu.ru/

Research article
UDC 624.011.1
DOI: 10.34910/MCE.135.6

Composite wooden beams performance under short-term loading

S.A. Isupov

Vyatka State University, Kirov, Russian Federation

Deka_1958@mail.ru

Keywords: TGK dowel plate, dowel, composite wooden beam, test scheme, strain gauges, stresses, beam deflection, relative deformations, elastic modulus

Abstract. This paper presents an experimental and theoretical study of composite beams made of two balks connected by TGk dowel plates under short-term loading. Composite wooden beams with cross-sections and TGk dowel plate connections are a relatively new solution for building structures and are increasingly used in the construction industry, as they provide high strength and rigidity at a relatively low cost compared to glued beams. The purpose of the study is to confirm the operational strength and rigidity of composite wooden beams on TGk dowel plates, as well as to analyze the stress-strain state of the beams depending on the type of force action and the method of arranging shear ties. To achieve this goal, a target experiment was planned and carried out to test beams made of two bars for transverse load. Beams of different length, three types of transverse load, with different arrangements of shear ties were tested. The beams were destructed under short-term loading in a rather wide range of applied forces, the safety factor fluctuated within 2.13...3.95. After testing the beams using the previously developed method, calculations were performed with linear and nonlinear diagrams of joint deformation. The difference between the experimental and theoretical values of deflections is within 20 %, which quite convincingly confirms the validity of the theoretical calculations.

Citation: Isupov, S.A. Composite wooden beams performance under short-term loading. Magazine of Civil Engineering. 2025. 18(3). Article no. 13506. DOI: 10.34910/MCE.135.6

1. *Introduction*

The potential of wood as a material for load-bearing building structures is currently far from being fully realized. The main reason may be the lack of sufficiently effective means of connection that adequately correspond to the structural qualities of wood itself and significantly reduce the impact of its inherent disadvantages.

Due to the rather large volumes of logging, there has been a tendency to reduce the cross-sectional dimensions of natural lumber. It is obvious that the increase in the efficiency of wooden structures is associated with the use of new types of connections that allow an increase in the load-bearing capacity of structures, including through the use of composite rods made of limited-range lumber.

Vyatka State University has developed dowel connectors, which are connecting elements for wooden structures containing a group of cylindrical dowels of increased diameter 5...8 mm with a denser arrangement and fixed on a common base [1–3]. The basic type of connectors (Fig. 1), called TGk metal connector plates, was developed mainly to produce composite wooden elements of increased cross-section. The base of such a connecting plate is made of metal, which is designated by the letter “T”. The letter “G” denotes dowels, pointed at both sides. The dowel is attached to the base by welding, designated by the letter “k”. Therefore, this type of connecting plate is marked TGk [4].

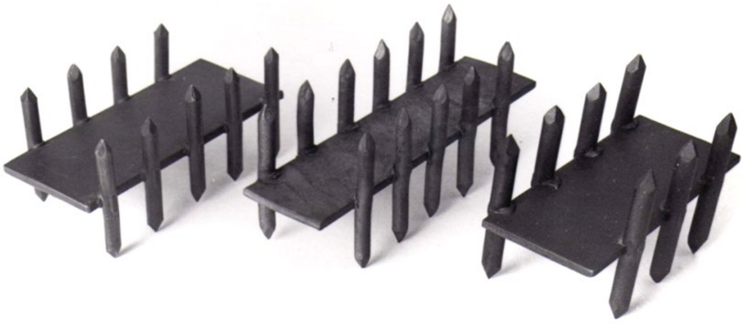

Figure 1. TGk metal connector plates.

The main advantage of such connections is the relative simplicity of manufacture and their functional versatility, which allows for the efficient production of composite beams and nodal joints of wooden structures. In addition, for most climatic regions of Russia, characterized by increased snow loads, such structures are not much inferior to glued structures and rod structures based on the latest types of dowel connecting elements [5–13].

Based on TGk dowel plates, composite elements with various cross-section configurations have been developed. The idea of such rods is to increase the cross-section of wooden elements significantly, using lumber of relatively small diameters. The general appearance of the main types of composite beams with connections on TGk plates is shown in Fig. 2.

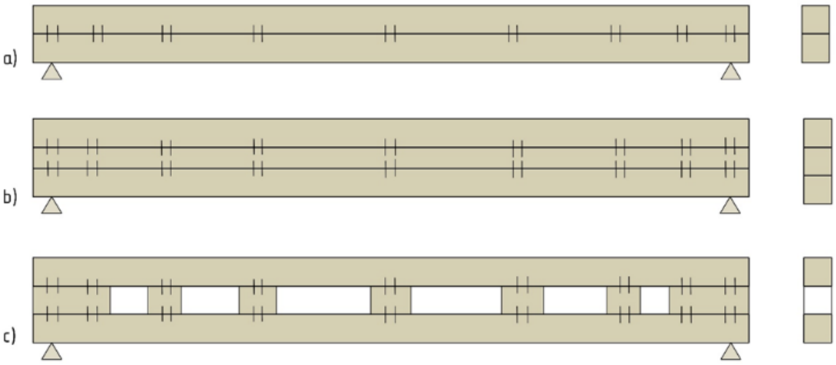

Figure 2. Main types of wooden composite beams: a) made of two beams; b) made of three or more beams; c) perforated composite beams.

Composite elements with connections on TGk dowel plates are considered along with wooden beams of composite section on various mechanical connections, as well as along glued elements of factory production to produce building structures for various purposes: rafter trusses, roof slabs, purlins, wall panels, composite columns, spatial structural forms, etc. Composite elements of type “c” allow saving wood directly, since in the central zone along the height of the cross-section of the element, where normal stresses are minimal, it is possible to significantly reduce the volume of material.

Numerous works [14–24] are devoted to studies on the assessment of the stress-strain state of composite wooden elements and the methodology for their testing, including various connections of composite wooden and composite beams.

Previously, at the first stage of comprehensive studies of connections on TGk dowel plates, short-term mechanical characteristics of dowel nest wood and deformation characteristics of dowel material were determined [25]. The results of experimental and theoretical studies on determining the bearing capacity and deformability of connections under short-term [26] and long-term [27] loading were obtained.

The relevance of further studies is due to the need for an experimental and theoretical analysis of structural elements – wooden composite beams based on the developed connections. The purpose of the research is to confirm the operational strength and rigidity of beams on TGk dowel plates, as well as to study the operation of beams depending on the type of force action and the method of arranging shear ties.

To achieve this goal the following tasks were set:

- to conduct experimental studies of wooden beams with short-term permanent loading;
- to establish the nature of the beams’ operation depending on the type of force action and the method of arranging shear ties based on experimental and theoretical analysis;

- to carry out an experimental verification of the calculation method for composite wooden bending rods with discrete shear ties.

The object of the study is wooden beams of composite cross-section of beams on TGk dowel plates, working on transverse bending.

The subject of the study is the stress-strain state of the proposed type of beams under the short-term loading.

2. Methods

For practical assessment of the bearing capacity and deformability of composite wooden beams, as well as experimental verification of the proposed method for calculating composite rods with discrete shear ties [28], tests of composite beams from two bars with connections on TGk dowel plates were carried out.

Short-term tests were carried out on a special stand for testing beams for transverse bending in accordance with the recommendations for testing wood structures of the Kucherenko Central Research Institute of Building Structures. The beams were installed on two supports: hinged movable and hinged fixed. The load on the beams was transferred by the pressure of a hydraulic jack installed in a rigid frame fixed to a power base. To simulate various types of transverse loads, special distribution devices were used shown in Fig. 3.

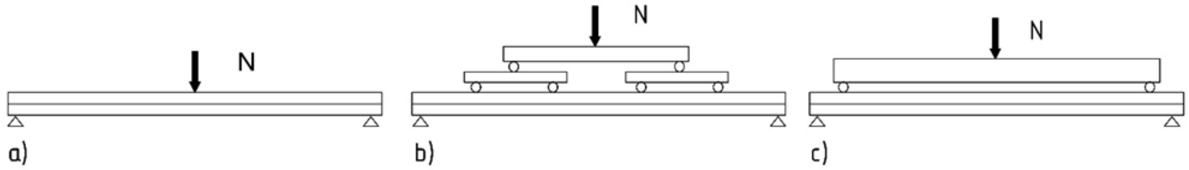

Figure 3. Schemes of application of transverse load during beam testing: a) concentrated load; b) distributed load; c) imitation of support bending moments.

The loading schemes selected are those most frequently used in practice: concentrated force, distributed load and bending moments at the ends of the beam.

During the test the following was determined:

- deflections in the middle of the span and at 2 intermediate points in the quarters of the beam span;
- displacements of the mutual shear of the ties along the shear joint of the bonding at several points along the length of the beam;
- relative deformations of the wood fibers in the section located at 150 mm from the middle of the span, at six points along the height of the beam on both sides.

To measure the deflections, 3 clock-type indicators ICh-50 with a measurement accuracy of up to 0.01 mm and 4 indicators ICh-10 on the supports were installed – to consider the deformations of the wood destructed under concentrated loading. The beam deflection in the span was determined as follows:

$$f_x = f - \left[\delta_1 + \frac{x\left(\delta_2 - \delta_1\right)}{L} \right], \tag{1}$$

where δ_1 and δ_2 are the deformations on supports.

The deflection f in the middle of the span was determined by the readings of the average indicator minus half the sum of the readings of the support indicators.

The shifts along the seam (deformations of the ties) were measured by the ICh-10 indicators Nos. 6, 7, and 10–13, which were attached to special devices installed along the plane of the bonding seam before pressing the beams. Indicators Nos. 6 and 7 were installed at the ends of the beams near the supports, and indicators Nos. 10–13 were installed at several points along the length of the beam.

The deformations of the wood fibers were measured using strain gauges with a 20 mm base, glued at 3 mm from the edge of each beam and in the center on the sides. The arrangement of the devices during beam testing is shown in Fig. 4.

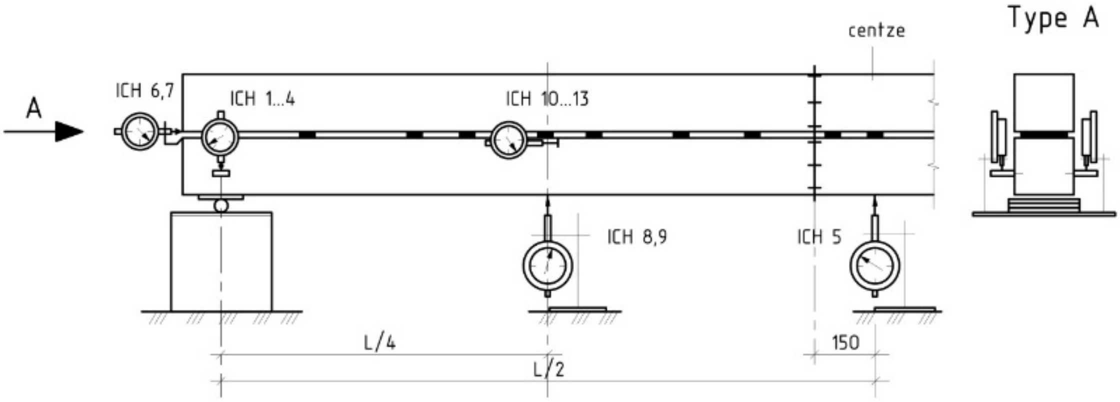

Figure 4. Diagram of the arrangement of measuring devices during beam testing.

The beams were tested at a constant loading rate in steps of 1/6...1/8 of the calculated load on the beam. The loading of a single stage was performed for 1 minute with subsequent readings from the instruments for 2 minutes. Preliminary tests of the 0-series beams were performed with loading up to the calculated value of the applied force with unloading to zero.

The testing of beams of the main series 1 and 3 was carried out in the following mode: loading the beam in stages up to the calculated value of the force, unloading up to the first loading stage, performing several loading-unloading cycles with subsequent unloading to zero, then loading in stages until destruction.

To determine the calculated deflections and edge normal stresses in composite beams, it is necessary to know the elastic modulus in bending E_b of the beams that make up the beam and the local modulus E_w at the spot where the strain gauge is located, since:

$$\sigma = \varepsilon E_w \frac{S_s}{S_w}, \tag{2}$$

where S_s / S_w is the conversion factor, the ratio of the strain sensitivities of the recording station, and the strain gauge.

The local modulus E_w and the elastic modulus in bending E_b of the beams that make up the beam were determined before the production (pressing) of the composite beams. Strain gauges were glued to each beam and loading was carried out with one or two concentrated forces with a span equal to the span of the composite beam. The loading was repeated 4 times in the range of 0.25...1.0 of the design load, the deflection in the middle of the span and the relative deformations of the wood fibers at the locations of the strain gauges were determined. The elastic modulus was determined as follows:

$$E_b = \frac{ML^2}{K_f JF}, \tag{3}$$

where K_f is the coefficient depending on the type of transverse load.

The local elastic modulus was determined for the compressed and stretched zones of the beam from the condition of equality of the external and internal moments in the section where the strain gauges are located:

$$M_{ext} = M_{int} = \int_F y \sigma dF, \tag{4}$$

where y is the coordinate of the beam section under consideration along the height; σ are the stresses in the section under consideration $\sigma = \varepsilon E_w$; ε is the relative deformations of wood fibers.

The deformations of the edge fibers were determined from the known deformations at the locations of the strain gauges from the similarity of triangles:

$$\varepsilon=\frac{h_i\left(\varepsilon_{up(low)}-\varepsilon_{mid}\right)}{h_i-2a}+\varepsilon_{mid},\tag{5}$$

where $\varepsilon_{up(low)}$ is the deformation by upper and lower strain gauges; ε_{mid} is the strain on average strain gauge; h_i is the height of the cross-section of the beam; a is the distance from the outermost fiber to the location of the strain gauge.

To determine the maximum stresses in the central section, the deformations were recalculated proportionally to the distance from the center of the beam to the section, in which the strain gauges were located.

3. Results and Discussion

At the preliminary testing stage (series 0), three different composite beams were manufactured on TGk dowel plates. Beam No. 2 is 3.5 m long with a cross-section of 2×140×130 mm, 11 dowel plates are installed at half the length with a minimum pitch in the zone of maximum shear forces – at the beam supports. Beam No. 4 is 2.7 m long with a cross-section of 2×140×125 mm, 5 dowel plates are installed at half the length with a uniform pitch. Beam No. 5 is 3.5 m long with a cross-section of 2×80×80 mm, 8 dowel plates are installed at half the length with a uniform pitch.

The beams were tested repeatedly under various types of transverse loads. They were brought to destruction during the final test with a concentrated force in the middle of the span. The main parameters of beam tests (calculated M_{cal} and destructive M_{dest} bending moments, experimental deflection in the middle of the span f, displacements of mutual shear of ties along the shear joint Δ_{sh}, relative deformations of wood fibers along the upper and lower strain gauges) are given in Table 1.

Table 1. Characteristics of beams of series 0 and main test results.

No.	L cm	$\frac{E_b}{E_w}$ (MPa)	Type of loading	M_{cal} (kN·cm)	Test results (mm)				M_{dest} (kN·cm)
					f	Δ_{sh}	ε_{up}	ε_{low}	
2	350	$\frac{12473}{12255}$	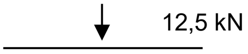 12,5 kN	1094	5.98	0.55	–130	+130	-
4	270	$\frac{9165}{12755}$	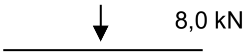 8,0 kN	540	3.43	0.22	–69	+78	1563
			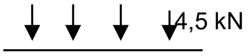 4,5 kN	540	4.47	0.30	–57	+65	
			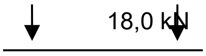 18,0 kN	540	4.95	0.36	–49	+66	
5	350	$\frac{7622}{10632}$	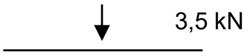 3,5 kN	306	16.8	0.43	–223	+170	1267

Relative deformations for the upper and lower strain gauges in the table are increased by $2\cdot10^5$ times.

The beams are usually destructed due to the rupture of wood fibers in the lower (stretched) zone. The safety factor for beam No. 4 was 2.59; for beam No. 5 – 3.52; beam No. 2 was not subject to destruction.

After the tests, the beams were calculated using the method described in [28] with linear and nonlinear diagrams of the bond deformation, which were obtained as a result of previous experimental and theoretical studies of connections on TGk dowel plates [27]. The calculation with the linear diagram $T-\Delta$ was performed for α_t = 0 and α_t = 0,85 cm (α_t is the distance from the bonding seam to the position of the shear force along the height of the beam cross-section). In this case, the possible spread of the deformation characteristics of the shear ties (lower and upper boundaries of the calculated bond deformation diagram) was taken into account. The main calculation results (deflection in the middle of the span f and maximum edge stresses σ) are summarized in Table 2.

Table 2. Comparison of test results of series 0 beams with calculation data.

No.	Parameter	Experiment	Calculation with a line $T–\Delta$	Calculation with a nonlinear $T–\Delta$			
				α_t = 0		α_t = 0.85 cm	
				$\dot{X}$	$X_{min} \dots X_{max}$	$\dot{X}$	$X_{min} \dots X_{max}$
2	f (mm)	5.98	5.64	5.28	5.15...5.50	5.99	5.87...6.18
	σ (MPa)	10.2	9.02	8.85	8.78...8.76	9.46	9.38...9.56
4.1	f (mm)	3.43	2.91	2.62	2.42...2.87	2.98	2.51...3.26
	σ (MPa)	4.94	5.82	5.46	5.27...5.71	5.68	5.47...5.94
4.2	f (mm)	4.47	3.74	3.53	3.23...3.23	3.68	3.38...4.01
	σ (MPa)	4.12	5.01	4.72	4.54...4.59	5.06	4.93...5.30
4.3	f (mm)	4.95	4.03	3.96	3.60...4.33	4.16	3.81...4.51
	σ (MPa)	4.18	4.71	4.53	4.37...4.76	4.95	4.87...5.14
5	f (mm)	16.79	15.59	14.91	14.3...15.7	19.07	18.5...19.8
	σ (MPa)	15.70	11.70	11.20	11.0...11.6	13.10	12.9...13.5

According to the data in the Table 2, it can be concluded that the results of the experiment and calculation are in satisfactory agreement with both linear and nonlinear diagram $T-\Delta,$ since all beams were tested in the calculated load range, where the deformation diagram has a significant linearity. It should be noted that the experiment and calculation are in greater agreement when taking into account the value $\alpha_t,$ as well as the calculation by the lower boundary of the diagram when applying a shear force along the edges of the beam-constituting bars.

Based on the preliminary tests of series 0 beams, a target experiment was planned to test composite beams for transverse load. The experiment planning matrix for short-term loading for series 1 and 3 is shown in Fig. 5.

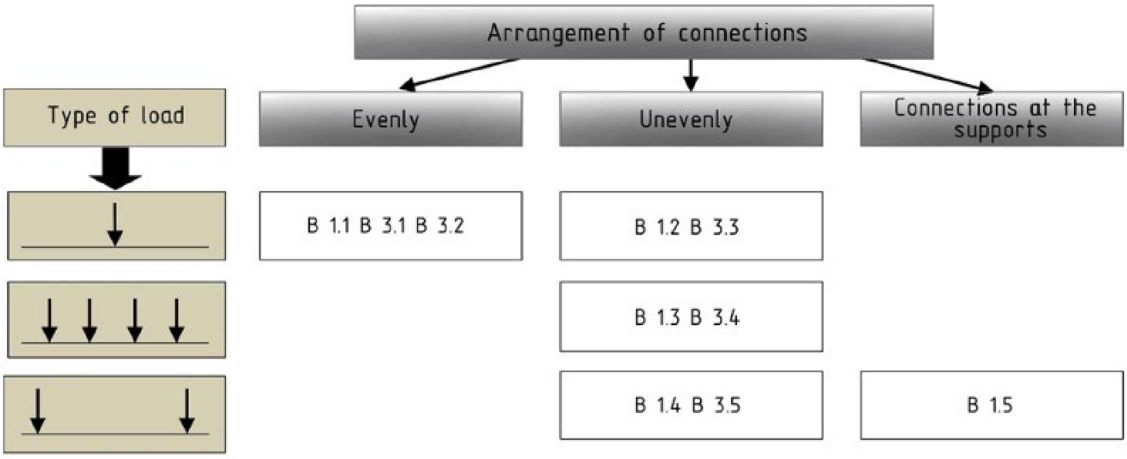

Figure 5. Experiment planning matrix.

In general, the experiment includes testing three series of beams with short-term and long-term loadings. Series 1 and 3 were performed to establish the nature of the work of composite beams depending on the type of force action and the method of arranging shear ties. Series 2 – testing beams with long-term loadings. All beams are made on TGk dowel plates with 5 dowels of 5 mm in diameter and 60 mm in length.

The dimensions of beams of series 1–3 are determined based on the condition of modeling the longitudinal rib of a roof slab with a span of 6 m with a ratio of L/h = 22. The basic size of the beam length is 350 cm with a cross-section of 2×80×80 mm. The ties in the beams are installed in three ways:

a) with a uniform step along the beam length;

b) with an uneven step according to the arcsine law in accordance with the Recommendations for the design and manufacture of wooden structures with connections on plates with cylindrical dowels (KirPI-TsNIISK systems);

c) with a minimum permissible step in the zone of the greatest shear stresses at the ends of the beam.

The main number of beams has an uneven arrangement of shear ties, as the most universal. The number of shear ties in the beams was determined in accordance with Code of Practice SP 64.13330.2017 “Wooden Structures” (issued by the Ministry of Construction and Housing and Communal Services of the Russian Federation) with a coefficient of Kt = 1.0 and amounted to n = 7 pcs per half-length of the beam. The transverse load on the beams was applied in three types according to Fig. 3.

The timber of the beams corresponds on average to grade 2 according to Interstate standard GOST 8486–86 “Softwood lumber. Technical conditions” with an average elastic modulus in bending E_b = 10590 MPa and elastic modulus of the timber at the location of the strain gauges E_w = 11570 MPa, the humidity at the time of testing was 7–10 %. The results of short-term tests for the first loading are given in Table 3. The photos in Fig. 6 show the beams during testing.

Table 3. Test results of composite beams of series 1 and 3.

No.	$\frac{M_{norm}}{M_{cal}}$ (kN·cm)	Deflections (mm)		Shifts (mm)		Relative deformations (mm x $2\cdot10^5$)		M_{dest} (MPa)	K_{sat}
		f_{centre}	f_l	Δ_{sup}	Δ_l	ε_{up}	ε_{lov}		
B1.1	240.10	11.92	8.93	0.07	0.15	–152	149	768.3	2.13
	360.15	18.91	14.12	0.15	0.35	–230	224		
B1.2	240.10	11.10	7.99	0.08	0.05	–142	161	802.4	2.23
	360.15	18.87	13.72	0.22	0.20	–241	270		
B1.3	215.90	13.96	10.61	0.31	0.26	–126	222	787.7	2.19
	359.90	25.19	19.61	0.72	0.67	–220	373		
B1.4	216.00	12.73	9.70	0.42	0.25	–112	94	570.0*	–
	360.00	23.98	18.54	0.95	0.55	–208	166		
B1.5	216.00	11.60	9.24	0.13	0.09	–123	120	819.0*	2.28
	360.00	21.98	16.64	0.44	0.31	–210	200		
B3.1	240.10	9.09	6.80	0.18	0.21	–117	104	1426.3	3.96
	360.15	15.81	11.85	0.47	0.51	–181	171		
B3.2	240.10	10.41	7.75	0.21	0.25	–141	107	1248.6	3.47
	360.15	17.38	13.00	0.47	0.54	–217	163		
B3.3	240.10	10.41	7.67	0.17	0.22	–111	121	1156.4	3.24
	360.15	18.15	13.30	0.43	0.48	–181	200		
B3.4	215.90	10.50	8.16	0.14	0.20	–99	117	1131.7	3.14
	359.90	20.12	15.74	0.47	0.55	–168	191		
B3.5	189.00	9.03	7.40	0.32	0.13	–94	103	905.6	2.87
	315.00	16.10	13.59	0.78	0.34	–160	173		

* not subject to destruction

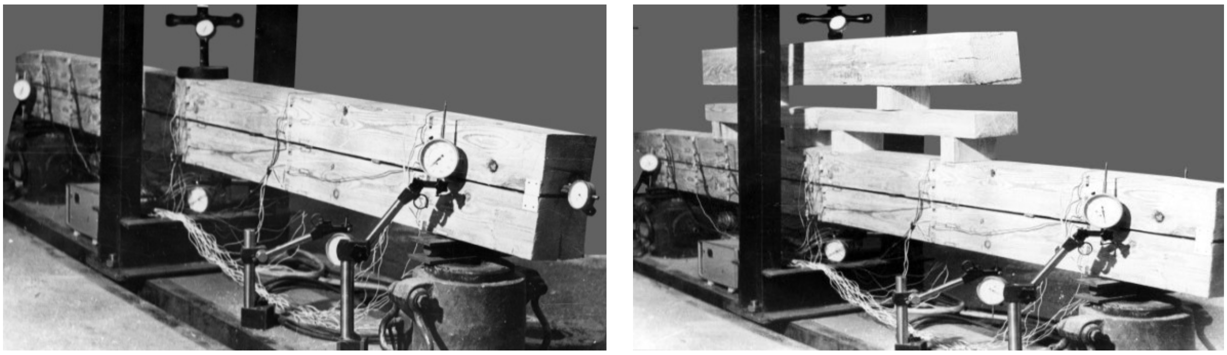

Figure 6. Beams during testing.

The destruction of the beams in the target experiment occurred mainly due to the rupture of fibers in the zone of action of the maximum bending moment in the stretched part of the beam cross-section. Longitudinal chipping of wood was also observed (chipping along the cross-grain or knot zone and chipping along the area of action of tangential stresses with subsequent rupture of wood fibers). The destruction occurred in a rather wide range of applied forces, the safety factor K_{sat} fluctuated within 2.13...3.95. The lower limit of the factor is due to the large ratio L/h of the beams, which leads to a decrease in the bending strength of the wood.

After testing the beams, each beam was calculated for the design load using the method developed in [28] with previously determined rigidity characteristics of the shear ties [27]. Table 4 provides a summary of the experimental and theoretical values of deflections f, edge stresses $\sigma_{up(low)}$ and shears along the bonding seam Δ for all beams in the target experiment.

Table 4. Comparison of calculation results with test data of composite beams of series 1 and 3.

	No.	Experiment				Calculation α_t = 0				Calculation α_t = 0.85 cm			
		f (mm)	Δ (mm)	σ_{up} (MPa)	σ_{lov} (MPa)	f (mm)	Δ (mm)	σ_{up} (MPa)	σ_{lov} (MPa)	f (mm)	Δ (mm)	σ_{up} (MPa)	σ_{lov} (MPa)
Series 1	B1.1	18.9	0.55	12.4	10.4	17.0	0.53	12.4	12.6	21.5	0.55	14.4	14.6
	B1.2	18.8	0.42	13.3	13.5	15.4	0.47	13.5	13.5	19.6	0.49	15.3	15.3
	B1.3	25.1	0.66	12.2	14.1	19.3	0.67	11.6	11.7	24.9	0.69	13.8	13.9
	B1.4	24.2	0.95	10.1	12.8	22.5	1.06	10.0	11.6	27.1	1.04	12.3	14.5
	B1.5	21.5	0.84	12.2	11.3	20.3	0.83	11.4	11.3	25.8	0.87	13.9	13.9
Series 3	B3.1	15.8	0.46	11.5	9.6	12.9	0.41	12.0	12.1	15.9	0.42	13.8	13.9
	B3.2	17.3	0.47	14.6	13.4	14.5	0.47	11.8	11.8	18.4	0.49	13.6	13.6
	B3.3	18.1	0.43	12.0	12.6	14.8	0.44	13.9	14.1	18.8	0.46	15.9	16.1
	B3.4	20.1	0.57	10.3	10.6	17.1	0.60	11.9	11.6	21.9	0.61	14.1	13.8
	B3.5	16.1	0.78	10.5	9.0	14.8	0.76	9.14	9.38	18.8	0.73	11.2	11.4

The difference in the indicated values between the theoretical and experimental values is generally small. On average, the experimental values are between the calculated values when calculating with α_t = 0 and α_t = 0.85 cm.

For beams loaded with a concentrated force in the middle of the span and four forces along the span, the closest theoretical value of deflections is α_t = 0,85 cm and exceeds the experimental values by 1–9 %. For beams loaded with concentrated forces at the supports, the closest theoretical values are deflections α_t = 0, which are less than the experimental values by 5.5–7.5 %. This is due to a decrease in the value of α_t when loaded with concentrated forces at the beam supports. In general, the difference between experimental and theoretical deflection values is on average 11 %, which quite convincingly confirms the validity of theoretical calculations.

A good convergence of the results is obtained for shears along the bonding seam. For edge stresses, the convergence of the results is somewhat worse, the maximum discrepancy reaches 39 %, although in the direction of increasing theoretical values, and the difference on average is 1.8–16 %. This is due to the relative accuracy of determining the elastic modulus of wood at the location of the resistance strain gauges E_w based on the internal moment in the beam section, compared to previously used methods.

4. Conclusion

As a result of the experimental and theoretical study of composite beams from two bars connected by TGk dowel plates under short-term loading, the nature of the beams' operation was established depending on the type of force action and the method of arranging shear ties.

An experimental verification of the calculation method for composite wooden bending rods with discrete shear ties was performed.

In general, the difference between the experimental and theoretical values of beam deflections is less than 20 %, which quite convincingly confirms the validity of theoretical calculations.

References

1. Isupov, S.A. Connections of wood structures on the basis of pin connectors. Regional architecture and engineering. 2017. 2. Pp. 100–104.

2. Piskunov, Iu.V. Soedineniia tipa “nagel'nye gruppy” i puti ikh ispol'zovaniia dlia izgotovleniia konstruktsii komplektnoi postavki [Dowel-type connections and their use in the manufacture of complete supply structures]. Proektirovanie i izgotovlenie dereviannykh konstruktsii s soedineniiami na metallicheskikh nagel'nykh plastinakh i nagel'nykh gruppakh [Design and manufacture of wooden structures with connections on metal dowel plates and dowel groups]. Kirov, 1992. Pp. 26−34.
3. Piskunov, Iu.V. Nesushchie dereviannye konstruktsii s soedineniiami na nagel'nykh plastinakh i elementakh [Load-bearing timber structures with connections on dowel plates and elements]. News of higher educational institutions. Construction. 1988. 6. Pp. 13–17.
4. Isupov, S.A. Experimental substantiation by choosing basic variant of plates with cylindrical dowels. IOP Conference Series: Materials Science and Engineering. 2020. 962. Article no. 022047. DOI: 10.1088/1757-899X/962/2/022047
5. Ling, T., Mohrmann, S., Li, H., Bao, N., Gaff, M., Lorenzo, R. Review on research progress of metal-plate-connected wood joints. Journal of Building Engineering. 2022. 59. Article no. 105056. DOI: 10.1016/j.jobe.2022.105056
6. Braun, M., Pantscharowitsch, M., Kromoser, B. Experimental investigations on the load-bearing behaviour of traditional and newly developed step joints for timber structures. Construction and Building Materials. 2022. 323. Article no. 126557. DOI: 10.1016/j.conbuildmat.2022.126557
7. Reynolds, T.P.S., Miranda, W., Trabucco, D., Toumpanaki, E., Foster, R.M., Ramage, M.H. Stiffness and slip in multi-dowel timber connections with slotted-in steel plates. Engineering Structures. 2022. 268. Article no. 114723. DOI: 10.1016/j.engstruct.2022.114723
8. Zhou, Y., Zhao, Y., Wang, C.-L., Zhou, Y., Zheng, J. Experimental study of the shear performance of H-shaped aluminum-timber composite connections. Construction and Building Materials. 2022. 334. Article no. 127421. DOI: 10.1016/j.conbuildmat.2022.127421
9. Sawata, K., Sasaki, T., Kanetaka, S. Estimation of shear strength of dowel-type timber connections with multiple slotted-in steel plates by European yield theory. Journal of Wood Science. 2006. 52. Pp. 496–502. DOI: 10.1007/s10086-006-0800-9
10. Zhuk, V.V., Shchevchuk, V.L., Antiporovich, A.V. Eksperimental'nye issledovaniia raboty soedinenii dereviannykh elementov na zhestkikh nagel'nykh plastinakh [Experimental study of the operation of joints of wooden elements on rigid dowel plates]. Problemy sovremennogo stroitel'stva [Problems of modern construction]. Minsk, 2019. Pp. 60–65.
11. Gappoev, M.M., Bazenkov, T.N. Issledovanie raboty nagelnykh soedinenij s metallicheskimi prokladkami [Study of the work of dowel joints with metal gaskets]. Issledovanie prochnosti i effektivnosti sovremennykh konstruktsij iz dereva i plastmass [Study of the strength and efficiency of modern structures made of wood and plastics]. Moscow: MISI, 1987. Pp. 45–48.
12. Zhilkin, V.A. Investigation of the strained state of a cylindrical pin in a symmetric double-shear connection of wood plates. Vestnik Cheliabinskoi gosudarstvennoi agroinzhenernoi akademii [Bulletin of the Chelyabinsk State Agroengineering Academy]. 2015. 71. Pp. 29–41.
13. Smirnov, P.N., Pogoreltsev, A.A. Opredelenie nesushchei sposobnosti nagel'nykh soedinenii na osnovanii standartnykh kharakteristik materialov [Determination of the load-bearing capacity of dowel joints based on standard material characteristics]. Sovremennye stroitel'nye konstruktsii iz metalla i drevesiny [Modern building structures made of metal and wood]. 2013. 17. Pp. 247–253.
14. Smorchkov, A.A., Shevelev, A.S. Study of operation of compound rods at discrete braces. Industrial And Civil Engineering. 2009. 1. Pp. 16–17.
15. Turkovskii, S.B., Pogoreltsev, A.A., Stoianov, V.O. Study of composite wooden beams with tilt-included relationship bonds from fiberglass fittings. Building and Reconstruction. 2018. 2 (76). 67–75.
16. Zhuk, V.V., Shevchuk, V.L., Kotsiura, I.P., Antiporovich, A.V. Issledovanie raboty dereviannykh sostavnykh balok iz tsel’noi drevesiny na nagel’nykh plastinakh [Study of the operation of wooden composite beams made of solid wood on dowel plates]. Teoriia i praktika issledovanii, proiektirovaniia i SAPR v stroitelstve [Theory and practice of research, design and CAD in construction]. Brest, 2020. Pp. 63–68.
17. Lin’kov, V.I. Issledovanie konstruktsii sostavnoi balki iz tselnoi drevesiny [Study of the design of a composite beam made of solid wood]. Razrabotka i sovershenstvovanie dereviannykh konstruktsii [Development and improvement of wooden structures]. Moscow, 1989. Pp. 54–59.
18. Jelušič, P., Kravanja, S. Flexural analysis of laminated solid wood beams with different shear connections. Construction and Building Materials. 2018. 174. Pp. 456–465. DOI: 10.1016/j.conbuildmat.2018.04.102
19. Jacquier, N., Girhammar, U.A. Evaluation of bending tests on composite glulam–CLT beams connected with double-sided punched metal plates and inclined screws. Construction and Building Materials. 2015. 95. Pp. 762–773. DOI: 10.1016/j.conbuildmat.2015.07.137
20. O’Loinsigh, C., Oudjene, M., Ait-Aider, H., Fanning, P., Pizzi, A., Shotton, E., Meghlat, E.-M. Experimental study of timber-to-timber composite beam using welded-through wood dowels. Construction and Building Materials. 2012. 36. Pp. 245–250. DOI: 10.1016/j.conbuildmat.2012.04.118
21. Karolak, A. Experimental investigation of timber beams with splice and scarf joints. Construction and Building Materials. 2021. 306. Article no. 124670. DOI: 10.1016/j.conbuildmat.2021.124670
22. Jasieńko, J., Nowak, T.P. Solid timber beams strengthened with steel plates – Experimental studies. Construction and Building Materials. 2014. 63. Pp. 81–88. DOI: 10.1016/j.conbuildmat.2014.04.020
23. Li, H., Lam, F., Qiu, H. Flexural performance of spliced beam connected and reinforced with self-tapping wood screws. Engineering Structures. 2017. 152. Pp. 523–534. DOI: 10.1016/j.engstruct.2017.08.032
24. Patalas, F., Karolak, A., Nowak, T.P. Numerical analyses of timber beams with stop-splayed scarf carpentry joints. Engineering Structures. 2022. 266. Article no. 114626. DOI: 10.1016/j.engstruct.2022.114626
25. Isupov, S. Mechanical characteristics of materials for joints of wooden structures on TGk dowel plates. AIP Conference Proceedings. 2023. 2497. Article no. 020024. DOI: 10.1063/5.0106025
26. Isupov, S.A. Bearing Capacity and Deformability of Connections of Wooden Structures on TGC Dowel Plates. Lecture Notes in Civil Engineering. 2023. 308. Proceedings of the 6th International Conference on Construction, Architecture and Technosphere Safety. ICCATS 2022. Pp. 157–167. DOI: 10.1007/978-3-031-21120-1_16
27. Isupov, S.A. Performance of TGk dowel connector plates in wooden structure joints under long-term load. Magazine of Civil Engineering. 2024. 17(2). Article no.12610. DOI: 10.34910/MCE.126.10

28. Isupov, S A. Calculation Methodology for Constituent Wooden Rods on Discrete Shear Bonds. Lecture Notes in Civil Engineering. 2024. 400. Proceedings of the 7th International Conference on Construction, Architecture and Technosphere Safety. ICCATS 2023. Pp. 67–77. DOI: 10.1007/978-3-031-47810-9_7

Information about the author:

Isupov Sergei*, PhD in Technical Sciences*
ORCID: https://orcid.org/0000-0002-3009-4293
E-mail: Deka_1958@mail.ru

Received: 16.10.2024. Approved: 15.05.2025. Accepted: 18.05.2025.

Magazine of Civil Engineering. 2025. 18(3). Article No. 13507

Magazine of Civil Engineering

ISSN
2712-8172

journal homepage: http://engstroy.spbstu.ru/

Research article
UDC 624
DOI: 10.34910/MCE.135.7

Bearing capacity of square footing resting on lime-sand soil

S.A.A. Younes, J.K. Thajeel , H.Al-R. Alaa
University of Thi-Qar, Nasiriyah, Iraq
jawad.Thajeel@utq.edu.iq

Keywords: bearing capacity, square footing, plate load, lime-sand, treated layer

Abstract. This study aims to evaluate the bearing capacity of shallow square footing resting on an artificially treated lime-sand soil layer, considering the influence of the treated layer thickness (H) and different dry unit weights of the soil layer beneath the treated layer. Additionally, the effect of lime content on the unconfined compressive strength (UCS) of lime-treated sand was also investigated. The data were obtained from loading tests carried out on a square steel plate model (89 mm length, 89 mm width, and 23 mm thick) placed on the top of an artificial lime-sand layer with H/B = 0.1, 0.3, 0.6, 1, where B is the width of the footing. The sand under the artificial layer was compacted with two dry unit weight values (14.4 and 15.8 kN/m^3), thus, achieving the loose (33 %) and dense (77 %) states, respectively. Different percentages of lime (5, 7, 10, and 15 %) were added to examine the strength of treated sand soil with lime. The results showed that the increased H/B ratio affected the stress-settlement curves and improved bearing capacity with the bearing capacity ratio (BCR) rising from 1 to 2 in loose state and from 1 to 1.9 in dense state. Small scale load tests of square footing resting on lima-sand treated layer on the top of sand with different dry unit weights revealed two failure modes. For H/B = 1 with the lowest dry unit weight, the treated layer punched through to the sand soil without visible fissures until reaching the bearing capacity of the underlaying sand. For lower H/B ratios (0.1, 0.3), the lime-treated soil layer fractured, forming cracks near the footing edge and central axis, whereas higher H/B ratios (0.6, 1) resulted in cracks primarily near the footing edge.

Citation: Younes, S.A.A., Thajeel, J.K., Alaa, H.Al-R. Bearing capacity of square footing resting on lime-sand soil. Magazine of Civil Engineering. 2025. 18(3). Article no. 13507. DOI: 10.34910/MCE.135.7

1. *Introduction*

Sandy soils cover certain areas of Iraq, presenting challenges, such as low bearing capacity, excessive settlement, and others. Therefore, this study aims to enhance the characteristics of clayey soil through chemicals or additives to improve its strength and durability, among other improvements [1].

Recently, various methods of soil stabilization through chemicals or various natural and synthetic materials have occurred. Chemical stabilization is the process of changing soil characteristics by adding chemically active element to improve its characteristics and increase its bearing capacity [2]. The soil improvement by chemical stabilization is more successful than deep foundations because, while reducing settlement, it can be expensive. The most common construction materials used for soil stabilization include lime, cement and pozzolanic materials [3].

Lime stabilization is a cost-effective method that reduces soil plasticity, improves soil workability, and enhances mechanical properties, such as California Bearing Ratio (CBR) values, unconfined compressive strength (UCS), shear strength, and tensile strength. This technique has a significant impact on fine soil and has many benefits [4, 5].

Soil stabilization with lime is not a new technique. In fact, the Chinese and Indians have used this particular mixture for centuries to build dams, bridge footings, and underground chambers [6]. Similarly, the Romans utilized lime-soil mixture for road sub-base [6]. The effectiveness of lime stabilization depends on several factors, including clay mineralogy, soil pH, silica-alumina content, lime type, water content, temperature, and curing duration [7].

Over the years, various methodologies [5, 8, 9] have been developed to determine the proper amount of lime required to adjust properties of soil and provide suitable durability and strength. Such methodologies usually aim to establish a threshold value that is intended to meet soil chemical requirements for lime, often serving as the baseline for construction purposes.

In [10], the effectiveness of applying quick and hydrated lime at different percentages (0, 2.5, 7.5, and 10 %) on the soil of tropical and subtropical regions (separately) was examined. The results showed that, regardless of lime type, it generally improves the compressive strength. In [11], the uncured effects of lime stabilization on fine-grained cohesive soil with 2, 4, and 6 % lime content were examined. The early strength and deformation properties (cone index, CBR, shear strength, and deformation moduli) of uncured lime-soil mixtures compacted wet of optimum showed substantial improvement compared to untreated natural soils. In [3], the impact of various lime and natural pozzolanic dosages on the geotechnical characteristics of silt sand soil has been studied. The results showed that lime improves compressive strength of the soil, while a combination of both lime and pozzolan significantly increased compressive strength – up to sixteen times that of untreated soil.

There have been several studies of shallow foundations in layered systems, most of them focus on sandy layer treated with cement or other stabilized agents [12–14]. Only a few [7, 15] dealt with lime-sand layers.

Plate load tests were conducted [15] on soil layers that had been compacted with lime and fly ash, resulting in increased bearing capacity and reduced settlement. As the H/D ratio increased, the test plates exhibited stiffer and stronger behavior.

In [7], plate load tests on layered systems consisting of compressible residual soil layer overlaid by three different top layers (sandy soil – bottom ash – carbide lime mixture, bottom ash – cement mixture, residual soil – cement mixture) that have been artificially cemented into place were studied. The results showed that using bottom ash and carbide lime on the treated top layer enhanced ultimate load capacity and reduced foundation settlements on processed cemented soil. The tensile cracking began at various locations according to the H/D ratio and maximum H/D value of about 1.0.

The main objective of this study is to investigate the bearing capacity and settlement of the shallow foundation resting on a lime-stabilized sand layers of varying thicknesses, considering two distinct states.

2. Materials and Methods

Materials

The sand air-dried soil used in this study was collected from a site near Nasiriya city, Iraq. The sand's physical properties are given in Table 1. The sand used in the study is classified as poorly graded sand (SP) according to the Unified Soil Classification System (USCS). Fig. 1 shows sieve analysis test results [16]. Hydrated lime (calcium hydroxide $Ca(OH)_2$), in a form of fine white powder was supplied by the Karbala lime plant. The characteristics of hydrated lime are given in Table 2. Tap water was used for all experimental procedures, with the exception of the specific gravity test, for which distilled water was used.

Table 1. Physical properties of sand.

GS	Cu	Cc	Classification of soil (USCS)	γ_d min., kN/m³	γ_d max., kN/m³	$e_{min.}$	$e_{max.}$	Angle of internal friction (φ) at	
								γ_d =15.8 kN/m³	γ_d =14.4 kN/m³
2.61	2.6	1.24	SP	13.5	16.6	0.54	0.89	35.6	31

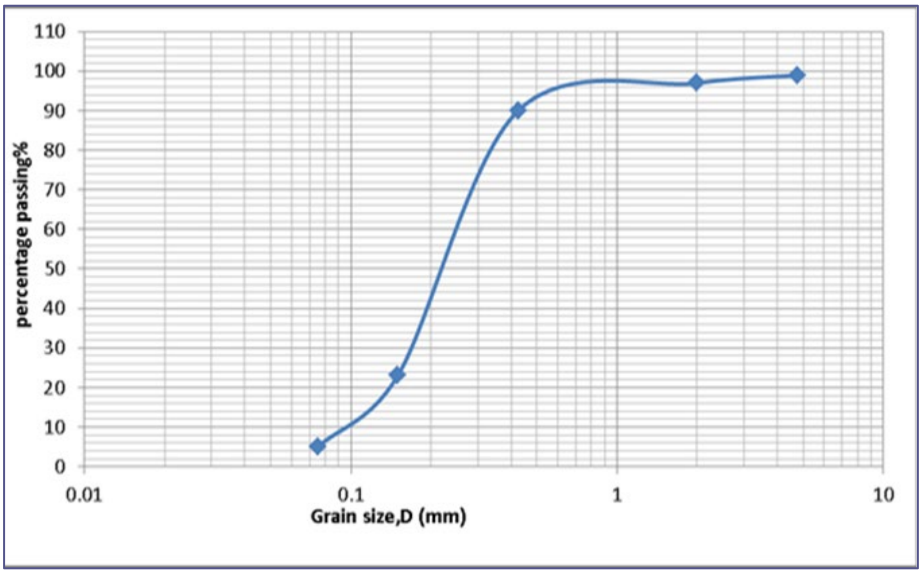

Figure 1. Sieve analysis test results.

Table 2. Characteristics of hydrated lime.

Property	Value
Form	fine white powder
CaO, %	66.851
$Ca(OH)_2$, %	88.572
CO_2, %	2.731
Specific gravity	2.321
Fineness of grinding on a sieve of 90 microns, %	6

UCS tests

UCS tests were conducted [17] on eight specimens of soil with lime contents of 5, 7, 10, and 15 %. Two different values of dry unit weights (14.4 and 15.8 kN/m^3) and a moisture content of 10 % were used. Cylindrical specimens measuring 42 mm in diameter and 84 mm in height were also used.

The lime and sand were thoroughly mixed to achieve a homogeneous mixture. The lime and water were weighed with the lime content for each mixture determined by the dry soil mass. After that, the water was added. The mixing continued until the mixture became homogenous. Each specimen was compressed in three layers within a greased cylindrical plastic mold, once each layer achieved the required dry density.

After molding, the specimens remained in the plastic mold, wrapped in a plastic sheet, and stored in airtight container for 28 days at a temperature of 22±1 °C. Fig. 2 shows the specimens during the curing. Prior to testing, the weight, diameter, and height of each specimen were measured. Fig. 3 shows the UCS test.

Figure 2. Specimens during the curing.

a) b)

Figure 3. UCS test: a) a specimen under load, b) a failed specimen.

Small-scale model tests

A steel model footing measuring 89 mm in diameter and 23 mm thickness was used in all tests as a shallow footing model. The soil container measuring 600 mm in length, 600 mm in width, and 600 mm in height was manufactured from 6-mm-thick steel.

To apply static vertical load to the footing, a testing frame was designed and manufactured. The 2-ton capacity piston of a hydraulic jack was supported by the testing frame. The hydraulic jack was attached to a 180 mm long nickel shaft with a hole on the other end that connected to the stainless-steel load cell with 2-ton capacity. The hydraulic jack contained a gauge that measured the applied pressure. Load measurements were recorded using a digital weighing indicator SI 4010. Settlement was measured using two dial gauges connected to magnetic supports with 0.01 mm precision (Fig. 4). Fig. 5 shows a sketch of the cross-section for the small-scale model test.

Figure 4. Complete test setup.

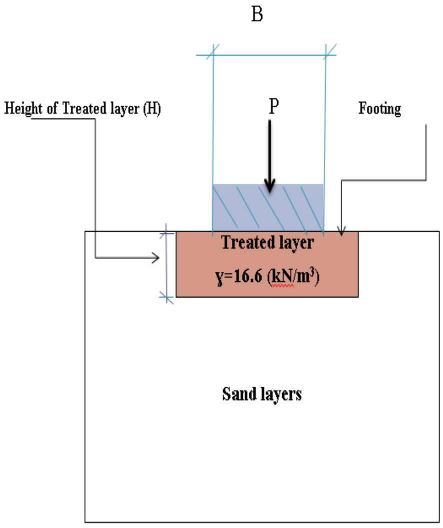

Figure 5. Sketch of the cross-section for small-scale model test.

Preparation of sand layers

Two series of models were tested using two different values of dry unit weights (14.4 and 15.8 kN/m^3). The first series examined untreated soil layers, while the second series evaluated artificially lime-stabilized soil layer. The soil tank was filled in five 120-mm-height layers. Each layer was filled with a certain weight of soil and compacted using a 10 kg steel hammer measuring 130 mm in diameter. The number of blows for every layer was not specified. The compaction continued until each layer was filled with a certain weight and the required dry unit weight was achieved. The sands exhibited effective peak strength values of c = 0 kPa with φ = 35.6° at γ_d =15.8 kN/m^3 and φ = 31° at γ_d =14.4 kN/m^3.

The soil was treated with 10 % hydrated lime content and compacted to 16.6 kN/m^3 dry unit weight after adding 10 % of moisture content as optimum value. The treated soil was cast in wooden mold outside the soil container to prevent disturbing loose sand. The molding method was essentially similar to UCS testing. Following the mixing, the treated soil was manually compacted in layers with equal thickness, ensuring that each layer satisfied the required dry density and water content requirements. To prevent moisture loss, the sample was wrapped in a plastic sheet. The samples were removed from the mold after 7 days of curing, and their dimensions and mass were measured with accuracy of around 0.1 mm and 0.01 g.

The sample was positioned at the center of the tank. Additional soil was manually added to the treated soil sides until it was level with the top. After that, the displacement gauges and loading piston were installed, and the small-scale square footing model was set up on the treated layer with thickness represented as the H/B ratios: 0.1, 0.3, 0.6, and 1. The treated layer width, curing period and foundation width were kept constant. Table 3 summarizes all experimental parameters considered in this investigation.

Table 3. Experimental parameters.

Test No.	Sand layers	Type and percent of stabilization agent	Dry unit weight of sand layers, kN/m^3	H/B
1	Untreated	_	14.4	0
2	Treated	Lime 10 %	14.4	0.1
3	Treated	Lime 10 %	14.4	0.3
4	Treated	Lime 10 %	14.4	0.6
5	Treated	Lime 10 %	14.4	1
6	Untreated	_	15.8	0
7	Treated	Lime 10 %	15.8	0.1
8	Treated	Lime 10 %	15.8	0.3
9	Treated	Lime 10 %	15.8	0.6
10	Treated	Lime 10 %	15.8	1

3. Results and Discussion

3.1. Results of UCS Tests

Table 4 contains some details of UCS tests, such as percentage of lime, dry unit weights, and results of UCS tests after 28 days of curing. The axial stress increases from 121.7 to 411 kPa for soil with γ_d = 14.4 kN/m^3 and from 714.6 to 1985.4 kPa for soil with γ_d = 15.8 kN/m^3 with increasing lime content from 5 to 15 % (Figs. 5, 6).

Fig. 7 shows that the strength increases almost linearly with increasing lime content for both treated soils. It is worth noting that with a higher sand density, the strength of the sample with a higher dry unit weight increases rapidly, while the strength of the sample with a lower dry unit weight increases at a slower rate.

Table 4. Details of UCS tests.

Samples No.	Percentage of lime, %	γ_d, kN/m^3	UCS for curing time = 28 days, kPa
1	5	14.4	121.7
2	7	14.4	235.7
3	10	14.4	352.3
4	15	14.4	411
5	5	15.8	714.6
6	7	15.8	801.5
7	10	15.8	1227
8	15	15.8	1985.4

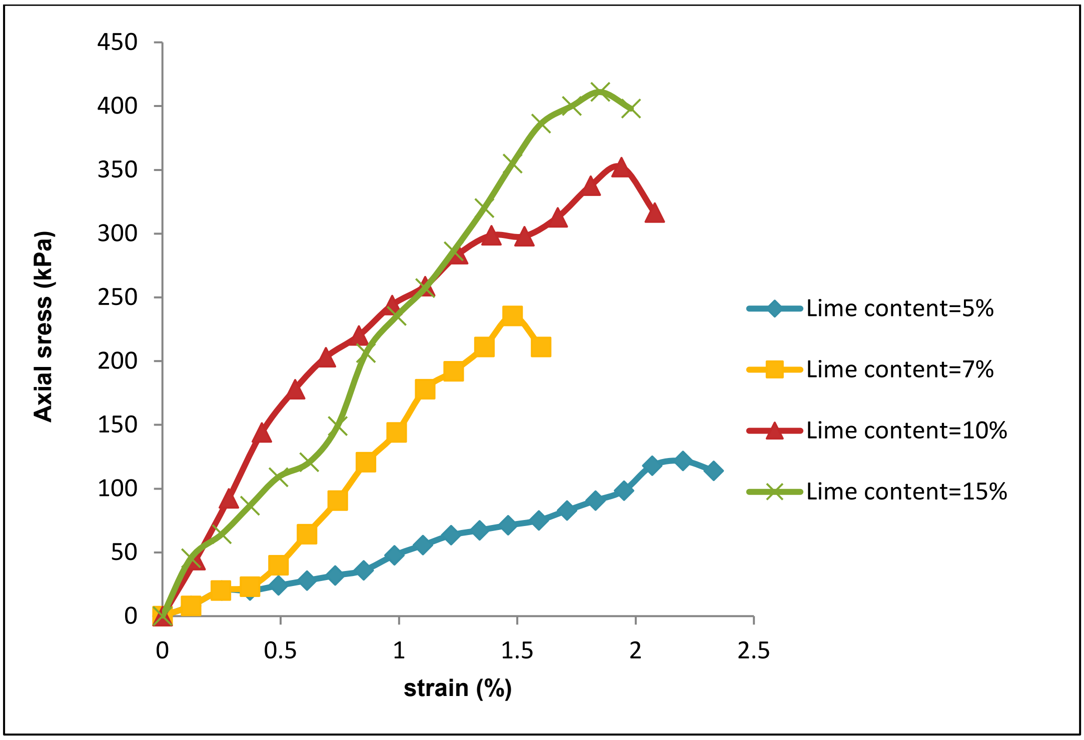

Figure 5. Stress-strain relationship for soil with γ_d = 14.4 kN/m^3 and different percentages of lime.

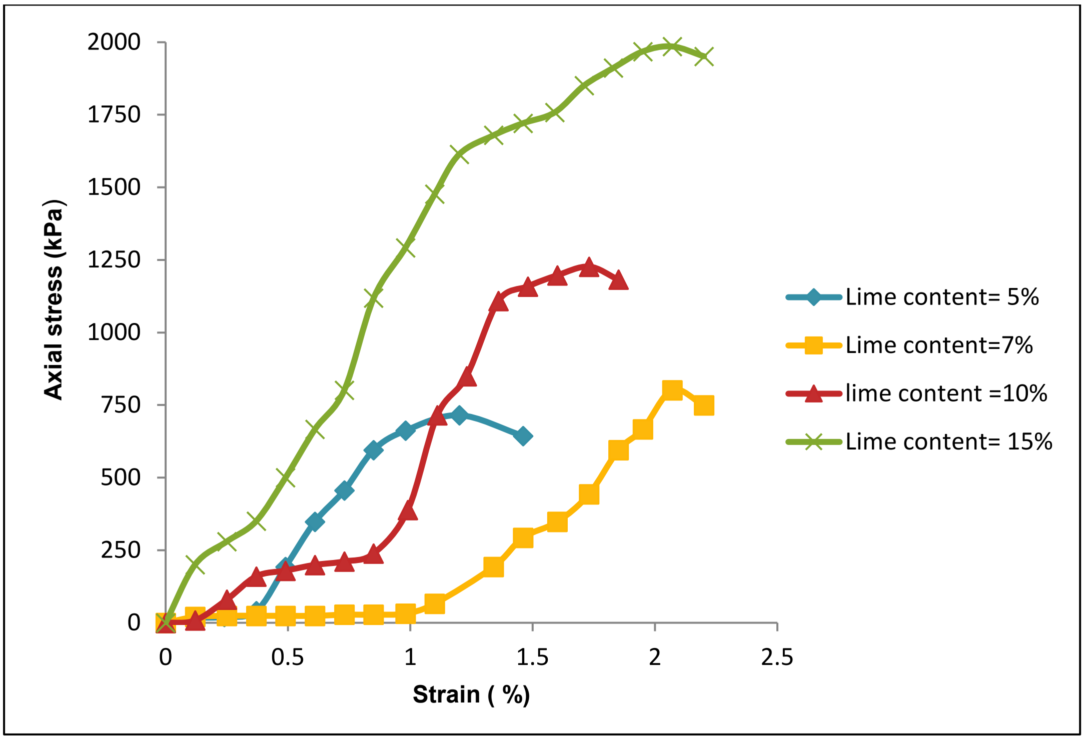

Figure 6. Stress-strain relationship for soil with γ_d = 15.8 kN/m^3 and different percentages of lime.

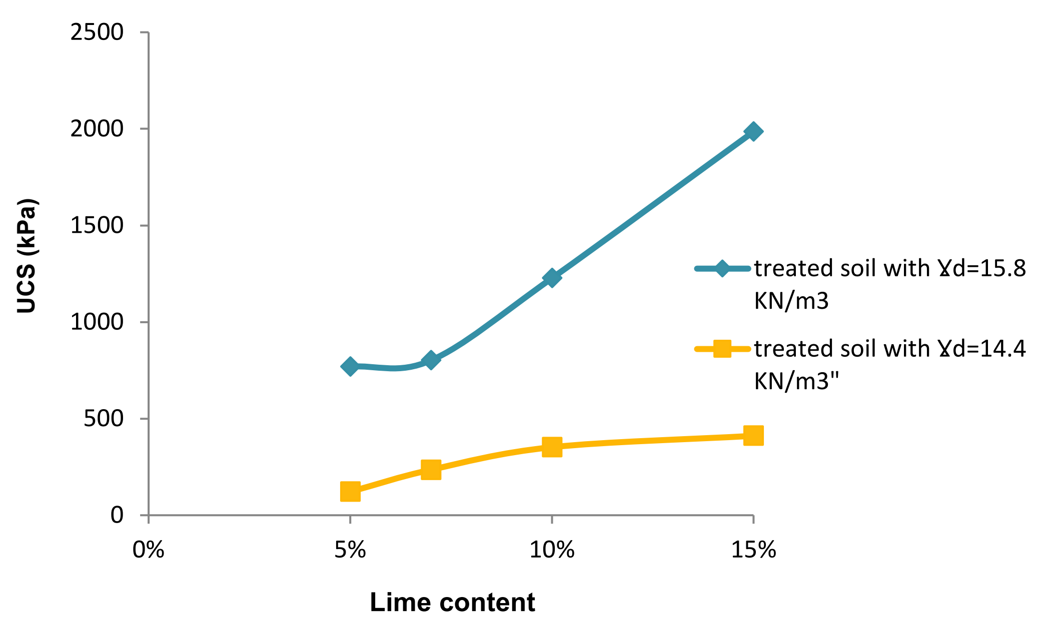

Figure 7. Axial stress for both treated soils with different dry unit weights and lime content.

3.2. Results of Plate Load Test

Plate load tests were performed on both natural and lime-treated sandy soils. The results of these tests are shown in Figs. 8, 9. Table 5 summarizes the key characteristics of the results, such as bearing capacity values, bearing capacity ratios (BCRs), failure modes, and the test sequences for each treated layer.

In this study, the bearing capacity was determined from plate load tests. The sand bearing capacity at γ_d = 14.4 kN/m^3 measured 70 kPa and at γ_d = 15.8 kN/m^3 – 255 kPa. Figs. 8 and 9 show stress-settlement curves for soils with γ_d = 14.4 kN/m^3 and 15.8 kN/m^3, respectively. Fig. 8 demonstrates how bearing increased from 70 to 76, 83, 118, and 144 kPa for treated layers varying in H/B ratios of 0.1, 0.3, 0.6, and 1, respectively. Fig. 9 demonstrates how bearing capacity increased from 255 to 268, 320, 396.2, and 473 kPa for treated layers varying in H/B ratios of 0.1, 0.3, 0.6, and 1, respectively.

Two distinct failure modes were observed in untreated soils during plate load tests. For foundation on sandy soil with γ_d = 15.8 kN/m^3, the failure appeared suddenly at the sand surface and significant bulging of the sheared mass of sand occurred with the failure. This type of failure was similar to general shear failure [13, 30]. For foundation on sandy soil with γ_d = 14.4 kN/m^3, penetration without bulging of the sand occurred, indicating punching failure [19]. The sand-lime layer exhibited fracturing at specific settlements. A sudden stress drop in the stress-settlement curves indicated the start of cracking. Cracking patterns varied by H/B ratio: near footing edges at H/B = 0.6 and 1, along the central axis and edges at H/B = 0.1 and 0.3, with no cracking observed at H/B = 1 in loose soil.

Increased layer thickness produced higher failure loads and stiffer stress-displacement responses. Greater stabilized soil height resulted in larger failure zone covered by resistant soil, thereby enhancing shallow foundation's bearing capacity. The test results showed stiffer and stronger behavior with increasing H/B ratio in both soils with different dry unit weights. Fig. 10 shows the increase in bearing capacity with increasing H/B ratios of treated soil in both dry unit weights, reaching maximum vertical stress of 140 kPa for lower dry unit weight, and maximum vertical stress of 473 kPa for higher dry unit weight. The BCR values increased from1 to 2 in loose state and from 1 to 1.9 in dense state. While lime stabilization is more common for fine-grained soils, its effectiveness in coarse-grained soils depends significantly on soil mineralogy. According to it, lime stabilization can lead to accelerated or moderate strength gain [20–26].

Table 5. Results of small-scale test.

Test No.	γ_d, kN/m^3	Lime content, %	H/B	S/B 10 %		Failure modes
				q_u, kPa	BCR	
1	14.4	10	0	70	1	Punching
2			0.1	76	1.08	Fissure
3			0.3	83	1.2	Fissure
4			0.6	118	1.7	Fissure
5			1	140	2	Punching
6	15.8	10	0	255	1	General
7			0.1	268	1.05	Fissure
8			0.3	320	1.25	Fissure
9			0.6	396.2	1.6	Fissure
10			1	473	1.9	Fissure

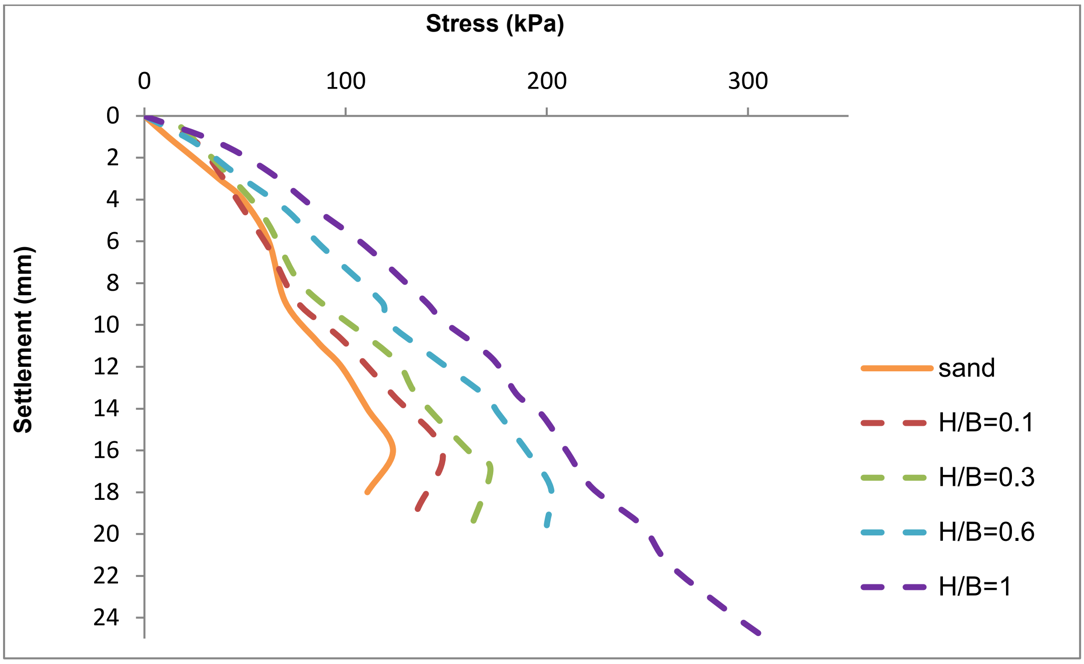

Figure 8. Stress-settlement curves for model footing trials with various H/B ratios. Lime treated layers and sand layer with γ_d = 14.4 kN/m^3.

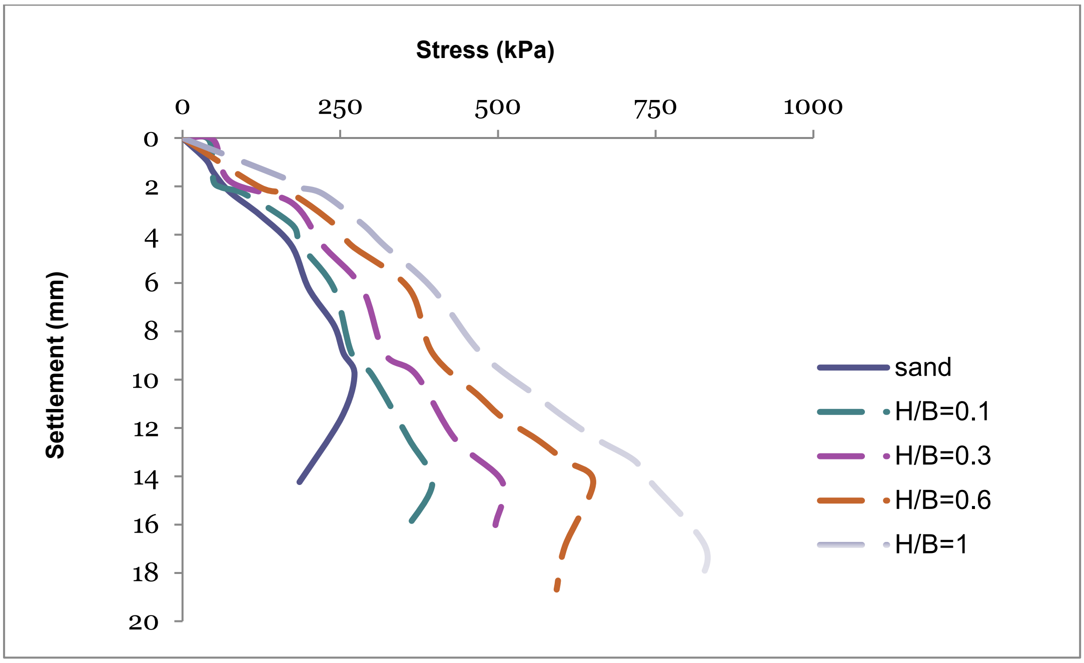

Figure 9. Stress-settlement curves for model footing trials with various H/B ratios. Lime treated layers and sand layer with γ_d = 15.8 kN/m^3.

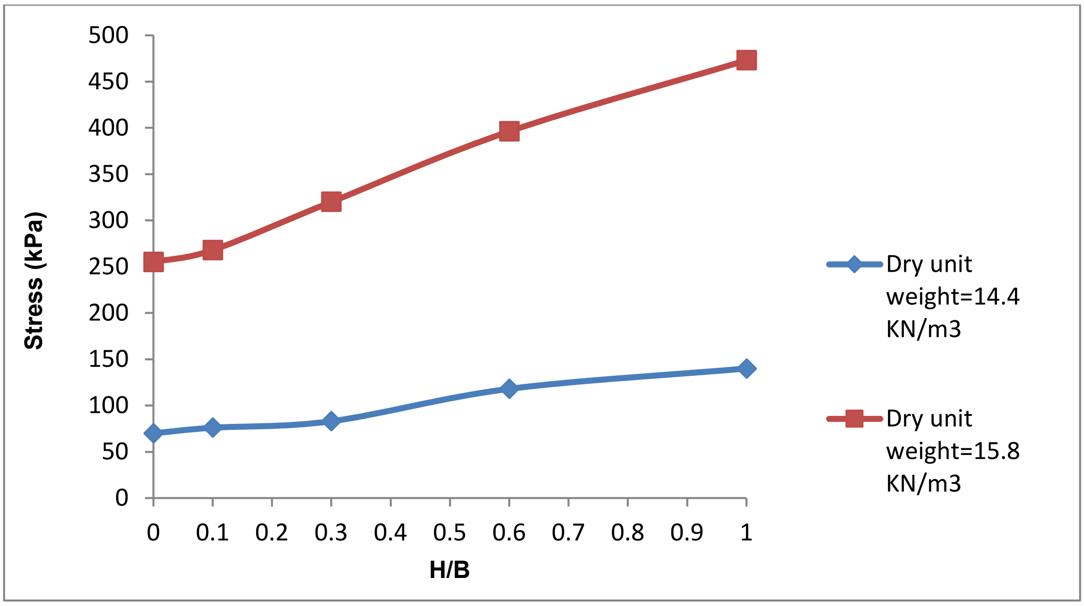

Figure 10. Relationship between bearing capacity and H/B ratio for lime-treated soil.

3.3. Bearing Capacity Analysis

Bearing capacity of untreated soil

According to [27], BCR represents the enhanced ultimate bearing capacity in non-dimensional form:

$$BCR = q_{u(R)} / q_u , \tag{1}$$

where $q_{u(R)}$ is the ultimate bearing capacity of treated soil and q_u is the ultimate bearing capacity of untreated soil.

The most commonly used bearing capacity equations for untreated soil, based on both practical and theoretical studies, define the ultimate bearing capacity as the pressure causing shear failure in the supporting soil beneath and adjacent to the foundation.

Historically, K. Terzaghi [18] proposed a superposition approach to calculate footing bearing capacity by summing contributions from various soil and load characteristics. Later, G.G. Meyerhof [28] modified Terzaghi's equation with following key differences:

- footing dimensions determine the shape factors;
- shear zone extends above the foundation level.

Additionally, G.G. Meyerhof [28] introduced the method of effective width (dimensions modification) for eccentrically loaded footings. Table 6 compares bearing capacities from plate load tests with theoretical values calculated using [18] and [28].

Table 6. Different methods of calculating the bearing capacity.

γ_d, kN/m³	q_u theoretical, kPa, at $Df = 0$		q_u experimental, kPa
	[18]	[28]	
15.8	34.4	49.3	255
14.4	14.5	19.3	70

Bearing capacity of treated soil

Unlike traditional methods, where bearing capacity factors depend solely on internal angle of friction, P. Purushothamaraj et al. [21] proposed factors that consider both layer cohesions in addition to internal angle of friction and ϕ for $\phi - c$ soils. The modified ϕ and c values are obtained as follows:

1. Calculating depth H = 0.5 B tan (45 + $\phi/2$) using ϕ for the top layer.
2. If $H > d1$, computing modified ϕ as:

$$\phi' = \frac{d1\phi1 + \left(H - d1\right)\phi2}{H}. \tag{2}$$

3. Similarly determining c'.
4. Using the bearing-capacity equation for q_{ult} with ϕ' and c'.

These steps will give us q'_{ult} as:

$$q'_{ult} = q''_{ult} + \frac{ppvks \tan\phi}{A_f} + \frac{Pd1c}{A_f} \le q_{ult}, \tag{3}$$

where q''_{ult} is the ultimate bearing capacity of the lower layer; p = 2(B + L) is the total perimeter for punching; p_v is the total vertical pressure computed as $p_v = \overline{q}d_1 + \int_0^{d_1} \gamma h dh$; k_s is the lateral earth pressure coefficient; p_{d1c} is the perimeter cohesion force; A_f is the footing area.

Table 7 demonstrates that when using method described in [21] at H/B = 1, the bearing capacity in the soil with lower dry unit weight is approximately equal to the bearing capacity in the soil with higher dry unit weight. This indicates comparable effectiveness of treatment thickness in both loose and dense states. Table 8 presents the treated layer properties.

Table 7. Geometrical properties of lime-sand layers, soils parameters, experimental bearing capacity, and method described in [21].

H/B	γ_{d1}, kN/m³	γ_{d2}, kN/m³	ϕ_1, °	ϕ_2, °	ϕ', °	c_1, kPa	c', kPa	Plate load test (q_u), kPa	[21], kPa
0.1	16.6	15.8	53	35.4	36.6	550	37.7	268	51.6
0.3					39		44.2	320	90.6
0.6					43.7		228.4	396.2	597.5
1					47.4		376.5	473	1561.4
0.1	16.6	14.4	53	31	32.5	550	37.6	76	29.7
0.3					35.5		114.2	83	154.9
0.6					40.1		228	118	574.7
1					46		376.5	140	1541.4

Table 8. Properties of treated layers.

Type of additives	Dimensions, cm	H/B	c, kPa	ϕ, °	WC, %
Lime	12×12	0.1, 0.3, 0.6, 1	550	53	10

4. Conclusions

This study investigated the bearing capacity of shallow square footing resting on lime-sand soil, yielding the following conclusions:

1. The H/B ratio and dry unit weight are seen as identical parameters regarding the bearing capacity of sand soil. They demonstrate comparable influence on sandy soil's bearing capacity, with both parameters showing positive correlation – as they increase, bearing capacity improves while settlement decreases. Specifically, the bearing capacity ratio increased from 1 to 1.9 for dense sand and from 1 to 2 for loose sand.
2. The artificial layer with H/B = 0.1 showed a very slight improvement, whereas H/B = 0.6 produced significant bearing capacity enhancement in both different dry unit weights of the sand used.
3. Axial stress analysis revealed that increased lime content (5–15 % for higher dry unit weight; 7–15 % for lower dry unit weight) leads to greater brittleness in treated soil.
4. The small-scale load tests identified two modes of failure:
   - untreated cases where the layer punched through to the sand without fissuring at H/B = 1 and lowest density,
   - treated cases exhibiting fractures – with cracks appearing near the footing's edge and central axis at low H/B ratios (0.1, 0.3) or solely near the edge at higher ratios (0.6, 1).
5. Based on method described in [21], it was confirmed that, at larger thickness of treated layer, loose and dense sands achieve nearly equal bearing capacities.

For future research, replicating this experimental approach with cement stabilization would be valuable as cement typically demonstrates superior sandy soil stabilization compared to lime, enabling direct performance comparison with these findings.

References

1. National Academies of Sciences, Engineering, and Medicine. Recommended Practice for Stabilization of Subgrade Soils and Base Materials. The National Academies Press. Washington, DC, 2009. 59 p. DOI: 10.17226/22999
2. Patel, A. Geotechnical Investigations and Improvement of Ground Conditions. Woodhead Publishing. Cambridge, UK, 2019. 201 p. DOI: 10.1016/C2018-0-01307-9
3. Abbasi, N., Mahdieh, M. Improvement of geotechnical properties of silty sand soils using natural pozzolan and lime. International Journal of Geo-Engineering. 2018. 9. Article no. 4. DOI: 10.1186/s40703-018-0072-4
4. Mallela, J., Quintus, H.V., Smith, K.L. Consideration of Lime-Stabilized Layers in Mechanistic-Empirical Pavement Design. The National Lime Association. Arlington, VA, 2004. Pp. 200–208.
5. Eades, J.L., Grim, R.E. A Quick Test to Determine Lime Requirements for Lime Stabilization. Highway Research Record. 1966. 139. Pp. 61–72.
6. Manzoor, S.O., Yousuf, A. Stabilisation of Soils with Lime: A Review. Journal of Materials and Environmental Science. 2020. 11(9). Pp. 1538–1551.
7. Consoli, N.C., Dalla Rosa, F., Fonini, A. Plate Load Tests on Cemented Soil Layers Overlaying Weaker Soil. Journal of Geotechnical and Geoenvironmental Engineering. 2009. 135(12). Pp. 1846–1856. DOI: 10.1061/(ASCE)GT.1943-5606.0000158
8. Harrison Hilt, G., Davidson, D.T. Lime Fixation in Clayey Soils. Highway Research Record. 1960. 262. Pp. 20–32.
9. Rogers, C.D.F., Glendinning, S., Roff, T.E.J. Lime modification of clay soils for construction expediency. Proceedings of the Institution of Civil Engineers – Geotechnical Engineering. 1997. 125. Pp. 242–249. DOI: 10.1680/igeng.1997.29660
10. Amadi, A.A., Okeiyi, A. Use of quick and hydrated lime in stabilization of lateritic soil: comparative analysis of laboratory data. International Journal of Geo-Engineering. 2017. 8. Article no. 3. DOI: 10.1186/s40703-017-0041-3
11. Neubauer, Jr., C.H., Thompson, M.R. Stability properties of uncured lime-treated fine-grained soils. Highway Research Record. 1972. 381. Pp. 20–26.
12. Consoli, N.C., Vendruscolo, M.A., Prietto, P.D.M. Behavior of Plate Load Tests on Soil Layers Improved with Cement and Fiber. Journal of Geotechnical and Geoenvironmental Engineering. 2003. 129(1). Pp. 96–101. DOI: 10.1061/(ASCE)1090-0241(2003)129:1(96)
13. Terzaghi, K., Peck, R.B. Soil Mechanics in Engineering Practice. Wiley. NY, 1948.
14. Foppa, D., Sacco, R.L., Consoli, N.C. Bearing capacity of footings on an artificially cemented layer above weak foundation soil. Proceedings of the Institution of Civil Engineers – Ground Improvement. 2019. 174(1). Pp. 1–16. DOI: 10.1680/jgrim.18.00089

15. Consoli, N.C., Thomé, A., Donato, M., Graham, J. Loading tests on compacted soil, bottom-ash and lime layers. Proceedings of the Institution of Civil Engineers – Geotechnical Engineering. 2008. 161(1). Pp. 29–38. DOI: 10.1680/geng.2008.161.1.29
16. ASTM D2487-17. Standard Practice for Classification of Soils for Engineering Purposes (Unified Soil Classification System). ASTM International. West Conshohocken, PA, 2020. 10 p. DOI: 10.1520/D2487-17
17. ASTM D2166-06. Standard Test Method for Unconfined Compressive Strength of Cohesive Soil. ASTM International. West Conshohocken, PA, 2010. 6 p. DOI: 10.1520/D2166-06
18. Terzaghi, K. Theoretical Soil Mechanics. Wiley. NY, 1943. DOI: 10.1002/9780470172766
19. Ladanyi, B., De Beer, E.E. Etude expérimentale de la capacité portante du sable sous des fondations circulaires établies en surface. Proceedings of the 5th International Conference on Soil Mechanics and Foundation Engineering (SMFE). 1. Paris, 1961. Pp. 577–581.
20. James, J., Sivakumar, V.L. An Appraisal on the Parameters Influencing Lime Stabilization of Soils. Journal of Materials and Engineering Structures. 2022. 9. Pp. 221–236.
21. Purushothamaraj, P., Ramiah, B.K., Venkatakrishna Rao, K.N. Bearing Capacity of Strip Footings in Two Layered Cohesive-friction Soils. 1974. 11(1). 32–45. DOI: 10.1139/t74-003
22. Al-Rkaby, A.H.J., Odeh, N.A., Sabih, A., Odah, H. Geotechnical characterization of sustainable geopolymer improved soil. Journal of the Mechanical Behavior of Materials. 2022. 31(1). Pp. 484–491. DOI: 10.1515/jmbm-2022-0044
23. Al-Rkaby, A.H.J. Performance of Zeolite-Based Soil–Geopolymer Mixtures for Geostructures under Eccentric Loading. Infrastructures. 2024. 9(9). Article no. 160. DOI: 10.3390/infrastructures9090160
24. Al-Rkaby, A.H.J. Strength and Deformation of Sand-Tire Rubber Mixtures (STRM): An Experimental Study. Studia Geotechnica et Mechanica. 2019. 41(2). Pp. 74–80. DOI: 10.2478/sgem-2019-0007
25. Al-Rkaby, A.H.J., Chegenizadeh, A., Nikraz, H.R. An experimental study on the cyclic settlement of sand and cemented sand under different inclinations of the bedding angle and loading amplitudes. European Journal of Environmental and Civil Engineering. 2019. 23(8). Pp. 971–986. DOI: 10.1080/19648189.2017.1327891
26. Saod, S.S., Al-Rkaby, A.H.J. Ground improvement using granular pile anchor foundation: A review. AIP Conference Proceedings. 2025. 3303(1). Article no. 090001. DOI: 10.1063/5.0263630
27. Das, B.M., Omar, M.T. The effects of foundation width on model tests for the bearing capacity of sand with geogrid reinforcement. Geotechnical & Geological Engineering. 1994. 12. Pp. 133–141. DOI: 10.1007/BF00429771
28. Meyerhof, G.G. The Ultimate Bearing Capacity of Foundations. Géotechnique. 1951. 2(4). Pp. 301–332. DOI: 10.1680/geot.1951.2.4.301

Information about the authors:

Samar Younes*,*
E-mail: samar.y@utq.edu.iq

Jawad Thajeel*, PhD*
ORCID: https://orcid.org/0000-0002-0556-1603
E-mail: jawad.Thajeel@utq.edu.iq

Hussein J. Al-Rkaby Alaa*, PhD*
E-mail: Alaa.Al-Rakaby@utq.edu.iq

Received: 12.02.2023. Approved: 11.04.2025. Accepted: 11.05.2025.

Magazine of Civil Engineering. 2025. 18(3). Article No. 13508

Magazine of Civil Engineering

ISSN
2712-8172

journal homepage: http://engstroy.spbstu.ru/

Research article

UDC 699.841

DOI: 10.34910/MCE.135.8

Nonlinear seismic response of a reinforced concrete large-panel precast building

Z.K. Abaev[1] , ***B.M. Yazyev***[2] , ***A.D. Valiev***[3]

[1] *Vladikavkaz Scientific Centre of the Russian Academy of Sciences, Mikhailovskoye, Prigorodny district, RNO-Alania, Russian Federation*

[2] *Don State Technical University, Rostov-on-Don, Russian Federation*

[3] *North Caucasian Institute of Mining and Metallurgy (State Technological University), Vladikavkaz, RNO-Alania, Russian Federation*

✉ *abaich@yandex.ru*

Keywords: large-panel buildings, precast reinforced concrete, nonlinear dynamic analysis, seismic performance evaluation

Abstract. This study investigates the seismic performance of reinforced concrete large-panel precast buildings, focusing on their nonlinear response under various earthquake scenarios. The widespread use of Large-Panel Buildings (LPBs) in seismically active regions, coupled with their unique structural properties and limitations of current analysis methods, requires a more comprehensive understanding of their behavior during earthquakes. A detailed numerical model was developed to capture the complex dynamics of LPBs, including nonlinear material properties, panel-to-panel interaction, and connection behavior under dynamic loading. The research methodology used advanced computational techniques, including nonlinear time history analysis and local response examination of critical elements, with a particular focus on connection regions. The results demonstrate significant differences between traditional code-based linear analyses and nonlinear dynamic analyses, especially in predicting damage distribution and interstory drift ratio (IDR). Specifically, the nonlinear analysis revealed a concentration of damage in lower stories, with maximum IDR values of 0.282 % in the first story for high-intensity scenarios, contrasting with the code-based predictions of 0.178 % in the middle stories. Furthermore, the study identified limitations in current industry-standard software, particularly in hysteresis modeling capabilities for LPB-specific behavior. These findings underscore the critical importance of employing nonlinear analysis techniques for accurate seismic performance assessment of LPBs and underscore the need for software enhancements to better represent the unique characteristics of these structures in seismic regions.

Funding: The research was supported by the Russian Science Foundation Project No. 24-79-00087, https://rscf.ru/en/project/24-79-00087

Citation: Abaev, Z.K., Yazyev, B.M., Valiev, A.D. Nonlinear seismic response of a reinforced concrete large-panel precast building. Magazine of Civil Engineering. 2025. 18(3). Article no. 13508. DOI: 10.34910/MCE.135.8

1. Introduction

Large-Panel Buildings (LPBs) have played a key role in the history of urban development and industrial construction worldwide. Introduced in the early 20th century and widely adopted in the post-World War II period, LPBs provided as a rapid and cost-effective solution to acute housing shortages, particularly in Eastern Europe and the former Soviet Union [1]. These structures, characterized by their prefabricated concrete panels assembled on-site, revolutionized the construction industry by offering significantly faster construction and reduced labor costs compared to traditional methods [2].

Despite their widespread use and the advantages they offered in terms of construction speed and cost effectiveness, the seismic performance of LPBs has been a subject of ongoing concern and study by structural engineers [3]. Another crucial aspect of LPB seismic behavior is the potential for progressive collapse. Inadequate connection design or its deterioration can lead to disproportionate failure under seismic loads, where the failure of a single structural element may trigger a cascading collapse of a larger portion of the building [4]. This risk underscores the importance of accurate modeling and assessment of connection behavior in LPBs.

Many LPBs have demonstrated surprising resilience during earthquakes, prompting further investigation of their complex behavior under seismic loads [5, 6]. This dichotomy underscores the need for more sophisticated analysis techniques to accurately assess and predict LPB performance in earthquakes. The variability in performance can be attributed to factors such as construction quality, regional design practices, and specific characteristics of seismic events [7].

Analytical studies of LPB seismic performance have evolved significantly over the years, reflecting advancements in both computational capabilities and understanding of structural dynamics. Early research focused on simplified linear models, which, while providing initial insights, failed to capture the full complexity of LPB behavior during seismic events [8]. These models were often based on assumptions that did not adequately represent the unique characteristics of precast panel structures, such as the behavior of connections under dynamic loading.

More recent studies have used advanced numerical methods and nonlinear analysis techniques to better understand the dynamic response of the structures [9]. These analyses have underscored the importance of several critical factors in LPB seismic performance: connection behavior under dynamic loading, panel-to-panel interaction, the influence of openings on overall structural integrity, and nonlinear material properties of precast concrete elements [10]. Taking these factors into account has led to more accurate predictions of LPB behavior under seismic loads but has also revealed the complexity of the problem and the limitations of current analytical tools.

Despite these advancements, there is still a pressing need for more sophisticated and accurate models to predict the seismic response of LPBs. The complexity of these structures, including the interactions between individual panels, the role of connections, and the nonlinear material behavior under extreme loading conditions, requires the development of comprehensive analytical tools [11]. Such models are crucial not only for assessing the safety of existing LPBs but also for developing retrofit strategies and designing new structures in seismic regions [12].

However, current industry-standard software is often unable to accurately model the unique characteristics of LPBs [13]. Common limitations include restricted options for hysteresis models, inability to modify parameters of standard hysteresis models, and a lack of specialized elements for modeling panel connections. These shortcomings can lead to potential misrepresentation of LPB behavior under seismic loads, especially when relying on traditional code-based or linear dynamic analyses [14, 15].

The importance of accurate seismic performance assessment for LPBs cannot be overstated. These structures continue to house millions of people worldwide, often in seismically active regions [16]. The aging of these buildings, combined with evolving seismic design standards, has created an urgent need for reliable assessment methods to inform decisions about renovation, retrofit, or replacement [17].

This study aims to address these challenges by presenting a detailed nonlinear seismic response analysis of a reinforced concrete large-panel precast building. Using state-of-the-art computational methods, the dynamic behavior of a representative LPB under various seismic scenarios is investigated. The analysis includes advanced material models specific to precast concrete behavior, detailed representation of panel connections and sensitivity analysis to damping variations.

By providing a comprehensive understanding of the structure’s response, including potential failure modes and performance limits, this research contributes to the broader goal of enhancing the seismic resilience of LPBs and similar precast concrete structures. The study specifically focuses on developing a numerical model for nonlinear analysis that can represent the particular seismic behavior of LPBs, comparing results from traditional code-based and linear dynamic analyses with those from nonlinear analysis, investigating the sensitivity of structural response to damping variations, analyzing local responses of critical elements (particularly in connection regions), and identifying shortcomings in current analysis software while proposing recommendations for their modernization.

2. Materials and Methods

The object of the study is a typical residential apartment building of reinforced concrete large-panel precast type series 92, located in Vladikavkaz city (Fig. 1): 9-story 1-section building with plan dimensions 24.6×12.6 m. The story height is 3 m. External walls are 300 mm thick panels, internal walls are 160 mm thick single-layer panels, partitions are 80 mm thick. Floor panels are 160 mm thick. Concrete grade – M150 (f_c' = 8.5 MPa, E_c = 24000 MPa), reinforcement – A-I (R_s = 240 MPa, E_s = 200000 MPa).

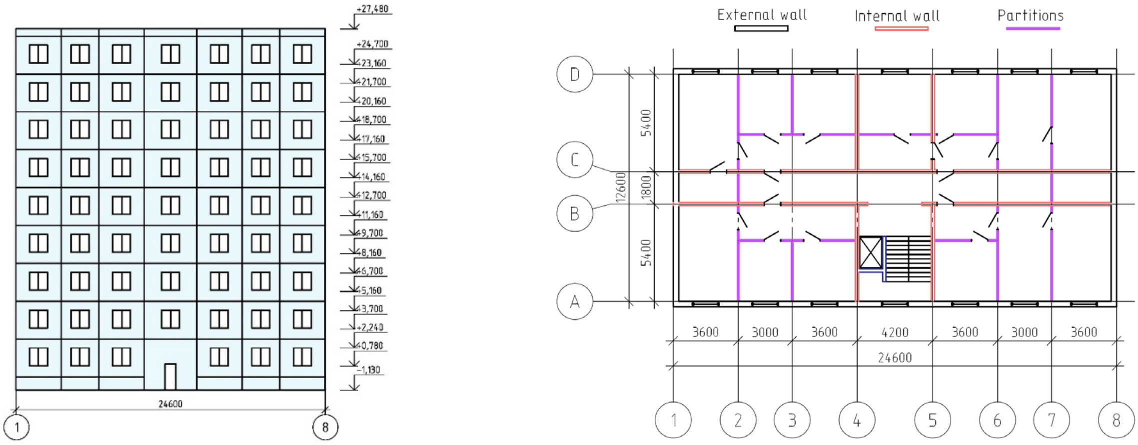

a **b**

Figure 1. Object of the study: a) elevation, b) plan.

The details of the horizontal and vertical panel connections are shown in Fig. 2.

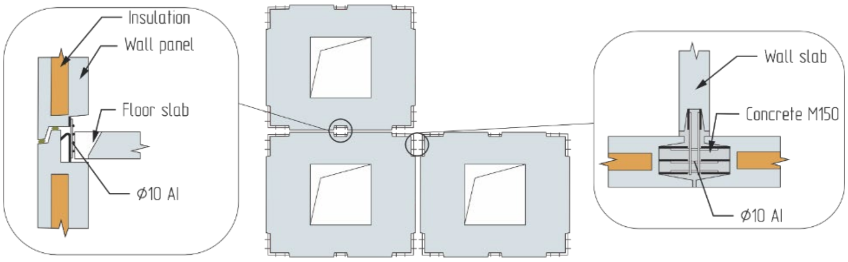

Figure 2. Details of the building.

3. Modeling Assumptions

In the modeling of large-panel precast structures, it is conventional to assume that the solid panels exhibit linear elastic behavior. This assumption is justified by the anticipated function of these elements within the structure's overall seismic response. Typically, wall panels are considered to behave in an elastic-brittle manner with respect to in-plane normal forces. Any potential nonlinear or inelastic behavior is often deemed negligible in the panels themselves and is concentrated in the connection regions, where it can be more effectively modeled and analyzed [11].

The floor system acts as a series of rigid diaphragms. The primary objective of the research is to evaluate the building's lateral load-resisting system and the global seismic response of the building. That's why the precast floor panels were replaced by continuous floor that ensures rigid diaphragm action for uniform force distribution, a key factor in global seismic performance [18].

The foundation is rigid.

The following assumptions are made for the connection [19]:

- all points of the horizontal section remain in one plane after the force is applied (plane sections remain plane);
- for the tensile zone of the section, the tensile strength of concrete is not taken into account;
- normal compressive stresses distribution along the section is linear or bilinear.

Linear normal stress distribution is taken when the maximum value of compressive stresses $\sigma_{\max}$ does not exceed the value of compressive strength of concrete R_c. Otherwise, a bilinear diagram consisting of two zones is taken, in the first of which, the compressive stresses change linearly from $\sigma_{\min} > 0$ (positive values are taken for the compressive stresses) to $\sigma_{\max} = R_c$, and in the second zone, the values are constant and equal to R_c. During the analysis, it is assumed that within the length of the linear zone, the material of the is elastic, and in the zone where $\sigma_{\max} = R_c$, it is in the plastic state.

The bilinear diagram of compressive stress allows to describe all designed situations and includes linear and rectangular diagrams of normal compressive stresses as special cases (Fig. 3).

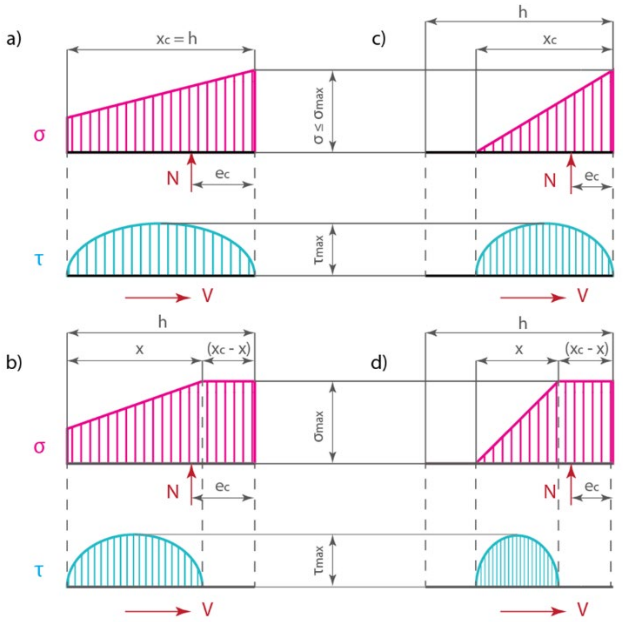

Figure 3. Normal σ and shear τ stress distribution in the horizontal connection in the combined shear-compression action: a), b) compression along the entire length of the section, respectively for linear and bilinear distributions; c), d) compression in portion of the length of the section.

The finite element method software LIRA-SAPR is used for numerical analysis.

Nonlinear behavior of the horizontal connection region is modeled by a combination of two finite elements (FEs) (Fig. 4) [20, 21]:

- 2-node link element (FE 255) for modeling shear keys (Fig. 5);
- shell element (FE 259) representing stress distribution in the connection region (Fig. 6).

The precast walls and floor panels are modeled with elastic shell element (FE 44). The connection behavior between floor and wall panels is modeled without any eccentricity, is also represented using FE 44.

Vertical connections, including shear keys, are simulated using 2-node link elements (FE 255), incorporating the total cross-sectional area of welded reinforcing steel bars to ensure accurate shear transfer [22].

The mechanical properties of FE 255 (for vertical connections) and FE 259 (for horizontal connections) are determined in compliance with the Code of Practice SP 335.1325800.2017 *“Large-panel construction system. Design rules”* (issued by the Ministry of Construction and Housing and Communal Services of the Russian Federation). The parameters presented in Table 1, including stiffness, strength, and deformation capacity, are derived from material properties (concrete grade, reinforcement yield strength) and shear key geometry (dimensions, reinforcement detailing).

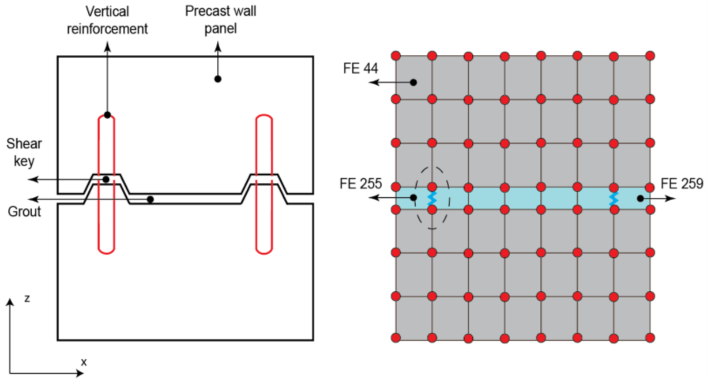

Figure 4. FE implementation of the horizontal connection region in LIRA-SAPR software.

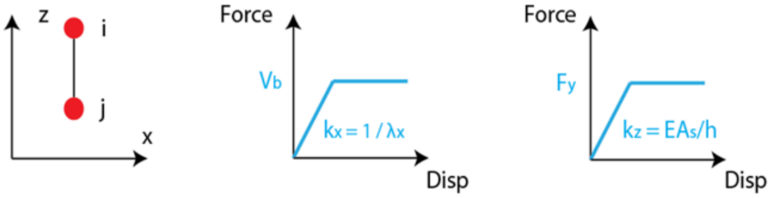

Figure 5. 2-node link element (FE 255).

Table 1. 2-node link element (FE 255) parameters.

Formula	Description
The design shear strength of one shear key: $$V_b = \min\begin{cases} V_{sh,b} = 1.5 R_{bt} A_{sh} \\ V_c = R_{b,loc} A_c \\ V_{crc,b} = 0.7 R_{bt} A_j \end{cases} \quad (1)$$	$V_{sh,b}$ – shear strength for shear; $V_{c,b}$ – shear strength for crushing; $V_{crc,b}$ – shear strength for shear cracks opening; R_{bt} – design tensile strength of grouting concrete; $R_{b,loc}$ – crushing strength, taken equal 1.5R_b – for single keys; A_{sh} – shear area; A_c – crushing area; A_j – cross-sectional area: $A_j = s_{bt} b_{mon}$, where s_{bt} – distance between shear keys; b_{mon} – wall thickness of the grouting area.
The elastic pliability of one shear key: $$\lambda_x^1 = \frac{l_{loc}\left(\frac{1}{E_{b,\omega}} + \frac{1}{E_{b,mon}}\right)}{A_{loc}} \quad (2)$$ The pliability after shear cracks: $$\lambda_x^2 = \frac{6}{d_s n_s}\left(\frac{1}{E_{b,\omega}} + \frac{1}{E_{b,mon}}\right) \quad (3)$$	A_{loc} – loaded area; l_{loc} – shear key height (recommended l_{loc} = 250 mm); E_b – elastic modulus of concrete precast element; $E_{b,mon}$ – elastic modulus of grouting concrete; d_s – connection rebars diameter; n_s – number of the connection rebars.
The elastic stiffness along z-axis: $$k_z = EA_s / h \quad (4)$$	F_y – yield strength of the rebar; E – elastic modulus of the rebar; A_s – rebar cross-sectional area; h – rebar length (equal to the connection height).

$\sigma - \tau$ relation for FE 259 that represents the theoretical assumptions for the connection section described previously are presented in Fig. 6a. In general, FE of platform connection behavior may be described with $\sigma - \varepsilon$ diagram presented in Figs. 6b, 6c.

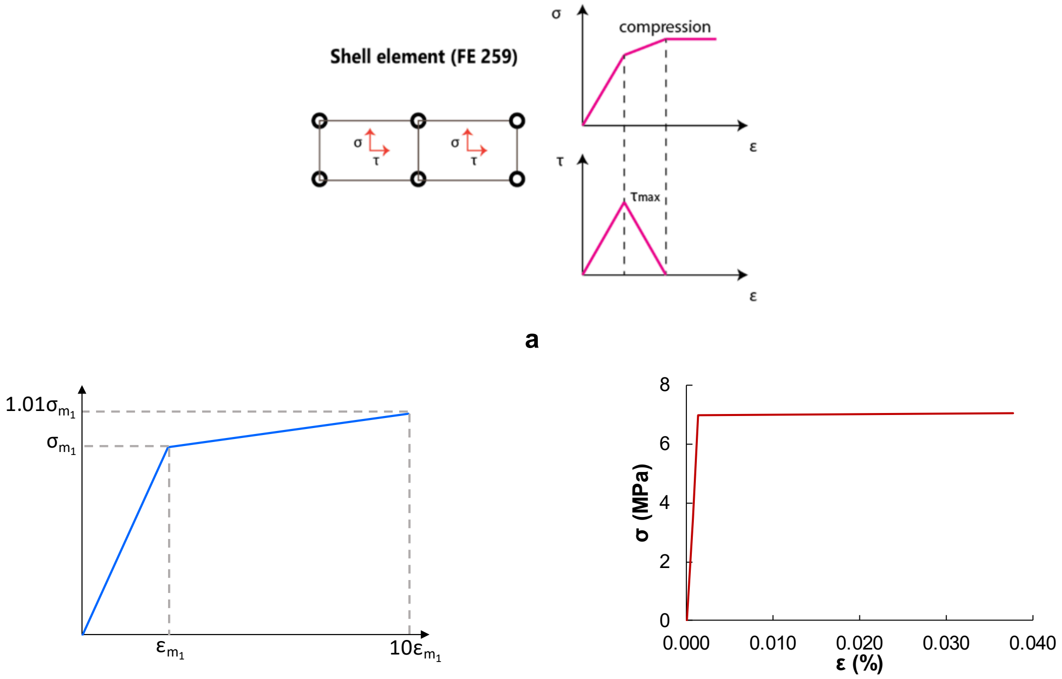

a

b

c

Figure 6. Shell element (FE 259): a) σ-τ relation, b) σ-ε diagram, c) σ-ε diagram for object of study.

During short-term compression for a mortar with a compressive strength of 1 MPa or more, with a connection thickness of 10–20 mm, pliability coefficient of the mortar bed joint λ_m, mm³/N:

$$\text{for } \sigma_m \le 1.15R_m^{2/3} - \lambda_m = 1.5\cdot 10^{-3} R_m^{2/3} t_m; \tag{5}$$

$$\text{for } 2R_m^{2/3} \ge 1.15R_m^{2/3} - \lambda_m = 5\cdot 10^{-3} R_m^{2/3} t_m. \tag{6}$$

Pliability coefficient of the connection:

$$\lambda_{c,pl} = \left(\lambda_m + \lambda'_m + \frac{h_{sl}}{E_b}\right)\frac{B_{pl}}{B_{pl} - h_v}, \tag{7}$$

where λ'_m and λ_m – upper and lower mortar bed connection flexibility coefficients; h_{sl} – floor panel height; B_{pl} – contact areas width; h_v – connection width between floor panels.

Strain:

$$\varepsilon = \frac{\lambda_i \sigma_i}{h_v}. \tag{8}$$

Stresses:

$$\sigma_m^1 = 1.15R_m^{2/3}; \tag{9}$$

$$\sigma_m^2 = 2R_m^{2/3}; \tag{10}$$

$$\sigma_m^y = 1.01\sigma_m^2. \tag{11}$$

This study prioritizes overall building performance, where precise opening effects are secondary to the global lateral resistance, therefore, the panels with openings were replaced with solid panels of reduced stiffness. The reduction factor was calculated as the ratio of the wall area with openings to the wall area without the openings. The reduced stiffness accounts for the weakening effect of openings while maintaining computational efficiency. For detailed local stress analysis (e.g., around openings), a refined micro-modeling approach should be adopted, which is the subject of future research. To reduce the computational time, the optimal FE mesh size was determined by considering three mesh sizes: 0.1 m, 0.2 m, and 0.4 m (Table 2). In the case of panels with openings, which complicate the computation by stress concentrations, these panels were replaced with solid panels of reduced stiffness. The reduction factor was calculated as the ratio of the wall area with openings to the wall area without the openings. Mesh sensitivity was conducted for nonlinear dynamic history analysis. The analysis time, maximum displacement and maximum interstory drift ratio (IDR) were compared with the reference model. As a result, the FE mesh of the wall panels was set to 0.4×0.4 m, and the FE mesh of the connections was set to 0.4×0.1 m.

The resulting FE model in LIRA–SAPR is shown in Fig. 7.

The self-weight and live load were applied according to the Code of Practice SP 20.13330.2016 *“Loads and actions”* (issued by the Ministry of Construction and Housing and Communal Services of the Russian Federation).

Table 2. Mesh sensitivity analysis.

No.	Description	Analysis time	Max displacement, mm	Max IDR, %	Error relative to Model 1, %
1	Mesh 0.1×0.1 m with openings	5'40"	93.9	0.457	–
2	Reduced (Mesh 0.1×0.1 m)	5'51"	94.7	0.473	3.383
3	Reduced (Wall Mesh 0.2×0.2 m; Connection Mesh 0.2×0.1 m)	3'10"	94.9	0.476	3.992
4	Reduced (Wall Mesh 0.4×0.4 m; Connection Mesh 0.4×0.1 m)	2'24"	94.8	0.48	4.792
5	Reduced (Wall Mesh 0.1×0.1 m; Connection Mesh 0.2×0.1 m)	5'32"	94.3	0.48	4.796
6	Reduced (Wall Mesh 0.1×0.1 m; Connection Mesh 0.4×0.1 m)	5'10"	91.9	0.48	4.79
7	Reduced (Wall Mesh 0.2×0.2 m; Connection Mesh 0.4×0.1 m)	3'19"	94.1	0.483	5.383

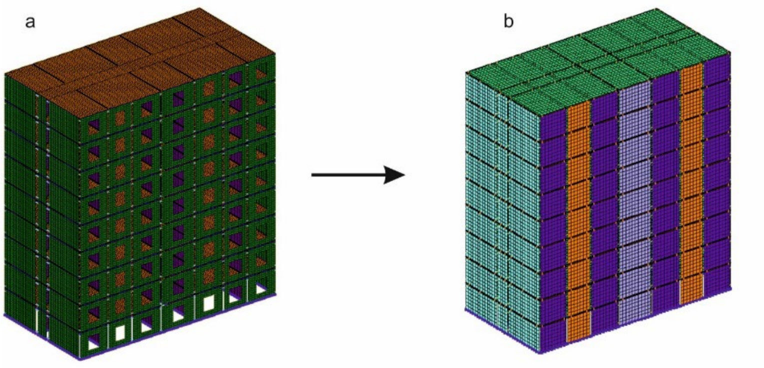

Figure 7. FE model of the building in LIRA-SAPR software: a) initial model with openings, b) model with solid panels.

4. Analysis Methods

The model was subjected to two components of ground motion of the 1988 Spitak, Armenia, earthquake (Figs. 7, 8). The earthquake, with a surface wave magnitude of 6.8 and a maximum MSK-64 intensity of *X* (Devastating), occurred in the northern part of the Armenian Republic of the Soviet Union on December 7, 1988, resulting in thousands of deaths and injuries [23]. The ground acceleration records are shown in Figs. 8, 9.

The following load cases were applied to the building model:

- Nonlinear dynamic analysis for two components of unscaled ground motion.
- Linear dynamic analysis for two components of unscaled ground motion.
- Linear code-based analyses according to the Code of Practice SP 14.13330.2018 *“Seismic building design code”* (issued by the Ministry of Construction and Housing and Communal Services of the Russian Federation) for intensity levels VII, VIII, IX of the MSK-64 scale.

- Linear response spectrum analysis for unscaled ground motion response spectrum shown in Fig. 10.

Four different damping ratio values were investigated in nonlinear dynamic load case, namely 2, 3, 4, 5 % of critical damping.

The ground motion was scaled for three different intensity levels for nonlinear dynamic load case with 5 % of critical damping to compare with code-based analyses, namely 0.1 g, 0.2 g, and 0.4 g.

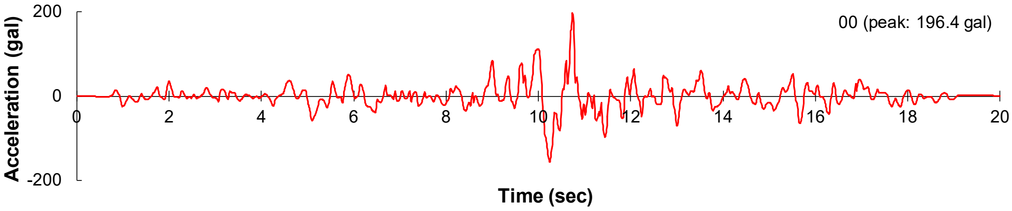

Figure 8. Ground acceleration record (Spitak, Armenia, 1988, Gukasian station, component 000).

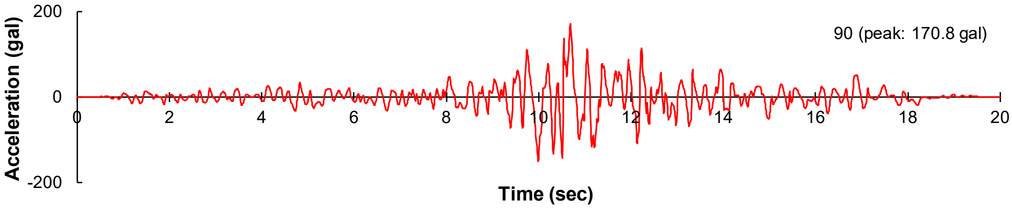

Figure 9. Ground acceleration record (Spitak, Armenia, 1988, Gukasian station, component 090).

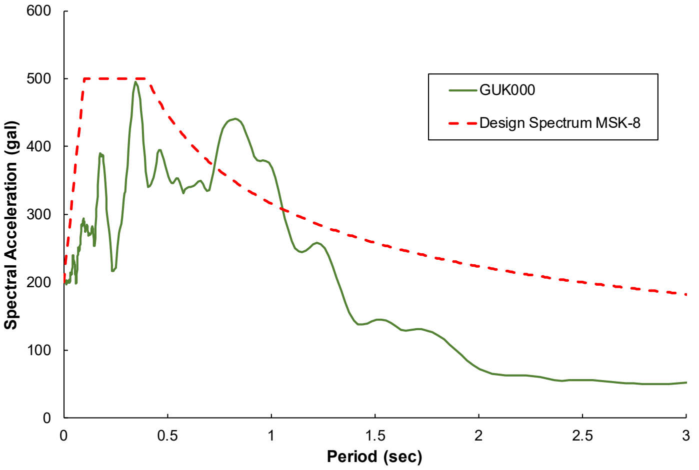

Figure 10. Response spectrum (Spitak, Armenia, 1988, Gukasian station, component 000).

The nonlinear and linear analyses were performed using an explicit integration of the equation of motion [24]:

$$M\ddot{x} + C\dot{x} + Kx = -Mea_0\left(t\right), \tag{12}$$

where $x = u$ – unknown vector of nodal displacements; $\dot{x} = v$ – nodal velocity vector; $\ddot{x} = a$ – nodal acceleration vector; $a_0\left(t\right)$ – ground acceleration; e – direction cosines vector; M – mass matrix; C – damping matrix; K – stiffness matrix.

Analysis parameters:

- Newmark-beta method (average constant acceleration with γ = 0.5 and β = 0.25) is used for direct integration of the equations of motion.
- Modified Newton–Raphson method is used for solving nonlinear equations at each time step.

LIRA-SAPR offers two predefined hysteresis models for nonlinear analyses: a peak-oriented model and an isotropic hardening model (Figs. 11a and 11b, respectively). For the current study, the peak-oriented hysteretic model (Fig. 11a) is used [25].

However, it is crucial to underscore a significant limitation of LIRA-SAPR: the inability to modify or customize the analytical parameters and parameter of these standard hysteresis models. While this constraint may be acceptable for conventional structures, it presents a considerable challenge when analyzing LPBs and other precast panel structures. LPBs exhibit unique strength and stiffness degradation behaviors that deviate from those of monolithic structures, primarily due to their distinct assembly methods and connection characteristics [26].

- Total integration time is 20 sec.
- Integration step is 0.01 sec.

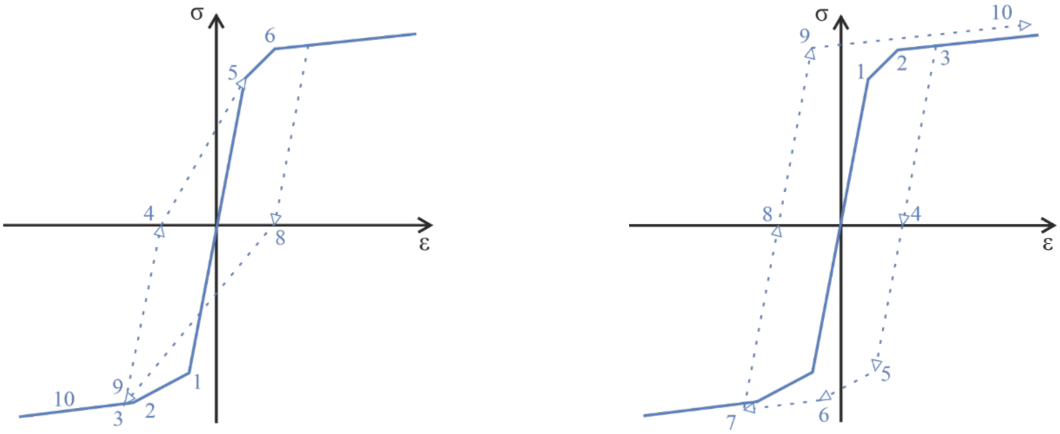

a

b

Figure 11. LIRA-SAPR's hysteresis models: a) peak-oriented model, b) isotropic hardening model.

5. *Results and Discussion*

The natural period of the structure is 0.367 sec in the Y direction (short), the second mode period is 0.211 sec in the X direction (long). The mode shapes are shown in Fig. 12.

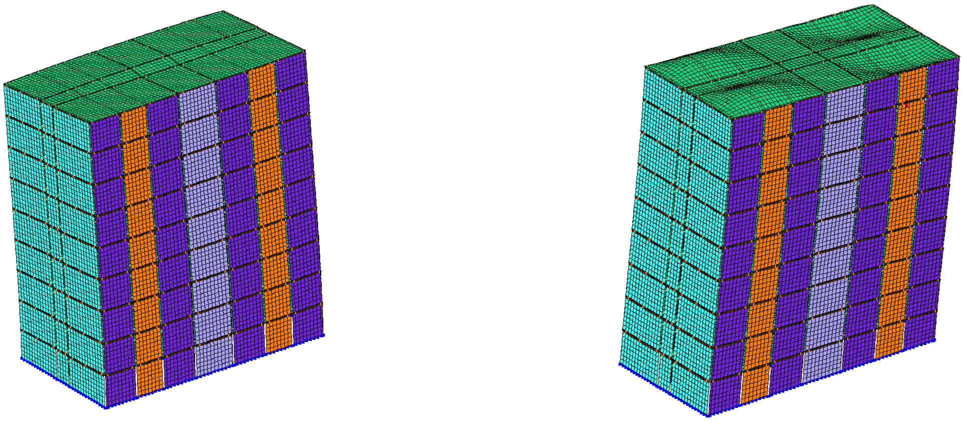

a

b

Figure 12. Mode shapes: a) first mode shape (T_1 = 0.37 sec), b) second mode shape (T_2 = 0.21 sec).

Fig. 13 illustrates the maximum displacement profiles for various analytical approaches: nonlinear and linear dynamic analyses, code-based MSK-8, and response spectrum methods. The results demonstrate good correlation along the building height, with slightly elevated values for the nonlinear case.

Notably, the roof displacement time history (Fig. 14) reveals significant discrepancies between linear and nonlinear dynamic load cases. While maximum positive displacements are comparable (19.5 mm for linear, 20.2 mm for nonlinear), the negative displacement in the nonlinear case is approximately half that of the linear case (–9.5 mm vs –18.9 mm, respectively).

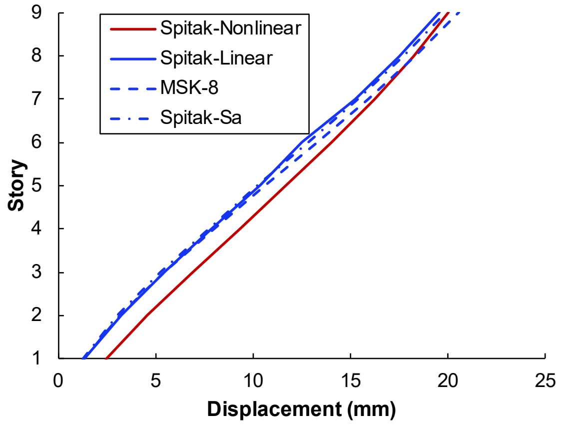

Figure 13. Displacements for different load cases.

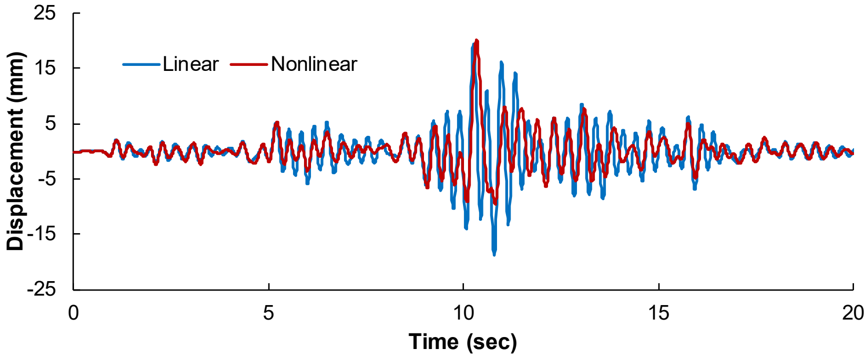

Figure 14. Roof displacement.

A critical finding pertains to the IDR response under varying seismic intensities. The IDR, a key indicator of structural damage [27], exhibits marked differences in both distribution and magnitude across analytical methods. Code-based analyses predict maximum IDR at mid-height, whereas nonlinear analyses indicate peak IDR in the first story. This disparity intensifies with increasing seismic intensity. For instance, under MSK-8 loading, the maximum IDR is 0.089 % (6th story) in code-based analysis versus 0.085 % (1st story) in the 0.2 g nonlinear case. For MSK-9, these values diverge further: 0.178 % (6th story) in code-based analysis compared to 0.282 % (1st story) in the 0.4 g nonlinear case. The damage pattern predicted by the nonlinear analysis, with concentration in the lower stories, aligns closely with observations from post-earthquake inspections of large panel buildings [28], lending further credence to the nonlinear approach.

These findings underscore the critical importance of nonlinear analyses in seismic performance evaluation, as traditional code-based analyses may yield potentially misleading results, particularly in damage distribution prediction and IDR estimation.

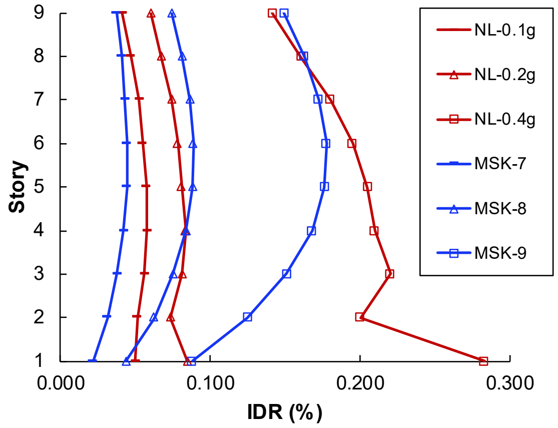

Figure 15. IDR for different load cases.

The graph of the IDR (Fig. 16) exhibits a similar pattern across different damping values, with the maximum drift occurring at the first story. However, the differences in these values are significant, with variations up to 25 %. This notable discrepancy underscores the importance of accurately determining the appropriate damping ratio, which necessitates thorough investigation in future research.

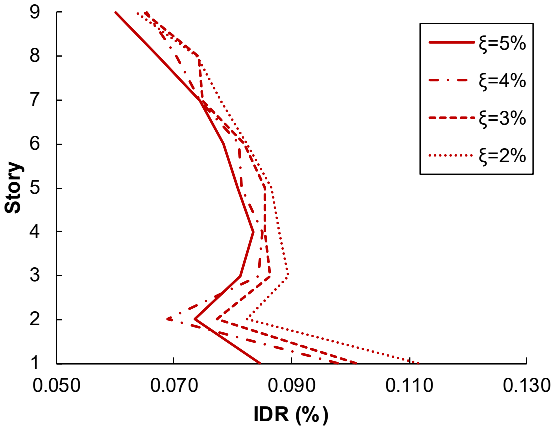

Figure 16. IDR for different damping ratios.

Despite the disparity in IDR values, the overall response in both cases remains relatively low when compared to the commonly accepted ranges for performance-based design as specified by building codes [29]. However, it is important to note that there are currently no established acceptance criteria specifically tailored for LPBs, underscoring the urgent need for the development of such criteria. These should account for the unique behavior and fragility characteristics of this structural type.

The local response of the connection region in the corner panel of the first story was examined for nonlinear dynamic load case. Particular attention was given to the behavior of specific FE within this critical area.

Fig. 17 illustrates the axial stress response for **FE 259**. The observed stress state is exclusively compressive, aligning with the initial modeling assumptions and the desired connection behavior. The ultimate strength of the element is 7100 kPa, while the maximum response reached 3071 kPa. This response indicates that the element experienced low to medium damage, which is consistent with the observed damages [7].

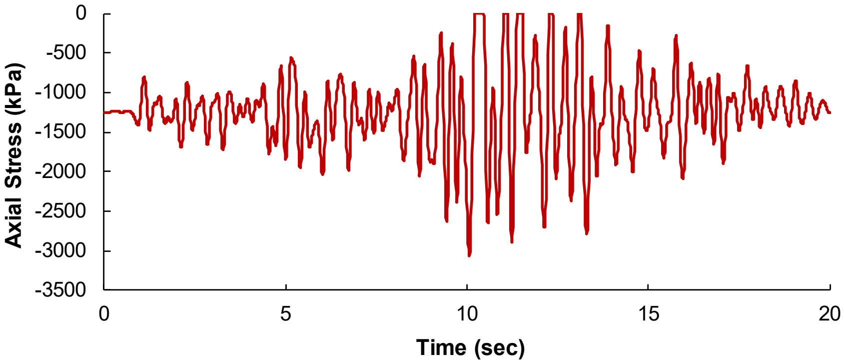

Figure 17. Axial stress response for FE 259.

The shear force response of the shear key element (FE 255) is depicted in Fig. 18. The ultimate shear strength of this element, as calculated using equation (1), is 45 kN. Fig. 19 presents the relationship between shear force and shear deformation for this element. The data indicate that the element attained its ultimate strength, suggesting the possibility of shear key failure [30]. It is noteworthy that the peak response for **FE 259** was recorded at approximately the same time step, underscoring the interaction between axial and shear responses in the connection region.

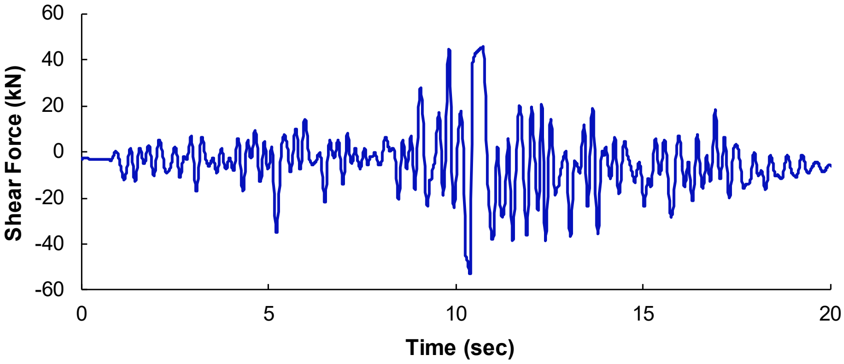

Figure 18. Shear force response for FE 255.

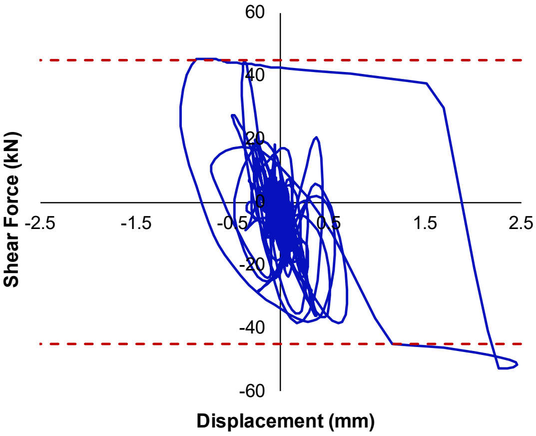

Figure 19. Hysteresis for FE 255.

6. Conclusions

The findings of this paper contribute to the understanding of LPBs seismic behavior and underscore the critical importance of nonlinear analysis in accurately assessing and predicting the seismic performance of these structures.

1. A comprehensive numerical model for nonlinear seismic analysis of LPBs was successfully developed. This model effectively captured the unique seismic behavior of LPBs, including panel-to-panel interactions, nonlinear material properties, connection behavior under dynamic loading.
2. Substantial differences were observed between traditional code-based and linear dynamic analyses versus nonlinear analysis:
   - IDR distribution: code-based analyses predicted maximum IDR at mid-height, while nonlinear analyses indicated peak IDR in the first story.
   - IDR magnitude: for MSK-9 intensity, code-based analysis predicted a maximum IDR of 0.178 % (6th story), whereas nonlinear analysis for 0.4 g PGA showed 0.282 % (1st story).
   - Damage pattern: nonlinear analysis results aligned closely with post-earthquake observations, predicting concentration of damage in lower stories.
3. These results underscore the importance of nonlinear analysis in accurately predicting LPB behavior under varying seismic intensities.
4. The notable discrepancy in response for different damping ratios (up to 25 %) was observed for the model.
5. Examination of local responses in critical elements provided valuable insights:
   - Shell element FE 259 (axial stress): maximum response of 3071 kPa, indicating low to medium damage state.
   - 2-node link element FE 255 (shear force): reached ultimate shear strength of 45 kN, suggesting potential shear key failure.

- Correlation observed between peak responses of FE 259 and FE 255, indicating interaction between axial and shear responses in connection regions.

6. To improve the accuracy of LPB seismic analysis, the following software modernizations are recommended:
   - Implementation of flexible, user-customizable hysteresis models.
   - Development of specialized elements for modeling panel connections and connections.
   - Enhancement of post-processing capabilities for detailed local response analysis.

References

1. Malaia, K. A Unit of Homemaking: The Prefabricated Panel and Domestic Architecture in the Late Soviet Union. Architectural Histories. 2020. 8(1). Article no. 12. DOI: 10.5334/ah.453
2. Malazdrewicz, S., Ostrowski, K.A., Sadowski, Ł. Large Panel System Technology in the Second Half of the Twentieth Century – Literature Review, Recycling Possibilities and Research Gaps. Buildings. 2022. 12(11). Article no. 1822. DOI: 10.3390/buildings12111822
3. Pekau, O.A. Structural integrity of precast panel shear walls. Canadian Journal of Civil Engineering. 1982. 9(1). Pp. 13–24. DOI: 10.1139/l82-002
4. Shapiro, G.I., Gasanov, A.A. Numerical solution of the problem of stability of the prefabricated building against progressive collapse. International Journal for Computational Civil and Structural Engineering. 2016. 12(2). Pp. 158–166.
5. Velkov, M. Behaviour of large panel building during the Romania earthquake of March 4, 1977. IABSE Symposium: Seminar on constructions in seismic zones. 1978. Pp. 32–42. DOI: 10.5169/SEALS-24183
6. Guri, M., Brzev, S., Lluka, D. Performance of Prefabricated Large Panel Reinforced Concrete Buildings in the November 2019 Albania Earthquake. Journal of Earthquake Engineering. 2022. 26(11). Pp. 5799–5825. DOI: 10.1080/13632469.2021.1887010
7. Freddi, F., Novelli, V., Gentile, R., Veliu, E., Andreev, S., Andonov, A., Greco, F., Zhuleku, E. Observations from the 26th November 2019 Albania earthquake: The earthquake engineering field investigation team (EEFIT) mission. Bulletin of Earthquake Engineering. 2021. 19(5). Pp. 2013–2044. DOI: 10.1007/s10518-021-01062-8
8. Clough, R.W., Malhas, F., Oliva, M.G. Seismic Behavior of Large Panel Precast Concrete Walls: Analysis and Experiment. PCI Journal. 1989. 34(5). Pp. 42–66. DOI: 10.15554/pcij.09011989.42.66
9. Cao, P., Kozinetc, G.L., Badenko, V.L., Markov, A., Zotov, D.K., Kozinets, P.V. Dynamic characteristics of a reinforced concrete frame under vibration load conditions. Magazine of Civil Engineering. 2024. 17(2). Article no. 12607. DOI: 10.34910/MCE.126.7
10. Baranski, J., Szolomicki, J., Latka, P. Numerical Analysis of the Joints of Prefabricated Elements in Large-Panel Buildings Located on the Areas of Mining Damages. Proceedings of the World Congress on Engineering and Computer Science. 2. San Francisco, 2017. Pp. 847-852.
11. Becker, J.M., Llorente, C., Mueller, P. Seismic response of precast concrete walls. Earthquake Engineering & Structural Dynamics. 1980. 8(6). Pp. 545–564. DOI: 10.1002/eqe.4290080605
12. Abaev, Z.K., Kodzaev, M.Y., Bigulaev, A.A. Earthquake resistance analysis of structural systems of multi-storey civil buildings. Structural Mechanics of Engineering Constructions and Buildings. 2020. 16(1). Pp. 76–82. DOI: 10.22363/1815-5235-2020-16-1-76-82
13. Abaev, Z., Valiev, A., Kodzaev, M. Methodology of the reinforced concrete large panel buildings modeling with SAPFIR-generator visual programming tool. AIP Conference Proceedings. 2023. 2833(1). Article no. 020024. DOI: 10.1063/5.0151656
14. Powell, G.H. Modeling for Structural Analysis: Behavior and Basics. Computers and Structures Inc. Berkeley, 2010. 365 p.
15. Yu, S., Zhang, Y., Bie, J., Zhang, W., Jiang, J., Chen, H., Chen, X. Finite Element Analysis of Hysteretic Behavior of Superposed Shear Walls Based on OpenSEES. Buildings. 2023. 13(6). Article no. 1382. DOI: 10.3390/buildings13061382
16. Srikanth, K., Borghate, S.B. Review on seismic performance evaluation of precast concrete buildings. Materials Today: Proceedings. 2023. DOI: 10.1016/j.matpr.2023.04.106
17. Wardach, M., Krentowski, J.R., Knyziak, P. Degradation Analyses of Systemic Large-Panel Buildings Using Comparative Testing during Demolition. Materials. 2022. 15(11). Article no. 3770. DOI: 10.3390/ma15113770
18. Rybakov, V., Lalin, V., Pecherskikh, M., Saburov, D. Accounting for rotational inertia in calculating structures for seismic impact. AIP Conference Proceedings. 2023. 2612(1). Article no. 040034. DOI: 10.1063/5.0113989
19. Ashkinadze, G.N., Sokolov, M.E., Martynova, L.D. Zhelezobetonnye steny seismostoikikh zdanii [Reinforced concrete walls of earthquake-resistant buildings]. Moscow: Stroyizdat, 1988. 504 p.
20. Gubchenko, V.E. Work with the ‘joint’ tool of software package LIRA-CAD. Zhilishchnoe Stroitel’stvo [Housing Construction]. 2018. 3. Pp. 30–35. DOI: 10.31659/0044-4472-2018-3-30-35
21. Vodopianov, R.Yu. Simulation and computation of large-panel buildings in PC LIRA-SAPR 2017. Zhilishchnoe Stroitel’stvo [Housing Construction]. 2017. 3. Pp. 42–48.
22. Rybakov, V.A., Tsvetkova, A.A. Stiffness of vertical keyed joints of large panel buildings before cracking. Construction of Unique Buildings and Structures. 2024. 3(112). Article no. 11201. DOI: 10.4123/CUBS.112.1
23. Noji, E.K. The 1988 Earthquake in Soviet Armenia: Implications for Earthquake Preparedness. Disasters. 1989. 13(3). Pp. 255–262. DOI: 10.1111/j.1467-7717.1989.tb00715.x
24. Chopra, A.K. Dynamics of Structures: Theory and Applications to Earthquake Engineering. 5th ed. Pearson. Hoboken, 2016. 960 p.
25. Lee, C.S., Han, S.W. An Accurate Numerical Model Simulating Hysteretic Behavior of Reinforced Concrete Columns Irrespective of Types of Loading Protocols. International Journal of Concrete Structures and Materials. 2021. 15. Article no. 5. DOI: 10.1186/s40069-020-00446-5
26. Abaev, Z., Valiev, A., Kodzaev, M. Large Panel Reinforced Concrete Buildings Inelastic Behavior Modeling Approach for Nonlinear Seismic Analysis. Lecture Notes in Civil Engineering. 2024. 400. Proceedings of the 7th International Conference on Construction, Architecture and Technosphere Safety. Pp. 162–174. DOI: 10.1007/978-3-031-47810-9_16

27. Yu, X., Li, X., Bai, Y. Evaluating maximum inter-story drift ratios of building structures using time-varying models and Bayesian filters. Soil Dynamics and Earthquake Engineering. 2022. 162. Article no. 107496. DOI: 10.1016/j.soildyn.2022.107496
28. Fintel, M. Performance of Buildings With Shear Walls in Earthquakes of the Last Thirty Years. PCI Journal. 1995. 40(3). Pp. 62–80. DOI: 10.15554/pcij.05011995.62.80
29. Magliulo, G., D’Angela, D., Lopez, P., Manfredi, G. Nonstructural Seismic Loss Analysis of Traditional and Innovative Partition Systems Housed in Code-conforming RC Frame Buildings. Journal of Earthquake Engineering. 2021. 26(15). Pp. 7715–7742. DOI: 10.1080/13632469.2021.1983488
30. Soudki, K.A., Rizkalla, S.H., LeBlanc, B. Horizontal Connections for Precast Concrete Shear Walls Subjected to Cyclic Deformations Part 1: Mild Steel Connections. PCI Journal. 1995. 40(4). Pp. 78–96. DOI: 10.15554/pcij.07011995.78.96

Information about the authors:

***Zaurbek Abaev**, PhD in Technical Sciences*
ORCID: https://orcid.org/0000-0002-6932-2740
E-mail: abaich@yandex.ru

***Batyr Yazyev**, Doctor of Technical Sciences*
ORCID: https://orcid.org/0000-0002-5205-1446
E-mail: ps62@yandex.ru

***Azamat Valiev**,*
ORCID: https://orcid.org/0000-0002-9436-3691
E-mail: azamatva1@yandex.ru

Received: 24.10.2024. Approved: 15.05.2025. Accepted: 15.05.2025.

Magazine of Civil Engineering. 2025. 18(3). Article No. 13509

Magazine of Civil Engineering

ISSN
2712-8172

journal homepage: http://engstroy.spbstu.ru/

Research article

UDC 624.011.1

DOI: 10.34910/MCE.135.9

CES-based model to predict the river rating curve

L.A.R. Alasadi ✉, ***T.H. Khlif, F.A. Hassan***

Department of Structures and Water Resources – Faculty of Engineering, University of Kufa, Najaf, Iraq

✉ *laitha.alasadi@uokufa.edu.iq*

Keywords: Kufa River, CES model, conveyance estimation system, rating curve

Abstract. Effective control of irrigation schemes and water resources is heavily dependent on the exact river discharge estimates, which are usually estimated by measuring the water level through phase-deviation conditions or rankings. However, the direct measurement of the river flow is often impractical or prohibitively expensive, which reveals the need for a reliable future model. The study focuses on the KUFA River in Iraq and applies the Transport Stimulation System (CES) model to estimate its assessment curve. The CES model integrates hydraulic geometry, channel succession, and flow resistance parameters to generate stage-discharge curves, while its "uncertainty estimates" also stand for underlying uncertainties through the component. Model assumptions were validated against the area measurement collected in several cross sections along the Kufa River.

To assess the accuracy of the model, statistical indicators, including prejudice, absolute errors (MAE), and Nash-Sutcliffe Efficiency (NSE) were calculated. The results revealed a strong agreement between CES-PRE-prescribed assessment curves and the observed field data, with most measured values falling within the limit. This river shows the reliability of the CES model to capture complex interactions between river morphology and flow resistance, even under different field conditions.

Conclusions suggest that the CES model is a valuable tool for hydraulic engineers and managers of water resources, which enables more informed decisions on the design and operation of river control, irrigation planning, and hydraulic structures. The ability to accommodate changes in channelling and morphology supports its application in the dynamic environment where the functions of the river develop seasonally or are caused by man-made effects. Overall, the CES model increases the future accuracy and supports the use of permanent water in the Al-Kufa River Basin.

Citation: Alasadi, L.A., Khlif, T.H., Hassan, F.A. CES-based model to predict the river rating curve. Magazine of Civil Engineering. 2025. 18(3). Article no. 13509. DOI: 10.34910/MCE.135.9

1. Introduction

Estimating water levels (stages) and river discharges is essential for effective water engineering management. Measuring the flow at a river's cross-section is usually impractical or highly costly. On the other hand, stages can be monitored continuously or at regular short periods with a relatively low amount of effort and cost. The relation between the stage and the discharge is known as the stage-discharge relation or the stage-discharge rating. Both terms refer to the same concept. This relationship can only exist at a specific location and a particular time [1].

Superficial stage-discharge relationships exist, in which discharge depends only on stage. Complex stage-discharge relationships arise when additional variables, such as the slope of the energy line or the stage change rate over time, are needed to define the relationship. An orthogonal plot of the experimental stage and discharge data can be used to determine whether a specific rating curve is necessary. This can be done by displaying the data on the graph. Because of the scatter on the plot, a reasonably precise estimate of the stage-discharge relationship required for the cross-section can be obtained.

As part of the stage-discharge method, a discharge is assumed to be identified for each stage. The rating curve changes with time whenever there is a change in the influencing factors, such as the growth of weeds at the cross-section and the exposure of the canal section to erosion and sedimentation factors. Rating curve errors can result from misidentifying patterns of change over time or mischaracterizing the curve at a certain point.

One of the 2D models used in estimating the rating curve at a specific cross-section is called Conveyance Estimation System (CES). The modeling equations contain various terms that correspond to the inputs for this two-dimensional method, such as the river's geometry and its parameters. On the other hand, the roughness coefficient plays a crucial role in establishing the grading curve. Several different approaches can be taken to anticipate this roughness factor. Empirical equations are taken into consideration in the published research. These equations require easily quantifiable variables that reliably exhibit both on-site and between-site impacts on resistance, and they necessitate that these variables be consistent [2]. Equations that can be used to forecast the roughness factor often have a margin of error of roughly 30 percent because they were generated by taking the typical variance across multiple sites as their starting point [3]

The form the rating curve takes and the changes the channel undergoes over time are rarely fully characterized by the gauges available in practice [4–6].

Used the current stage and discharge data to forecast discharge by combining stage, antecedent stages, and antecedent discharge values [7, 8]. Employed the Generalized Reduced Gradient (GRG) technique to find the rating curve's parameters. The rating curve for use at two different gauging locations in the United States, Walton on the Choctawhatchee River and Philadelphia on the Schuylkill River, was modeled using a spreadsheet-based nonlinear optimization approach. The stage-discharge correlations for the two sites were also created using a Genetic Algorithm (G.A.) and the more conventional approach of rating curves. According to the findings, rating curve equations established with the GRG approach are just as successful as those developed with the G.A. method. They are more accurate than the conventional rating curve method [9].

To measure the theoretical stage-discharge relationship in British Columbia for four field locations, a one-dimensional model is employed; each of these locations has varying sediment supply, hydrology, bed structure, and bed stability at different levels. The calculations were carried out at four other locations in British Columbia. The findings are consistent with the observations made by the Canada Water Survey, and the spatial diversity of the geomorphology within the channel reach produces variations in stage-discharge correlations. The presence of high silt accentuates these alterations. Alfa et al. developed a stage-discharge relationship for the Nigeria River (Ofu), where streamflow data are scarce. This was done because the design of water resource projects has been hindered by the lack of information [10–12]. The discharge was measured using a Valeport Current Meter from February 2016 to January 2017, and the stage measurement was obtained with a staff gauge at the Oforachi Bridge hydrometric station. Both measurements were taken simultaneously. Using regression analysis, we used the results of the discharge and stage measurements to specify the coefficient of the curve and the equation of the rating curve for the river at this specified station. Because the Oforachi Bridge acts as a constant control, the curvature may be relied upon. Water level discharge in a straight channel was estimated using the CES model. Use the CES model to confirm the assessment curve through experimental function. When using CES models and uncertainty estimates, the assessment curve was estimated using geometric and hydraulic data from experimental studies. Conclusions suggest that the step discharge curve manufactured by the CES model can match experimental values.

Analyzed the CES model to explore its capabilities for prediction [13–15]. The researchers demonstrate that using a suitable description of roughness is crucial. For instance, the optimum model result is achieved by using a roughness factor that has been calibrated for the entire cross-section, and the roughness magnitude is determined for banks using the CES roughness advisor. The current study aims to predict the water level-discharge curve to the Al-Kufa River using the CES. The importance of studying the rating curve of the Al-Kufa River stems from its significance in providing irrigation water for the agricultural lands it passes through and the population gatherings it serves. Therefore, it is considered the primary water source in the study area. And suffers from the impact residues of agricultural and civil activities [16–18].

The shape of the rating curve determines how well the rated channel characteristics resist flow. The more excellent the resistance, the deeper the water must transport a particular flow volume in a given amount of time. The measured phases are converted into the relevant discharges using the established rating relationship. A rating curve can be graphically depicted in its simplest form, as shown in Figure 1, by the average curve fitting, at any river section, the plot of scatter type between discharge (as abscissa) and water level (as ordinate) [19, 20].

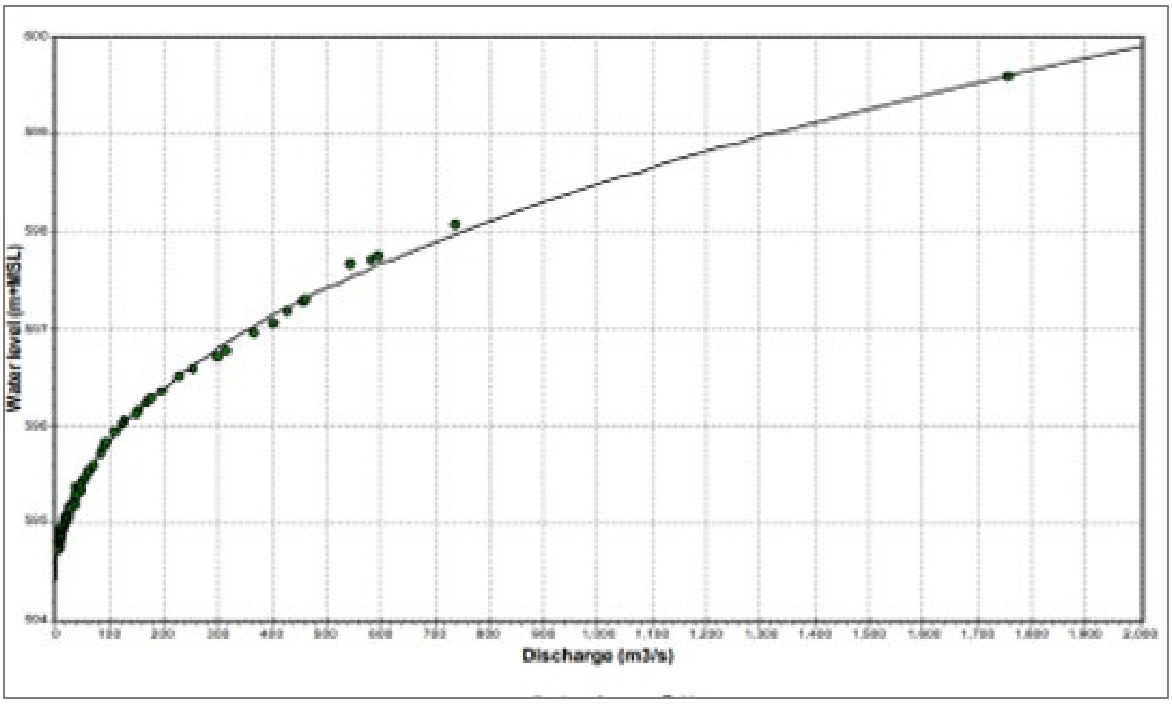

Figure 1. Typical simple rating curve.

The relationship can be represented analytically as $Q = f(h)$, where $f(h)$ is a function of water level. If we consider h and Q to be the water level and discharge, respectively, then the relationship between them can be presented as follows. Compared to an algebraic relationship, a graphical stage-discharge curve makes it much simpler to visualize the relationship and manually convert stages to discharges. However, an algebraic relationship is preferable for use in analytical transformation. The calibration of the rating curve equation is accomplished using field observations of water level and discharge [21, 22].

The stage-discharge rating's mathematical equation, known as Equation 1, establishes a connection between the actual channel control design and the shape of the rating curve [8, 23]. The variables that determine the relationship in this equation between stage (H) and discharge (Q) are a coefficient (C_o), an offset (e), and an exponent. These characteristics, in turn, relate to the channel's size, flow resistance, control level, and control form (Equation 1):

$$Q = C_o (H - e)^{\beta} . \tag{1}$$

The rating equation is primarily founded on the continuity equation, which may be found in Equation 2:

$$Q = V * A . \tag{2}$$

When applied to situations that involve open channels, the stage-discharge connection can be described as the product of a stage-velocity function and a stage-area function [4]. The geometry of the control section dictates the stage-area function, whereas flow resistance forms primarily determine the stage-velocity function. The geometry of the control section controls the stage-area function.

According to [3], the flow refers to the velocity of the cross-section being affected by elements that can be represented in the friction loss equation in its general form. Which is Equation 3:

$$V = C_1 R^x S^y , \tag{3}$$

where velocity(V) will be calculated by the product of C_1 (factor of flow resistance), S (friction slope), and R (hydraulic radius), the symbols *x* and *y* are exponents utilized to symbolize channel conditions in different cases [3].

With exponents of 0.5 and 0.67, respectively, for *y* and *x*, the Manning variation (also known as Gauckler–Manning or Gauckler–Manning–Strickler variation) (Equation 4) is the one that can be relied upon the most when dealing with open channel control situations:

$$V = \mu^{-1} R^{0.67} S^{0.5} . \tag{4}$$

In the Manning equation, the flow resistance factor is not the coefficient of friction as one might expect, but rather the inverse of the friction factor (C_1). When it comes to field measurements, the unlimited values of friction factor and slope in Equation 4 are not nearly as essential as the net change in flow resistance with time; instead, what counts most is the net change.

As shown by Equation 5 (Equation 4), the friction loss equation can simplify its complexity by combining the friction factor and slope components into a single element. This simplification is demonstrated by equation (C_2):

$$V = C_2 R^{0.67}. \tag{5}$$

Generally, it is safe to assume that the coefficient C_2 (net flow resistance) will fluctuate around the unity value when referring to alluvial channels [8]. During such times when C_2 does not change, the value of V is a function of the hydraulic radius. A modified friction loss equation (Equation 6) is derived to enhance the functional usefulness of removing an offset value (i.e., $H - e$) and utilizing the monitoring stage as a continuous measure of depth:

$$V = C_2 (H - e)^{0.67} \tag{6}$$

2. Materials and Methods

2.1. Description of the Case Study (Al-Kufa River)

Al-Kufa River, which branches from the Euphrates River, is about 5 km south of the city of Al-Kifl, and it enters the Najaf Governorate at the center of the Al-Kufa district after branching. It is called a local name (Shatt al-Kufa) concerning the area, in which it is located. It passes through it, as its length within the governorate is 28 km, and it flows through the Shatt al-Kufa in the center of the Al-Kufa district, with the outflows controlled by the Al-Kufa Barrage. The current study's scope extends from the Al-Kufa Barrage to the Al-Kufa Bridge, covering a distance of 17.7 Km. The average bed slope ranges from 7 to 12 centimeters per kilometer. The total area of agricultural lands that benefit from the waters of the Al-Kufa River is estimated at 150 acres. The barrage's intended outflow is 1400 m^3 /sec, and the upstream water level is 25.70 m above sea level. There are 7 slots, each measuring 6.312 m in length. The importance of studying the rating curve of the Al-Kufa River comes from its significance in providing irrigation water for the agricultural lands it passes through and the gatherings of the population. Therefore, it is considered the primary water source in the study area. And suffers from the impact residues of agricultural and civil activities, extending from the AL-Kufa Barrage to the Al-Kufa Bridge, as depicted in Figure 2.

Figure 2. The selected reach from Al-Kufa Barrage to Al-Kufa Bridge.

2.2. CES Rating Curve Model

In the CES, the conveyance is estimated using gravitational acceleration, channel slope, surface friction, and stream morphology. CES comprises a "Roughness Advisor", which advises on resistance, and a "Conveyance Generator", which evaluates the roughness and morphology of the channel to arrive at a capacity estimate for the channel. In addition, the CES consists of a third component known as an "Uncertainty Estimator", which is responsible for indicating the uncertainties connected to the conveyance calculations. Outputs of the CES model include the uncertainty estimator, the roughness advisor (which provides roughness values), the conveyance generator (which provides stage-flow values), and the roughness values (upper and lower bounds for the stage-flow curve). The channel's degree of unevenness is the primary line of defense against pressure imbalances or other influences that can impact fluid flow. The resistance is equal to the aggregate of the effects caused by all the resisting materials present in the channel, including things like the size of the bed material, the relative roughness of the bed, vegetation, impediments, fluctuations in channel width and depth, and channel curvature (e.g., relative bed roughness, material size, obstructions, vegetation, variations in channel depth and width, and channel curvature). The nature of this resistant force needs to be understood to determine the water level accurately. This is because a more significant resistance will result in a slower flow and a higher water level.

To reduce the uncertainty in water levels, the Department of Environment, Food and Rural Affairs created CES model. To help the decision makers make better decisions, they decided the level of uncertainty around the water level with a special flow rate and conveyed the uncertainty in a way that it was easy to understand. The CES model uses the average Navier–Stokes equations for flow, and its data processing method is controlled by deeply integrated Reynolds. The parameters of the model, including the secondary flow and Eddy viscosity, appear to remain stable based on the calibration basis within CES model. These parameters are put on their best performance values after completely analyzed. Consequently, the roughness field is the roughness values and their cross-sectional experts are calibrated. Therefore, changes in the roughness level have the most impact on the water level. [24].

This article collects all relevant hydraulic and geometric data on the Al-Kufa River. Cross sections are produced using displacement (*x*) and height (*Z*) data. The top and lower values of the roughness coefficient for staffing working in the CES model were determined by grain rumors, cross-sectional rule of control, murder patterns and access to pool point rod (Table 1). The equation adopted by the CES model was used to estimate the unity of the device:

$$n^* = (n_{or}^2 + n_{IRR}^2 + n_{veg}^2)^{1/2}, \tag{7}$$

where n_{sur}, n_{IRR} and n_{veg} represent roughness values, respectively, caused by vegetation, surface materials and irregularities.

Table 1. The selected minimum and maximum roughness values.

Zone type	Feature	Lower resistance	Unit roughness*	Upper resistance	Unit roughness*
River bed	skin friction	0.018	0.0196*	0.03	0.036*
	bed form	0.008		0.02	
Right and left banks	skin friction	0.017	0.026*	0.029	0.043*
	deposition and pool	0.020		0.033	

Figure 3 illustrates the distribution of roughness zone for the selected five cross-sections. When all the hydraulic and geometric variables have been allocated, it is possible to estimate the CES stage-discharge curve.

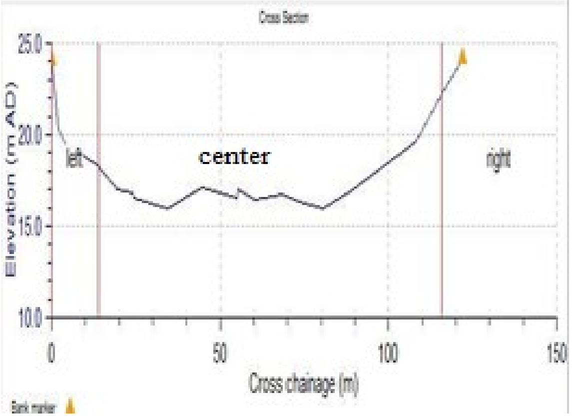

CS1

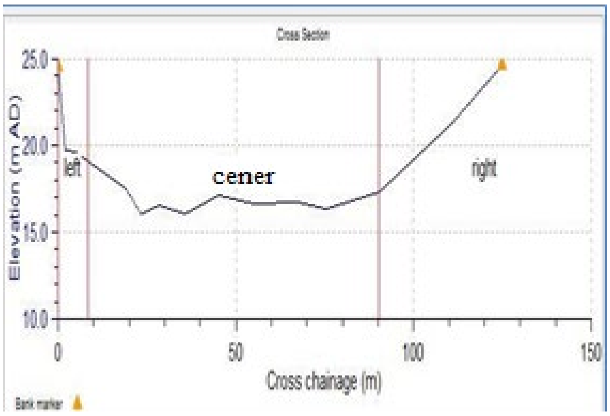

CS2

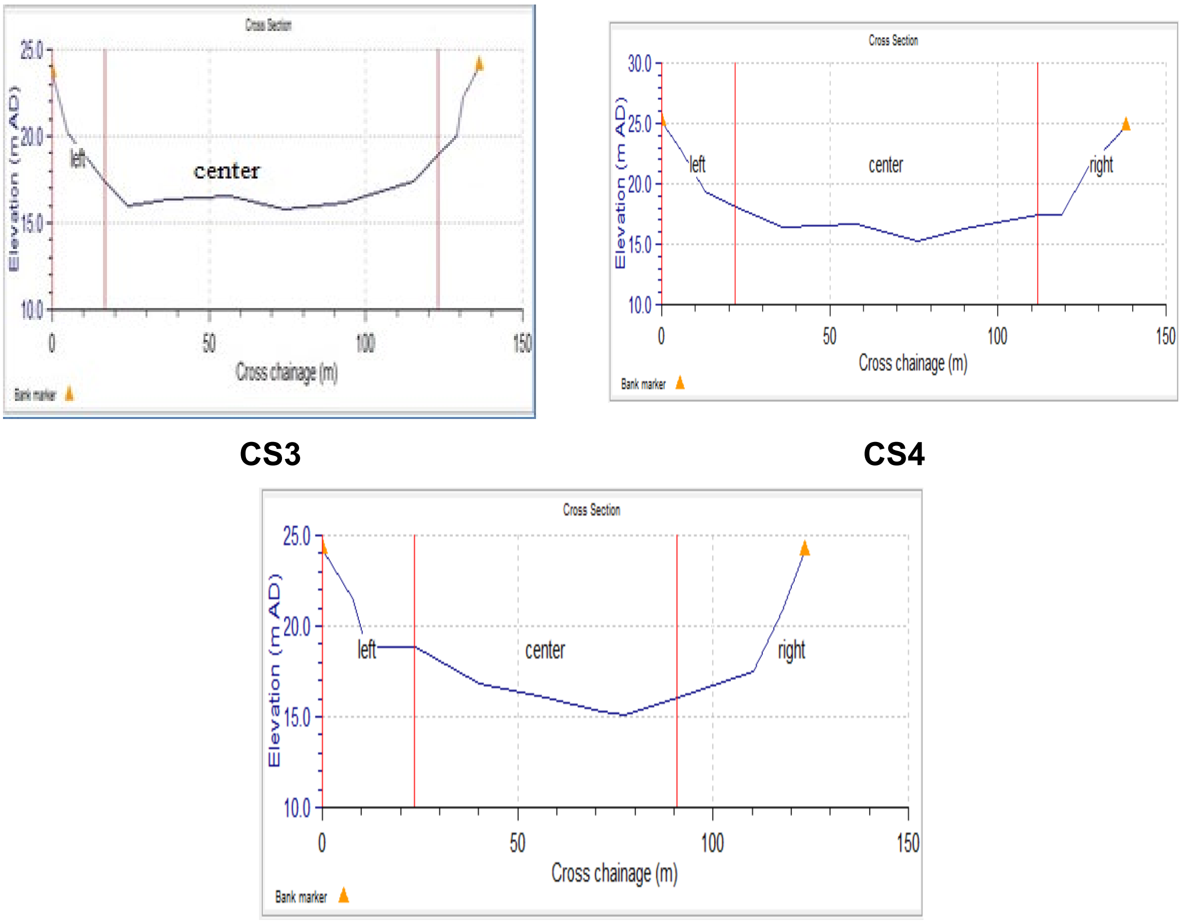

CS3 **CS4**

CS5

Figure 3. Cross sections CS1, CS2, CS3, CS4, and CS5.

3. *Results and Discussion*

3.1. *Results of the CES Model*

The data used for CES validation were taken from a measured rating curve in five cross-sections, which were compared with the model's outcomes. Five cross-sections (CS1, CS2, CS3, CS4, and CS5) were used in constructing the stage-discharge curves, which encompassed both the lower and top regions of roughness uncertainty (i.e., the maximum and minimum values of Manning roughness). The terms "central", "upper", and "lower" are used to refer to these three curves. The higher and lower curves, both caused by roughness uncertainty, are presented concurrently with the center rating curve to highlight the impact of roughness uncertainty on the central rating curve. Figures 4 through 8 present a comparative analysis of the rating curves for the various cross-sections.

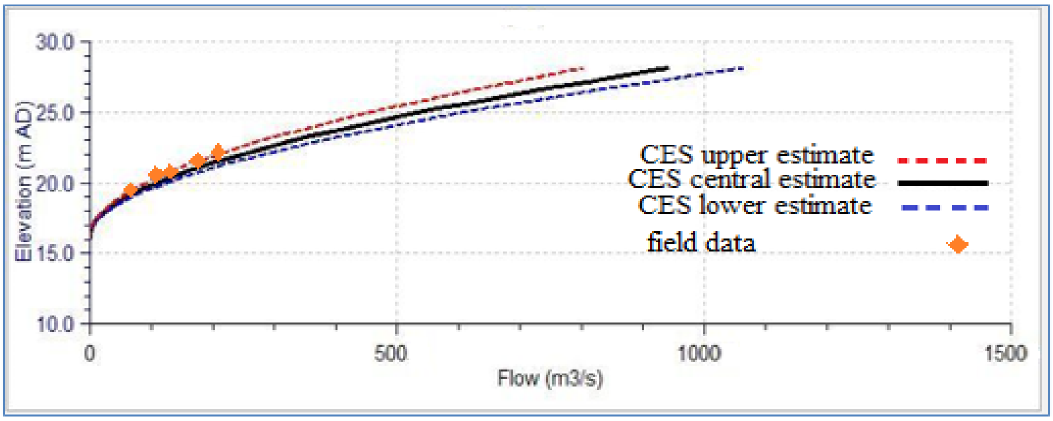

Figure 4. CES stage-discharge curve for CS1.

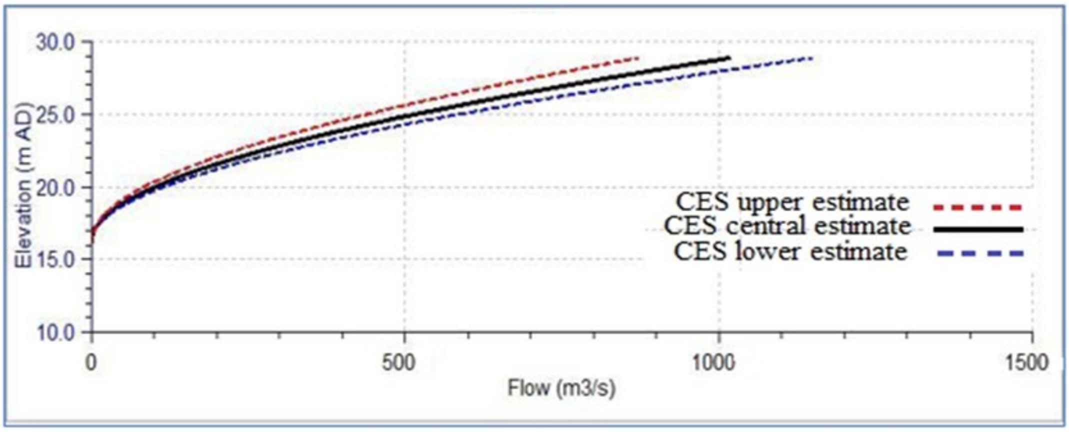

Figure 5. CES stage-discharge curve for CS2.

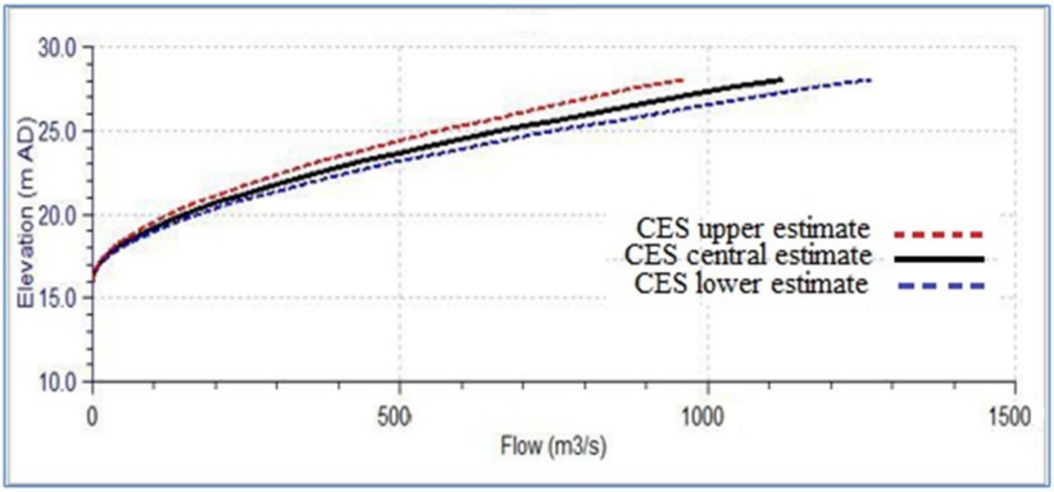

Figure 6. CES stage-discharge curve for CS3.

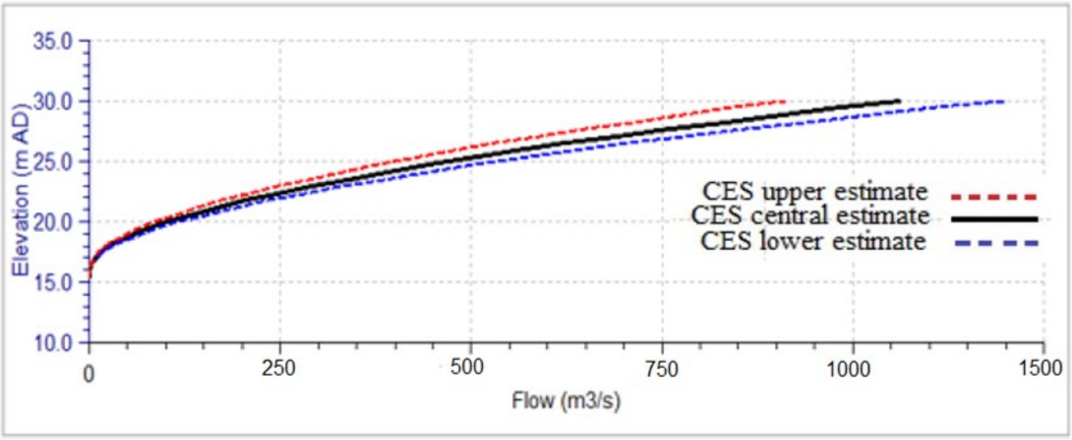

Figure 7. CES stage-discharge curve for CS4.

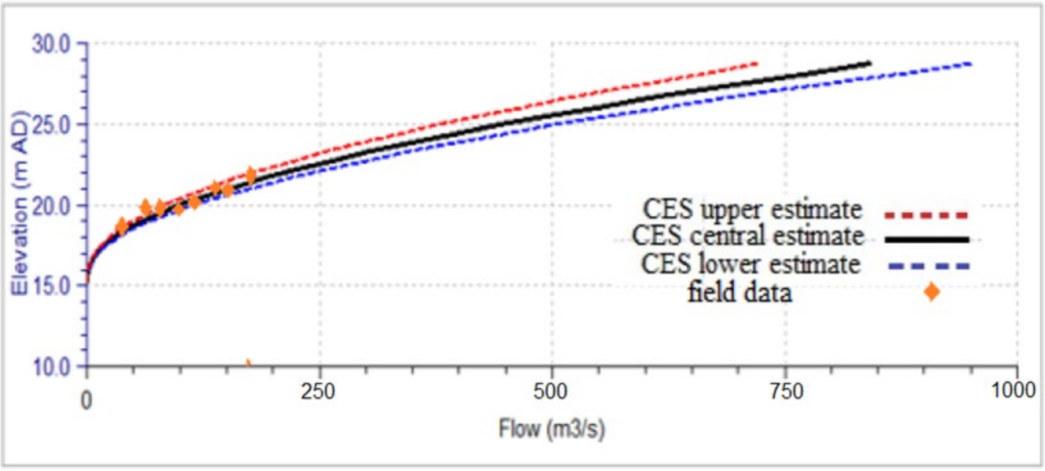

Figure 8. CES stage-discharge curve for CS5.

The findings of the CES were compared to the field data in the study's cross-sections (CS1 and CS5). These cross-sections were selected because field data is available on the water level and the discharge. Figure 4 illustrates that the computed and measured data match and that the field data falls within the uncertainty limits. Additionally, the uncertainty ranges are displayed. However, it is getting closer and closer to the maximum allowed. Figure 8 illustrates the distribution and trend of field data in comparison to the stage-discharge curve predicted for CS5.

On the other hand, the data collected in the field are located inside the uncertainty ranges and are thus much closer to the central estimate. The simulations demonstrate that the CES model can generate a curve of stage-discharge agree with the findings obtained in the field. According to the data presented, an increase in the forecasted roughness value leads to increase in both the water level and discharge, and vice versa. Despite some inconsistencies throughout the process at various phases, the CES model produced satisfactory results. Exploring the possibility of a better cross-sectional description of roughness leads to an accurate estimate of the discharge data and the water depth, which in turn helps make informed decisions in water management, particularly in the irrigation sector and other water uses, especially in areas where water is scarce.

3.2. Statistical Analysis

The Bias, Mean Absolute Error (MAE), and Nash–Sutcliffe Efficiency (NSE) are three statistical indicators used to assess the accuracy of the model results. These indicators were calculated using the following equations:

$$BIAS = \frac{1}{N}\sum_{i=1}^{N}(X_{estimate} - X_{field}) \tag{8}$$

$$MAE = \frac{1}{N}\sum_{i=1}^{N}\left|X_{estimate} - X_{field}\right| \tag{9}$$

$$NSE = 1 - \left[\frac{\sum_{i=1}^{N}\left(X_{field} - X_{estimate}\right)^2}{\sum_{i=1}^{N}\left(X_{field} - X_{field}\right)^2}\right] \tag{10}$$

$X_{estimate}$ and X_{field} denote the estimated and field values, respectively, while the number of measured data is represented by N. The best value for $BIAS$ is 0; positive values indicate a propensity to overpredict, while negative values indicate a tendency to underpredict the actual values observed. $BIAS$ evaluates the tendency of the anticipated values to be larger or smaller than their actual values. An ideal fit is denoted by a mean absolute error value of zero. Came up with the concept of the NSE, which demonstrates how well the plot of observed values vs. anticipated values follows the 1:1 line (line of perfect agreement) [25]. The number 1 represents the NSE that is ideal. However, acceptable performance levels are often between 0 and 1. In contrast, levels below 0 imply that the mean observed value is a better predictor than the simulated value, which indicates undesirable performance [26]. This suggests using this indication.

The statistical assessment of anticipated values for chosen cross-sections is presented in Table 2. The estimated NSE, MAE, and $BIAS$ values revealed acceptable agreement between the central rating curve and the field one.

Table 2. The statistical evaluation.

Cross section	Stage		
	NSE	MAE	$BIAS$
1	0.86	0.013	0.0011
5	0.91	0.053	0.00021

4. Conclusions

The estimated central rating curve and the field one agreed reasonably well, though a slight difference was noted at some stages. This subtle difference was caused by the significant variation of hydraulic and geometric values measured in the field. Good estimation at the stage and acceptance at discharge result from an adequate resistance coefficient. This study concluded that the CES model could be used as an estimation tool for the water engineering field to help in making informed decisions regarding the policies for designing and operating water systems, especially in rivers that are subject to continuously changing the roughness of the sections due to seasonal changes as well as changing the nature of flow in those rivers. It was also recommended to test the model in rivers that suffer from severe meandering to demonstrate its validity for use in those rivers.

References

1. Al-Yousefi, H.A., Kadhem, A.A., Alasadi, L.A.R. Effect of upstream side slope of crump weir on discharge coefficient. Kufa Journal of Engineering. 2024. 15(4). Pp. 69–77. DOI: 10.30572/2018/KJE/150404
2. Ferguson, R. Flow resistance equations for gravel- and boulder-bed streams. Water Resources Research. 2007. 43(5). Article no. W05427. DOI: 10.1029/2006WR005422
3. Bathurst, J.C. At-a-site variation and minimum flow resistance for mountain rivers. Journal of Hydrology. 2002. 269(1–2). Pp. 11–26. DOI: 10.1016/S0022-1694(02)00191-9
4. Manfreda, S. On the derivation of flow rating curves in data-scarce environments. Journal of Hydrology. 2018. 562. Pp. 151–154. DOI: 10.1016/J.JHYDROL.2018.04.058
5. Alasadi, L.A.R., Khlif, T.H., Hassan, F.A. Experimental investigation for the local scour around V-shaped spur-dikes. Scientific Review Engineering and Environmental Sciences. 2023. 32(1). Pp. 69–86. DOI: 10.22630/srees.4506
6. Williams, M.R., Penn, C.J., King, K.W. Hydrologic pathways and nutrient loading in the headwaters of the Western Lake Erie Basin. Journal of Hydrology: Regional Studies. 2025. 58. Article no. 102275. DOI: 10.1016/J.EJRH.2025.102275
7. Al-Abadi, A.M. Modeling of stage–discharge relationship for Gharraf River, southern Iraq using backpropagation artificial neural networks, M5 decision trees, and Takagi–Sugeno inference system technique: a comparative study. Applied Water Science. 2016. 6. Pp. 407–420. DOI: 10.1007/s13201-014-0258-7
8. Chen, B., Lu, Y., Imran, M., Adam, N.A., Jang, J. Evaluating and transferring social value of ecosystem services in urban wetland parks using the SolVES model. Ecological Indicators. 2025. 172. Article no. 113270. DOI: 10.1016/J.ECOLIND.2025.113270
9. Galarza, J.S.C., Castro, L.M.T., Alvarado, E.P.S., Martínez, A.O.A. On the Effect of the Refinement of the Roughness Description in a 2D Approach for a Mountain River: a Case Study. La Granja. 2021. 33(1). Pp. 91–102. DOI: 10.17163/LGR.N33.2021.08
10. Blair, T. Stage discharge estimation using a 1d river hydraulic model and spatially-variable roughness (T). University of British Columbia. Vancouver, 2009. VIII + 64 p. DOI: 10.14288/1.0068608
11. Nguyen, T.T.H., Vu, D.Q., Doan, N.P., Chi, H.T.K., Li, P., Binh, D.V., An, Y., Dung, P.T., Hoang, T.A., Son, M.T. Reconstructing suspended sediment concentrations in the Mekong River Basin via semi-supervised-based deep neural networks. Science of the Total Environment. 2024. 955. Article no. 176758. DOI: 10.1016/J.SCITOTENV.2024.176758
12. Xu, H., Wang, H., Liu, P., Zhang, X., Liu, W., Zhou, C., Ye, H., Lei, H., Liu, Y. What is the near-natural catchment? An application of hydrological signatures assessment. Ecological Indicators. 2025. 171. Article no. 113209. DOI: 10.1016/J.ECOLIND.2025.113209
13. Havaei, M.A., Malekitabar, H. Spherical sustainability in construction and demolition: How aligned are policies, goals, regulations, markets, and stakeholder mindsets? Cleaner Environmental Systems. 2025. 16. Article no. 100256. DOI: 10.1016/J.CESYS.2025.100256
14. Mihalakakou, G., Paravantis, J.A., Nikolaou, P., Menounou, P., Tsangrassoulis, A.E., Malefaki, S., Fotiadi, A., Papadaki, M., Giannakopoulos, E., Romeos, A., Escobar-Hernandez, H.U., Souliotis, M. Earth-sheltered buildings: A review of modeling, energy conservation, daylighting, and noise aspects. Journal of Cleaner Production. 2024. 472. Article no. 143482. DOI: 10.1016/J.JCLEPRO.2024.143482
15. Stelmaszczyk, P., Białkowska, K., Wietecha-Posłuszny, R. Paper-supported polystyrene membranes for micro-solid phase extraction of date-rape drugs from urine: A sustainable analytical approach. Analytica Chimica Acta. 2024. 1316. Article no. 342874. DOI: 10.1016/J.ACA.2024.342874
16. Maatooq, J., Hameed Alwaeli, L. Estimation of reliable Stage-Discharge Curve in meandering river using Conveyance Estimation System (CES) Model. IOP Conference Series: Materials Science and Engineering. 2020. 737. Article no. 012149. DOI: 10.1088/1757-899X/737/1/012149
17. Renfrew, D., Vasilaki, V., Katsou, E. Indicator based multi-criteria decision support systems for wastewater treatment plants. Science of The Total Environment. 2024. 915. Article no. 169903. DOI: 10.1016/J.SCITOTENV.2024.169903

18. Armenta-Castro, A., Núñez-Soto, M.T., Rodriguez-Aguillón, K.O., Aguayo-Acosta, A., Oyervides-Muñoz, M.A., Snyder, S.A., Barceló, D., Saththasivam, J., Lawler, J., Sosa-Hernández, J.E., Parra-Saldívar, R. Urine biomarkers for Alzheimer's disease: A new opportunity for wastewater-based epidemiology? Environment International. 2024. 184. Article no. 108462. DOI: 10.1016/J.ENVINT.2024.108462
19. Rataj, O., Alcorta, L., Raes, J., Yilmaz, E., Riccardo, L.E., Sansini, F. Sustainability vs profitability: Innovating in circular economy financing practices by European banks. Sustainable Production and Consumption. 2025. 53. Pp. 1–16. DOI: 10.1016/J.SPC.2024.11.025
20. Dietzel, M., Boch, R. Precipitation of $CaCO_3$ in natural and man-made aquatic environments – Mechanisms, analogues, and proxies. Geochemistry. 2024. 84(4). Article no. 126206. DOI: 10.1016/J.CHEMER.2024.126206
21. World Meteorological Organization (WMO). Technical Regulations. Basic Documents No. 2. Volume III – Hydrology. WMO. Geneva, 2002. 40 p. URL: https://library.wmo.int/records/item/35631-technical-regulations (reference date: 16.07.2025).
22. Alasadi, L.A.R., Albahrani, H.S., Alwaeli, L.K. Parametric Study for Design and Analysis of Box Culvert by Using Newton's-Raphson Method and MATLAB Software. Key Engineering Materials. 2020. 870. Pp. 11–19. DOI: 10.4028/www.scientific.net/KEM.870.11
23. Lang, M., Pobanz, K., Renard, B., Renouf, E., Sauquet, E. Exptrapolation des courves de tarage par modélisation hydraulique, avec application à l'analyse fréquentielle des crues [Extrapolation of rating curves by hydraulic modelling, with application to flood frequency analysis]. Hydrological Sciences Journal. 2010. 55(6). Pp. 883–898. DOI: 10.1080/02626667.2010.504186
24. Hamilton, S. Maynard, R., Kenney, T. Comparative Investigation of Canadian, US, and Australian Stage-Discharge Rating Curve Development. Australian Hydrographers Association. Canberra, 2016. 24 p.
25. Fisher, K.R., Dawson, F.H. Reducing Uncertainty in River Flood Conveyance: Roughness Review. Project W5A-057 – DEFRA Flood Management Division & Science Directorate, & Environment Agency. 2003. 204 p.
26. Nash, J.E., Sutcliffe, J.V. River flow forecasting through conceptual models part I – A discussion of principles. Journal of Hydrology. 1970. 10(3). Pp. 282–290. DOI: 10.1016/0022-1694(70)90255-6
27. ASCE Task Committee on Definition of Criteria for Evaluation of Watershed Models of the Watershed Management Committee, Irrigation and Drainage Division. Criteria for Evaluation of Watershed Models. Journal of Irrigation and Drainage Engineering. 1993. 119(3). Pp. 429–442. DOI: 10.1061/(ASCE)0733-9437(1993)119:3(429)

Information about the author:

Layth Abdulrasool Alasadi, *Doctor of Engineering*
ORCID: https://orcid.org/0000-0001-6244-7965
E-mail: laitha.alasadi@uokufa.edu.iq

Tagreed Hameed Khlif,
ORCID: https://orcid.org/0000-0002-0429-796X
E-mail: tagreedh.alabedi@uokufa.edu.iq

Fadhel Abdulabbas Hassan,
ORCID: https://orcid.org/0000-0003-1020-5133
E-mail: fadhil.alshitali@uokufa.edu.iq

Received 15.02.2023. Approved after reviewing 19.10.2023. Accepted 30.01.2025.

Magazine of Civil Engineering. 2025. 18(3). Article No. 13510

Magazine of Civil Engineering

ISSN
2712-8172

journal homepage: http://engstroy.spbstu.ru/

Research article
UDC 697.92
DOI: 10.34910/MCE.135.10

Characteristics of flow in the unit “elbow - supply opening”

***J.R. Kareeva*[1] ✉ , *A.M. Ziganshin*[1] , *K.I. Logachev*[2] , *K.A. Narsova*[1]**

[1] *Kazan State University of Architecture and Engineering, Kazan, Russian Federation*

[2] *Belgorod State University named after V.G. Shukhov, Belgorod, Russian Federation*

✉ *jkareeva2503@gmail.com*

Keywords: supply jet, unit “elbow - supply opening”, numerical study, vortex zones

Abstract. The existing literature provides formulas for standard air distribution calculations. However, the calculation coefficients are obtained experimentally for the ideal conditions of connecting air terminal devices. distributors to ducts. In practice, the design of the connection depends on the complexity of the ductwork in the building. This may affect the jet flow conditions and the air circulation in the room. The article considers the flow in the unit “elbow - supply opening” of the ventilation system. The aim of the study is to determine the dependence of the geometric and kinematic characteristics of the jet on the distance between the elbow and the supply opening. The problem is solved numerically in a two-dimensional formulation using the Fluent software package. A combination of the standard k-ε model and standard near-wall functions is used for the solution. As a result, the distribution of velocity and pressure at the outlet of the air terminal device is obtained. The dependences of the variation of the axis slope and axial velocity of the jet, as well as the kinematic coefficient of the supply opening on the distance between the elbow and the supply opening are constructed. The significant influence of the distance between the elbow and the supply opening in the unit on the kinematic characteristics of the jet is shown. The obtained dependencies should be taken into account when calculating air distribution. At distances between the elbow and the supply opening of more than 5 gauges, the characteristics of the jet tend to the characteristics of the jet flowing from the end opening.

Funding: The research was supported by the Tatarstan Academy of Sciences grant within the framework of the state program of the Republic of Tatarstan “Scientific and technological development of the Republic of Tatarstan”.

Citation: Kareeva, J.R., Ziganshin, A.M., Logachev, K.I., Narsova, K.A. Characteristics of flow in the unit “elbow - supply opening”. Magazine of Civil Engineering. 2025. 18(3). Article no. 13510. DOI: 10.34910/MCE.135.10

1. *Introduction*

The air quality in the working zone of the room and the energy consumption for the equipment operation determine the efficiency of the ventilation and air conditioning system. The existing methods of calculation of the air distribution in the room determine the main characteristics of the jet flowing from the supply opening, taking into account the influence of geometric characteristics of the grille through the known values of the kinematic (m) and thermal (n) coefficients. However, almost all coefficients m and n from the reference literature were determined experimentally with an ideal connection of the supply air device (AD) – at the end of a straight duct at a distance of at least 3 gauge with an equalizer or 20 gauge without it[1]. In practice, the specific design of the connection of the supply grille to the duct depends on technological necessity and the ductwork's tracing. ADs are often located on the side wall of the duct or at the end but immediately behind the 90° elbow. In this case, the distance from the elbow to the supply AD can be very small, which significantly changes the flow conditions and, therefore, the kinematic characteristics of the supply jet, which, in turn, results in a change in the air distribution in the room.

The parameters of supply jets flowing from different kinds of openings have been investigated for quite a long time. The analytical relationship between the axial velocity, the distance from the supply opening, and the distribution of the longitudinal velocity component in the cross-sections of the jet were obtained in [1, 2]. In [3], hot-wire anemometers and static pressure probes were used to experimentally obtain and generalize data on the distribution of static pressure and velocity, both axial and in the cross-sections of the jet, and in [4], shadowgraph technique was used. Nowadays, jets are constantly investigated using modern and detailed experimental methods. Particle image velocimetry (PIV) was used to determine the axial velocity and turbulence characteristics of the jet as it moved away from the supply opening [5, 6]. The numerical methods for such investigations are widely used. The influence of initial profiles of velocity and turbulence parameters on supply jet characteristics was studied in [7]. The obtained results were proposed to be used in the design of supply ADs. Studies [8, 9] were aimed at controlling the velocity profile of supply jets using screens.

Fewer works consider the parameters of the jet flowing at a non-frontal air supply. Obviously, with such air supply, the profile of the kinematic parameters at the outlet will be significantly irregular and asymmetric. This, in turn, results in differences in the kinematic characteristics of the jet development. The flows from openings of different geometry were studied in [1]. It was shown that the jet profile strongly depended on the velocity profile at the outlet. The length of the initial section changed, as well as the attenuation of the axial velocity. In [10], a flow from a slotted opening located in a duct wall was considered in the presence of a transit flow passing in the channel. This flow significantly distorted the profiles of the kinematic characteristics of the jet at the outlet. The distribution fields of longitudinal and transverse velocity and the static pressure fields, as well as velocity irregularity, were obtained by numerical method, and it was established that the static pressure was not equal to 0. These factors must be taken into account when calculating jet momentum and its kinematic and thermal characteristics. In [11, 12], the results of numerical studies of the flow from the last and middle lateral openings were given, and the relationship between the jet inclination angle and the relative flow velocity of the outflowing air (for the middle opening) and the relative size of the opening (for the last opening) were numerically found. A significant irregularity of velocity and pressure profile in the opening was shown, which apparently led to changes in the kinematic coefficient and the coefficient in the Reichardt exponential formula for the velocity profile in the cross-sections of the jet.

The studies of outflow from real air distribution devices are often conducted numerically [13, 14] and experimentally [15, 16], or both [17, 18], and may refer to very complex problems, such as ventilation in case of a fire in buildings [19] or the implementation of information modeling [20]. Fewer studies consider the influence of different connection options. In [21], numerical and experimental studies of the velocity distribution in the plenum box and at the AD outlet were carried out for the top and side of the plenum box. It was shown that, despite the presence of the plenum, there was a significant irregularity of velocity at the outlet of the AD, and as a consequence, the outflowing jet is deformed. The characteristics of jets flowing out of near-wall ADs were experimentally studied in [22], the velocity profiles and velocity distribution along the length were determined, taking into account the overlap on impermeable surfaces. The influence of the presence of impermeable surfaces on the jet characteristics was shown. Air distribution in a room using ceiling-mounted ADs was considered in [23], and the velocity fields were found experimentally and numerically. Using attaching to vertical surfaces – walls [24] and columns [25] – new ways of ventilation in various rooms were developed [26–28]. Although the parameters of supply jets are studied in the cited works, in most cases, the flow from end openings is considered, and no attention is paid to the change of jet parameters at the non-frontal air supply. For cases of individual ventilation, air distribution through side openings in channels is typically used, for example, in case of the underfloor air distribution system [29]. However, even in such works, the way air inflows into supply openings is often not taken into account.

In [30–32], the characteristics of a jet flowing from the opening, which is located immediately behind the 45° and 90° elbow, were considered. The influence of the distance between the elbow and the supply opening on the distribution of velocity and pressure components was studied at the supply opening cut, on the slope of the outflowing jet, and on the distribution of axial velocity. It was shown that the considered influence was rather significant, and a vortex zone was formed at some distances. The obtained results showed that the close location of elbows at 45° and 90° significantly affected the jet characteristics. In this

---

[1] European Committee for Standardization (CEN). Ventilation for buildings – Air terminal devices – Aerodynamic testing and rating for mixed flow application. EN 12238:2001. Brussels, 2001. 36 p.

case, a “non-frontal” air supply to AD was realized, which distorted the kinematic characteristics of the jet and resulted in their difference from the characteristics of the jet flowing from the end opening. Such flows remain practically unexplored.

It should be noted that in [31], the default values for turbulent parameters k = 1, ε = 1 were chosen for modeling free boundaries. Further numerical studies have shown that when air flows through the free boundary with very low velocities, the values of the turbulent characteristics are also close to zero, which may affect the calculation results. Therefore, numerical calculations are carried out with minimum values of k and ε equal to 0.

The presence of an elbow or other perturbing element leads to the distortion of flow parameters within the channel. The extent, to which this distortion affects the flow characteristics at the supply opening, depends on the distance l between the perturbing element and the supply opening. The first step to gaining a comprehensive understanding of this process and eliminating the influence of the air distribution system design is to investigate the elbow’s effect on the characteristics of the jet emerging from a free opening. Thus, this article aims to determine how the distance between the elbow and the supply opening influences the geometric and kinematic properties of the jet.

The following tasks are undertaken to achieve set aim:

- to develop numerical models of the “elbow - supply opening” unit and conduct a mesh convergence study;
- to determine the pressure distribution and velocity components at the supply opening cross-section;
- to analyze the dependence of the jet parameters on the distance between the supply opening and the elbow.

2. *Materials and Methods*

The problem has been solved numerically in two-dimensional formulation using the computational fluid dynamics (CFD) software package. The geometry of the investigated area is presented in Fig. 1: b_0 = 0.1 m is the width of the duct; L = 2.7 m is the width of the area; H = 2 m is the height of the area, is the distance from the elbow to the cross-section of the supply opening**,** which is measured relative to the ***BC'*** wall. The model with following different distances between the supply opening and the elbow were considered: l, m (l/b_0) = 0.05 (0.5); 0.1 (1.0); 0.15 (1.5); 0.2 (2.0); 0.25 (2.5); 0.3 (3.0); 0.5 (5.0); 0.6 (6.0); 0.7 (7.0); 0.8 (8.0) and 3.5 (35). The velocity at the supply boundary into the channel ***AB*** is given by a uniform profile with v_0 = 3 m/s. At the remote boundaries of the areas ***BG***, ***GK***, ***KI***, and ***IE****,* the pressure inlet boundary condition (BC) is used with set values of overpressure equal to zero and turbulent characteristics k and ε equal to 0. Impermeable boundaries ***AF***, ***FD***, and ***BC'C*** are simulated by means of wall BC, where the conditions of non-flow and non-slip are accepted.

The verification and validation of the problem of a flow in supply opening with elbow unit was carried out in [33]. Different combinations of turbulence models with wall functions were studied. The combinations of standard $k-\varepsilon$ model (SKE) with standard nonequilibrium wall functions (SWF, NEWF) and enhanced wall treatment (EWT); the $k-\varepsilon$ renormalized groups model (RNGKE), standard $k-\omega$ (SKW), $k-\omega$ SST (SSTKW); and the Reynolds stress model (RSM) combined with SWF, NEWF, and EWT was considered. The comparison of experimental and numerical studies with each other has shown that the combination of the SKE and SWF is the most appropriate for the considered problem and will be used further.

When studying the variant with flow from an opening located at a small distance from the elbow, an additional question arises about the possible influence of the impermeable boundary ***BC'*** (Fig. 1a) on the conditions of airflow to the flowing jet and its further development. Since the problem is solved in a two-dimensional formulation, the flow around the vertical channel (including the ***BC'*** boundary) is impossible, and, accordingly, the flow to the supply will occur differently. To investigate the degree of influence, a test numerical model (free) was created for the distance l/b_0 = 1.5. In this model, a border ***B'C'*** inclined at a small angle was created along the impermeable wall ***BC'***, for which the pressure outlet BC was set, thus simulating the permeable boundary (Fig. 1b), BC on the other boundaries is identical to the original problem (solid).

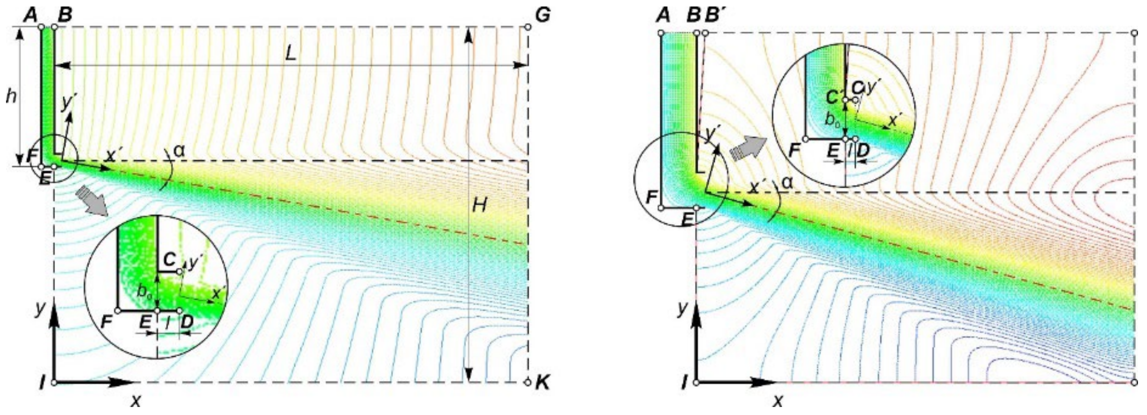

a) b)

Figure 1. Geometry and streamlines of the investigated flow: a) initial problem (solid); b) problem with permeable boundary *B′C′* (free).

It can be seen that, in the first case, the airflow to the jet from the surrounding space is limited and occurs only through the upper boundary along the impermeable wall. In the second case, air flows into the considered zone perpendicular to all permeable boundaries, which is more physical, but complicates the computer model. However, visually, the streamlines in the main area of jet development differ only slightly. Therefore, the need for such a model can be assessed by the degree of influence on the characteristics under study. For example, it is known from [10] that the jet development is influenced by the flow conditions, namely the distribution of velocity $\left(v_x/v_0,\ v_y/v_0\right)$ and pressure $\left(P_{st}/P_d\right)$ components (Fig. 2a) at the supply opening cut, as well as differences in the shape of the jet axis (Fig. 2b), here v_0 is the mean flow velocity in the channel equal to the velocity at the ***AB*** boundary, v_x, v_y are the longitudinal and transverse velocity components, respectively, $P_d = \rho v_0^2/2$ is the dynamic pressure.

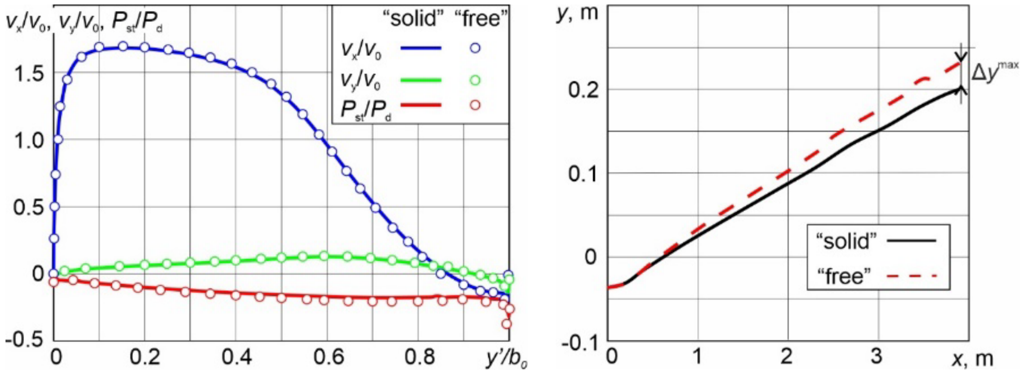

a) b)

Figure 2. Flow characteristics for two problems: a) variation of relative longitudinal, transverse velocity, and static pressure components for straight wall and straight wall with addition of permeable region; b) jet axis for straight wall and straight wall with addition of permeable region.

It can be seen that the distribution of relative velocity and pressure components (Fig. 2a) are different for the considered problems, but the maximum differences are: $\Delta v_x^{\max}$ = 0.9 %, $\Delta v_y^{\max}$ = 1 %, $\Delta P_{st}^{\max}$ = = 3 %. When analyzing the shape of the jet axis, it can be seen that the difference is not significant, and the maximum value is $\Delta y^{\max}$ = 15 % (Fig. 2b).

Thus, the presence of an impermeable boundary, for the case of a small distance from the elbow to the supply opening, leads to some insignificant differences in the jet characteristics during its development. This difference is slightly larger when considering the jet characteristics directly at the outflow. At the same time, it is clear that with increasing distance between the elbow and supply opening, the differences will decrease; therefore, it can be ignored, and the modeling can be carried out according to the solid variant.

When analyzing the velocity profile at a cut of the supply opening, it can be seen that its significant part is occupied by the vortex zone, which is formed when the flow comes off the sharp edge of the elbow and at such a small distance, does not have time to close on the duct wall. This zone leads to peculiarities and deformations of the supply jet development. Therefore, to assess the influence of the distance between the elbow and the supply opening $\left(l/b_0\right)$ on the jet development, the change of parameters at the supply opening cut and along the jet length is investigated when the distance l/b_0 changes from 0.5 to 35.

The profiles of relative longitudinal v_x/v_0 and transverse v_y/v_0 components of velocity and static pressure P_{st}/P_d are investigated at the supply opening cut in comparison with the symmetric profile of the outflow from the end opening without elbow. The presence of a vortex zone at the upper boundary of the region reduces the effective flow cross-section b_{eff}, the upper boundary of which was calculated from the coordinate, where v_{mag} = 0, when going from a negative value to a positive one.

Several quantities will be used to determine the effect of the elbow on the flow. Since the asymmetry of the velocity profile with respect to the channel axis is considered, it is logical to use the flow rates in the upper $\left(L_u\right)$ and lower $\left(L_d\right)$ parts of the channel. The flow rate is the integral of the velocity over the channel width and it represents the area under the velocity profile curve plotted over the channel cross-section. Then, the asymmetry coefficient k_{as} can be defined as the ratio of the difference of flow rates in the upper and lower parts to the total flow rate in this section. The flow rates are determined from the numerical determination of the velocity field:

$$L_u=\sum_{i=N}^{2N-1} v_i\left(\left(y/b\right)_{i+1}-\left(y/b\right)_i\right);\;\; L_d=\sum_{i=0}^{N-1} v_i\left(\left(y/b\right)_{i+1}-\left(y/b\right)_i\right).$$

Then, the asymmetry coefficient is

$$k_{as}=\frac{\left(L_u-L_d\right)}{\left(L_u+L_d\right)}. \tag{1}$$

Moreover, in [1], coefficients are used to estimate the irregularity of the velocity profile:

$$\text{Boussinesq}-\beta_0=\frac{\left(v_0^2\right)_{av}}{v_{0,av}^2}; \tag{2}$$

$$\text{Coriolis}-\alpha_0=\frac{\left(v_0^3\right)_{av}}{v_{0,av}^3}; \tag{3}$$

$$\text{Velocity fields}-k_0=\frac{v_{av}}{v_{ax}}, \tag{4}$$

where $v_{av}=\frac{1}{2N}\sum_{i=0}^{2N-1} v_i$ is the average velocity in the section; $\left(v_0^2\right)_{av}=\frac{1}{2N}\sum_{i=0}^{2N-1} v_{0,i}^2$ is the mean square of velocities in the section; $v_{0,av}^2=\left(\frac{1}{2N}\sum_{i=0}^{2N-1} v_{0,i}\right)^2$ is the square of the mean velocities in the section, $\left(v_0^3\right)_{av}=\frac{1}{2N}\sum_{i=0}^{2N-1} v_{0,i}^3$ is the mean cube of velocities in the section; $v_{0,av}^3=\left(\frac{1}{2N}\sum_{i=0}^{2N-1} v_{0,i}\right)^3$ is the cube of the mean velocities in the section.

The jet development can be characterized by several values. The variation of these values from that for the jet flowing from a straight channel shows the degree of influence of a nearby elbow. In this work, the inclination angle of the jet axis α is considered; the axial velocity distribution v_{ax}/v_m, the kinematic coefficient m, which is used in the practice of air distribution calculations to describe the jet attenuation. Moreover, the dependences on l/b_0 as the effective width of the supply opening (the width of the opening occupied by the outgoing flow, b_{eff}/b_0), the shape of vortex zones will be defined.

The jet axis is found as the point of maximum value of the velocity modulus. Since the axis is bent at the initial section, for each problem, the main section of the jet is found as a part where the axis is practically straight. The coefficient of variation $CV = \sqrt{\left(x-\overline{x}\right)^2/\left(n-1\right)}$, at this part (where x is the average value of the angle for the sample, and n is the sample size), when determining the average value of the jet angle does not exceed 20 %, and further its angle of inclination α to the geometrical (horizontal) axis passing through the center of the supply opening and counted counterclockwise. The kinematic coefficient m is determined from the results of numerical modeling by the axial velocity distribution:

$$m = \frac{v_{ax}^{mag}}{v_0} \cdot \frac{\sqrt{s}}{\sqrt{b_0}}, \tag{5}$$

where $s = x \cdot \cos\alpha$ (m) is the distance along the jet axis from the supply opening cut; v_{ax}^{mag} (m/s) is the axial velocity modulus at a distance s.

3. Results and Discussion

The numerical modeling was carried out for models with the distance between the elbow and the supply opening varying in the range l/b_0 = 0.5 ÷ 8.0. The design with the distance l/b_0 = 35 was accepted as a model, in which the influence of the elbow is small. Fig. 3 shows the streamlines for all investigated geometries. Fig. 4a shows the variation of the axis trajectory as a function of distance l/b_0. At distances l/b_0 = 0.5; 1.0; 1.5, it can be seen that the flow cut off from the sharp edge of the elbow is not closed on the channel wall. The resulting area of reduced pressure not only causes circulation of the main flow in the channel but also leads to the ejection of ambient air, drawing it from the outer area inside the supply channel (Fig. 3a–c) and significantly distorts the flow pattern. In addition, it can be seen that for the smallest distances l/b_0 = 0.5 and 1, the inclination angle has a negative value – the jet axis is directed downwards (Fig. 4a). The negative angle of jet inclination is due to the fact that the small size of the elbow does not allow the flow in the channel to fully complete the 90° turn from vertical to horizontal direction. The jet is formed under the influence of the vertical velocity component directed downwards. For distances $1 < l/b_0 \le 7$, the flow pattern begins to change qualitatively – this elbow length becomes sufficient for the flow to change its direction from vertical to horizontal. At the same time, the impact of the flow against the lower wall of the elbow and insufficient length of the upper wall leads to the opposite effect, and the jet leaves the supply directed upwards (Fig. 3c–i, Fig. 4a). Since the vertical component, in this case, is significantly smaller, the angle of inclination relative to the horizontal is also small (~ 4°, Fig. 4b). It can be seen, that the jet itself visually becomes more symmetrical as l/b_0 increases, and the angle of inclination of the jet axis becomes closer to the horizontal – the geometric axis (Fig. 4a). For l/b_0 > 7, it can be seen that the outlines of the vortex zone cease to change. It is difficult to distinguish such a jet from a jet flowing without the influence of the elbow.

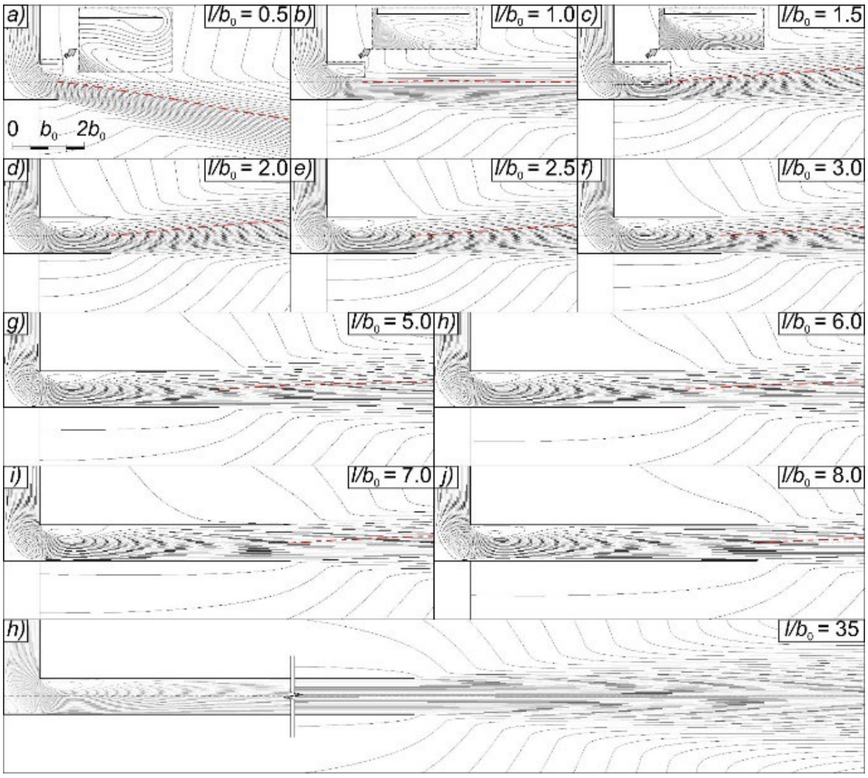

Figure 3. Flow lines for the investigated geometries.

Fig. 4a shows that at l/b_0 = 7, the axis trajectory is not yet horizontal, and the angle of deviation of the axis from the horizontal is small, but greater than 0 (Fig. 4b), and further tends to 0 at l/b_0 = 35. The shape of the axis is almost rectilinear at distances 2 ≤ x/b_0 ≤ 40.

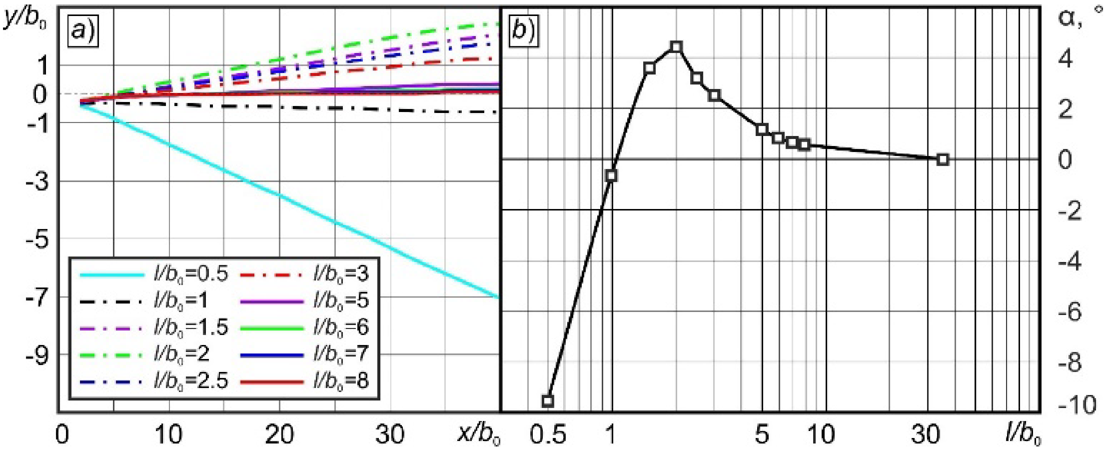

Figure 4. a) flow axis, b) angle of axis deviation from the horizontal.

Fig. 5 shows vortex zones occurring at l/b_0 ≥ 2 at the studied unit (marked as *elbow & supply*). Outlines of vortex zones in a unit are compared with the outlines of the vortex zones occurring in a single elbow (marked as *single elbow*) found analytically using the conformal mapping method and the potential flow theory in [34] (marked as *An. calc.*), experimentally in [35] (marked as *Exp.*), and numerically using CFD methods in [36] (marked as *CFD*). It is possible to confirm the adequacy of the numerical study and further to investigate the influence of closely coupled elbow fittings on the shape of vortex zones (Fig. 5).

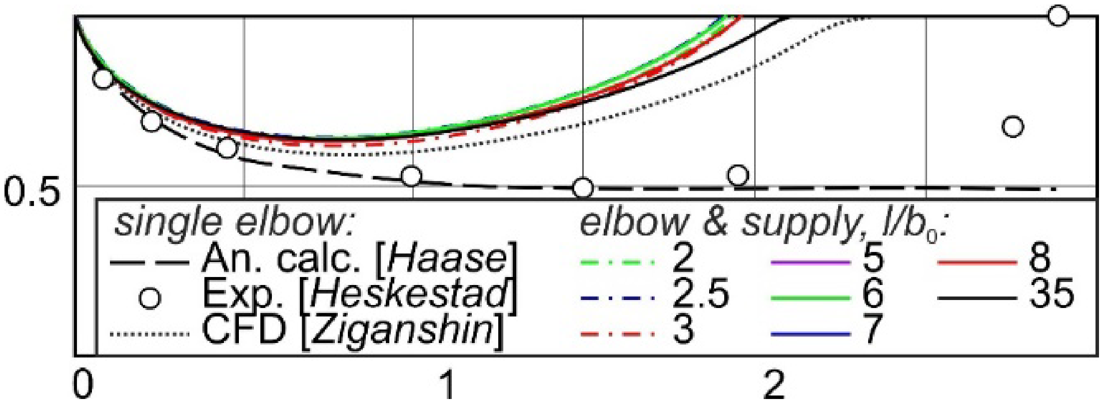

Figure 5. Outlines of vortex zones in an elbow.

It can be seen from Fig. 5, that for l/b_0 ≥ 2, the vortex zones outlines depend weakly and ambiguously on the distance between the elbow and the supply opening, because the elbow is upstream of the supply opening. It can also be noted that the outline of the vortex zone agrees well with other outline studies for a single elbow. Good agreement indicates that there is no upstream influence of the supply opening at distances greater than two gauges.

Next, a more detailed analysis of the effect of the distance from the elbow to the supply opening on velocity (components v_x/v_0, v_y/v_0, and module v_{mag}/v_0) and static pressure $\left(P_{st}/P_d\right)$ at the cut of the supply opening and along the length of the jet is performed.

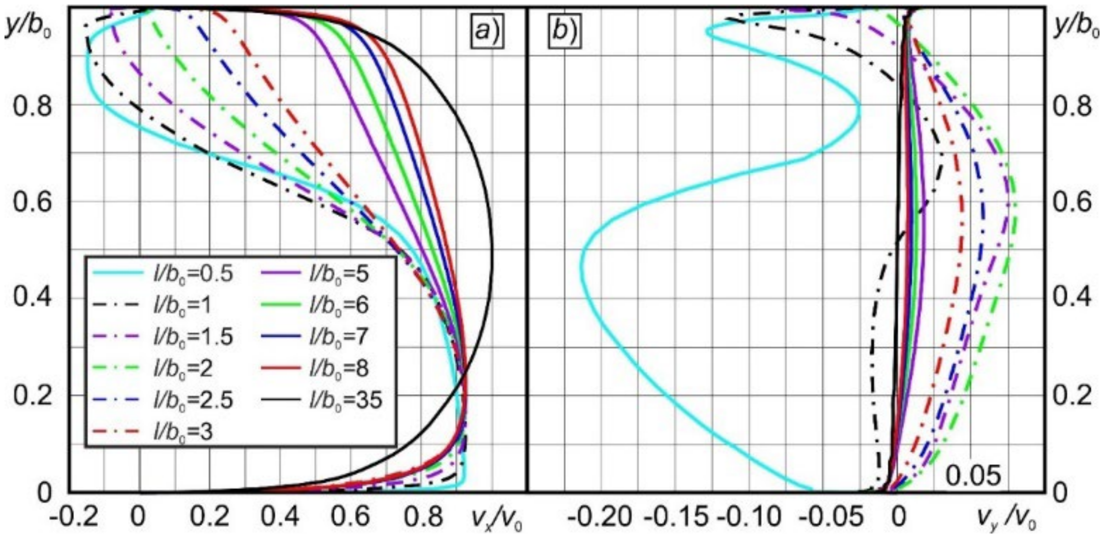

Figure 6. Distribution of components of longitudinal v_x/v_0 (a) and transverse velocity v_y/v_0 (b) of the flow at the supply cut for variation of l / b_0 = 0.5 ÷ 35.

Fig. 6 shows the variation of dimensionless longitudinal v_x/v_0 and transverse v_y/v_0 velocity components in the supply opening cut at different distances from the elbow. It can be seen that for l/b_0 < 8, the longitudinal velocity profiles v_x/v_0 remain irregular, implying that there is an influence of the elbow. For distance l/b_0 = 35, it can be seen that there is no such influence, and the velocity profile is symmetrical about the centerline. The longitudinal components also indicate the presence of a vortex zone – for distances l/b_0 ≤ 1.5, a region with negative values is observed.

The profile of the transverse velocity component in all sections considered is also irregular. However, it is more difficult to judge the size of the vortex zone from these profiles. The profiles at l/b_0 < 1.0, where the region with v_x/v_0 < 0, occupies a large part of the cross-section and practically coincides with the corresponding regions of the longitudinal velocity profiles v_x/v_0, are clearly highlighted. For distances

l/b_0 > 5, the values v_y/v_0 tend to 0, and the jet is equalized. Only a small deviation in the near-wall region, typical for a boundary layer flow, is observed.

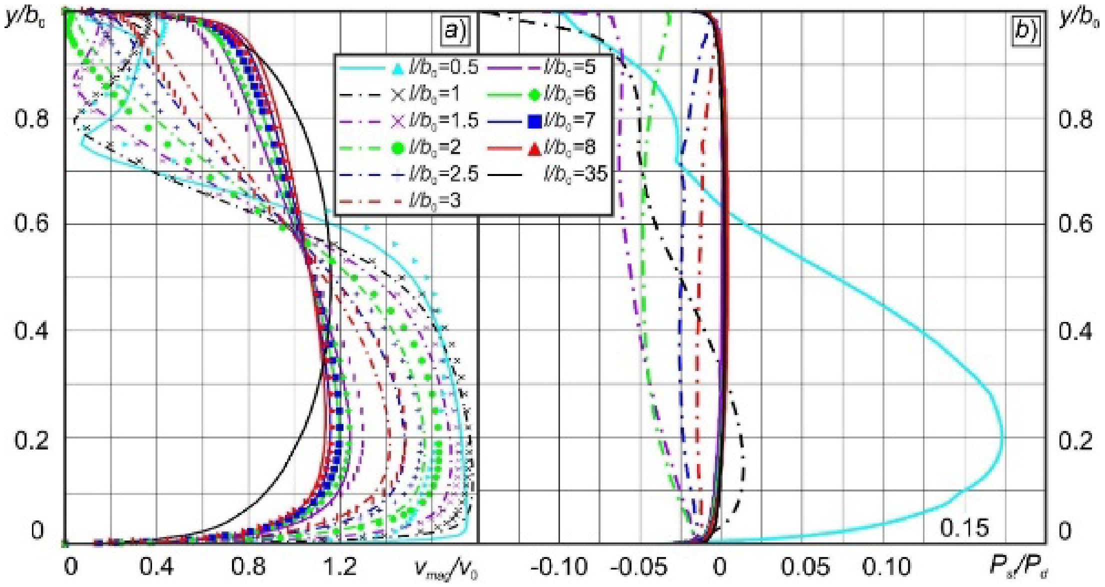

Figure 7. Distribution of relative velocity modulus v_{mag}/v_0 (a) and static pressure P_{st}/P_d (b) at the outflow for distances l/b_0 = 0.5 ÷ 35.

The profiles of the distribution of the relative velocity modulus $\left(v_{mag}/v_0\right)$ (Fig. 7a) show the presence of a vortex zone and demonstrate the influence of the elbow as a perturbing element. This influence can be seen from the analysis of the distribution symmetry of v_{mag}/v_0 relative to the channel axis (y/b_0 = 0.5). In Fig. 7a, the lines show the distribution of v_{mag}/v_0 at the outflow edge for the problems with different distances l/b_0. The icons, in Fig. 7a, show the distribution of v_{mag}/v_0 for one problem with distance l/b_0 = 35, but in the cross-sections of the channel after the elbow. To compare v_{mag}/v_0 in this problem cross-sections are located at the same distances from the outlet l/b_0. When analyzing the flow asymmetry for the cross-section at the outlet (lines in Fig. 7a), a significant asymmetry of the velocity profile is visible for distances l/b_0 ≤ 8. For l/b_0 = 35, the v_{mag}/v_0 profile is symmetric. Comparison of v_{mag}/v_0 distribution in the channel for l/b_0 = 35 (icons in Fig. 7a) shows a similar to v_{mag}/v_0 distribution at the outlet for various l/b_0 (lines in Fig. 7a) character, but slightly differs quantitatively. This comparison indicates that the flow in a long channel (l/b_0 = 35) is similar to a flow at the outlet for corresponding distances l/b_0 and that the influence of the presence of the supply opening is manifested by a decrease in the velocity value by about 4 %. The distribution of the relative static pressure P_{st}/P_d (Fig. 7b), as in [10], shows that, contrary to the usual simplified representation, the static pressure at the outlet is not equal to zero. Static pressure distribution is significantly affected by the flow deformation associated with the presence of the elbow, especially for l/b_0 ≤ 3. When the distance l/b_0 > 6 increases, the static pressure profile becomes symmetric and tends to zero. To quantitatively evaluate the asymmetry of the profile, the asymmetry coefficients k_{as}, Boussinesq β_0, Coriolis α_0, and velocity field k_0 calculated in the supply opening section using formulas (1–4) are used as described earlier (Fig. 8).

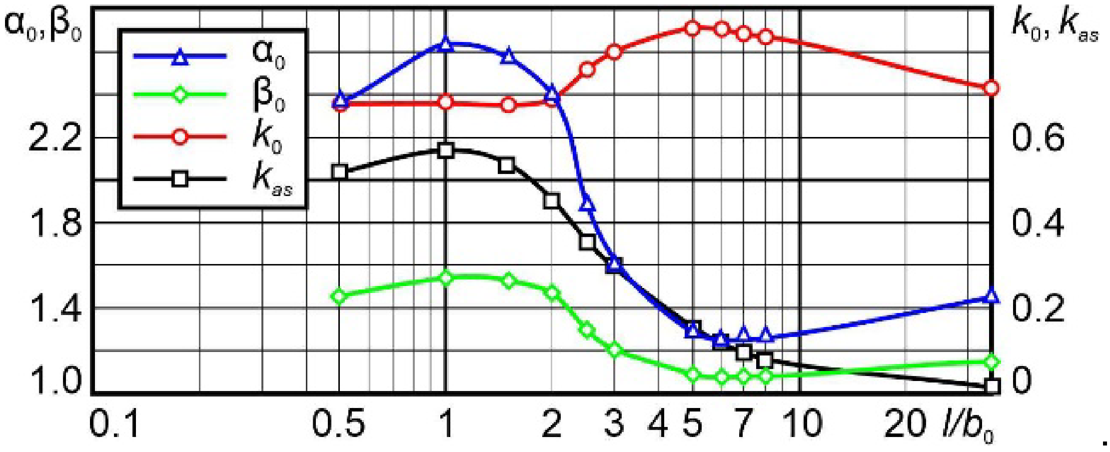

Figure 8. Relationship between the asymmetry coefficients and the distance *l/b₀*.

Here it can be seen that the asymmetry coefficient k_{as} increases with increasing distance l/b_0 from 0.5 to 1, which is due to the increase in flow deformation when the flow is rotated from 0 to 90°. Reaching the maximum of k_{as} ≈ 0.57 at l/b_0 = 1, the asymmetry begins to decrease, and at l/b_0 ≥ 8 it becomes less than 0.08, and at l/b_0 = 35 it is about 0.016, which can apparently be considered an error in numerical modeling. The variation of the Boussinesq coefficients β_0 and Coriolis coefficient α_0 has a similar character, except for the longest distance where the profile becomes more convex. The value of the velocity field coefficient k_0 has an inverse dependence in its formulation. All these coefficients should tend to unity. By the nature of the change of the last three coefficients, it can be seen that although the profile becomes more symmetric, it does not become completely uniform, which can also be seen in Fig. 7a.

The vortex zone formed after the elbow and significant flow irregularity leads to the fact that the jet exit from the supply opening does not occur along the entire cross-section. This jet narrowing leads to a local increase in velocity and errors in the calculations of air distribution devices. Therefore, it is of interest to find the dependence for the effective width of the supply opening on the distance l/b_0. The effective width is determined by the coordinate of the free streamline (outline of vortex zone) crossing the opening cut (Fig. 9).

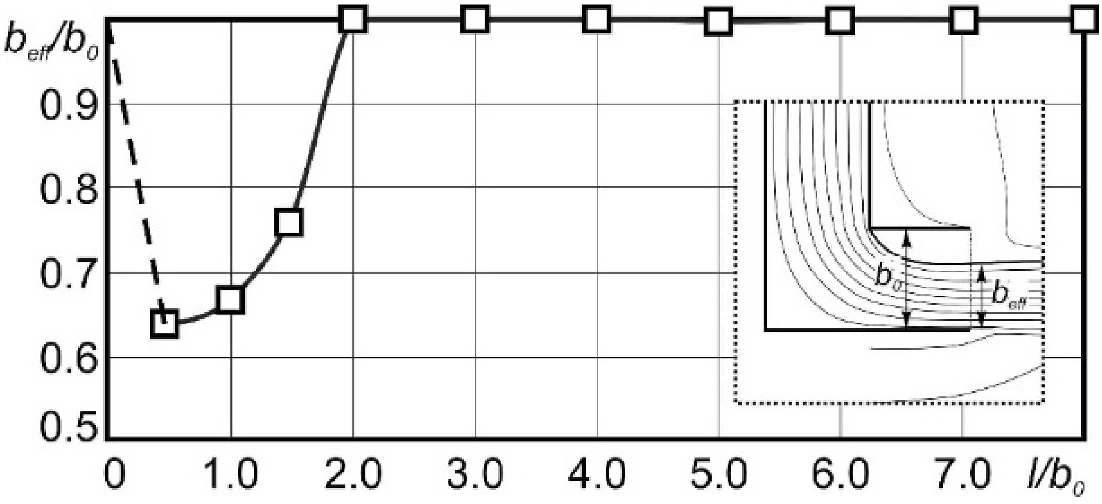

Figure 9. Variation of the effective width of the supply opening (*beff/b0*) for distances *l/b0* = 0.5 ÷ 8.

For l/b_0 = 0.5, a non-minimum value of b_{eff}/b_0 ≈ 0.7 is observed. For small distances to the elbow through the supply opening, the flow in the elbow does not have time to turn completely, and therefore the flow deformation is not maximized. It is clear that at l/b_0 = 0, i.e., when there is no elbow then the case of flow exit through the side end opening is realized. In spite of flow deformation present the effective width b_{eff}/b_0 = 1 [11] (shown by the dashed line). Further, with increasing distance l/b_0, the effective width first decreases, and at l/b_0 = 1 reaches the minimum of b_{eff}/b_0 ≈ 0.6, i.e., the maximum flow deformation and the size of the separation zone exiting through the supply opening are observed. Then, with increasing distance l/b_0, an increasingly smaller part of the vortex zone enters the elbow cross-section of the supply. The effective width begins to increase, and at $l/b_0 \geq 5$ b_{eff}/b_0 it reaches the value of 1, which indicates that the vortex zone ceases to occupy the area of the elbow cross-section of the supply.

The flow deformation introduced by the elbow and affecting the exit conditions will also affect the parameters of the jet flowing out of such an opening. The variation of axial velocity v_{ax}/v_0 along the jet length for cases with different distances l/b_0 is shown in Fig. 10. The variation of axial velocity is plotted using dependence (5) with the kinematic coefficient m = 2.62, which is given in [37] for flat supply openings. The velocity distribution plotted using the relation found analytically in [1] is also given there. The results of CFD and experimental findings of [17] are presented in Fig. 10 (marked with crosses). The mentioned relations are used only for the main section, which tentatively can be taken by the equality v_{ax}/v_0 = 1. It can be seen that at $l/b_0 \geq 2$, the character of the axial velocity change practically coincides with each other and with the data of other authors. This comparison indicates that the elbow does not influence the conditions of flow and jet development. At smaller distances, such influence leads to a difference in the change of axial velocity in the jet. While the character of attenuation remains similar, the velocity values are higher, and the distance l/b_0 is smaller, which is explained by the increase in the maximum velocity at the jet as the deformation increases.

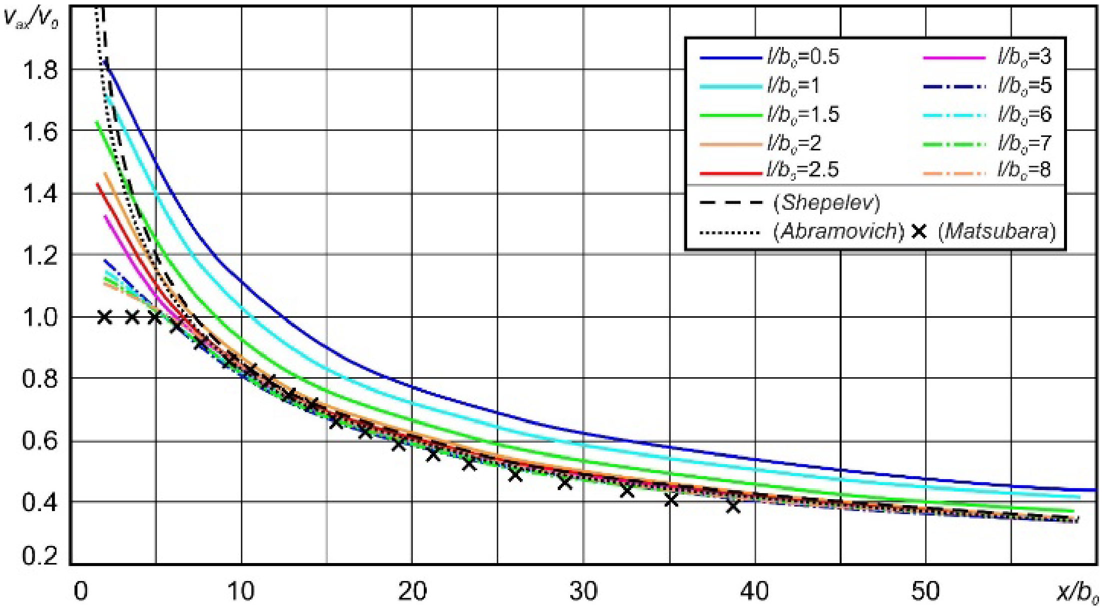

Figure 10. Variation of axial velocity along the jet length for different distances *l/b₀*, and according to [37] (*Shepelev*), [1] (*Abramovich*) and [17] *(Matsubara).*

Taking into account that the character of axial velocity change for small l/b_0 is identical, it is possible to determine the kinematic coefficient m and its dependence on l/b_0 (Fig. 11).

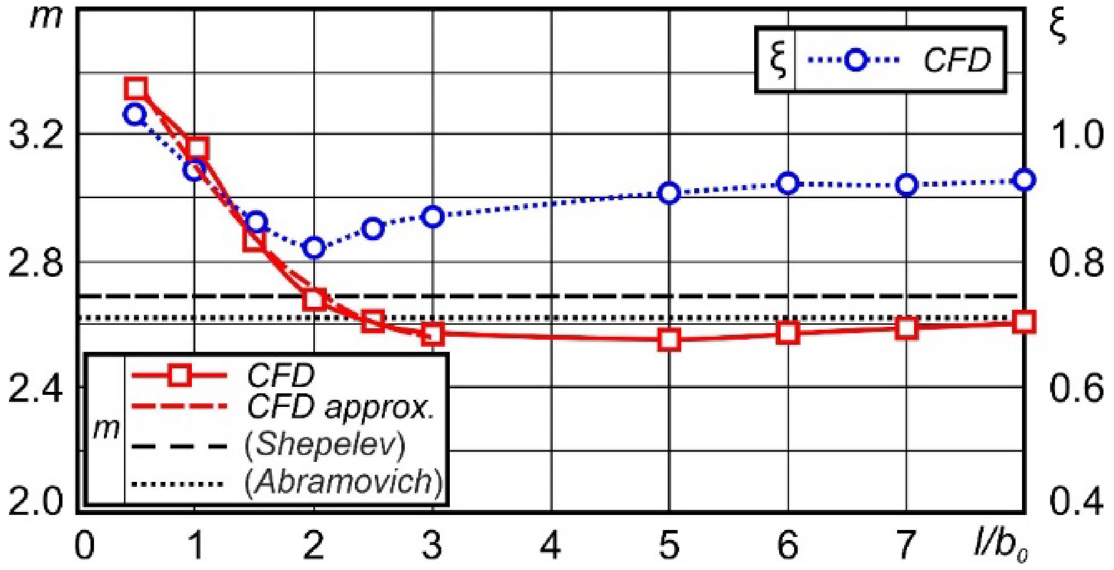

Figure 11. Relationship between m, ξ and *l/b₀*, and the values from [37] (*Shepelev*) and [1] (*Abramovich*).

It can be seen that for l/b_0 > 3 the coefficient m can be considered constant and equal in value to m = 2.56, which is close to the known value m = 2.62 [37]. Accordingly, the influence of the elbow at such distances on the jet development is insignificant. For the range 0.5 ≤ l/b_0 ≤ 3, the dependence of m on l/b_0 is well approximated (R^2 = 0.989) by a polynomial of the second order:

$$m = 0.119 \cdot l/b_0^2 - 0.7418 \cdot l/b_0 + 3.7182.$$

Besides, as stated in [1], the following relationships can be used to determine the change of axial velocity of the jet flowing with irregular initial profile:

$$\frac{v_{ax}^{mag}}{v_0} = \frac{3.8}{\sqrt{2}} \cdot \frac{\xi \cdot \sqrt{\beta_0}}{\sqrt{s/b_0}}, \tag{6}$$

where the Boussinesq coefficient β_0 and an additional coefficient ξ are introduced to account for the irregularity of the profile, which depends on the specific irregularity and the design of the AD and is proposed to be determined empirically. When comparing (6) with (5), it can be seen that the kinematic coefficient in this case will be equal to:

$$m = \frac{3.8}{\sqrt{2}} \cdot \xi \cdot \sqrt{\beta_0}, \text{ and } \xi = \frac{\sqrt{2}}{3.8} \cdot \frac{m}{\sqrt{\beta_0}}.$$

Since, in this case, the opening design is not changed and the irregularity of the profile depends on the distance from the elbow, the relationship between the coefficient ξ and the distance l/b_0 is plotted from the results of the numerical study (Fig. 11). This relationship can also be used to determine the attenuation of the axial velocity of a jet flowing out of a supply opening located after the elbow at the distance l/b_0.

4. Conclusion

1. The presence of the elbow before the supply opening significantly affects the profiles of the longitudinal and transverse velocity and static pressure components at the outlet. At l/b_0 < 5, this influence leads to significant flow deformations and must be taken into account. At l/b_0 > 5, the profiles begin to equalize. However, even at a distance of 8 gauge, the profile remains asymmetrical.
2. At l/b_0 < 5, the flow does not occur over the entire width of the supply opening.

3. At the minimum of the investigated distances l/b_0 = 0.5, the maximum negative angle of jet inclination relative to the geometric axis of the air distributor is observed. In the range of 1 ≤ l/b_0 ≤ 3, the jet inclination angle increases, and further, at a greater distance from the turn, the flow angle is 0.
4. The dependence of the kinematic coefficient m on the distance between the elbow and the supply opening for the range 0.5 ≤ l/b_0 ≤ 8 is plotted.

Thus, the presence of the elbow affects the flow characteristics both at the unit “elbow - supply opening” and at the characteristics of the supply jet. The influence is significant on downstream characteristics – jet and flow parameters at the outlet of the supply opening at the distances l/b_0 < 5. For such units, it is recommended to use the dependences found in this study. At distances l/b_0 > 5, the presence of an elbow before the supply opening can be neglected with accuracy sufficient for design calculations. For the upstream parameters – vortex zone outline, the influence is significant for distances l/b_0 < 2.

As limitations and further prospects for the development of the study, it should be noted that the flows in such units, where several shaped elements are in close proximity to each other, should also be studied from the point of view of aerodynamic resistance, as it is done, for example, in the works on the study of mutual influence of elbows [36, 38, 39]. For such a study, it is possible to use the existing computer models to obtain data on the pressure distribution in the studied units in order to determine the local drag coefficients, the lengths of influence zones, critical distances, and their dependence on the distance between the elbow and the supply opening. It needs experimental validation to obtain the design dependencies [40].

References

1. Abramovich, G.N. The Theory of Turbulent Jets. Cambridge: The MIT Press, 2003. 671 p.
2. Görtler, H. Berechnung von Aufgaben der freien Turbulenz auf Grund eines neuen Näherungsansatzes. ZAMM – Journal of Applied Mathematics and Mechanics / Zeitschrift für Angewandte Mathematik und Mechanik. 1942. 22(5). Pp. 244–254. DOI: 10.1002/zamm.19420220503
3. Miller, D.R., Comings, E.W. Static pressure distribution in the free turbulent jet. Journal of Fluid Mechanics. 1957. 3(1). Pp. 1–16. DOI: 10.1017/S0022112057000440
4. Gori, F., Nino, E. Fluid dynamics measurements and flow visualizations of a free slot jet of air. ASME 2003 International Mechanical Engineering Congress and Exposition. 2003. Pp. 187–192. DOI: 10.1115/IMECE2003-41027
5. Gori, F., Petracci, I., Angelino, M. Influence of the Reynolds number on the instant flow evolution of a turbulent rectangular free jet of air. International Journal of Heat and Fluid Flow. 2014. 50. Pp. 386–401. DOI: 10.1016/j.ijheatfluidflow.2014.10.001
6. Gori, F., Petracci, I., Angelino, M. Flow evolution of a turbulent submerged two-dimensional rectangular free jet of air. Average Particle Image Velocimetry (PIV) visualizations and measurements. International Journal of Heat and Fluid Flow. 2013. 44. Pp. 764–775. DOI: 10.1016/j.ijheatfluidflow.2013.10.006
7. Zhou, Y., Zhu, H., Wang, M., Wang, M., Wang, Y. Entrainment analysis based on the field synergy principle and air terminal device design. Procedia Engineering. 2017. 205. Pp. 1718–1724. DOI: 10.1016/j.proeng.2017.10.372
8. Ward-Smith, A.J., Lane, D.L., Reynolds, A.J., Sahin, B., Shawe, D.J. Flow regimes in wide-angle screened diffusers. International Journal of Mechanical Sciences. 1991. 33(1). Pp. 41–54. DOI: 10.1016/0020-7403(91)90026-Y
9. Noui-Mehidi, M.N., Wu, J., Šutalo, I.D., Grainger, C. Velocity distribution downstream of an asymmetric wide-angle diffuser. Experimental Thermal and Fluid Science. 2005. 29(6). Pp. 649–657. DOI: 10.1016/j.expthermflusci.2004.10.002
10. Posokhin, V.N., Ziganshin, A.M., Varsegova, E.V. Numerical determination of the supply of air terminal characteristics. Izvestiya KGASU. 2017. 1(39). Pp. 173–179.
11. Ziganshin, A.M., Batrova, K.E., Gimadieva, G.A. Chislennoe opredelenie kharakteristik techeniia cherez poslednee bokovoe otverstie v vozdukhovode [Numerical determination of flow characteristics through the last side opening in an air duct]. News of higher educational institutions. Construction. 2018. (7). Pp. 53–65.
12. Ziganshin, A.M., Gimadieva, G.A., Batrova, K.E. The pressure losses and the characteristics of the jet flowing through the middle lateral outlet. Izvestiya KGASU. 2017. 4(42). Pp. 257–265.
13. Denisikhina, D.M. Calculation of the air exchange coefficient based on CFD-simulation methods. News KSUAE. 2023. 4(66). Pp. 337–345. DOI: 10.52409/20731523_2023_4_337
14. Cehlin, M., Moshfegh, B. Numerical modeling of a complex diffuser in a room with displacement ventilation. Building and Environment. 2010. 45(10). Pp. 2240–2252. DOI: 10.1016/j.buildenv.2010.04.008
15. Kocharyantc, K.V., Tislenko, I.N. Experimental investigations of a non-isothermal air jet. News KSUAE. 2024. 2(68). Pp. 6–16. DOI: 10.48612/NewsKSUAE/68.1
16. Magnier, L., Zmeureanu, R., Derome, D. Experimental assessment of the velocity and temperature distribution in an indoor displacement ventilation jet. Building and Environment. 2012. 47. Pp. 150–160. DOI: 10.1016/j.buildenv.2011.07.029
17. Matsubara, M., Alfredsson, P.H., Segalini, A. Linear modes in a planar turbulent jet. Journal of Fluid Mechanics. 2020. 888. Article no. A26. DOI: 10.1017/jfm.2020.25
18. Yao, T., Lin, Z. An experimental and numerical study on the effect of air terminal layout on the performance of stratum ventilation. Building and Environment. 2014. 82. Pp. 75–86. DOI: 10.1016/j.buildenv.2014.08.016

19. Agafanov, B.A., Sarchin, R.R., Osipova, L.E., Varsegova, E.V. Calculation of a fire controlled by ventilation. Construction, buildings and structures. 2022. 1(1). Pp. 40–49.
20. Gabidullina, A.M., Krainov, D.V. Design of external and internal engineering systems of a sports complex with a swimming pool using information modeling technology. Construction, buildings and structures. 2023. 2(3). Pp. 27–36.
21. Halibart, J., Zwolińska, K., Borowski, M., Jaszczur, M. Analysis of the velocity distribution in the plenum box with various entries. Energies. 2021. 14(12). Article no. 3630. DOI: 10.3390/en14123630
22. Nielsen, P.V. Velocity distribution in a room ventilated by displacement ventilation and wall-mounted air terminal devices. Energy and Buildings. 2000. 31(3). Pp. 179–187. DOI: 10.1016/S0378-7788(99)00012-2
23. Aziz, M.A., Gad, I.A.M., Mohammed, E.S.F.A., Mohammed, R.H. Experimental and numerical study of influence of air ceiling diffusers on room air flow characteristics. Energy and Buildings. 2012. 55. Pp. 738–746. DOI: 10.1016/j.enbuild.2012.09.027
24. Yin, H., Li, A. Study of attached air curtain ventilation within a full-scale enclosure: comparison of four turbulence models. Indoor and Built Environment. 2016. 25(6). Pp. 962–975. DOI: 10.1177/1420326X16655593
25. Tian, X., Yin, H., Ji, D., Zhao, W., Shang, T., Hu, Z., Li, A. Airflow collision characteristics of double square column attachment ventilation. Building and Environment. 2024. 260. Article no. 111696. DOI: 10.1016/j.buildenv.2024.111696
26. Yin, H., Li, Y., Zhang, D., Han, Y., Wang, J., Zhang, Y., Li, A. Airflow pattern and performance of attached ventilation for two types of tiny spaces. Building Simulation. 2022. 15. Pp. 1491–1506. DOI: 10.1007/s12273-021-0876-6
27. Guo, J., Li, A., Gao, R., Hou, Y., Wang, T., Li, J., Yin, Y., Che, L. Analysis and comparison of airflow-respirable dust control and innovative ventilation environment in drilling construction tunnels. Atmospheric Pollution Research. 2023. 14(11). Article no. 101908. DOI: 10.1016/j.apr.2023.101908
28. Chang, Z., Zhang, C., Yin, H., Zhai, M., Li, Y., Shi, Z., Ma, Y., Tang, C., Li, A. An attachment oxygen supply method for improving the sleep space environment in the Tibetan Plateau. Journal of Building Engineering. 2024. 94. Article no. 109896. DOI: 10.1016/j.jobe.2024.109896
29. Kim, G., Schaefer, L., Lim, T.S., Kim, J.T. Thermal comfort prediction of an underfloor air distribution system in a large indoor environment. Energy and Buildings. 2013. 64. Pp. 323–331. DOI: 10.1016/j.enbuild.2013.05.003
30. Kareeva, J.R., Zakieva, R.R. Verification of the numerical model of the process of jet outflow from the inlet at an angle. Izvestija KGASU. 2021. 4(58). Pp. 82–89. DOI: 10.52409/20731523_2021_4_82
31. Kareeva, J.R., Varsegova, E.V., Bliznjakova, K.A., Zakieva, R.R. Research of the geometrical parameters of air inlet hole influence on the characteristics of jet. Izvestija KGASU. 2020. 4(54). Pp. 104–111.
32. Kareeva, J., Zakieva, R., Bliznjakova, K. Numerical study of the influence of the inlet geometric parameters on the jet characteristics. Proceedings of STCCE 2021. 2021. 169. Pp. 364–371. DOI: 10.1007/978-3-030-80103-8_39
33. Kareeva, J., Ziganshin, A., Narsova, K. Verification and validation of numerical model of flow in supply opening with elbow unit. Proceedings of STCCE 2022. 2023. 291. Pp. 343–352. DOI: 10.1007/978-3-031-14623-7_30
34. Haase, D. Strömung in einem 90°-Knie. Ingenieur-Archiv. 1954. 22. Pp. 282–292. DOI: 10.1007/BF00536548
35. Heskestad, G. Two-dimensional miter-bend flow. Journal of Basic Engineering. 1971. 93(3). Pp. 433–443. DOI: 10.1115/1.3425271
36. Ziganshin, A., Solodova, E., Logachev, K. Numerical simulation of a Z-shaped ventilation elbow and reduction of its resistance. IOP Conference Series: Materials Science and Engineering. 2020. 890. Article no. 012146. DOI: 10.1088/1757-899X/890/1/012146
37. Shepelev, I.A. Aerodinamika vozdushnykh potokov v pomeshchenii [Aerodynamics of indoor air flows]. Moscow: Stroyizdat, 1978. 144 p.
38. Idel'chik, I.E. Handbook of Hydraulic Resistance, 3rd ed. Boca Raton (USA): CRC Press, 1993. 816 p.
39. Solodova, E.E. Features of flows numerical modeling of Z-shaped elbows of ventilation and air conditioning systems of buildings and structures. Izvestiya KGASU. 2021. 1(55). Pp. 71–84. DOI: 10.52409/20731523_2021_1_71
40. Nigmatullina, G.F., Azizov, B.R., Varsegova, E.V., Osipova, L.E. Determination of coefficients of local resistances of press-fittings in laminar and transient modes of fluid flow. Construction, buildings and structures. 2023. 3(3). Pp. 18–26.

Information about the authors:

Julia Kareeva*,*
ORCID: https://orcid.org/0000-0002-9497-349X
E-mail: jkareeva2503@gmail.com

Arslan Ziganshin*,*
ORCID: https://orcid.org/0000-0001-7335-7797
E-mail: ziganshin.arslan@gmail.com

Konstantin Logachev*,*
ORCID: https://orcid.org/0000-0003-0632-6784
E-mail: kilogachev@mail.ru

Kseniya Narsova*,*
ORCID: https://orcid.org/0000-0003-3857-6980
E-mail: ksenia.bliznyakova@yandex.ru

Received: 19.02.2025. Approved: 15.05.2025. Accepted: 16.05.2025.